Detection of laser–accelerated protons

Sabine Reinhardt

München 2012

Detection of laser–accelerated protons

Sabine Reinhardt

Dissertation
an der Fakultät für Physik
der Ludwig–Maximilians–Universität
München

vorgelegt von
Sabine Reinhardt
aus Malsch, Kreis Karlsruhe

München, den 19.06.2012

Erstgutachter: Prof. Dr. Jörg Schreiber
Zweitgutachter: Prof. Dr. Jan J. Wilkens
Tag der mündlichen Prüfung: 08.08.2012

Contents

List of Figures

List of Tables

Zusammenfassung

Der Echtzeit (Online)–Nachweis Laser–beschleunigter Protonen stellt insbesondere aufgrund der sehr speziellen Zeitstruktur ($\leqq$ ns) und hohen Intensität ($\geqq 10^7$ p/cm^2) der generierten Ionen–Pulse eine große Herausforderung für elektronische Detektoren dar. Neben massiven Sättigungseffekten sind zusätzliche Probleme durch einen elektromagnetischen Puls (EMP) bei der Laser– Plasma–Wechselwirkung zu erwarten. Im Rahmen dieser Arbeit wurden für die speziellen Anforderungen der Ionen–Beschleunigung am MPQ–ATLAS Laser verschiedene Detektionssysteme aufgebaut, die eine quantitative Analyse des Protonenstrahles erlauben.
Ein Zellexperiment am ATLAS–Laser diente dazu, die Eignung Laser–beschleunigter Protonen für die Strahlentherapie zu zeigen. Zellen wurden bei einer Protonenenergie von 5 MeV mit Einzelschußdosen von mehreren Gy, die für die spätere Zellanalyse ortsaufgelöst nachgewiesen werden mussten, bestrahlt. Wegen der geringen Reichweite der Protonen kamen hierfür nur strahlen–sensitive Filme in Frage, die allerdings signifikante Quenching Effekte bei der verwendeten Protonenenergie zeigen. Dazu wurden umfangreiche Untersuchungen in einem Energiebereich von 3–200 MeV durchgeführt. Ein Film–basiertes Dosimetrieprotokoll für die nieder–energetische Protonenbestrahlungen wurde entwickelt, und dadurch die Messungen der Absolutdosis im Zellexperiment ermöglicht.
Die nicht–elektronischen Detektoren (Kernspurdetektoren, strahlen–sensitive Filme) sind nach wie vor Stand der Technik in der Diagnostik Laser–beschleunigter Ionen, obwohl diese Art von Detektoren nur einen zeitlich verzögerten (Offline) Nachweis erlaubt. Erstmals wurde für die laufenden Experimente am ATLAS Laser ein solches nicht–elektronisches System, basierend auf Image Plates, vollständig charakterisiert und kalibriert. Hauptziel der vorliegenden Arbeit war jedoch der Aufbau eines Echtzeit–Detektion–Systems, welches durch die zunehmenden Repetitionsrate des Laserbeschleunigers ($>$ Hz) dringend benötigt wurde, um die Parameteroptimierung bei der Laserbeschleunigung effektiv vorantreiben zu können. Geeignet sind beispielsweise Systeme, die auf Silizium–Pixeldetektoren basieren. Die Segmentierung der sensitiven Gesamtfläche in kleinere, individuelle Detektionseinheiten (Pixel) ermöglicht im Vergleich zu einem unsegmentierten Sensor gleicher Gesamtfläche die Messung höherer Flüsse—ein Konzept, dass auch am LHC Anwendung findet.
In dieser Arbeit wurden drei Pixeldetektoren unterschiedlicher Architektur in umfangreichen Experimenten auf ihre Eignung zum Nachweis Laser–beschleunigter Protonen untersucht. Das Ansprechvermögen der Detektoren auf ultra–kurze und hoch intensive Protonenpulse wurde an einem konventionellen Beschleuniger auf Linearität und Sättigungseffekte untersucht. Jedes der untersuchten Systeme war in der Lage einzelne Protonen nachzuweisen. Allerdings konnten nur zwei der Systeme einen Protonenfluss bis zu 10^7 p/cm^2/ns (20 MeV) ohne Sättigungseffekte detektieren. Für das final gewählte System wurde dies auch am ATLAS Laser demonstriert. Hier, wie am Astra–Gemini Laser mit bis zu 6 J Pulsenergie wurde keinerlei EMP–Empfindlichkeit festgestellt. Die Ausleseelektronik des Detektors

wurde mit einem Computer in einem eigenständigen System vereinigt und um eine benutzerfreundliche Software erweitert. Es stehen nunmehr ein kompaktes Online System sowie ein Dosimetrieprotokoll zur Verfügung, welche die Anforderungen des momentanen Stands der Laserbeschleunigung erfüllen können.

Abstract

Real–time (Online) detection of laser–accelerated protons is a challenge for any electronic detector system due to the peculiar time structure ($\leqq$ ns) and high intensity ($\geqq 10^7$ p/cm^2) of the generated ion pulses. Besides considerable saturation effects, problems are expected by an electromagnetic interference pulse (EMP), generated during laser–plasma interaction. In the scope of this work, different detection systems were built–up with regard to specific demands of laser–ion–acceleration at the MPQ ATLAS laser, which allow the quantitative analysis of the generated proton beam.
A cell irradiation experiment at the ATLAS laser was accomplished to demonstrate the usability of laser–accelerated protons for radiation therapy. Cells were irradiated with a single shot dose of few Gy for a proton energy of 5 MeV. The following cell analysis required the spatially resolved measurement of the dose distribution. Only radiation–sensitive films were applicable because of the small proton range, although they show significant quenching effects for the used proton energy. This was extensively studied in the 3–200 MeV energy range. A film–based dosimetry protocol for low–energy proton irradiations was developed, making the absolute dose determination in the cell experiment possible.
The non–electronic detectors (nuclear track detectors, radiation–sensitive films) are still state of the art in laser–accelerated ion diagnostics, although these detectors only allow a delayed in time (offline) detection. A non–electronic system, based on image plates, was thoroughly characterized and calibrated for ongoing experiments at the ATLAS laser, for the first time. Main objective of this work, though, was the set–up of a real–time detection system, which is urgently required, owing to increasing repetition rate of the laser accelerator ($>$ Hz), to advance the parameter optimisation of the laser–acceleration in an efficient way. Systems based on silicon pixel detectors are applicable for this purpose. Segmentation of the sensitive area into smaller, independent detection units (pixel) allows the measurement of a higher particle flux compared to an unsegmented sensor of the same size—a concept used at the LHC.
Within this work, three pixel detectors of different architectures were investigated in extensive experiments with respect to their applicability for laser–accelerated proton detection. The detector response to ultra–short highly–intense proton pulses was studied at a conventional accelerator in view of linearity and saturation effects. All systems allow single proton detection. However, only two of the systems were able to detect a proton flux of up to 10^7 p/cm^2/ns (20 MeV) without saturation. This was also confirmed at the ATLAS laser for the final selected system. No EMP sensitivity was observed there as well as at the ASTRA–GEMINI laser with up to 6 J pulse energy. The read–out electronic of the detector and a computer system were integrated into a stand–alone system, which was upgraded by an user–friendly software. Hence, a compact online detection system as well as a dosimetry protocol were made available, which fulfil the demands of the momentary state of affairs of the laser–ion–acceleration.

1 Introduction

Focused TW–laser systems are able to accelerate ions to energies in the MeV range within a few μm distances. Resulting ultra–short ion pulses ($> 10^7$ particles/cm^2/ns) pose a challenge for **electronic real–time detection**. The presence of a mixed radiation background, and, especially EMP, in the course of the laser–acceleration process, aggravates difficulties of electronic detection even further. Therefore, most laser–ion–acceleration experiments to date use non–electronic detectors. No prompt, quantitative information is available from these kind of detectors, additionally requiring replacement from laser shot to laser shot. Development of compact, high repetition rate laser accelerators is, hence, in an urgent need for online detection systems.

Though laser–based ion acceleration is still at an early technological stage, today, future application of laser accelerators in ion–based radiation therapy is already discussed all over the world. For this kind of application, quantitative real–time beam monitoring with accuracy better than 3–4 % is mandatory [1].

A favourable depth dose distribution of ions compared to photons allows a highly conformal radiation therapy. But, costs of an ion beam treatment place are out of all proportion to costs of conventional photon–based ones. This is caused by the required infrastructure for ion beam delivery, comprising accelerator, beam transport and, most notably, special gantry systems to rotate the beam around the patient. As a result, only a limited number of ion beam therapy facilities exists world–wide. The idea of utilizing laser accelerators as future medical accelerators takes advantage of short acceleration distances in the order of few μm. All concepts of a laser–based radiation therapy are based on ion beam generation in close distance to the patient, offering the potential to make a large amount of ion beam delivery infrastructure dispensable and ion beam therapy possibly more cost effective [2, 3].

However, many basic problems of laser ion acceleration itself, such as maximum achievable energies, shot to shot reproducibility or predictability of ion pulse spectra, still have to be addressed until feasibility and possible benefits in ion beam therapy can be clarified. In the radiation pressure acceleration (RPA) regime up to 10^{12} protons of 235 MeV are expected for a laser energy of 60 J in a single pulse of few tens of fs duration, which would be sufficient for particle therapy. Such a particle pulse number is comparable to bunch intensities at the Large Hadron Collider (LHC), offering the highest proton luminosity, today. Quantitative real–time detection of laser–accelerated ion beams is one task to be solved, a contribution to answer this problem is made by the present work.

In the following, physical fundamentals of laser–acceleration of ion beams are summarized by means of the two most important acceleration schemes today. Differences of resulting ion beams with respect to conventionally accelerated ones, are specified with emphasis on the consequences for their detection (sec. 1.1.4).

1.1 Laser–acceleration of particle beams

In 1960, the first laser, a pulsed ruby laser, was built and since then, fast progress in laser technology and especially intensity is observed (fig. 1.1).

Direct generation of laser intensities in the TW, or even PW, regime is not possible, as

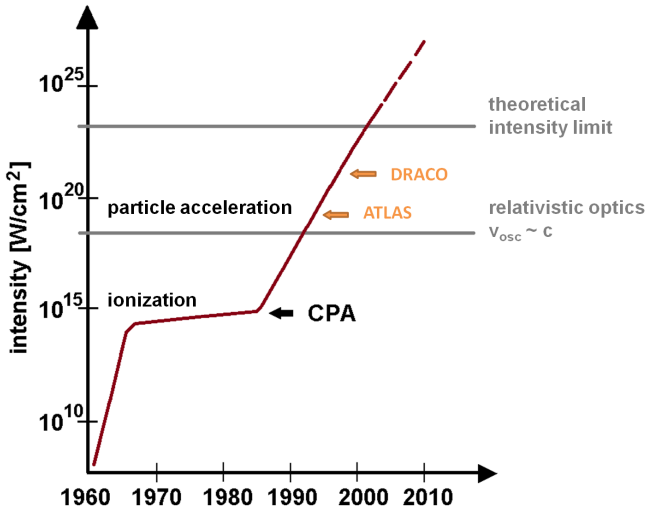

Figure 1.1: **Laser intensity evolution** (adapted from [4])
Laser technology experienced a strong and still ongoing evolution, in particular towards higher intensities. Laser–driven ion acceleration becomes feasible for intensities exceeding 10^{18} W/cm^2, available at different laser facilities such as the MPQ ATLAS or DRACO laser of the HZDR.

nonlinear effects would inevitably damage the amplifier medium. However, chirped–pulse amplification (CPA), first proposed by Strickland and Moureau in 1985 [5], presents a way to circumvent this problem. The basic concept of CPA is the reduction of the pulse peak intensity below the amplifier's damage threshold. This is achieved by temporal stretching of such a fs–laser pulse before it is allowed to enter the amplification medium. After amplification, re–compression of the pulse restores the original pulse width. Thus, amplification factors as large as 10^8 are possible, resulting in ultra–high intensities exceeding 10^{18} W/cm^2.

Today's high intensity laser systems in the TW regime, are pulsed lasers with several Hz repetition rate to single shots per hour, offering peak energies and pulse widths of up to few tens of Joule and femto–seconds, respectively (tab. 1.1). The experimental work of this thesis has been accomplished in parts at the ATLAS laser of the Max–Planck Institute for Quantum Optics (MPQ) in Garching and the DRACO laser of the Helmholtz–Zentrum Dresden–Rossendorf (HZDR), both Ti:Sapphire laser systems with up to 10 Hz repetition rate. Pulse energies of 2 J for ATLAS, and up to 3 J for DRACO, respectively, are delivered within 30 fs pulses.

Any short–pulsed laser has a temporal pedestal in the hundred ps time scale, emerging from amplified spontaneous emission (ASE) and imperfections of optical elements, which introduce ghost pulses in front or after the main laser pulse. A measure for the temporal pedestal is the so–called pulse contrast, defined as ratio of time–dependent pedestal intensity and

High repetition rate Ti:Sa laser systems

facility	amplifier	energy [J]	pulse width [fs]	power [TW]	repetition rate [Hz]
ASTRA GEMINI	Ti:Sapphire	2 × 15	30	2 × 500	0.05
ATLAS	Ti:Sapphire	2	30	100	10
DRACO	Ti:Sapphire	3	30	150	10
MBI	Ti:Sapphire	1.4	35	40	10

PW–class glass laser systems

facility	amplifier	energy [J]	pulse width [fs]	power [TW]	repetition rate [Hz]
PHELIX	Nd:glass	120	500	240	single shot
TRIDENT	Nd:glass	120	500	240	single shot
VULCAN (Petawatt)	Nd:glass	600	600	1000	single shot

Table 1.1: **Some high intensity laser facilities, collaborating in laser ion acceleration experiments with Munich (adapted from [6])**

main pulse intensity. A good contrast is required for efficient laser ion acceleration to prevent pre–pulses or the ASE pedestal from initiating the acceleration mechanism or, in the worst case, even destroying the target. Typical contrast values are of the order of 10^{-3}–10^{-10}, depending on the source of the preceding light. Improvement by more than two orders of magnitude is possible by means of double plasma mirrors [7–12].

1.1.1 Laser plasma interaction

Interaction of an ultra–high intensity laser with matter is essentially a laser plasma interaction. An intensity I exceeding 10^{12} W/cm^2 is sufficient to overcome the binding energy of a valence electron (fig. 1.1) [6]. Therefore, matter is rapidly ionized by high–intensity laser pulses, either by pre–pulse, or, in case of a high pulse contrast, by the rising pulse edge. Depending on the laser intensity, different ionization mechanisms are involved in plasma generation [6]. Multi–photon absorption, comparable to the photoelectric effect (sec. 2.1.1), but involving simultaneous absorption of multiple photons, is one possible process. Other ionization processes are based on the distortion of the Coulomb potential by the electric laser field, which allows electrons to escape (field ionization).
Interaction of an ultra–high intensity laser with matter gives rise to new physical regimes such as relativistic optics. In this regime, electrons oscillate in the electric field of the laser with relativistic velocities. Relativistic mass gain as well as magnetic contributions of the Lorentz force, neglected in classical optics, have to be considered and relativistic, non–linear effects such as relativistic self–focusing or profile steepening are observed [13].
In particular laser–driven acceleration of ions is an important application that becomes feasible in the relativistic optics regime. Several MeV of ion energy can be gained over distances of a few micrometers. So far, maximum laser intensities of $\ll 10^{24}$ W/cm^2, are not sufficient for direct ion acceleration due to the high ion masses. Ion acceleration is a two step process,

involving the generation of a charge separation field and subsequent ion acceleration therein. Interaction of an electromagnetic laser field (wavelength $\lambda_0 = 2\pi c/\omega_0$) with electrons (charge e, mass m_e, velocity $\vec{\beta}$) causes the generation of the required charge separation field. The electromagnetic field is described by the vector potential $\vec{A}_0(\vec{r},t)$, from which both, electric ($\vec{E}(\vec{r},t)$) and magnetic field vector ($\vec{B}(\vec{r},t)$) can be derived (eq. 1.1).

$$\vec{A}(\vec{r},t) = \vec{A_0} \cdot \cos(\vec{k}\cdot\vec{r} - \omega_0 \cdot t) \tag{1.1a}$$

$$\vec{E}(\vec{r},t) = \frac{\partial \vec{A}(\vec{r},t)}{\partial t} \tag{1.1b}$$

$$\vec{B}(\vec{r},t) = \nabla \times \vec{A}(\vec{r},t) \tag{1.1c}$$

The Lorentz force (eq. 1.2) describes the equation of motion of a single electron.

$$\frac{d\vec{p}}{dt} = -e[\vec{E} + c\vec{\beta} \times \vec{B}] \tag{1.2}$$

$$= -e[\frac{\partial \vec{A_0}(\vec{r},t)}{\partial t} + c\vec{\beta} \times \nabla \times \vec{A_0}(\vec{r},t)] \tag{1.3}$$

Without loss of generality, a plane wave ($\vec{A_0} = A_0\widehat{e_x}$) , propagating in z–direction $\widehat{e_z}$ is assumed, yielding.

$$\frac{d\vec{p}}{dt} = 2\pi a_0 \frac{m_e c^2}{\lambda_0}(-(1+\beta_z)\widehat{e_x} + \beta_x \cdot \widehat{e_z}) \cdot sin(kz - \omega_0 t) \tag{1.4}$$

Here, the laser field vector potential has been transformed into the dimensionless parameter a_0.

$$a_0 = \frac{|\vec{A_0}| \cdot e}{m_e \cdot c} \tag{1.5}$$

For non–relativistic electron velocities ($\beta \ll 1$), influence of the magnetic field component can be neglected and electron motion is described by an oscillation in the electric laser field. For relativistic electron velocities $\beta \approx 1$, the magnetic field component leads to an additional electron motion in direction of the propagating laser field. The Lorentz force also acts on the ions (ze, m_{ion}), but due to their higher mass, resulting ion motion can be neglected for all available laser intensities, today. Electron motion is only maintained during laser–electron interaction. Hence, in the simple picture of a plane wave, electrons do not gain any net energy in this process. However, so far, only the interaction of a single electron with a high intense electromagnetic field has been considered. On the other hand, plasma, as a collective of stationary ions and free electrons, also has an impact on the laser pulse itself. Electrons and thus, electron density n_e, oscillate with the plasma frequency ω_p. ϵ denotes the dielectric constant of the plasma in eq. 1.6 and the Lorentz factor $\gamma = \sqrt{1-\beta^2}^{-1}$.

$$\omega_p = \sqrt{\frac{n_e \cdot e^2}{\epsilon \cdot \gamma \cdot m_e}} \tag{1.6}$$

The proportion of plasma and laser oscillation frequency ω_0 determines if laser propagation in the plasma is possible. This is related to the critical plasma density n_c, which is defined by the case that the plasma frequency equals the laser frequency ($\omega_p = \omega_0$) (eq. 1.7).

$$n_c = \frac{\gamma m_e \cdot \epsilon \cdot \omega_0^2}{e^2} \tag{1.7}$$

For $\omega_p \gg \omega_0$ propagation is inhibited and the skin depth, $l_s = \frac{c}{\omega_p}$, describes the maximum penetration depth of the laser in the plasma, which is said to be overdense ($n_p > n_c$). Solid targets, which are mostly used for laser ion acceleration, fulfil this condition.
For any laser plasma interaction, both, laser and plasma influence each other. There are different absorption mechanisms, such as resonant absorption, Brunel absorption or JxB heating, that allow an energy transfer from the laser pulse to the plasma electrons [12]. As a result, electrons are accelerated. Different electron acceleration mechanisms exist, depending on laser as well as plasma parameters. Electron acceleration is an important prerequisite for the generation of a charge separation field and, thus, ion acceleration. However, details on electron acceleration mechanisms are beyond the scope of this work, but can be found e.g. in [14, 15].
Different ion acceleration mechanisms have been reported depending on laser but also target parameters. A detailed review of the physical processes of laser–acceleration of ions can be found in references [12, 16]. In the following, two of these different ion acceleration regimes, target normal sheath acceleration (TNSA) and radiation pressure acceleration (RPA) are shortly presented. Both acceleration mechanisms rely on the interaction of a laser with a solid target. Usually thin metallic or diamond like carbon (DLC) foils of few μm (TNSA) to nm (RPA) thickness are used [8, 17]. A high intensity laser focused onto such a target immediately ionizes a thin surface layer of the foil, generating an overdense surface plasma. TNSA and RPA are the two most important acceleration schemes, as they represent extreme cases of all possible acceleration mechanisms. In TNSA, the ion energy distribution scales with the laser energy, requiring an efficient energy transfer from the laser to the target, which is usually few μm thick. The resulting ion beams have a broad energy spread of several MeV and large divergence angle. RPA relies on the momentum transfer from the laser to the target, thin foils of few nm thickness. In RPA, mono–energetic ion spectra can be obtained, which is, therefore, the most promising acceleration mechanism for future application of laser–acceleration in radiation therapy.

1.1.2 Target Normal Sheath Acceleration (TNSA)

Fig. 1.2 depicts a schematic sketch of the TNSA mechanism, where ions are accelerated in charge separation field normal to the target rear side. A p–polarized laser pulse is focused on the target surface. Laser energy is transferred to the target, heating the electrons. Different absorption processes are responsible for electron heating. In the TW intensity regime, collisions of oscillating electrons and ions are not efficient as both, electron (quiver) velocity and thermal velocity are comparable [18].
Therefore, collision–less absorption processes are dominantly responsible for plasma heating [18]. Surface electrons are pushed into the vacuum by the ponderomotive force of the laser pulse, thereby gaining some net kinetic energy before being re–absorbed in the plasma.

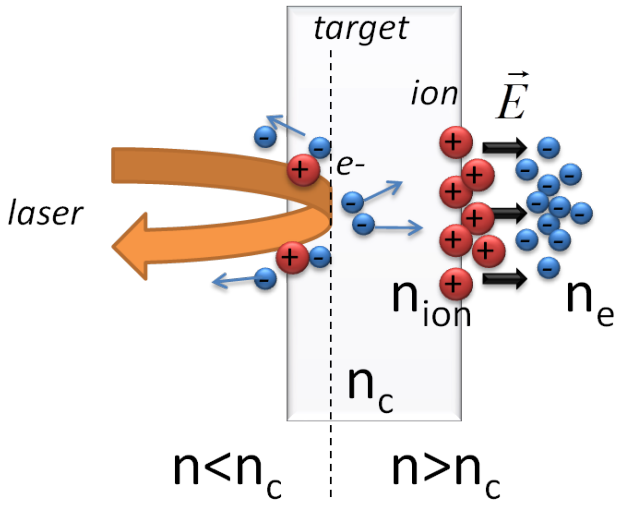

Figure 1.2: **Schematic sketch of the TNSA mechanism**
A thin target surface layer is immediately ionized by the incident laser pulse, which is reflected at the critical density plane n_c. Electrons, heated by the laser energy that is transferred to the plasma, are able to leave the target foil at the front and backside, forming an electron layer. An ion layer builds up at the target surface, giving rise to a quasi–static electric acceleration field, oriented normal to the target surface, in the order of TV/m.

This mechanism, occurring during one half laser cycle, is known as vacuum heating.
Another process is the resonance absorption. In the plasma, a density gradient exists between its surface ($n < n_c$) and the remaining part of the foil with solid density($n > n_c$) (fig. 1.2). The critical density surface reflects the incident laser pulse and a plasma wave is excited by the electric field component of the laser light. Electrons oscillating along the density gradient are accelerated [18].
By means of these processes, up to 50 % of the laser energy can be transferred to the electrons [19]. The resulting hot electron temperature is usually assumed to be equal to the ponderomotive potential (eq. 1.8). Although this approach is highly debated as the hot electron temperature depends on the actual experimental parameters such as plasma scale length, good agreement has been reported for many experiments [12].

$$\overline{W_{kin,e}} = m_e \cdot \gamma \cdot c^2 \approx m_e \cdot c^2 \cdot (\sqrt{1 + a_0^2} - 1) \tag{1.8}$$

Typical values of the laser potential a_0 of 1–5, yield average kinetic electron energies in the MeV range. The bunch of hot electrons is able to traverse, and finally exit the target at the back side and a sheath of hot electrons is formed over the Debye length (eq. 1.9), which is in the order of few μm. Atoms at the back surface are ionized and the emerging quasi–static charge separation field, oriented normal to the target surface, finally accelerates the ions (ion charge ze, density n_{ions}). The electric field strength is proportional to the quotient of average electron energy $\overline{W_{kin,e}}$ and Debye length, yielding en electric field strength in the

order of TV/m for typical few MeV energy and μm lengths.

$$\lambda_{Debye} = \sqrt{\frac{\epsilon \cdot \overline{W_{kin,e}}}{z \cdot e^2 \cdot n_{ion}}} \tag{1.9}$$

Acceleration efficiency depends on the charge to mass ratio of the ions, as ions with different charge to mass ratios are separated in the electric field. High charge to mass ratio particles, leading the ion bunch, effectively shield the acceleration field from trail ions. In almost any experiments, hydrogen contaminants are present at the target surface, therefore, proton acceleration dominates the TNSA regime [16].
First results on proton acceleration in this regime were published in 2000, reporting on proton energies up to 58 MeV and 10^9 protons/MeV for the highest energy. [20]. A Boltzman–like hot electron distribution yields an exponentially decaying ion energy spectrum. Coulomb explosion of the ions during acceleration results in an ion energy spread as large as 100 %. The potential of target design (e.g. micro–structured foils, spherical targets) for improvement of energy and ion distributions, has been investigated in the last years [8,21]. However, the maximum achievable energy and corresponding energy spectrum has not improved since the first TNSA results were published [20], which are, still, the major limitations of TNSA.

1.1.3 Radiation Pressure Acceleration (RPA)

RPA is based on the ponderomotive pressure of the laser pulse, accelerating the target foil as a whole, without generation of a hot electron spectrum. Therefore, narrower energy distributions, compared to TNSA, are expected and first experimental results indicate the feasibility of this acceleration regime [11].
Direct ion acceleration by radiation pressure requires laser intensities exceeding even the presently highest ones by at least three orders of magnitude. However, changing the laser polarization from a linear to a circular one, it is possible to prevent unwanted electron heating and associated drawbacks concerning the ion energy distribution [16, 22].
The ponderomotive force of the laser pulse pushes electrons in forward direction. For circularly polarized light, no longitudinal electron oscillations are driven by the magnetic Lorentz force component. Hence, electron heating is strongly reduced compared to TNSA and linear polarization, respectively. As another consequence, electrons are spatially confined in a small bunch that piles up at the front of an emerging cavity. A charge separation field is generated, pulling surface ions towards the electron spike. The density of the electron bunch exceeds the critical density and totally reflects the laser pulse. In this process, the so–called laser piston is formed, a double layer structure, separating the plasma–free laser propagation path from the shocked plasma. A schematic sketch is depicted in fig. 1.3. The radiation pressure of the laser is balanced by the dynamic pressure of the piston particles, yielding

$$\frac{2I}{c}\frac{1-\beta_{piston}}{1+\beta_{piston}} = 2(m_{ion} + zm_e)n_{ion}c^2\gamma^2\beta_{piston}^2 \tag{1.10}$$

in the piston reference frame [16].
The laser piston propagates with the velocity β_{piston}, thus, pushing the plasma in forward

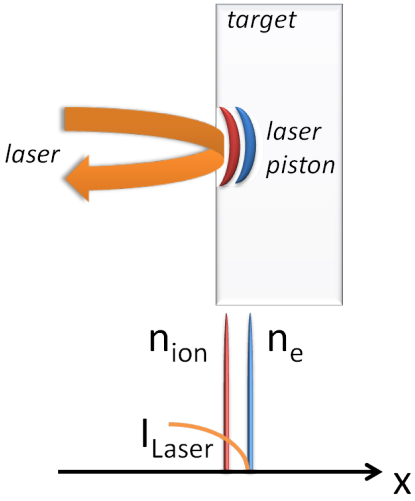

Figure 1.3: **Schematic sketch of the laser piston acceleration**
The laser piston, a hetero–layer of electron and ion bunch, develops due to the ponderomotive force of the laser pulse. Reflection of the laser pulse at the electron spike, pushes the laser piston as a whole in a forward direction.

direction. Using eq. 1.10, the piston velocity and therefore, ion velocity (eq. 1.11) can be determined [16],

$$\beta_{ion} = \frac{2\beta_{piston}c}{1+\beta_{piston}^2} \tag{1.11}$$

$$E_{ion} = m_{ion}c^2(\gamma_{ion}-1) \tag{1.12}$$
$$= 2m_{ion}c^2\gamma_{piston}\beta_{piston} \tag{1.13}$$

The kinetic energy of the ions (eq. 1.12) depends on the piston velocity and is, thus, independent on the ion charge (eq. 1.10) [16]. Therefore, in contrast to TNSA, where light ion, i.e. proton, acceleration is favoured, acceleration of heavy ions is possible, even in presence of hydrogen–containing target contaminations.
Other benefits, compared to TNSA, are not only a narrower energy distribution but also a theoretically predicted higher laser–ion energy conversion of about 13 % [16].
A special case in the RPA regime exists, if very thin targets in the order of few nm are used, where target and piston thickness are of the same order of magnitude. As a consequence of this so–called 'light sail' regime, the piston oscillates and crosses the foil several times if the laser pulse duration exceeds the time required for piston foil crossing. Ions are accelerated during each crossing, resulting in higher final ion energies compared to thick targets [16].
The efficiency η of RPA (eq. 1.14) allows to determine the total number of ions $N_{ion} = \frac{M_{ion}}{m_{ion}}$ that can be accelerated by a laser of energy E_{laser} to a velocity of β_{ion} assuming only a single ion species and non–relativistic ion velocity ($\beta_{ion} \ll 1$). M_{ion} denotes the total mass of all ions. Assuming a laser energy E_{laser} of 60 J and proton velocity of 0.5 c, corresponding to an energy of 235 MeV, up to 10^{12} protons can be accelerated by a single laser pulse.

$$\eta \propto \beta_{ion} = \frac{E_{laser}}{M_{ion}c^2} \qquad \text{for} \beta_{ion} \ll 1 \tag{1.14}$$

However, experimental investigations of the RPA regime just started [11] and theoretical predictions still have to be validated [23, 24]. Encouraging results of ion energies exceeding 100 MeV have been reported recently with the TRIDENT laser of the Los Alamos National Laboratory, delivering 80 J pulse energy to the target. The corresponding conversion efficiency of about 0.3 is comparable to the example given for 235 MeV protons.

1.1.4 Detection of laser–accelerated ions

Laser–based acceleration differs strongly from any conventional process. The main difficulty in detection of laser–accelerated ions is certainly the high instantaneous pulse flux. For both presented acceleration regimes, laser plasma interaction, responsible for ion acceleration, maintains as long as the laser pulse impinges on the target. Hence, generated ion bunches, as a first approximation, mirror the time structure of the laser beam. TW–laser systems have pulse widths of few tens of fs, the ATLAS laser, for instance has a pulse duration of 30 fs. Bunch charges in the order of μC are possible, equivalent to approximately 10^{13} particles per bunch, yielding an instantaneous pulse flux of approximately 10^{12} ions/fs originating from the target interaction point. No electronic detector exists, able to handle a particle number of this order.
During laser–acceleration, not only ions and electrons, but also X–rays are generated. Interaction of these energetic particles with structures within the vacuum chamber, or, the chamber itself, produces additional secondaries, thus, increasing the background of the mixed radiation field, further.
Another problem, relevant for all electronic detectors, is the generation of a large electromagnetic pulse (EMP), which depends amongst other things on pulse energy [25]. Effects of EMP range from an increase in noise to complete signal distortion or even damage of the detection system [25, 26]. Many laser–acceleration experiments, thus, rely on non–electronic particle detectors, such as Image Plates (IP), radiochromic film (RCF) or solid–state nuclear track detectors (SSNTD) (sec. 3.1.1 – 3.1.3).
In any conventional accelerator, the energy spectrum of the particle beam is easily controlled by electric and magnetic fields, typically yielding an energy spread below 0.1 % [27, 28]. In contrast, up to 100 % energy spread is observed for TNSA. Even for optimized targets or RPA, energy resolution of the ion beam cannot compete with conventional accelerators. Moreover, it is not yet possible to control the laser–based acceleration process to yield reproducible ion pulses. Therefore, fluctuations in the measured ion distribution arise from shot to shot and ion detection, able to resolve such shot to shot fluctuations, is all the more an important issue.
Ion detection close to the target is a major challenge. No detector system exists, able to unambiguously discriminate ions from the mixed radiation background and quantitatively measure the energy spectrum of these ion pulses. EMP interference is also most pronounced close to the target. So far, RCF stacks have been used to some degree for ion detection in proximity to the interaction point. Though EMP is no problem for these passive detectors, they primarily only yield estimations for the proton distribution.
The development of laser ion accelerators aims for higher particle energies and improved energy resolution. Quantitative measurement of ion spectra is essential to understand the

influence of various acceleration parameters such as target thickness, laser energy or intensity.
Hence, ion diagnostic usually relies on a combination of an energy selection system such as a Thomson spectrometer and position–sensitive ion detector in the spectrometer's dispersive plane. Charged particles are dispersed by energy and charge–to–mass ratio while propagating through the crossed electric and magnetic fields of the spectrometer, thus, allowing ion separation from unwanted background radiation. Propagation paths through the spectrometer are in the order of $\approx$ 1–2 m, introducing a temporal spread of the ion pulse to few nanoseconds.
Another characteristic of laser–accelerated ion bunches are large divergence angles of tens of degrees [29]. Divergence angles also have shown to depend on ion energy, relating higher energies to smaller source sizes. However, assuming an opening angle of the emerging ion beam of 10 ° regardless of ion energy and a distance of 1 m between target and spectrometer entrance, an ion number of 10^{12} particles corresponds to a fluence of 10^9 particles/cm^2 at the spectrometer entrance. Usually, a small aperture of few mm diameter defines the energy resolution of the system. Even for a 1 mm diameter aperture, ion pulses with more than 10^7 particles/cm^2/ns have to be detected at the spectrometer exit, still being a challenge for any electronic detector system.
Although the use of a spectrometer is beneficial with respect to the mixed radiation background or, to some extend, also pulse flux, many ion acceleration experiments rely on IPs or SSNTD for ion detection. Processing times required to obtain reliable quantitative results of few minutes in case of IPs and up to days for SSNTDS are a major drawback for optimization of the laser–acceleration process. Furthermore, with increasing pulse repetition rates from several shots per hour to maximum rates of several Hz, mandatory detector changes become a major limitation. Hence, laser ion acceleration is in an urgent need for **online** detection systems.
High instantaneous pulse flux certainly poses the strongest difficulty in electronic detection of laser–accelerated ions. If only information on total particle number is required, some beam instrumentation of the Large Hadron Collider (LHC), having a similar pulse flux ($\leqq 1.5 \cdot 10^{11}$ particles/ns) as laser ion accelerators, might also be applicable to laser–accelerated ions, although energy regimes differ by 6 orders of magnitude [30]. For instance, intensity measurements by fast current transformers are specified to measure the lowest LHC bunch charge of $2 \cdot 10^9$ protons on a bunch–by–bunch base [31].
However, the focus of ion diagnostic in laser–acceleration experiments is on the ion spectrum. A detector system to be used in the dispersive plane of a spectrometer is developed within the scope of this work in particular for proton detection. The following summary of an ideal detector system is, therefore, given in this context.
The saturation level is the most important criterion for or against a detector system due to the high particle number per pulse. However, the most interesting region of the spectrum is the high–energy tail, containing only few events. Hence, high or even better single ion sensitivity is also desirable for a potential online detector system. The dynamic range is, thus, predominantly affecting the choice of a detector system.
Good spatial resolution is beneficial to resolve particle traces of different ion species in the spectrometer plane which start to overlap at high particle energies. An additional, but even more important challenge of any electronic detector system is it's reliable operation in pres-

ence of an electromagnetic interference pulse (EMP) during laser–target interaction.
A wide variety of different types of electronic detectors exists among which ionization chambers (IC), scintillators, micro–channel plates (MCP) and semiconductor pixel detectors are currently being investigated for laser–accelerated ion detection [32–35].
ICs are standard particle detectors in many different fields of applications, particularly in radiation therapy. However, charge carrier recombination and associated saturation effects are a known problem of this kind of detector when operated in pulsed beams. Particularly with regard to the peculiar short pulse structure and high intensity of of laser–accelerated ions applicability of this type of detector for absolute dose measurements is limited [36]. In the dispersive plane of the spectrometer, position–sensitive detectors are required. Besides the recombination problematic, arrays of ICs or multi–wire proportional chambers (MWPC) offer a spatial resolution of only few mm, which limits the possibility to discriminate individual ion traces when combined with a spectrometer. Micro–pattern gaseous detectors (MPGD) such as GEMs (Gas Electron Multiplier) offer spatial resolution of few tens of μm and a factor of 10 higher rate capability as standard MWPCs [37]. However, there is a high risk of electrical breakdown due to discharges that are triggered by incident high intense ultra–short ion pulses.
Scintillators monitored by digital camera systems are rather simple detector systems, allowing to cover large areas and offering high spatial resolution. A low light yield of about 1 photon per 100 eV energy deposition is associated with organic scintillators [28] which makes them in principle suitable for the detection of high particle fluences. Their single particle detection capabilities are, therefore, limited even when using highly sensitive EMCCD (electron multiplying charge coupled device) cameras [38]. Organic scintillators are also known to show a LET–dependent response, requiring elaborate calibration measurements not only over the whole investigated energy range but also for different ion species. Scintillation efficiency with respect to a high instantaneous pulse flux as from a laser–accelerated is not yet known. Furthermore, as being a combined system of scintillator and camera system, response of the imaging device and reliability of operation in presence of EMP have to be investigated in addition.
The MCP allows single particle detection with spatial resolution of few tens of μm when used as particle detector. The detection efficiency of a MCP–based system, strongly depends on the secondary electron emission probability which is only in the order of few per cent for proton energies of few MeV. This is a major limitation in the high–energy tail of the ion spectrum although being beneficial with respect to the saturation level. Furthermore, the MCP has the most demanding operational requirements as high vacuum (10^{-6}–10^{-7} mbar) conditions are mandatory for high voltage operation.Usually, vacuum in laser–acceleration systems is of the order of 10^{-4} mbar.
In the scope of this work pixel detectors are investigated as position–sensitive online detectors. The idea of using pixelated devices is related to the fact that each pixel represents an individual particle detector. Megapixel detectors with pixel sizes smaller 10 μm are available, today. The incident particle number per pixel is clearly reduced with respect to the total particle fluence, for instance, 10^8 particles/cm^2 correspond to a single particle per μm^2. A square pixel of 10 μm side length, thus only needs to detect 1 millionth of the incident particle flux. This concept also holds for other position–sensitive detectors such as MCPs with small channel diameters of the same order of magnitude. However, MCP based detection

system are more complex as phosphor screen and camera system are additionally required to monitor the electron distribution of the MCP and vacuum operation is mandatory. The excellent energy resolution of semiconductors, wide availability of different detector architectures and in particular single particle sensitivity are further arguments for this approach. Pixelation of semiconductors is also beneficial with respect to their radiation hardness, which limits the usefulness of these devices for this kind of application. Nevertheless pixel detectors offer a large potential to fulfil many desired characteristics of an 'ideal' detector for laser–accelerated ion diagnostic.

1.1.5 Thesis outline

General aspects of detection of ionizing radiation as well as detector types commonly used in laser–acceleration experiments, are discussed in detail in the second chapter (chapter 2), with emphasis on pixel detectors. Notably, on overview of available pixel detector architectures, radiation hardness issues as well as their field of applications is given.
The detector systems in general, experimental setups and simulation and analysis tools which have been used, are given in chapter 3. IP detectors have been standard detectors used in spectrometers in many laser–acceleration experiments, up to now. Therefore, thorough understanding of these detectors is essential to understand requirements of an electronic system which is able to replace IPs. Parallel to the development of such a pixel detector based system, calibration measurements of IPs have been accomplished for ongoing laser–acceleration experiments (chapter 4).
The special pulse structure of laser–accelerated ions does not only have consequences for their detection, but, thinking of using them in ion beam therapy, response of biological samples also has to be investigated. For bio–medical experiments using low–energy proton beams with water–equivalent ranges limited to few mm, thin RCF films have been used for dose verification measurements. Extensive calibration and energy dependence measurements, spanning the gap from energies as low as 3 MeV to a typical medical energy of 200 MeV, have been accomplished (chapter 5).
In chapter 6, the three different pixel detectors — two commercially available and one scientific system — are described in detail, which have been investigated with respect to single particle detection efficiency, maximum saturation level in pulsed beams as well as radiation hardness. All these tests have been accomplished at the Tandem accelerator, offering unique possibilities to investigate detector response to high intense proton pulses under controlled conditions. Results of the performance of the developed system at a laser accelerator are presented and in chapter 7 compared with other currently employed laser ion diagnostic.

2 Detectors for ionizing radiation

Any particle detection is based on the interaction of particles with matter. Particles partially, or even completely, lose energy while passing through matter. The amount of energy deposited to the absorbing medium, depends on particle species, energy and the medium itself. As few eV of energy are sufficient to ionize absorber atoms, all radiation types whose initial energy exceeds the absorbers ionization threshold, are referred to as ionizing radiation. Quantitative radiation detection requires to establish a defined relation between deposited energy and detector response. The response signal can represent itself in different ways, depending on detector type. However, all forms of detector response can be classified into two categories, electronic signals (e.g. current, voltage), and non–electronic ones (e.g. change of detector medium properties), respectively. While the first yield prompt information on the incident radiation, quantification of material changes usually requires time–consuming analysis methods.
A detailed review on the topic of interaction of ionizing radiation with matter is given in the 2010 edition of the Review of Particle Physics [28] as well as standard textbooks such as [39,40]. An overview of different types of detectors can be found in e.g. in [1,28,39]. In the following, important aspects of the interaction of ionizing radiation with matter are briefly summarized. Presentation of detector systems is restricted to systems that are currently used, or potentially useful, for laser–accelerated ion detection, with emphasis on systems used in the scope of this work.

2.1 Interaction of ionizing radiation with matter

The term ionizing radiation comprises charged as well as uncharged particles. Interaction of ionizing radiation is categorized by four different particle groups, electrons, (heavy) ions, neutrons and photons. Here, the focus is on interaction of (heavy) charged particles with matter. As secondary electrons are produced in any interaction of ionizing radiation with matter, electron interaction is also briefly summarized. Photonic interaction is mentioned for completeness.
Any interaction of projectiles and absorber atoms can be split into nuclear and electronic interaction and corresponding Coulomb fields, respectively. Interaction cross–sections of uncharged radiation such as photons is much lower than for charged particle radiation.

2.1.1 Photon interaction

The number of photons (energy E) passing through a homogeneous absorber medium (density ρ, proton number Z) decreases exponentially with propagation length x. This is known as

Beers law (eq. 2.1), where absorption is defined by μ, the so–called attenuation coefficient, which is related to the cross–section σ by the density $\rho_{scatter}$ of scattering centres in the absorber medium. N(x) and N_0 are photon number at absorber depth x and initial photon number, respectively.

$$N(x) = N_0 \exp(-\mu x) = N_0 \exp(-\sigma \rho_{scatter} x) \tag{2.1}$$

Different photon interactions are possible, all depending on absorber density and nuclear charge, as well as photon energy. They are only listed here, in short. For details refer to e.g [28, 40]. Fig. 2.1 shows the corresponding interaction cross–sections against photon energy for two different absorbers, carbon and lead, respectively.

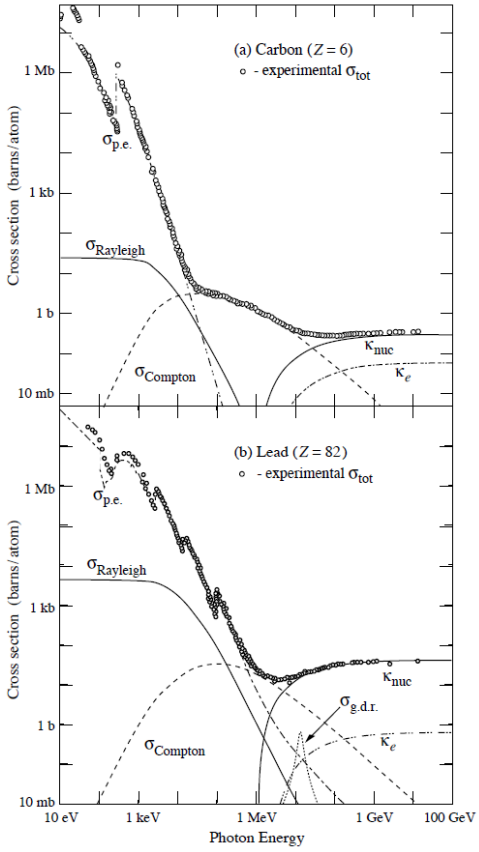

Figure 2.1: **Photon cross–section as a function of energy for carbon and lead** from [28]
The total cross–section, equivalent to the attenuation coefficient, is a superposition of all individual interaction cross–sections, such as photoelectric effect ($\sigma_{p.e.}$), Rayleigh scattering ($\sigma_{Rayleigh}$), Compton scattering ($\sigma_{Compton}$), pair production (κ_{nuc}, κ_e) and photo–nuclear interactions ($\sigma_{g.d.r}$), the latter only relevant for lead.

Rayleigh scattering ($\sigma_{Rayleigh}$) A photon is absorbed by an electron and re–emitted under a different angle. No net energy is transferred to the absorber in this elastic scattering process.

Photoelectric absorption ($\sigma_{p.e.}$) A photon is completely absorbed by an atom and a photo–electron is emitted. This is the most dominant effect in the energy regime below 1 MeV. Due to the quantum nature of the bound states, absorption edges are present in the corresponding cross–section (fig. 2.1).

Compton scattering ($\sigma_{Compton}$) Up to about 10 MeV, Compton scattering is the most efficient process. It describes the inelastic scattering of an incident photon at an absorber electron which is initially at rest. Energy is transferred from the photon to the electron, yielding a directional change for both.

Pair production (κ_{nuc}, κ_e) If the energy of an incident photon exceeds twice the electron rest mass $m_e c^2$, spontaneous decay of the photon into an electron–positron pair is possible in the vicinity of a nucleus. This process is called pair production and is the dominant interaction mechanism of high–energy photons. Pair production is also possible in the vicinity of an absorber electron, however, in this case, the energetic pair production threshold is increased by a factor of 2.

Photonuclear interaction ($\sigma_{g.d.r}$) Similar to the photo effect in the atomic shell, a photon can be absorbed by the nucleus under emission of a nucleon.

2.1.2 Charged particle interaction

Interaction processes of a charged particle are based on Coulomb interactions with shell electrons or the nucleus of absorber atoms. Projectiles lose their energy in a large number of collisions, hence, continuously slow down. During each of these processes only a small amount of energy is imparted to absorber atoms, which are excited or ionized.

Heavy charged particles

For heavy charged particles (nuclear charge z, velocity $v = \beta c$, mass m), collisions with electrons of the absorber atoms are responsible for the main part of the energy loss, the so–called electronic energy loss. A formula for the energy loss can be derived from the classical Rutherford–cross–section, describing the scattering of a charged particle in the Coulomb potential of a free electron , initially at rest. The assumption of a free electron is valid as long as the amount of energy, T, transferred from projectile to electron in single collision, is much larger than the binding energy and thus, for high–energy projectiles.
Eq. 2.2 describes the Rutherford cross–section in terms of the energy transfer T [41]. The term in brackets is a quantum–mechanical correction, accounting for the electron spin.

$$\frac{d\sigma}{dT} = \frac{2\pi z^2 e^4}{m_e c^2 \beta^2 T^2} \cdot (1 - \beta^2 \frac{T}{T_{max}}) \tag{2.2}$$

$$T_{max} = \frac{2m_e c^2 \beta^2 \gamma^2}{1 + 2\gamma\frac{m_e}{m} + (\frac{m_e}{m})^2} \approx 2m_e c^2 \beta^2 \gamma^2 \tag{2.3}$$

T_{max} is the maximal possible energy transfer in a single collision, equivalent to reversion of the electron direction in the projectile rest frame [41]. In the present work, only proton energies below 1 GeV are relevant. The denominator in (eq. 2.3) is, therefore, ≈ 1 without loss of generality. The mean energy loss per unit path length due to collisions with energy transfer in the interval [T, T+dT] is defined as

$$\frac{dE}{dx}(T) = N_{atoms} Z \int_T^{T+dT} T \frac{d\sigma}{dT} dT \tag{2.4}$$

with Z, the number of electrons per atoms and N_{atoms} the number of absorber atoms. So far, an energy transfer, exceeding the mean binding energy of an electron, $T > \langle I \rangle$, was assumed. A correct quantum mechanical treatment for energy losses $T < \langle I \rangle$ was first obtained by Bethe in 1930. Taking both energy loss regimes into account, the so called Bethe–Bloch formula for the linear stopping power $S = -\frac{dE}{dx}$ is obtained.

$$-\frac{dE}{dx} = 4\pi N_{atoms} Z \frac{z^2 e^4}{m_e c^2 \beta^2} \left[\ln \frac{2\gamma^2 \beta^2 m_e c^2}{\langle I \rangle} - \beta^2 - \frac{\delta(\beta\gamma)}{2} \right] \tag{2.5}$$

Using this formula, good results with few % accuracy are obtained in the energy range of 0.1–1000 MeV [28]. For projectiles velocities $\gamma\beta < 1$, the mean energy loss is dominated by the $1/\beta^2$ dependence. The influence of the logarithmic term increases with particle velocity. The term $\frac{\delta(\beta\gamma)}{2}$ is the density effect correction. For low projectile velocities $\gamma\beta \ll 1$ the atomic binding of electrons cannot be neglected. Therefore, an additional shell correction term $\frac{C}{Z}$ has to be introduced in eq. 2.5. Further low energy corrections are the Barkas– and Bloch corrections [28].
Fig. 2.2 shows the stopping power as a function of energy for a proton in water. The total stopping power is a superposition of the electronic and nuclear energy loss contributions. However, nuclear interaction cross–sections are much smaller than electronic ones. As a result, contributions of the nuclear stopping power can be neglected for proton energies exceeding 100 keV. Besides collisional energy losses, radiative losses in form of Bremsstrahlung also contribute to the total energy loss. However, for heavy charged particles such as protons, radiative losses are only relevant for relativistic particles.
During particle passage through matter, electrons can be transferred between projectiles and absorber atoms. To account for these charge state changes, effective charge numbers, representing average charge states, have to be used in eq. 2.5. During slowing down, electron pick–up plays a major role for heavy ions. The increase in energy loss with decreasing particle velocity is, thus, competing and finally compensated by the energy loss decrease associated to the reduction of effective charge. Electron pick–up is a simple explanation for the typical depth dependent energy loss behaviour (fig. 2.3). The curve is characterized by the so–called Bragg Peak at the end of the particle's range R due to nuclear stopping.

$$R(E) = \int_{E_0}^{0} \left(-\frac{dE}{dx} \right)^{-1} dE \tag{2.6}$$

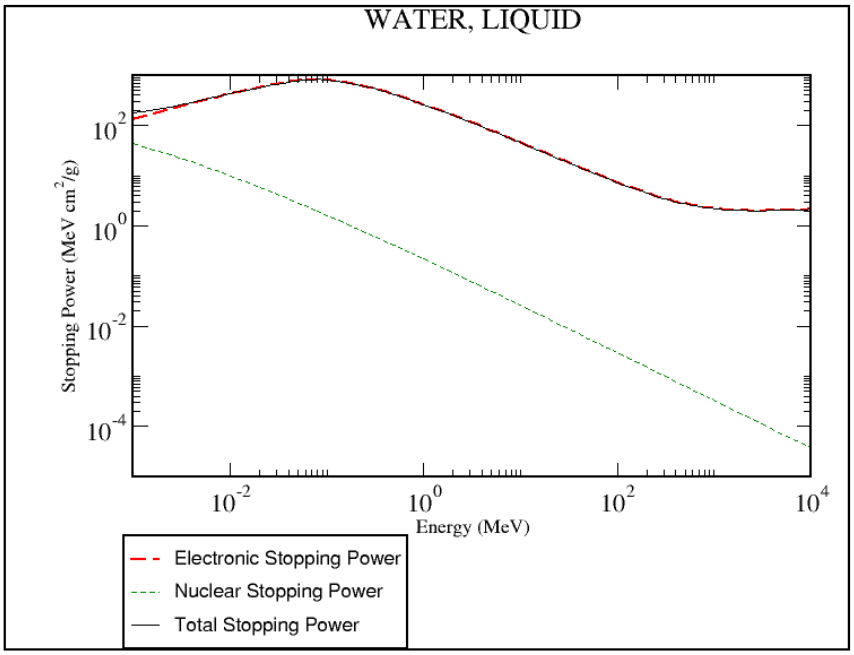

Figure 2.2: **Stopping power of protons in water** from [42]
The dominant energy loss is electronic, due to interaction of the proton with valence electrons of the water molecules.

The existence of a well–defined range, approximated by eq. 2.6, is a characteristic of heavy ions. The ion mass exceeds the electron mass by several orders of magnitude. Hence, particle deflection in electron collisions can be neglected and therefore, heavy charged particles are only slightly deflected from their direction of incidence. Lateral straggling of the particle beam is, therefore, primarily attributed to multiple Coulomb scattering from the nucleus, described in the theory of Molière.
Collisions are statistical processes. As a consequence, the energy distribution of an initially mono–energetic particle beam spreads with increasing absorber depth. For particles, completely stopped in the absorber, path length fluctuation, known as range straggling, also show the statistical nature of interaction processes. For protons, both, energy loss and range straggling are in the order of few percent.
For a large number of collisions, with small energy loss in each, derived energy loss distribution are usually described by Landau functions.

Electrons

Electrons have an exceptional position in the charged particle group. Due to their lower mass, compared to heavy charged particles, radiative losses have not only to be taken into account for energies in the MeV range but dominate for most materials and energies exceeding few tens of MeV [28]. For radiative energy losses the so–called radiation length, where the electron energy is decreased to 1/e of the initial one, is a characteristic parameter

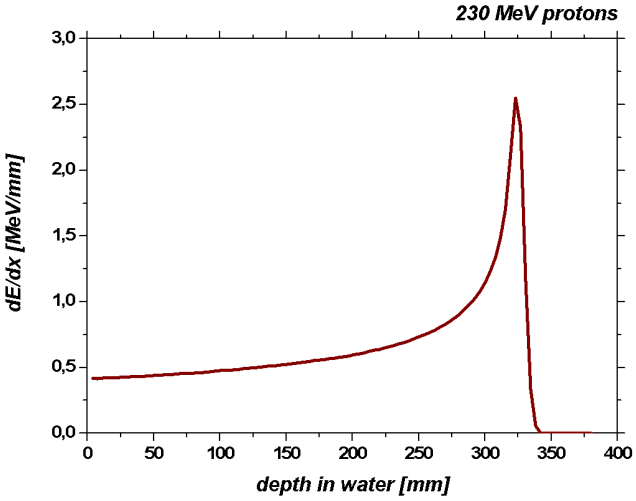

Figure 2.3: **Bragg curve of 230 MeV protons in water**

in describing electron matter interactions. The emission angle of bremsstrahlung photons depends on both, electron energy and absorber thickness, showing the typical distribution of a dipole field for low energies (< 100 keV) and thin absorbers in the rest frame of the incident electron. With increasing energy, photon emission occurs preferentially in direction of the incident electrons [40].
For low electron energies, ionization losses dominate. Large angle deflections occur in nuclear as well as electronic collisions, resulting in large spatial scattering of an incident electron beam. Furthermore, a kinematic correction has to be introduced in the Bethe formula (eq. 2.5), as collisions with the atomic shell, represent an interaction of identical particles [41], yielding

$$-\frac{dE}{dx} = 4\pi N_{atoms} Z \frac{z^2 e^4}{m_e c^2 \beta^2} \left[\ln \frac{\sqrt{2}\gamma\beta\sqrt{\gamma-1} m_e c^2}{\hbar \langle\omega\rangle} - \beta^2 - \frac{\delta(\beta\gamma)}{2} \right]. \tag{2.7}$$

Radiative energy loss increases as a good approximation linearly with energy while ionization losses, which are dominant for low–energy electrons, increase logarithmically according to eq. 2.7. In the majority of collisions, secondaries are low–energy and, therefore usually absorbed in close vicinity to the original interaction point. Radiative losses can, therefore be neglected. However, energetic electrons, so–called δ electrons, originating from hard projectile–electron collisions, are able to carry energy away from the original interaction region. This characteristic of δ–electrons is of particular interest in dosimetric measurements [1].

2.2 Electronic detector systems

2.2.1 General characteristics of electronic detectors

A typical electronic detector system can be divided into three parts: first, a sensor, generating the basic electronic signal, second, analogue electronics for signal amplification and

shaping and third, an analogue–to–digital converter (ADC) to generate the final digital output. However, only the first part is mandatory for particle detection. The simplest detector structure can, thus, be depicted as a planar geometry, having two electrodes on opposite sites of a sensitive material (e.g. air, silicon). An applied voltage and electrometer, used to measure the generated signal current, complete the simple detector circuit.

Signal formation

Incident radiation results in excitation and ionization of the sensor material, generating pairs of free charge carriers. An important parameter is the mean energy required to form a charge carrier pair in the absorber medium, W(E). For projectile velocities exceeding typical velocities of orbital electrons the value of this average charge carrier generation energy is approximately constant (W(E)≈ W), though strongly depending on the absorber medium. As some amount of energy is lost to excitation of absorber atoms or molecules, W usually is somewhat larger than the typical average ionization energy $\langle I \rangle$ of the medium.
Hence, any quantitative measurements relies on the linear dependence of the number of generated charge carrier pairs, yielding the signal charge Q_s, and the amount of deposited energy, ΔE, with W as proportionality factor. But, most important, the proportionality of signal charge and energy deposition or dose is only valid, if recombination losses can be neglected (sec. 2.2.2).

$$Q_s \propto \frac{\Delta E}{W} \tag{2.8}$$

Reliable knowledge of the W–factor in air is of particular importance in dosimetric measurement. A comparison of two dosimetric protocols for proton therapy [43,44] shows that a main difference of both protocols is associated with the recommended W–value [45]. Evaluation of available W–values in air yield a value of 34.2 $\frac{J}{C}$ in agreement with recommendations of the TRS 398 of the IAEA [44, 46].
According to Ramo's theorem [47], charge is induced on each of the electrodes while charge carriers drift in the applied electric field. The associated current is proportional to the generated charge, –Ne, the velocity $\vec{v}$ of the charge carriers and the applied electrical field $\vec{E}$ (eq. 2.9).

$$I = -Ne\vec{v}\vec{E} \tag{2.9}$$

It represents the basic electronic input signal for the usually following signal processing chain.

Signal processing

Generated charges are typically in the order of few fC to tens of fC. For instance, an energy deposition of 1 MeV in an air–filled IC (W=34.23 J/C) corresponds to a signal charge of 5 fC, which is about a factor of ten higher when using a silicon sensor. An important component in the signal acquisition chain is, therefore, the first amplification stage by pre–amplifiers. Any noise introduced during this stage is subsequently amplified in successive amplification steps and thus, finally limiting the overall signal–to–noise ratio (SNR) of the system.
Radiation detectors are commonly used either in current or pulsed mode. In current mode,

the time–dependent evolution of the signal is monitored. Ionization chambers (sec. 2.2.2) are usually operated in this mode. Pulsed mode operation offers sensitivity to individual particles and recording of pulse height additionally, yields information on the generated charge. Therefore, pulsed mode is the most important operational mode of radiation detectors.
The choice of a pre–amplifier depends on the operational detector mode. Voltage– or charge–sensitive amplifiers are used in pulsed mode, while current–sensitive amplifiers are used in current mode [48].
The equivalent circuit of any electronic detector is represented by a load resistor R_D and capacitance C_D , with a current source i_s representing the momentary current signal in the detector (fig. 2.4). The output voltage of the amplified signal is given by eq. 2.10, assuming

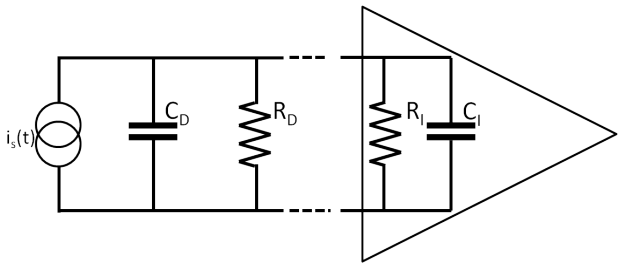

Figure 2.4: **Equivalent circuit of an electronic detector system**
The detector, represented by a current source $i_s(t)$, resistance R_D and capacitance C_D is connected to a first amplification stage (R_I, C_I).

a time–dependent input current $i_s(t) = \frac{Q}{\tau} \exp\left(\frac{t}{\tau}\right)$ with a characteristic decay time constant τ [48]. In this simple picture the rise time τ_R of the signal, primarily determined by the charge collection time, is equal to 0.

$$v_s = \frac{QR_{tot}}{R_{tot}C_{tot} - \tau}\left[\exp\left(\frac{t}{R_{tot}C_{tot}}\right) - \exp\left(\frac{-t}{\tau}\right)\right] \tag{2.10}$$

R_{tot} represents the series resistor of detector(R_D) and amplifier resistance(R_I), C_{tot} the total capacitance of the combined detector–amplifier circuit and τ the time constant of an arbitrary current signal $i_s(t)$ (fig. 2.4). The signal form is determined by the ratio of the circuit time constant $R_{tot}C_{tot}$ to current time constant τ.
Further signal optimization by means of pulse shaping techniques is required to fulfil requirements of the particular application such as amplitude or timing measurements. A simple shaper consist on a sequence of a high–pass and low–pass filter, time constant of both, determine the final signal amplitude and total noise of the system [49]. Both quantities play an important role in determination of detector sensitivity and resolution.

Detector resolution

Energy resolution Equation 2.8 relates signal charge and energy deposition of incident radiation. The energy resolution of a detector system is defined by the full width half maximum (FWHM) $\Delta_{S_0,FWHM}$ of a measured signal distribution centred around a peak position S_0.

$$R = \frac{\Delta_{S_0,FWHM}}{S_0} \tag{2.11}$$

In any detector system, the lower limit of the achievable resolution is determined by statistical noise, characterized by the dimensionless Fano factor F (eq. 2.12) [50]. The number of charge carriers generated by absorption of incident particle of energy E randomly fluctuates from particle to particle. The energy of an incident particle is absorbed in steps i, where the sum of all energy depositions per step ΔE_i corresponds to the energy of the incident radiation quantum. Therefore, fluctuations in charge carrier numbers deviate from Poisson statistics as individual energy deposition steps are not independent from each other. The Fano Factor accounts for this fact and is defined by the ratio of observed charge carrier fluctuations $\sigma^2_{N,measured}$ to Poisson variance $\sigma^2_{N,Poisson}$.

$$F = \frac{\sigma^2_{N,measured}}{\sigma^2_{N,poisson}} \tag{2.12}$$

Any additional source of noise, resulting in signal fluctuations, adds to the statistical noise, thus decreasing the resolution of the detector system. According to eq. 2.9, current fluctuations arise from fluctuations in particle number as well fluctuations in charge carrier velocity, yielding different contributions to the spectral noise power density [49].

Spatial resolution For the simplest detector geometry — a sensitive absorber placed between two electrodes — the exact impact point of the particle is unknown. Position–sensitive detectors are able to provide additional spatial information on a particle hit, based on segmentation of one, or even both, electrodes. The minimum attainable physical position resolution is defined by the spacing of the electrode segments.
While arrays of ICs or multi–wire proportional chambers offer only electrode spacings of few mm, new developments in gaseous detectors, MPGDs, offer few tens of μm spatial resolution. Even smaller sizes of individual detector segments are offered by position–sensitive semiconductor detectors such as pixel detectors. Pixels with side lengths of few μm are easily available, today.
However, charge carrier drift in the electric field is always superimposed by random thermal diffusion. As a result, charge can be distributed over adjacent electrode segments. This effect, known as charge sharing or blooming, is particularly found in CCD detectors, as being favoured by their read–out mode. Charge sharing does not necessarily decrease the positional resolution. The determination of the centre of mass of such spatially extended charge distributions in some cases even allows an improvement of the positional determination.

2.2.2 Gaseous detectors

Gas–filled detectors such as ICs—the simplest type of these detectors—are one of the most common detectors in particle physics. For a better understanding of detection difficulties, some main characteristics of ICs are briefly summarized with emphasize on consequences for pulsed beam detection. In the following, a plane–parallel IC, similar to the basic detector described in the previous section, is assumed.

Recombination To obtain reliable, quantitative results on the amount of deposited energy, complete charge collection is mandatory. Different collisional processes occur in the gas while charges drift in the applied electric field. Charge transfer collisions between a positive ion and a neutral gas molecule do not alter the number of free charge carriers and thus, the total charge. Primarily, the ion pair number is also unaffected by the formation of a negative ion, where an electron is attached to a neutral gas molecule. Only collisions of carriers of opposite charge, forming a neutral gas molecule by recombination, effectively reduce the number of free charge carriers. Two types of recombination are distinguished.

Initial recombination Initial recombination is related to the high ionization density along a single particle track, describing the recombination of ion pair constituents of the same track. This form of recombination strongly depends on the linear energy transfer (LET) of the particle. Therefore it is most pronounced for heavy charged particles.

Volume recombination Recombination of charge carriers originating from different tracks in the drift field of the IC is assigned to volume recombination. This form of recombination is ionization or, respectively, dose rate dependent.

Negative ions are more prone to recombination than electrons. As their formation dominates in air filled chambers, recombination is an important issue in air–filled IC dosimetry. In principle, recombination losses can be avoided by application of an appropriate voltage. The corresponding voltage range is assigned to a region of ion saturation, where nearly all generated ion pairs are collected, the operational region of ionization chambers. However, complete elimination of recombination is not achievable, as the maximum saturation voltage is limited by the onset of charge multiplication.
In radiation therapy, air–filled ICs represent the dosimetric standard in absorbed dose determination [44]. The absorbed dose to water $D_{w,Q}$ at a reference depth z is determined by a formalism correcting the electro–meter reading M_{Q_0} for all possible influence quantities, differing from specified reference conditions such as beam quality Q (eq. 2.13).

$$D_{w,Q} = M_{Q_0} \cdot N_{D,w,Q_0} \cdot \prod c_i \tag{2.13}$$

N_{D,w,Q_0} is the chamber calibration factor obtained in a reference beam of quality Q_0. Additional correction factors c_i, accounting for instance for the ICs temperature and pressure dependence or recombination losses, are summarized as $\prod c_i$. Accurate dose measurements are only possible for complete charge collection, understanding of recombination losses and, if necessary, appropriate recombination corrections are, hence, of particular importance.
Volume recombination depends on pulse intensity and, hence, is an important issue in IC–based detection of high–intense ultra–short laser–accelerated ion pulses. A theory for recombination correction in continuous as well as pulsed beams has been developed by Boag et al. (e.g. [51, 52]). However, in particular in proton therapy, a general valid recommendation for recombination correction not yet exists [53].
For both, continuous as well as pulsed beams, recombination correction depends on beam parameters as well as chamber geometry. For recombination correction in pulsed beams, pulse widths much shorter than the ion charge collection time and low pulse repetition rates, ensuring single pulses during charge collection are assumed. The following formula for a

planar chamber geometry with electrode spacing d and applied voltage V_0 is, thus, obtained according to Boag's theory.

$$\frac{Q_{coll}}{Q_{tot}} = \frac{1}{u}\ln(1+u) \tag{2.14}$$

$$u = \frac{\alpha}{e(\mu_- + \mu_+)} \cdot \frac{\rho d^2}{V_0} \tag{2.15}$$

α is the recombination factor, $\mu_{+/-}$ are the ion mobilities and ρ is the initially created charge density.
Ion mobilities and, hence, recombination factor, depend on gas composition, applied field as well as environmental conditions. A value of $3.02 \cdot 10^{10}$ m V C^{-1} for air is given the first quotient of equation 2.15 in [54]. Assuming a pulse dose of 1 Gy, delivered to an air–filled parallel plate chamber with sensitive volume of 1 cm ^{3} and 1 mm electrode spacing, a charge collection efficiency of about 0.51 can be calculated.
So far, experimental recombination correction is tested for pulse durations of few μm and few tens of mGy per pulse as available in clinical linear accelerators, yielding pulse dose rate of approximately 10^9 Gy/s. In this regime, there is a good agreement between measurement and theory. Assuming the same dose per pulse for laser–accelerated ions, the peculiar time structure of these pulses of about 1 ns, yields at least three orders of magnitude higher pulse dose rates. Validity of recombination theory under these conditions, thus, still has to be experimentally investigated [32].

Position–sensitive gaseous detectors

Particle tracking in high energy physics require high rate capability as well as sub–mm spatial resolution. Due to the low level of initially generated charge from an incident minimum ionizing particle (MIP), position–sensitive gaseous detectors are operated in the proportional counter regime and widely used in this field. One of the oldest types of position–sensitive gaseous detectors is the multi–wire proportional chamber (MWPC). In this detector type, the anode is formed by a set of parallel wires —typically spaced by few mm and with diameters of few tens of μm—which are placed between two cathodes, thus forming a sequence of proportional counters. To obtain spatial resolution in two dimensions, segmented cathodes can additionally be used. The feasible spatial resolution of about 50–100 μm is limited by space charge effects and diffusion processes [28]. The MWPC typically has a maximum rate capability of 10 kHz/mm^2. Application of this kind of detector under high radiation flux is further limited due to ageing effects, associated with the formation of polymer deposits on the wires and performance degradation with respect to gain or spatial resolution.
Use of photo–lithographic fabrication technology allows miniaturization of position–sensitive gaseous detectors. These micro–pattern gaseous detectors (MPGD), feature not only an improved spatial resolution compared to MWPCs, but also an increase in rate capability to about 25 kHz/mm^2 [28]. Two common detectors of this group of MPGDs are gas electron amplification (GEM) detectors [55] and micro–mesh gaseous structures (Micromegas), a parallel–plate gas avalanche counter [28, 37].
A GEM consists of a metallized insulator foil, perforated by a matrix of small holes. A typical

GEM has, for instance, a 50 μm thick Kapton foil with holes of 70 μm diameter and pitch distances of 140 μm [37]. The GEM is placed between two electrodes, with a voltage in the order of few hundred Volts applied to both metal layers. Electrons, generated by an incident particle in the gas, drift towards the GEM and into the holes, where the strong dipole field yields electron amplification. The potential difference between anode and GEM extracts the electrons which are finally collected by the anode. To allow high electron amplification, often two or three layers of GEMs are used.
A Micromegas uses only a single amplification stage, formed by a cathode micro–mesh (about 10 μm hole diameters) in close distance ($\sim$ 100 μm) to the anode which is placed between both electrodes of a parallel plate chamber [37]. Field strengths of several tens of keV/cm within the amplification region yield an electron avalanche. As anode a printed circuit board (PCB) segmented into strips or pads is typically used. New developments start to use pixelated semiconductor read–out chips such as *Timepix* as anode [56, 57].
A potential problem of MPGDs, particularly when operated under high gain, are discharges within high field regions. Particularly heavily ionizing particles but also high particle flux can trigger discharges due to the high initial charge generated within the sensitive volume. The concept of using multiple amplification stages in a GEM detector, allows to decrease the risk of gas discharges as lower voltages are required on each of the GEM foils to achieve the same total gain as in a single GEM [58]. For Micromegas combined with pixel chips, discharges are a severe problem as they are able to destroy the read–out chip. However, use of a high–resistivity protection layer on top of the read–out chip has shown to increase the lifetime of the chip even in presence of discharges [59].
The risk of discharges and, thus damage of MPGDs has substantially decreased within the last years due to improvements in fabrication technology, allowing to operate these devices with maximum particle rates of $10^8/\mathrm{cm}^2/\mathrm{s}$. Nevertheless, there is a high risk that all these improvements are not sufficient to allow safe operation of these kind of devices with the high instantaneous flux of a laser–accelerated ion pulse.

2.2.3 Semiconductor detectors

Semiconductors are widely used as particle detectors due to special electronic properties resulting from band gap energies in the order of few tenth of eV to $\lesssim$ 2 eV. Mean energies required for generation of charge carriers are about one order of magnitude smaller compared to gases, i.e. 3.63 eV in case of silicon, the most common semiconductor detector material. Hence, semiconductors are attractive for particle detection, as they do not only offer higher sensitivity but also higher initial signal levels compared to gas–filled detectors.
While semiconductors are isolators at T=0 K, thermal excitation results in a small, but still measurable conductivity at room temperature, with contributions of both, electrons in the conduction band, as well as holes, vacant states in the valence band. The intrinsic electron and hole concentration, n and p, are identical in case of an ideal semiconductor. However, at room temperature only a limited number of intrinsic charge carriers is available, for instance, in silicon, the most common material for semiconductor detectors, the intrinsic charge carrier density is only $1.45 \cdot 10^{10}/\mathrm{cm}^3$ [49].
Doping with a small amount of impurities is an efficient means to increase the charge carrier concentration. Depending on the type of dopant atom, with exactly one valence electron

in excess (donor) or spare (acceptor) compared to the semiconductor material, additional energy states are introduced close to the band gap edges, which are thus, easily excited. Doped semiconductors are classified as n– and p–type material depending on concentration difference of acceptor (N_A) and donor (N_D) atoms and therefore, the charge carrier type that primarily contributes to the conductivity of the material (majority carriers). The Fermi level of a doped material, with E_i denoting the chemical potential of the intrinsic material is given by eq. 2.16.

$$E_F = E_i - k_B T \log \frac{N_A - N_D}{n_i} \tag{2.16}$$

pn–junction

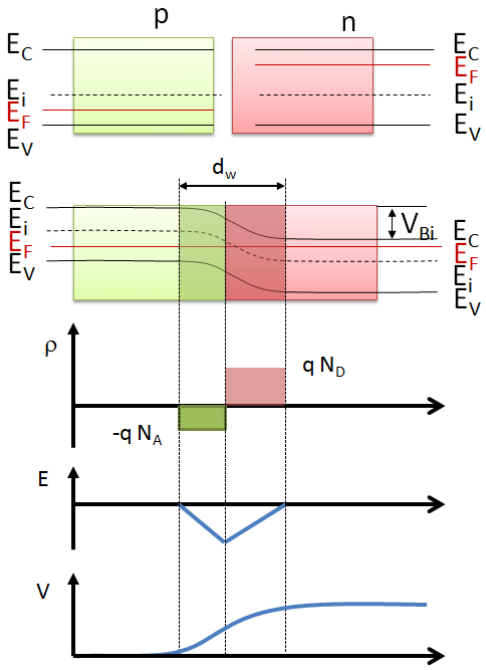

Figure 2.5: **pn–junction in thermal equilibrium**
The Fermi level F has to adjust under contact of p– and n–type material. As a result, the band structure is bended in the space charge region of width w_d, represented by a built–in potential V_{bi}.

The basic structure of any semiconductor detector is a pn–junction (fig. 2.5). Charge equalization by diffusion of majority carrier from both junction sides results in majority carrier recombination and built–up of a space charge region. The emerging electric field opposes a drift motion on the initial diffusion motion, resulting in full depletion of mobile charge carriers of the space charge region. The associated built–in potential V_{bi} of the so–called depletion region balances the difference in the Fermi levels (eq. 2.16) of the both formerly isolated junction regions.

$$V_{bi} = \frac{k_B T}{e} \log \left(\frac{N_A N_D}{n_i} \right) \tag{2.17}$$

The depletion zone acts as capacitor of capacity C (eq. 2.18), defined by the dielectric material constant ϵ, the junction area A and depletion width w_d.

$$C = \epsilon \frac{A}{w_d} \tag{2.18}$$

The width of the depletion region w_d depends on the built–in potential and, therefore, acceptor and donor concentration. Application of an external bias voltage V_{bias} causes a change in the depletion width. For detection of ionizing radiation, a large sensitive volume, as represented by the depletion zone, is beneficial. Under reverse bias, the depletion width increases proportional to $\sqrt{V_{bias}}$ (eq. 2.19), which is, hence the operation mode of a diode detector [60].

$$w_d = \sqrt{2\epsilon \frac{V_{bi} + V_{bias}}{Ne}} \tag{2.19}$$

Although the increase in depletion zone also increases the potential barrier, charge carrier flow due to thermal excitation is not completely inhibited. As a result, a small amount of current flow through the junction, known as dark or leakage current I_d, is always present (eq. 2.20). It strongly depends on the temperature, thus cooling of the device yields a reduction of this noise source.

$$I_d \propto T^2 \exp\left(-\frac{E_{gap}}{kT}\right) \tag{2.20}$$

The Shockley–equation is the base equation describing current flow J in a biased diode (eq. 2.21), derived as solution of the Diffusion equation [49].

$$J = q_e n_i \left(\frac{D_n}{N_a L_n} + \frac{D_p}{N_d L_p}\right) \cdot \left(\exp\left(\frac{q_e V_{bias}}{kT}\right) - 1\right) \tag{2.21}$$

$D_{n/p}$ and $L_{n/p}$ are diffusion constants and corresponding diffusion length of electrons and holes, respectively. Under forward bias, the voltage–current characteristic is defined by an exponential increase in current with increasing bias voltage. Under reverse bias, the contribution of the exponential term decreases with increasing absolute values of the negative bias voltage, asymptotically achieving a saturation value.

Fig. 2.6 shows the cross–section of a typical silicon pn–diode detector in planar geometry. The bulk material is usually a n–type material, with a typical wafer thicknesses of 300 μm for fabrication of radiation detectors. Details on the individual steps of the fabrication process are given in [60]. The junction is formed by a small, additional layer of doped p–type material at the surface. The doping concentration of the p–type material usually exceeds the bulk doping ($N_A \gg N_D$). Hence, application of a reverse bias results in an extension of the depletion zone into the bulk region. In silicon detectors, electrical contacts are usually made of aluminium, providing good ohmic contact. Surface passivation is usually obtained by a thin silicon dioxide layer, as thermal expansion coefficient of both, silicon and silicon dioxide, closely match.

Roughness at the material borders is a crucial problem in device fabrication. High leakage current is associated to device edges, which limits the overall performance of the device. Guard ring structures of similar doping as the main junction are, therefore, introduced. These contacts are beneficial in two ways: first by isolating the junction from the edges and

second by defining the electrical device boundary. However, guard ring structures introduce dead detector areas, which can not be used for particle detection and are a disadvantage in certain applications [61, 62]. Therefore attempts are made to reduce these dead areas by development of so–called edgeless detectors [61–63].

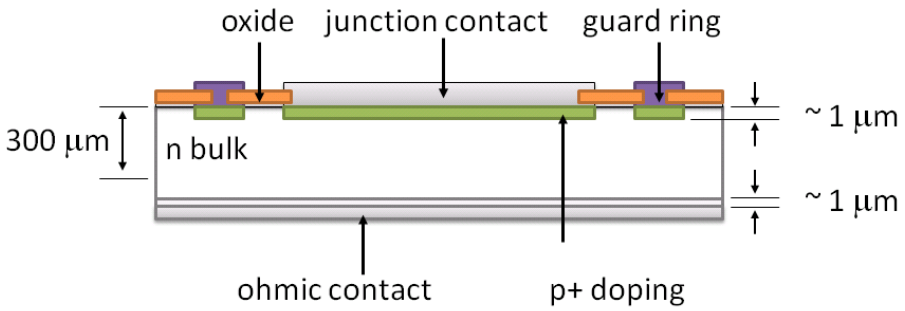

Figure 2.6: **Cross–section through a planar type pn–junction** from [49]
A pn–junction in planar geometry is usually asymmetric, built from a large n–type bulk material and a small highly doped p–type region (p^+). Guard rings are implemented to compensate leakage currents, due to roughness at the device edges. A few µm thick silicon dioxide layer on top of the p^+ layer protects the device from environmental influences.

Radiation damage in silicon detectors

Performance of semiconductor diode detectors decreases due to radiation damage. Two main categories of damage mechanisms are distinguished, displacement damages and ionization damages.
Displacement damage, mainly present in bulk material, is related to non–ionizing energy loss (NIEL). An energy deposition of about 25 eV is already sufficient to displace a silicon atom from a lattice site [64], forming a point defect known as Frenkel pair, a interstitial Si–atom and a vacancy at the corresponding lattice site. Depending on energy transfer in this process, the silicon recoil atom is able to produce further point defects or even point–defect clusters, i.e regions with a dense defect distribution. Primarily generated displacement defects are not stable. On the one hand, migration of defects resulting in defect recombination or dissociation yields a characteristic temperature dependent annealing with time. But, on the other hand defect interaction also results in generation of stable defects, able to permanently change electrical device properties and, hence, performance.
A defect is represented by a supplementary energy level within the band gap, the associated defect occupation is defined by a Fermi distribution. Any displacement damage primarily affects the current flow in the device. Different processes are responsible for the observed current changes, depending on the defect level position with respect to the band gap.

Charge carrier emission and capture Emission and capture of charge carriers are the most probable processes for defect levels situated in the middle of the band gap. The defect

level acts as a intermediate step for charge carrier transitions between valence and conduction band. Thus, generation as well as recombination of charge carriers is possible. However, in a reverse–biased diode, charge carrier generation dominates, thus increasing the leakage current of the device with incident particle fluence and characteristic damage constant α.

$$I_{dark} = \alpha\Phi \tag{2.22}$$

Charge carrier trapping Defect levels close to the band gap edges act as trapping centres for charge carriers. This kind of defect influences the device current in two ways. Charge carrier trapping reduces the signal current in the diode, first. Second, traps act also as additional source of noise, as charge carriers will escape with time.

Change in doping concentration Defect states can alter the electrical properties of the material. A dopant atom may become inactive by interaction with a vacancy next to it, or electrical neutral atoms start acting as dopant. As a result, the doping concentration is effectively changed, in the worst case resulting in complete type inversion. As a consequence, voltage characteristics of the depletion region are affected.

The NIEL scaling hypothesis is used to compare displacement damage of different types of radiation depending on energy. The effect of a displacement damage is related to the displacement damage cross section (NIEL value), assuming a linear scaling of of the damage effect with the imparted energy [65].
Displacement damage plays a major role in the bulk material and thus, depletion zone of the detector. Another form of damage, ionization damage, is primarily associated to the passivated insulator layer on the detector surface, usually SiO_2 in silicon detectors. As the lattice structure of SiO_2 is per se more irregular than in the bulk silicon, displacement damage by non–ionizing interaction can be neglected. Ionization damage, is associated with charge carrier generation and subsequent trapping in the oxide layer. As hole mobility is much lower than electron mobility, a positive space charge due to hole trapping builds up near the SiO_2–Si interface. As a result, voltage characteristics of the semiconductor–isolator interface change [66]. This form of radiation damage is of special importance for active pixel sensors, incorporating MOSFET structures on a pixel base.
Radiation damage effects both, the sensor and associated read–out electronics. Long–term operation even at high damage levels, is an important issue for detector application e.g. as inner tracker in high energy physics experiment or radiation detectors in space missions. Characteristic annealing with time and temperature can be used to increase detector lifetime. Many work is done to further improve the radiation hardness of silicon, for instance doping with impurities such as oxygen or carbon which are able to capture radiation induced Frenkel pairs [67].

Diamond detectors

Diamond detectors are primarily used for particle detection if radiation hardness requirements limit the utilization of silicon–based detectors. With a bandgap energy of 5.45 eV and displacement energy of 43 eV, diamond is intrinsically more resistant against radiation

damage than silicon [68]. Diamond detectors are marked by a low leakage current even at room temperature, as charge carrier generation by thermal excitation is strongly inhibited due to the large band gap. The average energy required to generate an e–h pair is about a factor of 4 higher compared to silicon, thus limiting the sensitivity of diamond. However, the combination of low leakage current as well as low dielectric constant and, therefore low detector capacitance, yields a low detector noise and accordingly high SNR [68]. Furthermore, the higher mobility of electrons as well as holes compared to silicon, allows faster response signals.
The typical geometry of a diamond detector is based on a bulk of intrinsic diamond of few hundred μm thickness with electrodes placed on both sides, thus forming a solid–state ionization chamber. The sensitive area, typically about 1 cm^2, can even exceed 10 cm^2 while electrodes can be as small as few tens of μm by means of lithography [69].
An important parameter of a diamond detector is the charge collection distance defined as the average distance an electron or hole can drift before being trapped and, thus, removed from the signal charge. The charge collection distance initially increases with the applied electrical field before it eventually saturates at field strengths of about 1 V/μm [69]. For many applications, sensors of few hundred μm thickness and, hence, charge collection distances of the same order of magnitude are required. The wide–spread use of diamond detectors is still limited due to the availability of high–quality synthetic diamond with appropriate charge–collection distances, despite many beneficial characteristics of diamond for particle detection.
Synthetic diamond, grown by a chemical vapour deposition (CVD) technique, is classified as poly–crystalline (pCVD) or single–crystal (sCVD) diamond. A disadvantage of pCVD is associated to the inhomogeneous structure of the material, being composed of small crystals, which can introduce a significant non–uniformity in signal response. Use of pCVD for spectroscopic measurements is, therefore, not possible. Nevertheless, in particular pCVD diamond has been used for detectors in the past decade, due to limited availability of detector–grade sCVD. For instance, beam condition monitors for the CMS (Compact Muon Solenoid) or ATLAS (A Toroidal LHC ApparatuS) experiments at LHC are based on pCVD diamond [70, 71]. First pixel detector modules based on sCVD diamond have recently been built with standard ATLAS pixel detector geometry [72] and tested as candidates for the intended luminosity upgrade of the LHC.
For this kind of application radiation hardness up to doses of $2 \cdot 10^{16}$ particles/cm^2 has been demonstrated [68, 73, 74].
Diamond is also an attractive detector material for application in radiation therapy due to its nearly tissue equivalence and, particularly in ion beam therapy, also radiation hardness [75–78]. The possibility to built devices with sub–mm spatial resolution makes diamond also suitable for dose verification measurements in IMRT [75].
The intrinsic radiation hardness of diamond detectors can not only be exploit for particle detection close to interaction points of large collider experiments but also for in–line beam monitoring of heavy ions. Application of a bias, allows to measure a current proportional to beam intensity, as demonstrated for single proton bunches of 40 ns duration containing 10^{11} protons [69]. Even shorter pulses of 1.5 ns duration with up to $5 \cdot 10^5$ have been measured in the past [79]. Both experiments clearly indicate the applicability of diamond as beam monitor for intense ion pulses.

Particle detection using pixel detectors

Segmentation of the sensitive area of detectors offers several benefits in particle detection. First of all, spatial resolution is increased, e.g. providing the possibility to distinguish close tracks of individual particles. Assuming a constant fluence of Φ_0 on the detector surface, division of the detector into N identical sub–units decreases the fluence per sub–unit Φ_0/N. For instance, a fluence of 10^8 particles/cm^2 is reduced to a single particle per μm^2. Therefore, segmented detectors offer the potential advantage to handle higher particle rates.
Other benefits are associated to the reduced capacity of each diode (e.q. 2.18) due to a reduced electrode area. Sensitivity and leakage current can thus be improved, the latter especially beneficial with respect to radiation damage [49].
One form of position–sensitive semiconductor detectors are strip detectors, which are classified as single– or double–sided if one or both electrodes are segmented, the latter with strips of different sides oriented orthogonal to each other. Position ambiguities arise when multiple hits are registered at the same time, which is a main drawback of these detectors particularly for applications requiring high rate capability.
Pixel detectors, a different form of segmented semiconductor detectors, offer spatial resolution in two dimensions without problems associated to multiple hit ambiguities. Therefore, they are widely used as inner tracking detectors in collider experiments such as CMS [80–82] or ATLAS [83,84] at the LHC. High rate capabilities are required for these experiments as the design luminosity of 10^{34} cm^{-2}s^{-1} associated to a collision rate of 40 MHz of the 7 TeV proton and anti–proton bunches, yields approximately 20 interactions per bunch crossing [85]. All detectors must be able to survive 10 years of operation, corresponding to a 1 MeV–neutron equivalent fluence of 10^{15}/cm^2, with still reasonable performance characteristics at the end of the LHC operation time. For this kind of application, only pixel detectors are able to fulfil requirements on radiation hardness, event rate capability and spatial resolution the same time.
Silicon tracker detectors have successfully applied the concept of detector segmentation to yield devices with high spatial resolution, high rate capability and high radiation hardness. The main problem in detection of laser–accelerated ions is the combination of the short pulse duration ($\sim$ 100 fs to $\sim$ ns) and high particle fluence ($> 10^7$/cm^2) per pulse. Tracking of individual ions of a laser–accelerated ion pulse is not possible, as all particles basically arrive at the same time for any read–out electronic. A high rate capability with respect to count rate is, therefore not relevant for this kind of application, but, definitely the reduction of the total fluence impinging on an individual pixel per pulse. The dynamic range in terms of minimum and maximum detectable energy per pixel is the relevant figure of merit. For the feasible energy range of laser–accelerated ions, radiation hardness is also an issue.
Many advances in development of pixel detectors have been triggered by needs of high energy physics before being transferred to wider fields of application. In particular the fabrication technology of diamond detectors has evolved in the past years due to HEP detector R &D. Besides diamond detectors [86] or radiation hardness, also improvements in the edge sensitivity are some actual topics investigated not only for the traditional planar Si–detector design [87] but also for new detector geometries, so–called 3D detectors [88, 89].
One of such a past development, the *Timepix* chip, is investigated for laser–accelerated proton detection in real time in the scope of this work.

Pixel detector architectures

There are two main types of detector systems: hybrid detectors, where pixelated sensor and read–out chips are connected to each other via bump–bonds and monolithic systems, where sensor and associated read–out electronics are integrated on a single chip. In the hybrid design space requirements associated with the pixel read–out electronics set a lower limit to the achievable pixel size which are in the order of few ten to hundred μm while pixel structures below 10 μm can be obtained exploiting modern fabrication technologies of monolithic pixel devices.

CCD–Technology

An example for a monolithic pixel system is a charge coupled device (CCD). A review on CCD technology can be found in e.g. [90]. Pixels sizes below 10 μm are readily available today. In Fig. 2.7 a schematic sketch of a cross section of a three–phase CCD and the corresponding mode of operation are depicted. In a three–phase CCD each pixel comprises three

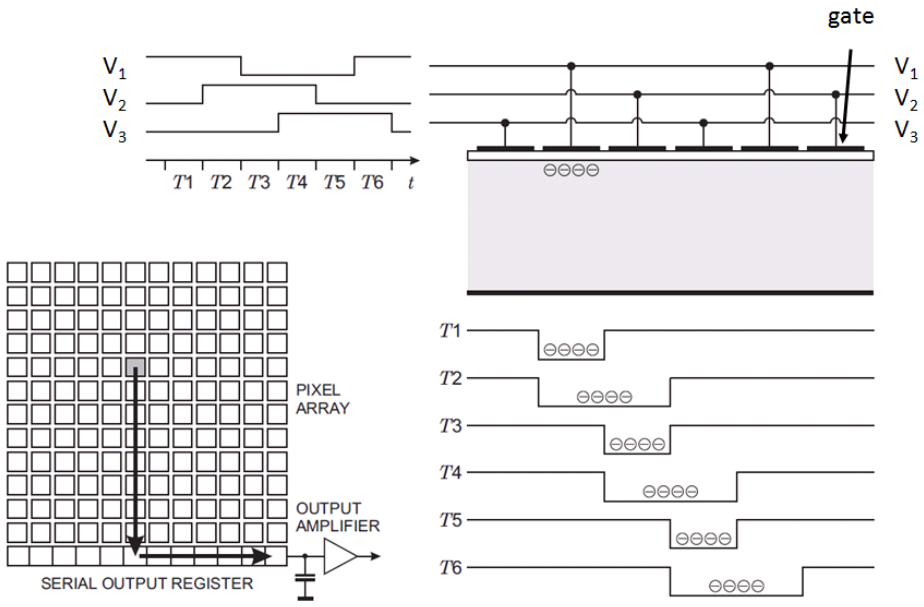

Figure 2.7: **Schematic sketch of a three phase CCD** adapted from [49]
The generated charge is shifted from pixel to pixel to the serial output register. A single output amplifier is typical for CCDs. In a three–phase CCD charge transport is accomplished by means of three different periodically changing potentials (V_1, V_2, V_3) which are applied to subsequent gate electrodes.

electrodes. Time varying potentials are applied to each electrode forming a timing sequence that manages the transfer of the accumulated charge to the next pixel. In each row of a CCD array, a pixel–wise charge transfer to a horizontal read–out register is accomplished. Hence, charge transfer efficiency must be close to unity to prevent signal losses during this

read–out process where the maximum number of transfer steps for pixel in the first column can exceed several thousand. Typically, only a single read–out electrode and amplifier are used to transfer the signal to subsequent electronics. This serial read–out also limits the attainable read–out speed of these devices. Typical clocking frequencies are in the order of few MHz. Assuming a read–out rate of 5 MHz for an pixel array containing 10^6 pixels, a maximum rate of 5 images (or frames) per second is obtained. Low noise requirements prevent faster read–out clocks, thus also limiting the frame transfer rate of CCDs.
CCD detectors are widely used in standard digital cameras. For detection of visible light (400–700 nm) a depletion thickness of up to 7 μm is sufficient. Therefore, thickness of the passive surface layers (metallization, passivation layer) is reduced to minimize absorption in these layers and increase the quantum efficiency of these devices at shorter wavelengths [49]. In astronomical observations large integration times up to hours are required as the photon flux from the observed objects is rather low. Hence, low noise is an important issue in astronomical CCDs. Typically, back–thinned CCDs are used under back–side illumination to increase the spatial resolution and avoid losses in the passivation and metallization layers [90]. Cooling of the CCD leads to a further reduction in noise levels.
Radiation–hard CCD technology finds their application as X–ray detectors on space telescopes [91] or vertex detector in colliders [92, 93].

CMOS Pixel detectors

Many solid-state imaging detectors are monolithic active pixel sensors (MAPS) based on photodiode detectors with integrated read–out electronics in each pixel. Devices are fabricated in a standard sub–μm CMOS (Complementary Metal–Oxide Semiconductor) technology featuring low production costs but also low power consumption during operation.
The integration of sensitive detector and read–out electronics per pixel, yields typical fill factors of only 20–35 %. A typical pixel design, so–called 3T pixel, contains a photodiode and three transistors for reset, buffering and multiplexing.
Intentionally designed for visible light detection there is a growing interest in application as X–ray [94] or direct charged particle detector [95–97]. In particular for charged particle detection, radiation damage of both, detector as well as read–out electronics can degrade device performance with respect to SNR. Due to MOSFET read–out electronics ionizing radiation damage as well as displacement damage are relevant for MAPS [98]. However, use of very thin high quality gate oxides strongly reduced the radiation induced threshold voltage shift typical for MOSFETs.

2.2.4 Other detector types

Due to the high pulse flux of laser–accelerated ion beams the majority of today used detectors are passive devices. However, increasing repetition rates of laser systems used for ion acceleration require detectors with a prompt quantitative response. A summary of other electronic detector systems is given which are currently investigated for detection of laser–accelerated ion pulses.

Scintillation detectors

The principle of a scintillation detector is based on the conversion of deposited particle energy into visible light, subsequently detected for instance by a photomultiplier or photodiode.
Two groups of scintillating materials are used, organic and inorganic scintillators. To be appropriate as scintillation detector, several requirements have to be fulfilled, regardless of the type of scintillator. A scintillator has to be transparent for the wavelength of scintillation light emission and a large fraction of the deposited energy should be converted into a prompt fluorescence signal.
In a large number of organic scintillators, molecules have a π–electron structure. Incident radiation causes excitation of higher electronic states. Transitions from the short–lived first excited singlet state to the ground state and corresponding vibrational levels, leads to emission of prompt scintillation light. However, a small amount of excitation energy is transferred to states with longer lifetime, resulting in a delayed light emission. Therefore, time response of a scintillator is characterized by the three time constants. First, the time required to populate the upper transition state τ_p, second, the time for the prompt decay of the excited state τ_{fd} and finally, the time for the delayed decay τ_{sd}. Typical decay constants of organic scintillators for the fast decay are in the order of 1–4 ns.
In case of an ideal scintillator, the amount of luminescence per unit path length $\frac{dL}{dx}$ is proportional to the energy loss $\frac{dE}{dx}$. In a real scintillator a finite probability for radiation less transitions, summarized as quenching, results in a smaller scintillation efficiency. The relation of luminescence depending on specific energy loss is is described by Birks formula.

$$\frac{dL}{dx} = \frac{S\frac{dE}{dx}}{1 + kB\frac{dE}{dx}} \tag{2.23}$$

S is the efficiency factor in absence of quenching and the parameter kB accounts for quenching losses. The light yield of an organic scintillator is, thus, LET dependent. As a result, higher values of the light yield for electrons compared to heavy charged particles of the same energy are observed [39].
In an inorganic scintillator impurities, denoted as activator centres, are responsible for the emission of scintillation light. Activator states are situated in the band gap of the crystal lattice. Lifetimes of these states are in the order of several 10–100 ns, as a result, the response of inorganic scintillators is a factor of 10–100 times slower than for an organic one. The light yield by the slow decay component is also more pronounced resulting in a higher background during measurements. But inorganic scintillators are less prone to quenching effects, resulting in better proportionality of the light yield with deposited energy.
For detection of laser–accelerated ions, organic scintillators are investigated as position–sensitive elements in the spectrometer plane [38] as well as a scintillator stack for ion beam profile measurements [33, 99].

Micro–channel plate (MCP)

A micro–channel plate is an electron multiplier built from a bundle of parallel channels, usually tiled at a small angle of about 8 ° with respect to the MCP surface (fig. 2.8) [100,101].

Many different geometries covering large areas of several cm^2 are, therefore, possible.
Secondary electrons, generated by collision of the incident particle with the channel wall,

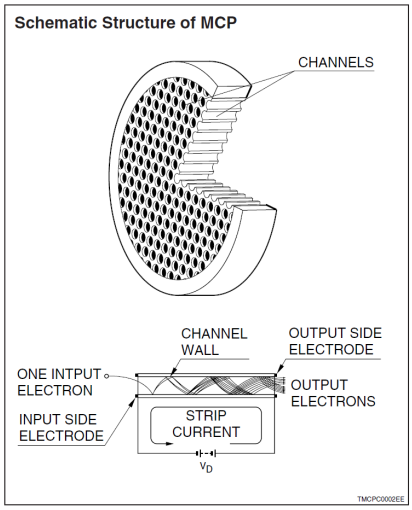

Figure 2.8: **Schematic sketch of a micro–channel plate** from [101].
A micro–channel plate is first and foremost an electron multiplier. An incident electron, accelerated in the applied electric field of an individual MCP channel, generates secondary electrons by wall collisions. This process repeats itself, for both, primary and secondary particles, during their drift along the channel, thus, amplifying the electron number.

made of a highly resistive material, are accelerated in the electric field which is applied along the channel length. Secondaries experience several wall collisions themselves during their drift along the channel yielding multiplication factors as large as 10^7 [100].
The applied potential difference across the channel length as well as the length to diameter ratio α (typically $\sim$ 40–100) determine the gain of the multiplier which is limited by space charge saturation at the channel output.
The MCP operation requires a vacuum better 10^{-6} mbar. However, collisions of electrons with residual gas molecules are able to generate positive ions, in particular in the high charge density region a the channel end. To prevent ion feedback from ions drifting towards the channel input, a two stage MCP, the so called Chevron, is typically used. Ion feedback is suppressed by introduction of a directional change of the channel orientation between both MCP stages [100].
When used as particle detector, MCPs are usually coupled to a phosphor screen to convert the amplified electron distribution into visible light which is in turn detected by a CCD camera system. The high gain of the MCP enables not only low signal levels, but in principle even single particles to be detected. However, the efficiency of single particle detection strongly depends on the secondary electron emission probability which scales with the energy loss and, hence, is particle dependent [102]. The maximum probability is, therefore typically in the keV range. For protons of 230 MeV, the emission probability is, for instance, as low as 4–5 % [103].
MCPs are sensitive to any kind of radiation. In laser–acceleration experiments, where ions,

photons and electrons are present, this can be a major limiting factor for their applicability. Nevertheless, the combination of a Thomson spectrometer and a MCP coupled to a phosphor screen has been investigated for prompt ion diagnostic in laser–plasma experiments in many cases [34, 104–106].

3 Experimental methods and data analysis

The Tandem accelerator of the Maier–Leibnitz–Laboratory (MLL) in Garching offers unique possibilities to investigate detector response under different irradiation conditions, allowing exposure to a single ion as well as up to 10^9 protons/cm^2 within a single ns–pulse. The latter, thus, offers comparable pulse intensities as a laser–accelerated ion pulse in a few MeV broad energy interval, but with major advantages of no parasitic background radiation whatsoever and full beam control. For bio–medical experiments, accomplished at the Tandem accelerator as well as ATLAS laser, a film based dosimetry has been established. Calibration measurements span the gap from low–energy 3 MeV protons, at the Tandem accelerator, up to therapeutic relevant energies of about 200 MeV, available at the Rinecker Proton Therapy Center (RPTC).
Test measurements of the developed online diagnostic system were accomplished in a laser–accelerated proton beam at the ATLAS and DRACO laser, respectively.

3.1 Detector systems

Different types of detector systems, non–electronic and electronic, have been investigated and calibrated for detection of laser–accelerated proton beams.
CR39, a nuclear track detector for protons, is employed for absolute fluence determination in calibration measurements. IPs were wildly used in all Munich laser–acceleration experiments so far. In these measurements, different types of IP and IP readers have been employed. As IP and scanner form a measurement system, calibrations are required for any IP–scanner combination. The same is true for radiochromic EBT2 films and associated scanner systems, used for dose verification in low–energy proton irradiation of biological samples. Three pixel detectors, based on different architectures were investigated for real–time detection of laser–accelerated proton beams.

3.1.1 CR39—a nuclear track detector

CR39, a solid state nuclear track detector (SSNTD), is widely used for quantitative ion detection in laser–acceleration experiments [34]. It offers two major advantages in the mixed radiation background of these experiments: first, it is insensitive to electrons, gammas or light, thus, only detecting the ion signal, and, second, even sensitive to single ions. Depending on etched track diameter and microscopic resolution, spatial resolutions is in the order

of 1 μm.

Track formation in CR39

In the scope of this work, 1 mm thick plates of CR39[1], a clear plastic solid of poly allyl diglycol carbonate (PADC, $C_{12}H_{18}O_7$, $\rho = 1.3$ g/cm^3) were used [107].
Tracks are formed, if the energy deposition of a charged particle exceeds a material dependent threshold value. For CR39, this is the case for protons with energies exceeding 20 keV [108, 109]. The majority of the insulating solids, representing the group of SSNTDs, is only sensitive to heavy ions, a possible explanation for the track formation under these conditions is given by the ion explosion spike mechanism [110]. CR39 is among a small group of polymers which are also sensitive to protons or deuterons. In this case, breaking of covalent bonds in the polymer is the main mechanism of track formation. Track diameters are in the order of 50 Å. For efficient track counting under a microscope, enlargement by chemical etching is necessary. The minimum required pit diameter for microscopic analysis of about 1 μm imposes an upper limit on the detectable particle energy. The track diameter distribution for protons has a maximum well below 1 MeV for all practical etch times of up to 20 hours [108, 111]. A decrease in proton track diameter with increasing proton energy, yields a track diameter of only about 2 μm for the highest investigated energy of 6 MeV [112]. For CR39, efficient microscopic analysis is, thus, limited to proton energies below 4 MeV. A second, higher energy range becomes accessible by back–side analysis of the CR39, provided the residual energy of particles at the back surface is sufficiently low to allow analysis of etched tracks.

Track etching

A qualitative picture of the track etching mechanism is depicted in fig. 3.1a. The etching rate of the track differs from the one in the undamaged bulk region, which is approximately one order of magnitude smaller [39]. Hence, material removal is much faster along the track, yielding a pit in the surface of the etched nuclear track detector.
However, this is only true, if the particle' s angle of incidence θ is not too shallow. Track visibility requires, that the track depth d_τ, obtained in a etch time τ, exceeds the thickness of removed bulk surface b_τ. Neglecting changes in the track etching rate with increasing particle range, a minimum angle of incidence θ can be determined from the simple picture of fig. 3.1a.

$$\theta > \arcsin\left(\frac{v_0}{v_{track}}\right) \tag{3.1}$$

A track corresponds to a densely damaged region and can, thus, anneal with time. Therefore, irradiated detector plates were etched within a few days after exposure. As etching reagent a six–molar caustic soda (NaOH) solution was used. A constant temperature of 80 ℃ was maintained during the etching process. A magnetic stirrer ensured a homogeneous distribution of both, temperature and reagent concentration, during the 90 minute long etching

[1] TASL, Track Analysis Systems Ltd., Bristol, UK

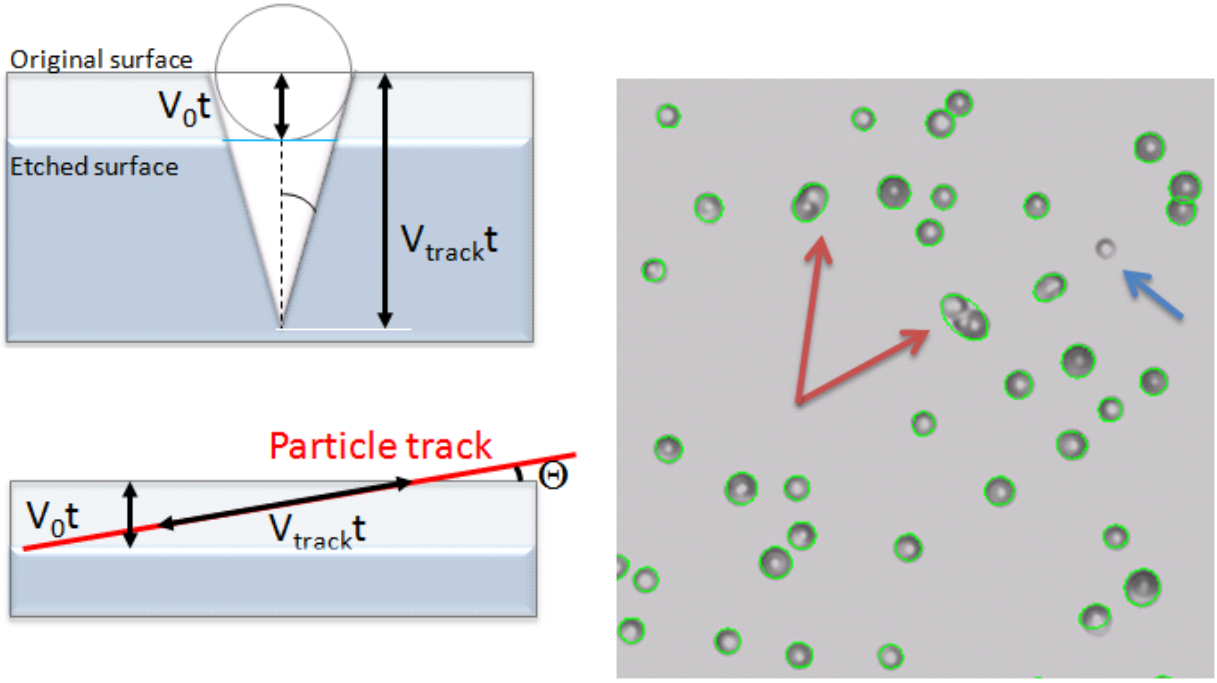

(a) (b)

Figure 3.1: **CR39 track etching**
a) The visibility and form of etched tracks is related to a difference in etching velocities of bulk material and track as well as angle of incidence of impinging particles.
b) Microscopic image of etched proton tracks under normal incidence. Green frames around the tracks mark elliptical fits of the measurement system on the automatically detected tracks. Coloured arrows mark errors in the automatic track analysis, introduced by track overlapping (red) and bad contrast (blue).

process.

Track analysis

Manual track counting is impractical for large numbers of tracks. Therefore, an automatic track counting system has been employed for track analysis. The used system is an improvement of a system that was originally developed in Siegen [113, 114]. It consist of a Zeiss Axiotron II microscope [115] equipped with a CCD camera and motorized stage. Minimum required track diameters are about 1.5–2.0 μm. The scanning procedure is controlled by the pattern recognition software, *Samaica* [116]. During this procedure, images acquired by the microscope' s CCD camera, are immediately analysed. Recognized particle tracks are fitted with ellipses (fig. 3.1b) and fit parameters are stored with additional track information such as e.g. brightness, position or ellipticity for further analysis. During analysis of etched CR39, problems related to the automatic focus control of the microscope, initiated regular dead locks of the program. In an early version of *Samaica* a restart of the scan was necessary.

In particular for analysis of large CR39 areas (i.e. 25 cm^2), where a complete scans requires approximately 24 hours to complete, this was not tolerable. Although a software upgrade allowed to continue the scan after the program freeze, the problem was finally solved by a regular reset of the auto–focus control. Another problem of long–term scans is associated with dust deposit on the CR39 surface, particularly as the automatic track counting system is not located in a dust–clean environment. However, dust–introduced track artefacts can typically be filtered from the data, as the pit form of true tracks, which depends on particle type, energy and angle of incidence, differs significantly.
Information on the incident radiation can be gained by analysis of the track pit, if the etching channel does not exceed the range of the particle. In this case, the track pit has a cone shaped form. The angle of incidence can be obtained by measuring the ellipticity of the cone's basal plane. For normal incidence, circular pits are observed (fig. 3.1b), distorting into elliptically ones with decreasing angle of incidence. The track etching velocity, v_{track} depends on the number of broken bonds and thus, on particle type and associated energy loss. If the etching velocity v_0 of the undamaged bulk is known, simple geometrical considerations yield the track etch rate and the corresponding energy loss [13].
Unambiguous distinction of individual particle tracks is essential for track analysis. A SSNTD is saturated if the majority of particle tracks overlaps (fig. 3.1b), posing a major problem for automatic track counting [109]. The saturation fluence depends on the pit diameter and, thus, also on etching time. For the used proton etching procedure, an etch time of 90 minutes results in typical track diameters of 2–3 μm in diameter, yields a saturation fluence of up 10^8 particles/cm^2 [105]. However, practical saturation levels are generally further limited by the increase of the track overlapping probability with fluence.

3.1.2 Image plate

Image plates are two–dimensional detectors that belong to the group of optically stimulated or photo–stimulable luminescence (PSL) detectors. They are often also referred to as storage phosphor due to the composition of their sensitive layer.
IP detectors have a large amount of trapping centres within their band gap. Depending on stopping power of incident particles, a significant amount of generated charge carriers is trapped, thus, storing a latent image of the incident radiation [117]. The trap escape probability is rather low for thermal excitation energies. However, a small amount of trapped charges will escape with time, yielding a characteristic fading of the stored signal.
For analysis, an energy transfer is required, which is sufficient to elevate trapped electrons to the conduction band, which emit light during decay. To maintain the spatial information of the trapped charge distribution, the energy transfer has to be insufficient to simultaneously free holes. Hole trapping sites, thus, act as recombination centres for electrons, moving in the conduction band. Stored information can be completely erased by the same process, allowing reuse of luminescence detectors. This is a major advantage compared to film detectors, described in section 3.1.3.
In an ideal detector, i.e. in absence of any fading effects, the number of emitted photons is proportional to the number of trapped electron–hole pairs. Therefore, a clear relationship between deposited energy and light yield exists.
IPs are highly sensitive to any kind of radiation. Their field of application does not only

span the detection of laser–accelerated ion [118] or electron [119, 120] beams, but also heavy charged particle [121, 122] or neutron [123] detection in general. Even depth dose measurement in clinical proton beams have been reported [124].

Fujifilm Image Plates

In the scope of this work, IPs of the TR– and MS–type from Fujifilm [125] are used. TR–type plates are widely used in laser–ion diagnostic. However, detector stability and, thus reliability, is a critical point for this kind of IP due to the lack of an active layer protection. As an intermediate step in improvement of existing ion diagnostics, suitability of MS–type IP, being more robust in handling, is investigated.
Though both plates possess the same sensitive component—$BaFBr_{0.85}I_{0.15} : Eu^{2+}$, a Eu–doped phosphor incorporated in a binding agent of urethane—response differences arise from their layer configuration (tab. 3.1). Sensitive layer thickness of both IP–types differs by more than a factor of two, being 115 μm or 50 μm for MS– and TR–type plate, respectively. TR–type plates offer a higher sensitivity to low–energy particles than other IP–types. However, their lack of a protection layer is a major disadvantage when used in laser–acceleration experiments where shot to shot replacement is required. There is a high risk of mechanical damage of the surface which can limit the reliability of results. Furthermore, a decrease in sensitivity upon water contact, resulting in a yellowing of the IP, is reported by the manufacturer. A check on visible changes in the surface layer is mandatory before each use. MS–type plates, which are protected by a 9 μm thick surface layer of polyethylene terephthalate, do not show such limitations. They can easily be reused 1000 times without change in the IP characteristics [126] and are better adapted to laser–acceleration experiments concerning their handling and re–usability capability.

IP type		**TR**	**MS**
protection layer	$[\mu m]$	0	9
phosphor layer	$[\mu m]$	50	115
support layer	$[\mu m]$	250	190
magnetic layer	$[\mu m]$	160	160

Table 3.1: **Configuration of MS– and TR–type IP** [126]

Photo–stimulated luminescence process

Fig. 3.2 shows a simplified energy level diagram for Eu–doped phosphor, explained in detail in ref. [127,128]. In short, vacancies of the halogen ions (Br, I) in the crystal lattice, so–called F^+–centres, are generated in the phosphor layer during the manufacturing process.
Relevant transitions for the PSL process are attributed to the dopant Eu^{2+} ions, partly exchanging Ba^{2+} ions. A part of the Eu^{2+} ions is ionized by incident radiation, resulting in a distribution of Eu^{3+} ions, representing trapped holes. Liberated electrons are elevated to the conduction band and finally also trapped in one of the halide vacancies, forming a F–centre. Latent images of the incident radiation are, thus, stored in meta–stable trap states.

For read–out, IPs are illuminated by red light, e.g. a He–Ne laser. Electrons, trapped at the F–centres, are liberated to the conduction band and finally recombine via excited Eu^{2+} states with trapped holes, transforming Eu^{3+} back to Eu^{2+}. Blue light with a central wavelength of 385 nm is emitted by this recombination process, which is detected by the read–out system.

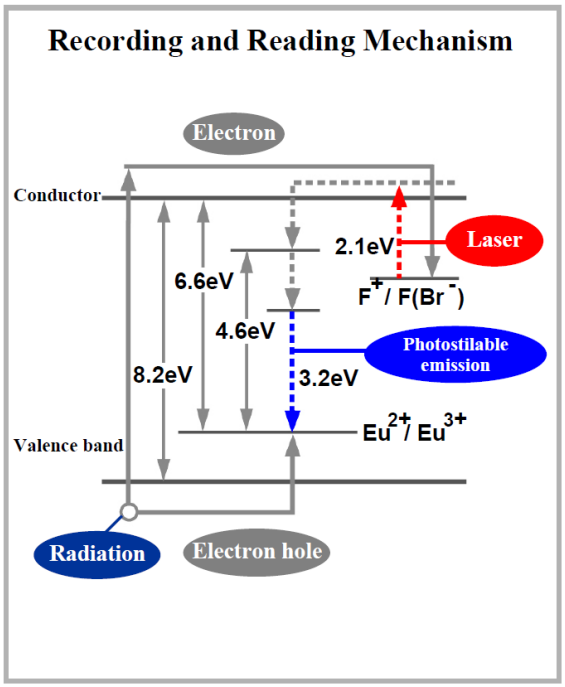

Figure 3.2: **IP energy level structure** (from [126])
Incident radiation yields a population of Eu^{3+} states (i.e.holes) and electrons in F–centres. Excitation by red laser light allows trapped electrons to escape and recombine with holes, emitting blue luminescence light.

Signal fading characteristic

Spontaneous escape of trapped electrons leads to a characteristic fading of the signal with storage time between exposure and read–out. In refs. [129,130], fading behaviour, in terms of the relative signal at time t with respect to a reference time t_0, is expressed by a superposition of two exponential decay functions (eq. 3.2). Each of them accounts for a characteristic half life (T_1, T_2) of the stored signal charges. a_1, $a2$ as well as T_1 and T_2 are fitting parameters in equation 3.2.

$$\frac{I(t)}{I(t_0)} = a_1 \exp\left(-\ln 2 \cdot \frac{t}{T_1}\right) + a_2 \exp\left(-\ln 2 \cdot \frac{t}{T_2}\right) \tag{3.2}$$

The observed fading behaviour depends mainly on the storage temperature until read–out. Higher temperatures result in higher signal loss. However, a weak dependence on the type of incident radiation has also been found [130, 131].
Although fading is an intrinsic characteristic of the storage phosphor, the read–out process

by the scanner system has a major influence on the measured signal level, which will be explained in the next section. Hence, individual fading characterizations are required for any combination of an IP and scanner system.

Read–out systems

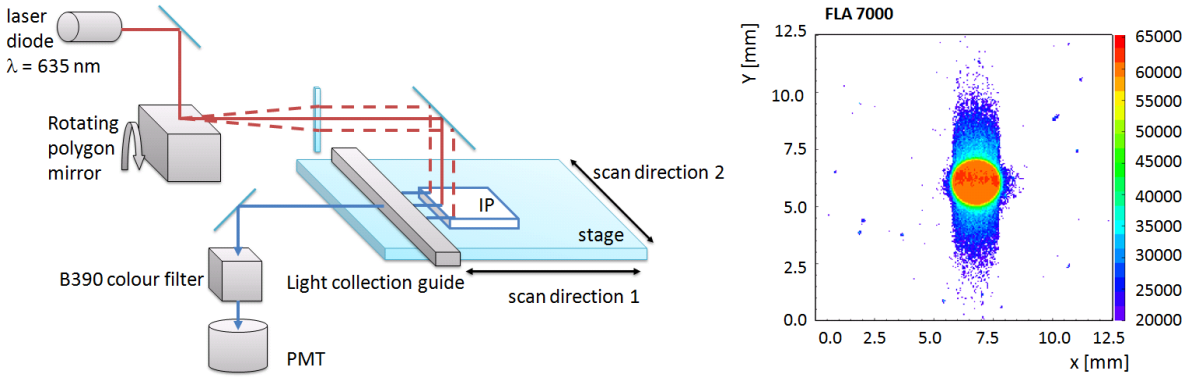

(a)

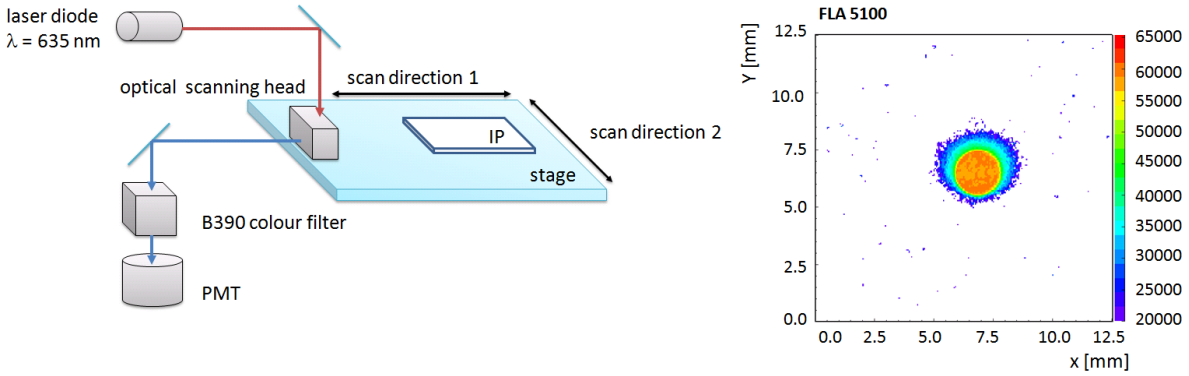

(b)

Figure 3.3: **Schematic sketch of IP scanner systems**
a)FLA–7000 scanner
The combination of a rotating polygon mirror for scanning and light collection guide, covering the whole scanning width, introduces large smearing artefacts in the scanned image.
b)FLA–5100 scanner
Smearing artefacts are minimized by means of a sophisticated optical system for scanning and directed light collection.

Special scanner systems are required to read–out information stored in IPs. Some basic components are common to all IP scanner systems: A red laser diode and scanning unit for IP stimulation and a photomultiplier tube (PMT) equipped with colour filter to separate all contributions of the original laser light from the emitted blue luminescence light.
However, the main component that determines the performance of a read–out system is the

scanning unit. Different methods exist to scan the red laser light on the surface of the IP, each of them offering their own advantages and disadvantages.
The collected signal level depends on different factors. Primarily, it is determined by the number of trapped charges. However, the IP's sensitive thickness defines the total number of available trapping centres and also has an influence on signal levels.
Photo–stimulated luminescence is characterized by a characteristic decay constant. Luminescence light of an Eu^{2+} transition, centred at a wavelength of 385 nm (3.22 eV), exhibits a lifetime of $3.3 \pm 0.1\ \mu s$ [132]. The amount of collected light increases, therefore, with the illumination time of a read-out spot.
Within this work, two different read–out systems from Fujifilm, a *FLA–5100* and a *FLA–7000* have been used [133, 134]. Both systems differ in the scanning technique, as schematically illustrated in fig. 3.3, together with examples of corresponding radiation images.
The *FLA–7000* is a so–called flying spot scanner [135], which is the older one of the two scanning techniques presented here. Two scanning directions can be distinguished. The first direction (scanning direction 1) is scanned either by movement of the scanning unit or the IP stage. The second direction (scanning direction 2) is actively scanned by the scanning unit. The heart of this unit is a rotating polygon mirror that moves the incident laser light along a row of the IP. Emitted luminescence light is collected by a light collection guide, filtered and transferred to the PMT. Fast scans are possible using this scanning technique. However, the illumination time per read–out spot is in the order of the luminescence emission time, thus, introducing artificial patterns in the obtained image (fig. 3.3a). The light guide optics do not only collect the signal of the momentarily stimulated spot but also after–glow of surrounding, previously read–out pixels. As a result, a smearing of the two–dimensional signal distribution along scanning direction 1 is observed (fig. 3.3a).
The scan head used in the *FLA–5100* is moved along both scanning directions. It contains optics to direct light to and from an illuminated spot, thus preventing light collection from surrounding spots. The *FLA–7000* allows read–out of an area of $24 \times 25\ cm^2$ at $50\ \mu m$ resolution within 2 minutes [134]. About twice the time is required for a 24–fold smaller area in case of the *FLA–5100*, which features a much longer light exposure per read–out spot than the *FLA–7000*. Hence, smearing effects are almost completely suppressed in case of the *FLA–5100* reader (fig. 3.3b).

3.1.3 Radiochromic films

One of the oldest types of passive detectors are radiographic films. The sensitive layer of such a film usually contains an emulsion of small silver halide crystals suspended in a gelatin binder. Interaction of electrons, generated by incident radiation, and silver ions, yields a small number of silver atoms on the surface of the silver halide grains. These atoms act as activation centres during chemical development of the radiographic film. Exposed silver halide crystal are reduced to elemental silver, finally resulting in film darkening. Hence, a measurable change in optical density (OD)—defined by the negative decade logarithm of the light transmission T (eq. 3.3)—is observed [1]. A linear measuring range exists, showing a well–defined relation of absorbed dose and the background corrected OD, the so–called

netOD.

$$OD = -log(T) \tag{3.3}$$

$$netOD = OD_{irr} - OD_{background} \tag{3.4}$$

A modern development of film detectors are radiochromic films (RCF). The detection principle, relating an observed change in optical density to the amount of deposited energy, is the same as for radiographic films. However, as other chemical processes yield an OD change, these kind of films have the major advantage of being self–developing.

EBT and EBT2 films

Within this work, a special type of RCF, Gafchromic EBT2 [136], was used for dosimetry in bio–medical experiments. Standard dosimetric protocols such as TRS 398 specify dose determination with ionization chambers in the therapeutically relevant energy range from 50–250 MeV (cf. sec. 2.2.2, [44]). However, for experiments within this work with low–energy proton beams (E <25 MeV) and water–equivalent ranges below 7 mm, this kind of dose determination formalism is not suitable. Therefore, EBT2 films were chosen for dose verification measurements.
EBT2 films as well as their predecessor, EBT, were introduced for quality assurance (QA) in intensity modulated radiotherapy (IMRT), as they are offering sensitivity in the relevant dose range of 0.2–8.0 Gy [137, 138]. Another beneficial feature of these kind of films is their nearly water equivalent effective charge. Detailed specifications on these films are given in [136, 139], a comparison is found in [140].
Binder material as well as the layer configuration has been changed upon introduction of EBT2 film. In the older EBT films, two independent active layers of 17 μm were symmetrically centred around the middle of the film. The two active layers have been replaced in the EBT2 film by a single 30 μm thick active layer, asymmetrically sandwiched between two protective polyester layers (fig. 3.4). Furthermore, an additional marker dye has been incorporated in the active EBT2 layer, enabling the correction of thickness variations in the active layer. Although film uniformity is improved by means of the manufacturers thickness correction algorithm, uncertainty in dose measurement is increased by one order of magnitude with respect to the standard analysis methods without thickness correction [141]. Despite aforementioned configuration changes, the radiation sensitive component of the active layers of both film types is the same. Therefore, performance characteristics of EBT films are initially assumed to be valid for EBT2, as well.
The sensitive component of EBT films is the Lithium salt of pentacosa–10,12–diynoic acid (PCDA), a micro–crystalline diacetylene, where the hydrogen atom of the carboxyl end group is replaced by lithium [136, 142]. Polymerization of the PCDA monomer yields two mesomeric polymer structures (fig. 3.5) [143]. Energy deposition by incident ionizing radiation randomly starts solid state polymerization of the diacetylen monomers in the active layer [144]. Triple bond breaking generates intermediate radical states, acting as active centres for monomer attachment. Each of the initiated polymer chains grows independently from the others. As a first step, polymers with a butatrien–like structure are formed, which are finally rearranged into an acetylen–like structure.

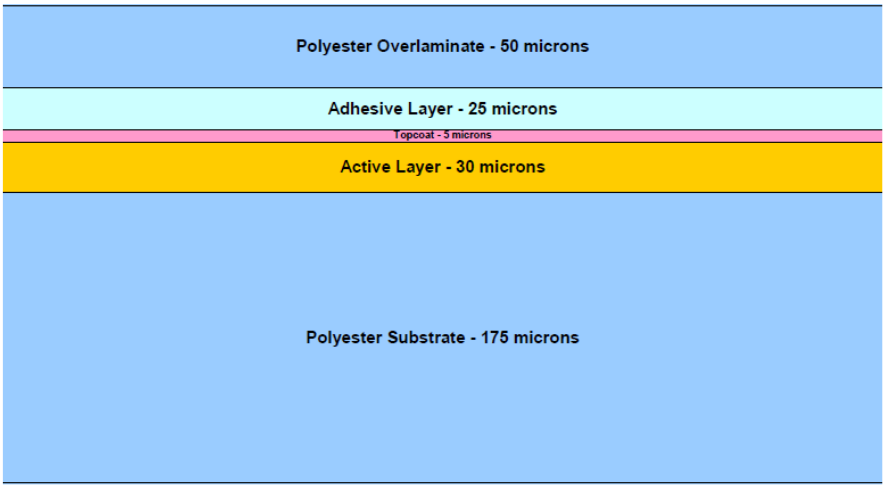

Figure 3.4: **Configuration of Gafchromic EBT2 films** from [136]

The amount of initialized active centres depends on absorbed energy and, thus, dose. As diacetylen polymers form a blue–coloured dye with additional absorption peaks in the red, film colouring is, therefore, a measure for the deposited dose.

Post–exposure growth of optical density

The polymerization process starts immediately and proceeds further after irradiation. As a result, post–exposure growth of film darkening of up to 9 % within 24 h after irradiation is observed [145]. Corresponding optical density values logarithmically increase with time [136]. To obtain reliable, quantitative results, a minimum waiting period between irradiation and readout of 1–2 hours is suggested by the manufacturer. However, in medical centres using these kind of films, post–exposure waiting times of 24 hours are common practice to minimize dose uncertainties related to density growth according to recommendations of the AAPM (American Association of Physicists in Medicine) for radiochromic film dosimetry [146].

Film dosimetry in proton beams

Gafchromic films were developed for application in external beam therapy with photons. Their excellent spatial resolution, compared to other two–dimensional detectors, is especially beneficial in highly conformal therapies. Therefore, this kind of film is also applied for proton beam dosimetry.
The response to protons and photons is comparable. Though, compared to photons, an under–response is reported for heavy ions due to their higher LET value [147, 148]. This result agrees with quenching effects observed in proton Bragg peaks, already known from other types of films, such as the MD–55–2 [149], used before introduction of the EBT–films [150, 151].
Recent studies, using EBT films, investigate the energy dependence of these films in proton and heavy ion beams [147, 152] but also electron and photon beams [153, 154], showing only

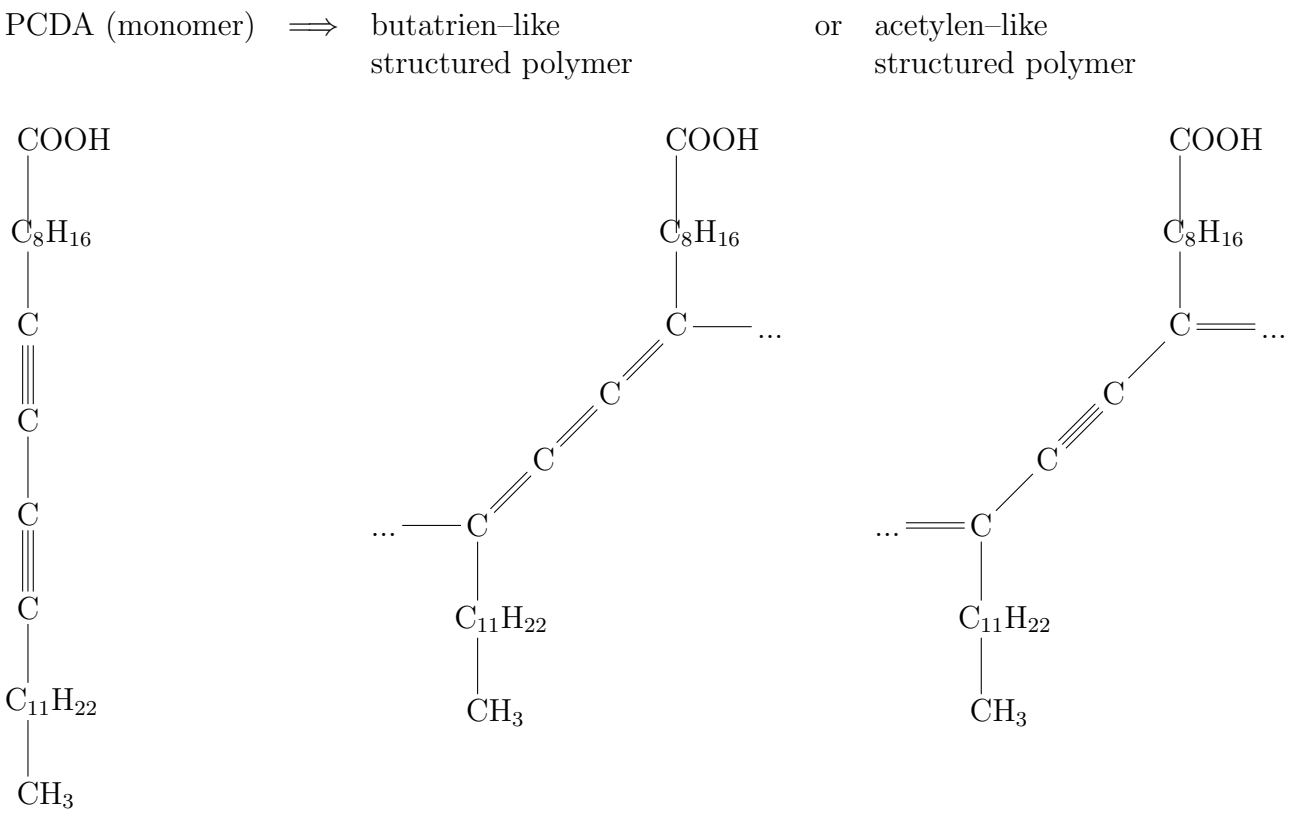

Figure 3.5: **Structural formula of pentacosa–10,12–diynoic acid (PCDA)**
Polymerisation of PCDA yields two mesomeric polymer structures. In RCF films, the acetylen–like structure is responsible for film darkening due to irradiation.

a week dependence on particle type for clinical relevant energies. However, in case of proton beams, comparing the dose measured with a Markus ionization chamber with one measured by the film, a deviation of more than 10 % for proton energies below 3.2 MeV [152] is observed. Hence, increasing dose uncertainty for low–energy proton beams when no under–response corrections are used.

Film read–out

Gafchromic films can be read–out using conventional colour flat–bed CCD scanners [155–157]. An unexposed film has a peak in the absorption spectrum, centred around 420 nm, that is related to the active' s layer marker dye. The polymerization reaction introduces additional absorption peaks in the red part of the spectrum [158]. Hence, in the dose range up to 10 Gy, the best film response is measured in the red colour channel [156].
Film response strongly depends on the film orientation with respect to the scanning direction [159]. This effect is related to the needle–like structure of the formed polymers, which have a diameter of 1–2 μm and length of 15–25 μm according to the manufacturer. Additionally, these structures align preferably parallel to the films coating direction, the short side of a whole film sheet, resulting in different light scattering properties for landscape and portrait orientation [136, 160]. Hence, it is important to always maintain the same scanning

orientation in scanner–based film dosimetry.
Anisotropic light scattering also results in a non–uniformity over the scanning field, perpendicular to the scanning direction [157, 160]. As a result, signal levels decrease from the middle of the scan bed to systematically lower values at the horizontal scan bed boundaries, in uniformly irradiated films. It has been reported, that this deviation increases with dose, up to 9–19 % for a 7 Gy dose, depending on the scanner system [157].
Another issue concerning film orientation is related to the film side facing the scanner. With new EBT2 film batches, a note was delivered by the manufacturer, reporting on deviations in film response for the same scanning orientation when different sides of the film were facing the scanner. This effect is of special importance when scanning films in reflective mode [161]. Therefore, side orientation also has to be maintained when using a film–scanner system for dosimetric measurements.
The asymmetric film configuration of EBT2 has also to be considered when exposing the film to low–energy protons. A *TRIM* simulation of an incident proton beam of 8 MeV energy shows up to 12 % difference in energy loss within the active layer when different film sides are facing the beam. In all EBT2 measurements presented within this work, the same film side orientation with respect to the beam was, therefore, used, with the overlaminate layer facing the beam.
Very recently, EBT3 films have been introduced as successor of EBT2, to eliminate orientation dependence associated with the asymmetrical layer configuration of EBT2. As the active component remained unchanged, the same dose response and energy dependence has been found as for EBT2 films [162].

Digitization and scanning procedure

The scanner system used for measurements presented here, is the Epson Perfection V700 Photo [163]. Scans can be performed in transmission as well as reflective scanning mode. The CCD array of this scanner has a physical resolution of 1200 dpi and offers up to 48 bit digitalization for colour images. For data acquisition, the manufacturers software *EPSON*

Scan settings for EBT2 film dosimetry	
Scanner	Epson Perfection V700 Photo
Software	Epson Scan Professional mode
Filme type	positive film
Scan resolution	1200 dpi
Image type	48–bit RGB
File format	uncompressed TIFF
Image correction methods	OFF
Number of preview scans	5
Waiting period until read–out (nominal)	48 h

Table 3.2: **Scanning protocol for EBT2–films**

Scan was used in professional mode, enabling turn–off of all available image correction methods. To minimize the influence of all film specific effects a common scanning protocol has

been used for read–out (tab. 3.2). Due to the small size of exposure areas in radio–biological experiments, the full physical resolution of 1200 dpi was chosen, different to typical clinically used scanning resolutions of 72 dpi. To allow the scanner temperature to stabilize, a total number of 5 preview scans were obtained before film scanning. All films were scanned in landscape orientation in transmission mode as 48–bit RGB–images with the thicker polyester layer facing the scanning bed. Images were saved in the uncompressed tagged image file format (TIFF). To account for post–exposure growth in optical density, films were scanned not earlier than 44 hours after exposure. This prolonged time period compared to the commonly used one is solely attributed to practicability issues in this work.

3.1.4 Silicon pixel detectors

Three different kinds of pixel detectors have been investigated for use in the online diagnostic system (tab. 3.3). Two of the detector systems, *Kappa DX–4* and *RadEye*, are monolithic, commercially available silicon detectors. Both are optimized for visible light detection, where absorption length of the incident photons are in the order of few μm. Therefore, depletion depths in these devices are in the order of only 2–3 μm. The third system, *Timepix*, is a hybrid detector based on 300 μm thick silicon sensor, bump–bonded to the *Timepix* read–out chip. Costs of both commercial systems are below 10 k€, read–out electronics represent

detector system	***Kappa DX–4***	***RadEye***	***Timepix***
system type	monolithic	monolithic	hybrid
sensor material	Si	Si	Si
pixel pitch [μm]	7.4	48	55
sensor type	CCD	photodiode array	bulk
sensitive area [mm^2]	7.4 x 7.4	25 x 50	14 x 14

Table 3.3: **Pixel detector systems**

the major part (˜3 k€). In addition, sensors can be easily replaced when damaged, single sensor modules of both, *Kappa DX–4* and *RadEye* system, cost less than 1 k€. The *Timepix* system is only available for members of the Medipix collaboration. A single detector system is rather expensive (>20 k€). Replacement of the sensor chip is not possible due to the bump–bonding technique, which makes this system even more expensive if replacement due to radiation damage is required.

Kappa DX–4

The *Kappa DX–4* system is a commercially available industrial camera system, based on a Kodak Interline Transfer CCD sensor, KAI 1020 [164, 165]. The interline transfer architecture, schematically depicted in fig. 3.6, is optimized for optical detection. Each pixel is divided into a light–sensitive photodiode and light–shielded vertical charge transfer region. At the end of a pre–selected exposure time, charge accumulated in the photodiode region is transferred to the vertical shift register. While charge of the previous image still is transported to the read–out node, the next image acquisition can already proceed. Subdivision

into different functional areas of a single pixel, results in a smaller fill factor of these kind of CCDs. Therefore, micro–lenses are applied to focus incident light onto the light sensitive area and thus, increase the optical quantum efficiency. Nowadays, the majority of optical CCD systems is based on this design.
However, for charged particles the light–shield, typically a thin aluminium layer, is not sufficient to stop particles from crossing the charge transfer region. Hence, effects related to charge generation in the shift register have to be considered. The most important sensor

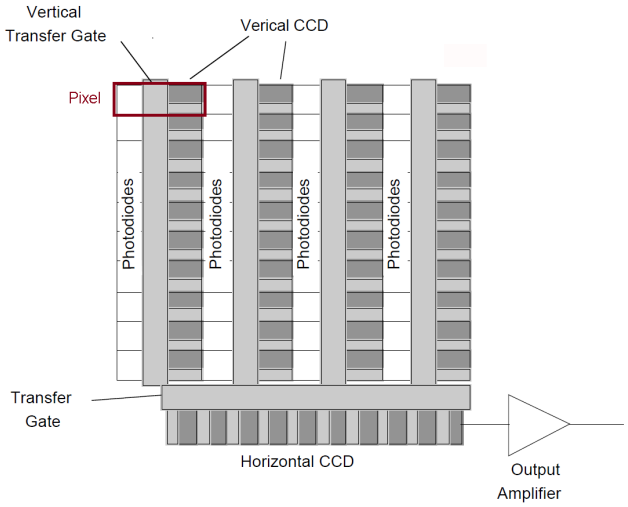

Figure 3.6: **Layout of an interline transfer CCD** adapted from [166]
In an interline transfer CCD, only a part of each pixel is sensitive to incident light (photodiode). In the remaining space, a light–shielded charge transfer region (vertical transfer gate and vertical CCD) is incorporated.

parameters are summarized in the following, for details see [165]. The KAI 1020 sensor has a matrix of 1004 x 1004 square pixels with 7.4 μm pixel pitch, resulting in a sensitive area of 7.4 mm $\times$ 7.4 mm. No exact value for the thickness of the depletion depth is published by the manufacturer, only an estimated value of 2–3 μm is given [167]. For any energy loss simulation a sensitive thickness of 2 μm is assumed. The saturation level is about 40000 electrons, corresponding to a maximum energy deposition of 144 keV per pixel. A 20 MeV proton loses approximately 10 keV of energy in the sensitive area of the detector, yielding a saturation fluence of about $2 \cdot 10^7$ protons/cm^2.
For the purpose of ion detection, a monochrome sensor without micro–lenses and without protective cover glass was chosen. To allow use as transmission monitor, the sensor chip is placed on a separate board (fig. 3.7). Board material, lying within the sensor socket boundaries, is removed to further decrease the amount of material in the beam.

RadEye

The *RadEye* 1 detector is a commercially available, two–dimensional, large area CMOS imager, designed for digital radiography applications such as mammography or industrial inspection [168–170]. A scintillator screen, converting incident X–rays into visible light, is

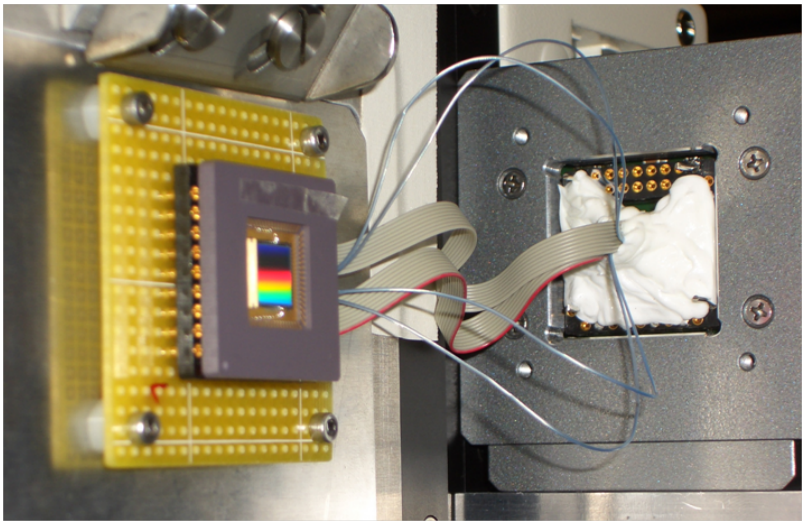

Figure 3.7: ***Kappa DX–4* system**
The sensor of the Kappa DX–4 system is separated from the read–out electronic box to allow beam monitoring in transmission geometry.

usually directly coupled to the sensor for this kind of applications [170].
The photodiode matrix of 512 by 1024 active pixels, spaced by 48 μm each, thus, covers an exceptional large sensitive area of 24.58 x 49.15 mm^2. Additional sensor modules can be tiled at three sides of the sensor to cover even larger areas (fig. 3.8).
A pixel capacitance of approximately 0.15 pF, yields a depletion depth of about 2 μm (eq. 2.19) [170]. The SiO_2 passivation layer on the sensor surface has about the same thickness [171]. Therefore, all energy loss simulations are based on 2 μm thick layers, as in the previous section for the *Kappa DX–4* system.
A small connector placed at a short sensor side, provides all operational signals. All necessary control circuitry is already integrated on–chip, yielding a pixel fill factor of about 80 % [170].
The dynamic range of the detector of approximately 80 dB, is associated with a high saturation level of $2.8 \cdot 10^6$ electrons per pixel. Using the same 20 MeV proton energy loss estimation as for the *Kappa DX–4* sensor, the given saturation level corresponds to a maximum fluence of $4.4 \cdot 10^7$ protons/cm^2. Although the *RadEye* sensor has about a factor of two higher saturation level per pixel as the *Kappa DX–4* system, approximately the same saturation fluence is calculated due to the larger pixel size.
In the present work, a Remote *RadEye* Camera System with Ethernet interface, based on a Pleora iPort IP engine, is used [172]. The IP engine, acting as frame grabber, as well as further control electronics, supplying all required functionality for read–out, amplification and digitalization of the sensor's differential voltage output, are separated from the sensor [173]. The camera systems allows parallel read–out of up to 4 sensors, hence covering a sensitive area as large as 50 cm^2. For all test measurements, engineering grade sensors without scintillator were employed, initially showing up to 10 % defect pixels [174].

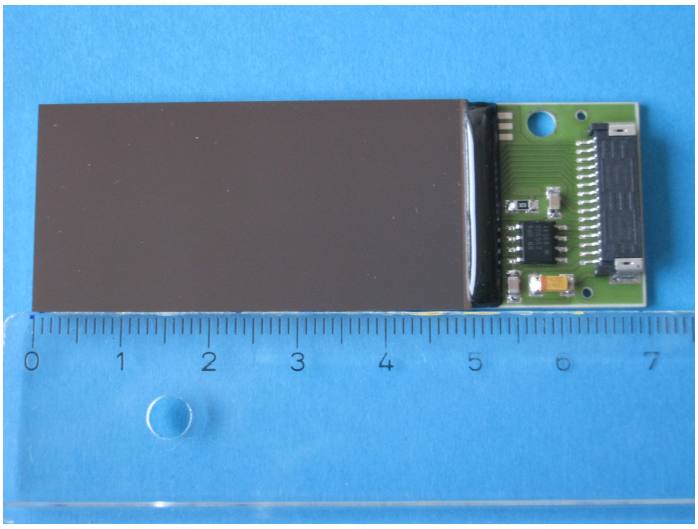

Figure 3.8: ***RadEye* 1 sensor module**
The RadEye CMOS imager has a large sensitive area of 25 x 50 mm^2 that allows the attachment of additional sensors.

Timepix System

The *Timepix*–based system is the only non–commercial system, which was tested with a team from the Czech Technical University in Prague, being member of the Medipix collaboration [175, 176]. Both commercial systems, introduced in the previous sections, are charge integrating devices. *Timepix*, in contrast, is a single–quantum counting device, offering different operation modes on a per pixel base.
The detector system is based on the *Timepix* chip, a successor of the Medipix2 read–out chip, developed in the framework of the CERN Medipix collaboration.
Timepix is a hybrid detector system. Hybrid detector technology allows use of different sensor materials, besides silicon e.g. GaAs or CdTe, while the read–out chip benefits from established silicon manufacturing technology [175].
The *Timepix* read–out chip has a matrix of 256 x 256 pixels with 55 μm side length, each. All operational input and output signals are applied on one side of the chip. Hence, additional chips can be attached at the remaining free sensor sides, allowing to further increase the rather small sensitive area of only 1,98 cm^2.
Manufactured in CMOS technology, analogue as well as digital signal processing circuitry is integrated in each pixel. The analogue part contains pre–amplifier and discriminator, comparing the amplified signal charge with a pixel–dependent threshold level and, thus, providing the input signal for the digital circuit part.
Compared to Medipix2, only offering a particle counting mode, *Timepix* additionally allows arrival time or energy measurements. Key components of the digital circuit are, a *Timepix* synchronization logic and 14–bit shift register [176]. During read–out, the shift–registers transports charge from pixel to pixel. In acquisition mode, however, the shift register behaves as a counter, with saturation limit of 11810 counts. The logic unit of each pixel synchronizes the discriminator output with an external reference clock, providing a clock

signal, specific to each operational mode, to increment the counter.

- Medipix mode—particle counting
  The counter is incremented each time a signal charge, generated by an incident particle, exceeds the threshold level of the pixel. In contrast to Medipix, using two threshold levels per pixel to form an energy window, only a single threshold is available for the *Timepix* chip [175].

- Time mode (TIM)—arrival time measurement
  In TIM, the arrival time of incident particles is registered. The number of counts, measured in the time period between first threshold crossing and end of integration time, represents the arrival time of the particle. The time resolution is, therefore, determined by the reference clock frequency of up to 100 MHz [176].

- Time over threshold mode (TOT)—energy measurement
  The TOT mode, the counter works as Wilkinson type ADC. The discharge time of the ADC capacity, depending on signal height and, thus energy, is represented by the number of counts [177].

Each pixel can be independently operated in any of these modes. Threshold levels are adjusted for each pixel by a 4–bit ADC to allow signal detection just exceeding the noise floor. Additionally, individual (usually noisy) pixels can be turned off [176].
Timepix has been applied for radiography with X–rays, neutrons and heavy charged particles [177]. In TOT mode, saturation of a single pixel starts for an energy deposition of about 1 MeV. However, the corresponding saturation fluence strongly depends on detector settings such as threshold levels and bias voltage, the latter controlling the depletion width [178]. Furthermore, charge sharing effects have been observed for *Timepix*, as well as Medipix2, respectively, for heavy charged particle detection [179–181].
In this work, a USB–based detector read–out interface was used for data acquisition [182]. An energy calibration for each pixel, when measured in TOT mode, is obtained by irradiation with different characteristic fluorescent X–ray lines [180]. The most common detector configuration, a 300 μm thick silicon sensor bump–bonded to the *Timepix* chip, was employed for all measurements (fig. 3.9).

3.2 Experimental setups

3.2.1 Setup at the Tandem van de Graaff accelerator

At the MLL, a conventional electrostatic 14 MV–Tandem van de Graaff accelerator is available. The maximum applicable terminal voltage is 13 MV, which is in practice limited to about 12 MV for reliable operation. A large number of different ion species can be accelerated to energies of few MeV/u with an energy resolution of $\frac{\Delta E}{E} \approx 10^{-4}$. The available proton

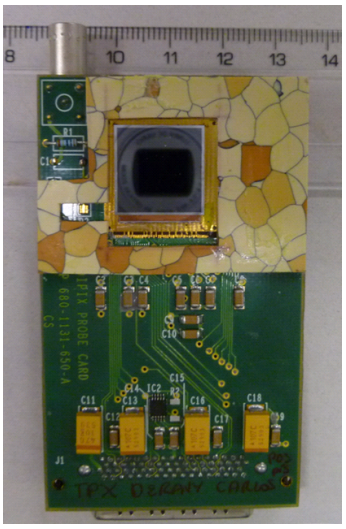

Figure 3.9: ***Timepix***
The sensor chip and electronics of the Timepix PCB are connected by small bonds on the lower edge of the sensor. The yellow plastic frame surrounding the Timepix chips serves as bond protection. Only the PCB is shown, here, which has to be connected to the USB–based read–out box.

energy range of 8–24 MeV covers all energies achievable in laser–acceleration experiments at the MPQ ATLAS laser, today.
Investigation of detector response requires not only reproducible but, even more important, predictable irradiation conditions. Particle fluence as well as energy have to be controlled to a great extent to determine the detector response in a reliable way. Laser–acceleration lacks all these requirements, today, and even further introduces additional difficulties associated to a mixed background radiation or EMP. However, particle pulses with the same time structure and intensity as laser–accelerated proton beams are not readily available at other, conventional accelerators, as these pulse characteristics represent a unique peculiarity of the laser–acceleration process itself.
The Munich Tandem accelerator offers a continuous as well as pulsed beam mode. Pulse widths as low as 1 ns are feasible in the latter mode, thus, being comparable to a laser–accelerated pulse. Moreover, preparation of such ns–pulses with a maximum flux of 10^9 particles/cm^2/ns is possible, a unique feature of the Munich Tandem accelerator. In the past, such pulse intensities were only feasible by means of the ion micro–probe SNAKE (Superconducting Nanoscope for Applied nuclear (Kern–) physics experiments) where pulses with typically 10^5 protons, focused to a beam spot of about 100 μm, yield fluences of up to 10^9protons/cm^2 and ns–pulse. Additionally, delivery of single ions is enabled by this instrument [183, 184]. In the meantime, a high intensity multicusp ion source with extraction current of up to 1.5 mA, has been installed at the Tandem accelerator [185]. Similar pulse flux is feasible without the need of time–consuming strong beam focusing to only few hundred μm diameter. Hence, detector response can be investigated under similar conditions, with respect to time structure and intensity, as typical for laser–accelerated protons, in an inimitable way.

The facility offers a unique possibility to investigate and compare detector response under well–defined conditions in single ion, continuous as well as pulsed irradiation mode.

Large area irradiations at the I–40 beam line

All irradiations, except for some *Timepix* measurement, have been accomplished in air (fig. 3.10), where the beam exits through a circular Kapton window of 10 mm diameter. The window thickness was 130 μm for all continuous measurements while under pulsed beam conditions with lower beam intensity window thickness of 50 μm were used. Two different removable beam diagnostic tools are available, a calibrated Faraday Cup (FC) for current measurement and CsI crystals for visual beam control. In continuous beam mode, diagnostic is primarily used for beam preparation as a particle flux of approximately $10^4/\mathrm{cm}^2/\mathrm{s}$ is below the response limit of both detectors. In contrary, in pulsed beam mode, determination of pulse intensity relies on the current measurement with the FC (eq. 3.5).

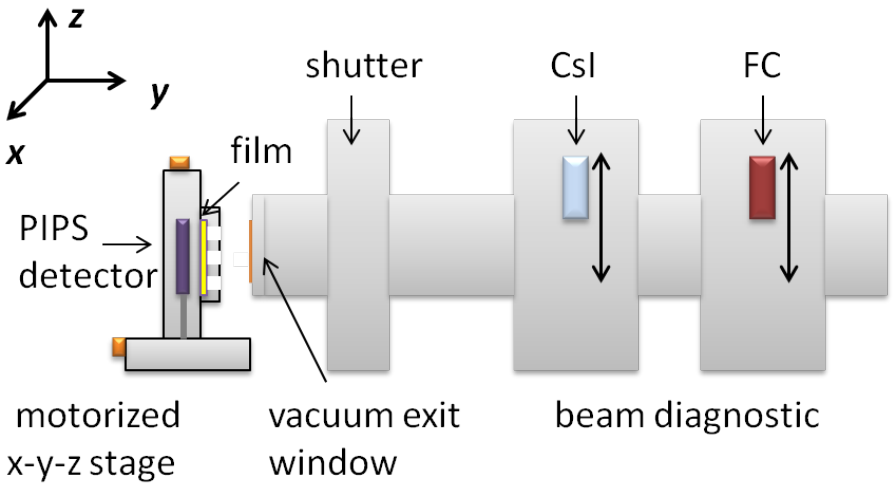

Figure 3.10: **Setup for large area irradiation**
The setup comprises a motorized x–y–z–stage for detector mounting and a removable PIPS detector for fluence determination. Beam diagnostic is composed of a Faraday Cup and CSI crystal.

IP and RCF calibration

IP and RCF calibrations were carried out in a continuous proton beam for different energies up to 20 MeV. The same calibration setup is used for both film detectors, IP and EBT2, as well.
A film is attached to the back of 2 mm thick aluminium aperture plate, mounted on a motorized x–y–z–stage (fig. 3.10). All protons with energies $\leqq$ 20 MeV are blocked by the solid material, thus, defining a circularly shaped exposure area of 2 mm diameter. All calibration

measurements required a homogeneous irradiation of the exposure area and, moreover an accurate determination of the particle number. A passivated implanted planar silicon (PIPS) detector, placed downstream of the film, was, therefore, employed to measure number and energy of particles behind the aperture. The detector has an active area of 50 mm^2, 8 mm in diameter, and a depletion width of 100 μm. The relatively small aperture size is required to ensure that all particles hit the sensitive area of the PIPS detector, despite lateral beam straggling, introduced by film detectors as well as exit window. Under these conditions, fluence is well–defined by the measured particle number and aperture area. The plate contains a matrix of 5 x 5 apertures spaced by 10 mm, which allows irradiation of equally defined areas on a single film by movement of the matrix plate.
The PIPS detector offers an energy resolution of 12 keV at a maximum count rate of about 10 kHz. Dose levels of few Gy are required in RCF calibration measurements with proton energies of 12 MeV and 20 MeV, respectively. A dose of 1 Gy, deposited by protons with 20 MeV energy, corresponds to about $2.5 \cdot 10^8$ protons/cm^2. An irradiation time of approximately 7 hours is, thus, obtained for the maximum count rate. Maximum dose levels were, therefore, restricted to about 1 Gy and 2 Gy for 20 MeV and 12 MeV calibrations, respectively.
For all IP calibration measurements, fluence maxima, determined by saturation effects, are more than an order of magnitude smaller than in RCF calibration, clearly showing the different sensitivity of both film detectors. All irradiations were accomplished within few minutes, count rate limitations of the PIPS detector are, therefore, only a minor problem. However, exposure times of several hours are a clear disadvantage of choosing a PIPS detector as particle counter in RCF calibration measurements. Improvement by at least a factor of ten is possible by means of a scintillation counter, which was not available at that time.
A flux of 10^9 protons/s corresponds to a current of 160 pA, easily measurable by a FC. Irradiation with defined time intervals of few hundred milliseconds to seconds with sub–ms time resolution represents another option for RCF calibration. A fast beam switch is required for this approach, offered at the SNAKE micro–beam, where the majority of RCF calibrations, with proton energies up to 20 MeV, has been accomplished. RCF calibrations related to different fluence determination methods (i.e. PIPS and FC) have been compared to investigate the dose–rate dependence of these films.
Another possibility is the use of the NE–chopper of the pulsing system, allowing to decrease the pulse intensity by a reduction of 2^n ($n \in \mathbb{N}$, $n \leqq 12$). Details on the pulsing system are given in the following section.

IP calibration

Calibration measurements have been accomplished in a continuous proton beam with 8 to 20 MeV energy. Each type of IP was calibrated with three nominal fluence values, spanning approximately two orders of magnitude to allow additional dose response measurements. The dynamic range of the IP reader's photomultiplier usually defines the saturation level of the IP system, although the IP is not yet saturated. To account for the saturation limit of the read–out system, fluence was varied between $10^5 - 10^7$ protons/cm^2 for the TR–IP and $10^5 - 10^6/cm^2$ for the MS–IP measurements, respectively, where no saturation of the IP system was observed. Actual fluence values are determined by the number of particles

within a circular aperture area of 2 mm in diameter , counted by a PIPS detector behind the IP.
For the lowest calibration energy (8 MeV), protons were stopped in the supporting layer of the IP. Therefore, no energy spectrum could be obtained with the PIPS detector for fluence analysis. In this case, the number of particles was measured with the PIPS detector in between IP exposure to obtain an average count rate. The nominal fluence is, thus, defined by exposure time and average count rate. However, this approach is only valid for a stable particle flux. In addition to count rate checks before and after each IP spot exposure, the count rate stability has also been monitored over a time period of 2 hours by alternating irradiation of the PIPS detector and a CR39. An average count rate of 525 ± 180 protons/s is determined from PIPS measurement during IP and CR39 irradiation. The cross–check with a CR39 yields a flux of 527 ± 180 protons/s, showing an excellent agreement with the PIPS measurement and, hence, stability of the average count rate. Nevertheless, the occurrence of momentary strong fluctuations from the average count rate during IP exposure can not be excluded for these measurement.
Spontaneous signal fading has shown to be most pronounced during the first few hours after irradiation (sec. 4.2.1). The steepest signal decrease is found within the first hour, after two hours only about 10 % of the initial fading rate are observed. A waiting period of two hours was, therefore, maintained for all energy calibration measurements.
Significant noise levels are accumulated by background radiation as IPs are highly sensitive to any kind of radiation. Hence, prior to irradiation, all IP pieces were erased for approximately 20 minutes. Background levels as low as $2 \cdot 10^{-3}$ % of the saturation level were, thus, feasible. To prevent signal fading by ambient light until read–out, IPs have been wrapped into light–tight aluminium foils of 11 or 22 μm thickness, respectively. IPs have been kept at room temperature during irradiation and storage period, temperature dependent effects are, therefore, negligible.
Scanner settings are defined by four parameters: pixel size, digital resolution, sensitivity and dynamic range. The same settings were used for both IP readers, if possible. For all measurements, the full digital resolution of 16 bit was used. A good SNR was obtained with a pixel size of 50 μm. Sensitivity and dynamic range are pre–set values in case of the *FLA–5100*. For the *FLA–7000* a dynamic range of 10^5 was used, as it matches the *FLA–5100* setting. However, available sensitivity settings of the *FLA–7000* system differ from the *FLA–5100* sensitivity. The maximum available sensitivity has therefore been chosen for this system.

Pixel detector irradiation

All pixel detector systems have been tested in continuous as well as pulsed beam mode, thus spanning the gap from single proton detection to intense ns–pulses.

Continuous irradiations

During all measurements in continuous beam mode, beam flux was reduced to a level of approximately 10^4 protons/cm^2/s, where individual particle hits are discriminated by all employed electronic detector systems. To ensure homogeneous exposure of the sensitive detector area, the beam was homogeneously distributed over an area of up to 1 cm^2 by means of a magnetic wobbler.
All tests of the *RadEye* and *Kappa DX–4* detector were accomplished in air. Both detector systems are highly sensitive to ambient light which increases the noise level significantly. The Timpix device was tested in vacuum as well as air. For vacuum measurements a large

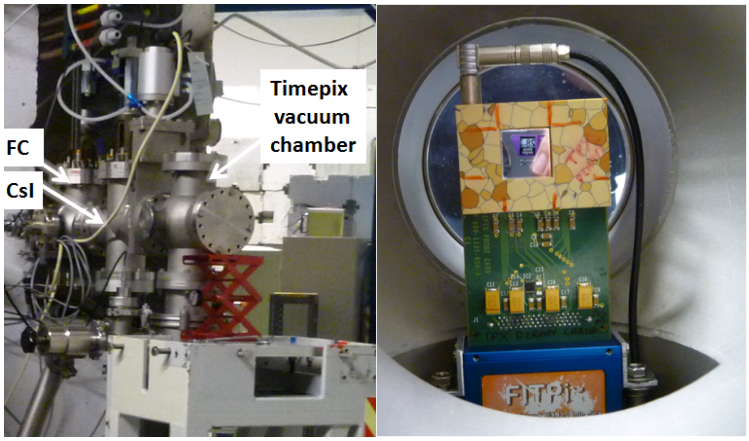

(a) (b)

Figure 3.11: **Vacuum setup *Timepix***
a) The Timepix vacuum chamber replaces the exit flange of the large irradiation setup.
b) Timepix PCB connected to the USB–read–out box mounted in the chamber.

vacuum chamber was used to house the sensor and read–out electronics (fig. 3.11).

Pulsed irradiations

All measurements in pulsed mode were accomplished in air, using the same setup as for continuous irradiations.
For preparation of short ns–pulses, comparable to laser–acceleration experiments, only the pulsing system on the low–energy side (NE–chopper and NE–buncher) of the accelerator has been used [186]. In fast pulsing mode, the NE–chopper is controlled by the NE–buncher's 5 MHz pulsing frequency which can be further reduced by a reduction of 2^n ($n \in \mathbb{N}$). The maximum pulse reduction of 4096 ($n = 12$), yields a pulse period of only 0.8 ms, which is much faster than typical read–out periods of the order of 10–1000 ms for the investigated pixel detectors. Therefore, an external signal with a small repetition rate is additionally applied to the NE–chopper control, forming an AND–gate with the fast pulsing input. This so–called slow+fast (S+L) pulsing mode, thus, enables a temporal pulse spacing, matching

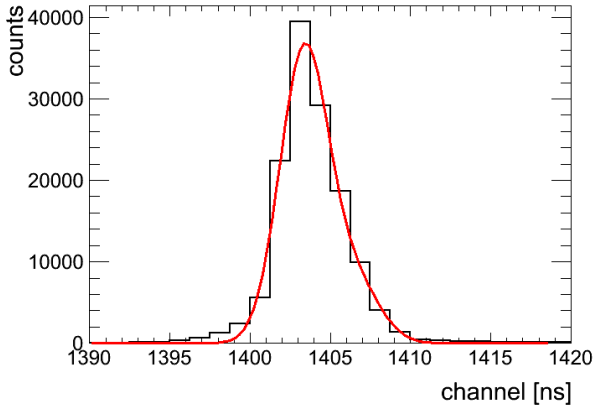

Figure 3.12: **Pulse width spectrum**
Typical pulse width spectrum of 4 ns FWHM that was measured during irradiation of the RadEye *detector.*

the read–out periods of the detector systems.
In fast pulsing mode, the beam current I_{FC} measured with a calibrated FC yields the number of protons per pulse, ppp, according to eq. 3.5.

$$ppp = \frac{I_{FC} \cdot 2^n}{e \cdot 5MHz} \tag{3.5}$$

For measurements in pulsed mode, a multi–cusp ion source for negative hydrogen ions, manufactured by HVEE, was used. It provides a maximum current of 10 μA for injection into the Tandem accelerator [185], thus, allowing to increase pulse intensities up to 10^7 particles per cm^2 for pixel detector tests.
For pulse duration measurements a plastic scintillator with photomultiplier was used. The system was placed downstream and sideways of the beam exit window to detect scattered protons from the pulse. PMT and fast NE–chopper signal provided start and stop signal, respectively, for the time to amplitude converter (TAC). An average pulse duration of 5.6±2.1 ns was, thus, obtained. A typical pulse width spectrum is depicted in fig. 3.12.

Microbeam irradiation at SNAKE

The SNAKE micro–probe is an unique instrument, able to deliver proton beams focused to sub–μm spot sizes in continuous beam mode. In pulsed beam mode a fluence of 10^9 protons/cm^2 can be delivered within a single ns. Furthermore, targeted irradiation with single ions and sub–μm–accuracy is possible.
Opposite the beam exit window, a 7.5 μm thick Kapton foil, a motorized x–y–stage is fixed on the vertical table of a microscope. All irradiation targets (e.g. detector, cells) are mounted on the x–y–stage in close distance ($<$ 1 mm) to the beam nozzle. Electrically and magnetically scanning of the ion beam, allows homogeneous irradiation of small fields with of up to 3 mm side lengths. However, larger fields in the order of cm^2 can be built from small fields, set together by movement of the x–y–stage.

Single ion irradiations

Single ion irradiation is a powerful tool in detector response tests, especially for pixel detectors. Targeted irradiation of individual pixels is feasible due to the excellent spatial resolution of the micro–probe. However, thickness of pixel detectors and available maximal proton energies are major limitations for full exploitation of this tool, due to requirements of the single ion preparation process [187]. In short, a chopper is used to dump a low particle rate beam until a trigger, applied to the chopper, allows the particles to pass. The signal of a scintillation counter, placed behind the target, is used to close the passage gate of the chopper system, once the required number of protons has been detected [187]. Single ion exposure per defined irradiation spot is, thus, ensured. For this method to work, a target thickness is required that allows transmission of a single proton with a remaining energy that yields sufficient light output for detection.
The single ion irradiation mode was used for an IP fading measurement in a 20 MeV proton beam and EBT2 film calibration with 11.1 MeV protons. Films, stuck in front of a cell sample, were exposed to dose levels between 0.5 and 2 Gy in steps of 0.5 Gy. An area of 3.7 mm^2 was homogeneously irradiated, counting each of the particles required for one of the corresponding dose levels by a scintillator. Thus, total fluence uncertainty of $\pm$ 3.8 % is mainly attributed to an uncertainty of $\pm$ 3 % in determination of the field size.
An additional calibration was carried out with a second film attached to the back of the cell holder to investigate the film response to an incident proton energy of 3.1 $\pm$ 0.24 MeV on the film, the same as in the ATLAS cell experiment (sec. 5.3.2). The response to such low proton energies was investigated for 6 dose levels of up to 4 Gy at cell position. For these experimental conditions, particles are stopped at the back layer of the second film. The control of the gate length by the scintillation counter, which is required for single ion preparation is, therefore not possible. For a maximum dose of 5.6 Gy, up to 10^7 protons/cm^2 are required using this proton energy. A fixed gate length was used to deliver the desired fluence with an average particle rate of 100 $\pm$ 10 kHz. Using this rate, it was possible to irradiate the maximum dose level within less than 2 minutes. The average stability of the count rate was checked in between calibration measurements by the scintillation counter. The particle number that is required for a dose level, is determined by the irradiation time. For this measurement uncertainty in dose determination is dominated by count rate fluctuations in the order of 10 %. For the 3.1 MeV calibration, energy straggling within the active layer introduces an additional dose uncertainty of 3.0 %.
The *Kappa DX–4* system is the only pixel detector that has been tested under single ion irradiation using 20 MeV protons. No particle were able to cross the sensor chip. Hence, a fixed gate length had to be used, only in average giving single particle hits.

Dose verification for irradiation of subcutaneous tumours in mouse model

Medical application of laser–accelerated protons, requires biological effectiveness measurements, due to their peculiar pulse structure. So far, only response on cellular level has been investigated at laser accelerators (sec. 5.3.2) [188]. Maximum proton energies and the corresponding number of protons with these energies, obtained at high–repetition rate laser systems, are not yet sufficient for extended tumour irradiation studies in an animal model.

Tumour growth delay of human cancer cells in a mouse model was, therefore, investigated at the conventional Tandem accelerator[2]. The SNAKE micro–probe allows direct comparison of continuous as well as ns–pulsed dose delivery, as it offers the unique possibility to deliver a dose of 20 Gy in a single ns–pulse [184]. A detailed description of technical setup (fig. 3.13) and irradiation procedure is given in [189].

As mouse model, 8–12 week old female NMRI (nu/nu) mice were used with small human–

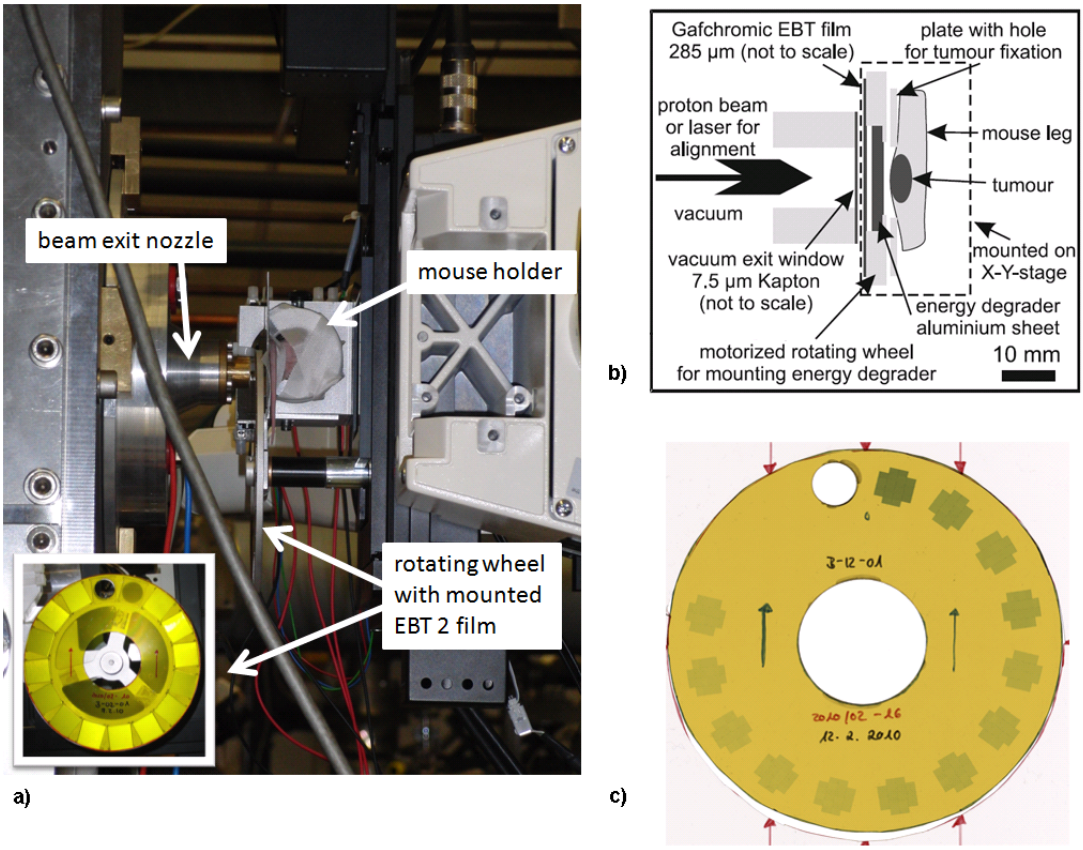

Figure 3.13: **Setup for tumour irradiation**
a) Overview and b) schematic cross–section of the irradiation setup
c) Measured dose distribution for each of the 13 energy layer of the SOBP.

derived head and neck tumour cells of two cell lines (XF354 and FaDu) transplanted to their left hind leg. During irradiation, the mouse was sedated for approximately 90 minutes and placed into a heatable tube, where temperature was controlled to be 37 °C to prevent hypothermia.

For irradiation 23 MeV protons were used, having a range of 5.4 mm in water according to a *SRIM* calculation [190]. For dose verification measurements, EBT2 films were used due to their water equivalent thickness of only about 300 μm. Proton range and a depth safety margin of 1 mm limit the maximum tumour depth to 4 mm, which has been selected for

[2]The experiment was accomplished according to the Protection of Animals Act, Article 20a of the Basic Constitutional Law of the federal republic of Germany. It was authorized by the regional animal ethics committee under the project licence 55.2–1–54–1531–37–09.

irradiation. This was measured on a regular base by ultra–sound to decide when the tumour had to be irradiated. A tumour dose of 20 Gy was delivered in a single treatment, lasting for about 40 minutes, to a cylindrical target volume of 5 mm depth and 9 mm diameter. The spread–out Bragg peak (SOBP) was generated by modulating the beam energy in 13 steps by means of aluminium absorbers with thicknesses in the range of 0–2.4 mm.
EBT2 film is placed in front of the rotating absorber wheel to measure the dose distribution for each energy layer of the SOBP (small inset in fig. 3.13). No online dose control is feasible by this approach. However, film darkening, starting immediately upon irradiation, was monitored by a small web cam to be able to detect irregularities in dose delivery and, if necessary, abort irradiations. All energy layers were subsequently irradiated, starting with the deepest layer. Films were removed and stored at room temperature, in a light–tight envelope, until read–out was accomplished. Energy loss in the films active layer is the same for all energies of the SOBP. The same proportionality factor between dose and fluence is, thus, valid for all layers. For each of the irradiated mice the real delivered dose was calculated from the measured dose (fluence) values.

3.2.2 Synchro–cyclotron at the Rinecker Proton Therapy Center (RPTC)

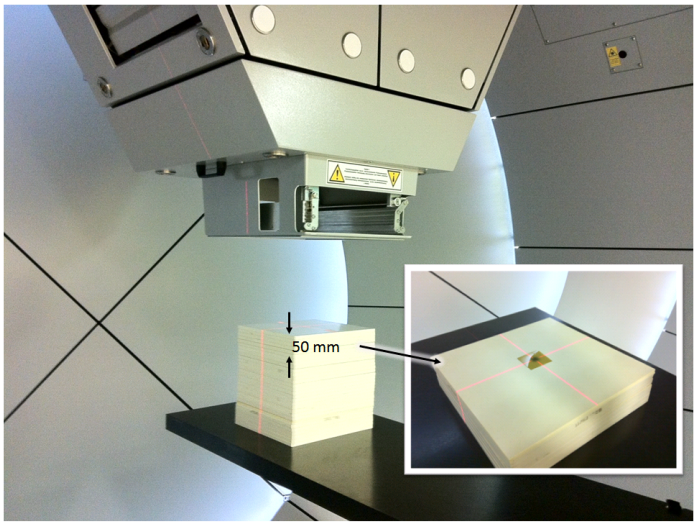

Figure 3.14: **Setup at the RPTC**
The picture shows the beam exit nozzle and PMMA phantom used for calibration measurements. EBT2 films were placed in the centre of the phantom in a reference depth of 50 mm (small inset).

The RPTC, the first industrial proton therapy facility, started treating the first patients in March 2009. It has four treatment rooms equipped with a gantry (fig. 3.14) and one with a fixed horizontal beam line. As accelerator, the superconducting cyclotron 'COMET', developed by ACCEL, is installed, described in detail in [191]. Though a maximum proton energy of 250 MeV is available, only the energy range of 90–230 MeV is used for therapy,

adjusted by a degrader based energy selection system. Dose is delivered in a spot scanning technique, allowing to cover field sizes of up to 30 x 40 cm^2 by means of a magnetic beam scanning system, implemented in the beam nozzle (fig. 3.14) [192].
For a future application of IMPT (intensity modulated proton therapy), dose verification of treatment plans is required for quality assurance. EBT2 films are well suited for this purpose due to their high spatial resolution and sensitivity in the required dose range. Films were, therefore, calibrated in a proton beam of 228 MeV initial energy, equal to a water–equivalent range of 320.46 mm. Additional depth dose measurements allow investigation of energy dependence of EBT2 films down to few MeV energy.
Calibration measurements were accomplished in a PMMA phantom at a reference depth of 50 mm, corresponding to a proton energy of 203.7 ± 0.8 MeV. Films were, thus, lying within the plateau region before the Bragg peak, where no energy dependence is expected, according to experience with older types of Gafchromic film. The phantom had a total volume of 30 x 30 x 30 cm^3 built up of individual plates of 1 cm. A field of 5 x 5 cm^2 was homogeneously irradiated for each calibration step (Δ D = 0.5 Gy) in the dose range from 0.33 Gy to 8.0 Gy.
Reference dosimetry for calibration measurements was carried out with a 0.125 cm^3 Semiflex Chamber from the PTW [193]. Chamber readings have been corrected according to TRS–398 for environmental influence quantities (temperature, pressure) and beam quality [44], only.
Depth dose measurements have been accomplished in a solid–water phantom, as available plates of 1 mm thickness allow sub–mm–resolution of the Bragg Peak. The same area was irradiated as for calibration measurements, though a 200 MeV proton beam, having 260 mm range in water, was used, here. The distance of measurement points of the the depth dose curve was reduced with increasing depth to obtain a good resolution over the whole Bragg curve.

3.2.3 ATLAS laser system

Both non–electronic detectors, IP and EBT2 film, as well as the *RadEye* detector system were used at the ATLAS system in a laser–accelerated proton beam. ATLAS is a Ti:Sapphire TW–laser system, able to deliver a peak pulse energy of 2 J at a wavelength of 795 nm within a 30 fs pulse (FWHM). Maximal pulse repetition rate is 10 Hz, however, all experiments accomplished within this work, were single shot experiments.
Free standing, 5–40 nm thick DLC foils are used for ion acceleration [17]. Protons as well as C–ions are accelerated by the laser–foil interaction. The use of nm–target foils offers the advantage of a reduction in background radiation by one order of magnitude but requires a high pulse contrast, to prevent foil destruction by pre–pulses in the pedestal. The ATLAS system offers an initial contrast of 10^{-4} to 10^{-5}, which is not sufficient for these foil thicknesses. A double plasma mirror system is, therefore, installed which allows contrast improvement by 3 orders of magnitude, at a cost of laser energy that is reduced to 400 mJ on target. Spot diameter (FWHM) of the laser pulse, focused by a 90 ° off–axis parabolic mirror on the target surface, is approximately 3 μm. Thus, peak intensities of $4 \cdot 10^{19}$W/cm^2 are achieved.
Two different spectrometers are currently employed at the ATLAS laser, in the following re-

ferred to as small (SAS)– and wide–angle spectrometer (WAS). The main difference of both spectrometers is the design of the spectrometer entrance, besides magnetic field strength and spectrometer dimensions. In case of the SAS, a small aperture, typically 1–2 mm in diameter, is used, allowing to cover only small solid angles of typically $\ll 1$ msr. The WAS allows to measure an angular–resolved energy spectrum due to a long entrance slit of 14 cm length and 300 μm width, oriented parallel to the vertical magnetic field lines. The energy resolution at the spectrometer plane is in the order of few tens of keV in the MeV proton range. A single magnetic dipole (580 mT over 10 cm length) is used for particle deflection from the central beam axis according to the particles energy and charge–over–mass ratio in case of the SAS, while the WAS uses a set of dipole magnets, 100–200 mT over 20 cm length. Unwanted background radiation, associated to uncharged particles such as X– or γ–rays, is not interfering with ions on the detector site due to the magnetic deflection. No electric field has been applied for all experiments in the scope of this work, as thin absorbers in front of the detectors are usually sufficient to filter all C–ion contributions from the proton spectrum. Fig. 3.15a shows a schematic sketch of the SAS setup, the corresponding energy dispersion relation for protons is plotted in fig.3.15b. Energy is defined by the distance of particle deflection to the zero deflection point (or baseline in case of the WAS), marked by the central beam axis. The detectable energy range on the detector, thus, depends on the dimension of the sensitive area in y–direction as well as position of the detector system with respect to the central beam line. While the upper energy cut–off solely depends on the laser–foil interaction, a lower energy limit of about 4 MeV is obtained for all detectors, due to the setup used, here (3.15b). The vacuum chamber of the *RadEye* system is also used in combination with the WAS, which offers a lower energy limit of about 0.8 MeV at the detector plane.

Cell irradiation experiment

A cell irradiation experiment was accomplished at the ATLAS laser to demonstrate the feasibility of laser–accelerated proton beams from nm–thin foils in combination with a plasma mirror for biological applications [194]. As the maximum proton cut–off energy is about 8 MeV, radiochromic EBT2 film was chosen for dose verification measurements, once again.
Dose was deposited by a single laser shot, although, varying from shot to shot, but, allowing to investigate cell response to single ns–proton pulses. Minimum cell dose levels of 0.2 Gy are required for microscopic analysis of irradiated cell samples as well as EBT2–based film dosimetry. Hence, single shot dose level of at least 0.2 Gy are required, corresponding to a minimum fluence of $1.5 \cdot 10^7/\mathrm{cm}^2$ for protons of 5 MeV energy. Therefore, a small, permanent quadrupole doublet with 554 and 518 $\frac{T}{m}$, respectively, is placed behind the target to focus protons in the energy range 5.2 ± 0.15 MeV onto the cell irradiation plane (fig. 3.15a).
The cell container is placed downstream of the 50 μm thick Kapton exit window, which stops all contributions of C–ions with typical energies of 1 MeV/u. A film is attached to the back foil of the cell container, where an etched grid allows the determination of cell coordinates. Three identification marks on the film are used for film and cell coordinate co–registration under a microscope, required for correct assignment of film dose and irradiated cells during analysis.

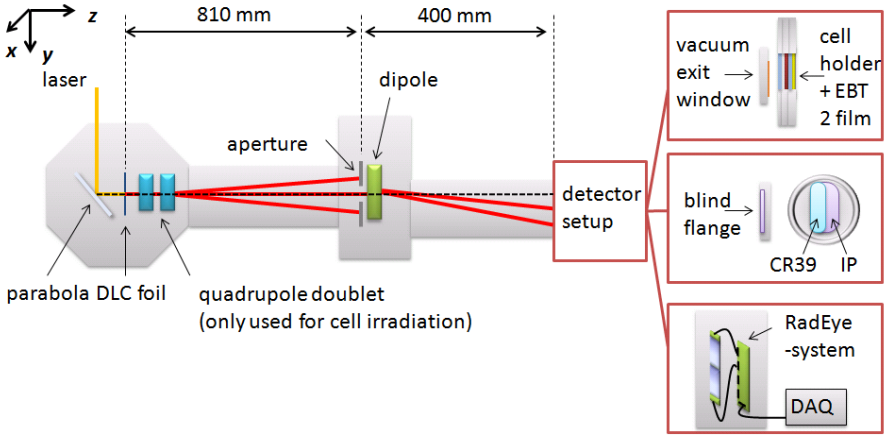

(a)

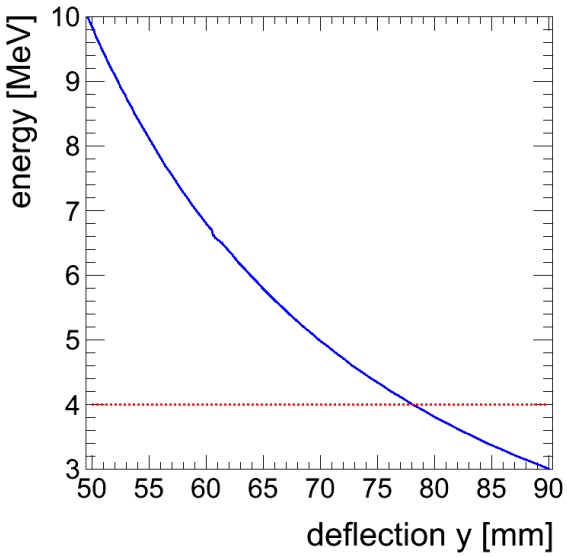

(b)

Figure 3.15:
Setup at the ATLAS laser
a) Ions (red), accelerated by laser–foil interaction are deflected in y–direction by the magnetic component of the small angle spectrometer (SAS). Different setups are used for cell irradiation and detector tests.
b) The energy dispersion curve of the SAS for protons. The deflection distance is measured with respect to the central beam axis (dashed line in a) The red line shows the low–energy cut–off in detector cross–calibration and cell irradiation experiments.

3.2.4 DRACO laser facility

The DRACO laser is a 150 TW, 10 Hz Ti:Sapphire laser system, delivering 3 J pulse energy within 30 fs pulses (FWHM). To test the *RadEye* detector system in a laser–accelerated proton beam the setup of Dresden cell irradiation experiments, IDOCIS, was used [36, 188]. Protons are accelerated in the TNSA regime, with more than 10^{21} W/cm^2 peak intensity

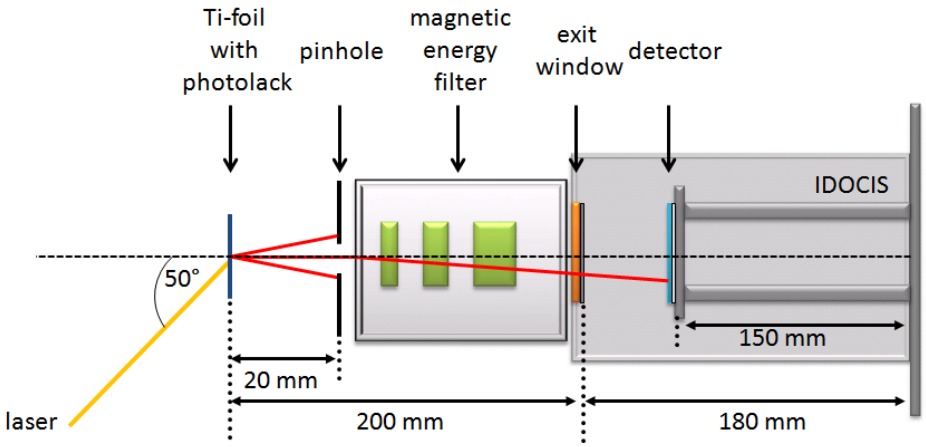

(a)

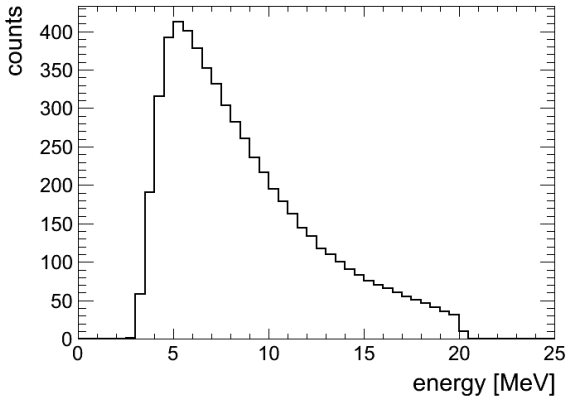

(b)

Figure 3.16:
Setup at the DRACO laser
a) Protons, accelerated from a Ti–foil, pass through a magnetic filter system before entering the IDOCIS chamber, where the RadEye detector is placed approximately 30 cm downstream from the beam exit window.
b) Average proton energy spectrum at the detector site

on the target, a 2 μm thin Titan foil covered with photo–lack. Maximum proton energies of approximately 20 MeV are, thus, available. Emerging particles enter a magnetic energy filter, built of three consecutive dipoles, through a pinhole of 2 mm in diameter. The entrance of the IDOCIS setup is a 25 μm Kapton window, 35 mm in diameter, followed by a thin metallized Mylar foil for light shielding of the sensitive detector area (fig. 3.16a). As a result of all ion–optic and energy degrading elements in the ion beam path, an average proton energy spectrum in the range of 3.0–20.0 MeV, peaked at about 6.0 MeV, is present at the detector site (fig. 3.16b).

3.3 Simulation tools

Different simulation tools have been employed to calculate the energy loss of protons travelling through matter. *SRIM* and *SIMNRA* are Windows based programs, offering interactive graphical user interfaces (GUI) for parameter setting and run of the simulation. *Geant4*, certainly the most powerful simulation tool kit out of these three, requires development of a complete C++–based programme code, to simulate the required particle–matter interaction for a given experimental setup [195].

3.3.1 SRIM

SRIM is a software package for ion stopping and range calculations in matter [196]. It consist of two main components, *SRIM* (The **s**topping and **r**ange of **i**ons in **m**atter)—for quick calculations of stopping and range tables—and *TRIM* (The **TR**ansport of **I**ons in **M**atter)—a tool to simulate ion transport in matter.
The simulation tool is based on the binary collision approximation, using a Monte Carlo method. Impact parameters for the quantum–mechanical treatment of independent ion–atom collisions are randomly selected from a material dependent probability distribution. A screened Coulomb collision describes the interaction of an ion, having an effective, velocity dependent charge state, with a single atom. Long range interactions of ion and the whole target as a collective of atoms are also included [197].
In the basic *TRIM* program, mono–energetic ions are emitted from a point source and enter the target with a fixed angle of incidence, thus omitting any real beam parameters. The target is defined by individual elemental or compound layers. A small database of common compounds is already included in the program.
No experimental stopping power data are available for both non–electronic detectors used within this work. Corresponding energy loss simulations, therefore, only rely on the Bragg–Kleeman rule (eq. 3.6), which can be used to calculate the stopping power of a compound. It is based on the assumption that the stopping power can be additively calculated from the stopping power of the constituent elements weighted by their atomic fraction.

$$\frac{1}{N_{compound}}\left(\frac{dE}{dx}\right)_{compound} = \sum W_i \frac{1}{N_i}\left(\frac{dE}{dx}\right)_i \tag{3.6}$$

However, stopping power depends on the exact electronic structure of the absorber medium, thus limiting the accuracy of the Bragg–Kleeman approach. Whenever applicable, *SRIM*, therefore, uses the Core and Bond approach, where the stopping of each constituent atom with respect to the corresponding bonding type is linearly added to the Bragg–Kleeman result [196].

3.3.2 SIMNRA

SIMNRA is a program used in ion beam analysis for simulation of scattering spectra in any possible scattering geometry [198]. Using a transmission geometry, it allows easy calculation

of the projectile energy spectra after passage through a target, which is similar built–up as in *SRIM*.
SIMNRA uses a Taylor expansion to calculate the energy E_1 of an incident particle with initial energy E_0 after passage through a small target layer of thickness Δx, associated with an energy loss $\frac{dE}{dx} = -\epsilon$ [199].

$$E_1 = E_0 + \Delta x \epsilon \frac{1}{2} \Delta x^2 \epsilon' \epsilon + \frac{1}{6} \Delta x^3 (\epsilon'' \epsilon^2 + \epsilon'^2 \epsilon) \tag{3.7}$$

The same electronic stopping power values are available as used in *SRIM*. However, contrary to *TRIM* simulations, information on projectile energy is available at each layer boundary and not only at the end of the target. Even more important, real experimental conditions (e.g. beam size, energy spread of incident particles) are included in the simulation setup [199].

3.3.3 Geant4

Applications of the object–oriented *Geant4* simulation tool–kit span a wide field from HEP, accelerator physics, space physics and medicine [200].
Even for the simplest simulation, detector geometry, particle source as well as associated physical interactions have to be defined by the user. A simulation run processes a sequence of events, which are among others represented by primary particles and vertices. Particles, primaries as well as generated secondaries, are tracked through the detector geometry by a step by step transport, which is the basic concept of a *Geant4* simulation [195, 201].
The execution of a step can be divided into three parts. First, the step length determination, second, execution of physical actions and third, a final update of all tracking and simulation information, required for the next step.
Each possible physical process, discrete as well as continuous, is associated with a step length. Actions, related to these processes, such as energy loss or decay, can either take place along such a step, at the end of a step or when the particle is finally at rest. The step length, is, therefore an important parameter in each simulation. The so–called physical step length, defined by the minimal possible step length of all relevant processes, is determined in each step. Additionally, a geometrical step length is defined by the distance to the next geometric boundary. Within a single step, boundary crossing of a particle is forbidden. The true length of a step is, therefore, either physically or geometrically defined, depending which one is the smaller one.
All active continuous and discrete physical processes of a step, are sequentially invoked, starting with the continuous ones. Associated cross–sections are assumed to be constant along a step [202]. Track information such as particle energy or position are updated after completion of all continuous as well as discrete processes. Secondaries, generated in continuous physical processes, are stored for later tracking.
The whole stepping procedure repeats itself until the particle is either tracked through the whole simulation geometry or finally at rest and decays.
In contrast to *TRIM* or *SIMNRA*, where only stacks of different material layers can be simulated, complex geometries are applicable in *Geant4*. Physical processes are divided into different categories such as electromagnetic, hadronic, transportation or decay [195]. No

default processes are given, thus, offering the freedom of choice to use the physical model that is best adapted for the experimental context.

3.4 Analysis Tools

The amount of data produced by non–electronic systems is usually manageable due to limited number of detectors. However, pixel detectors with read–out periods of few hundred ms, are able to produce large data sets with several hundred individual images, within minutes. Therefore, data analysis is based on *ROOT*, especially developed for the easy and fast handling of large amount of data [203].
ROOT–based analysis tools and corresponding graphical user interfaces have been developed for all three detector types, presented in the scope of this work. Each detector system is associated with an own C++ class, which characterizes detector and data acquisition (DAQ) parameters. All parameters relevant for detector response, are organized in event classes, adapted to both, detector system and analysis. All detector systems are two–dimensional, offering few μm resolution of the spatially distributed detector response. Areas for analysis are defined by a pre–selection of a so–called region of interest (ROI).

3.4.1 Hit analysis

In case of IPs and RCFs, exposed areas are coherent. Therefore, a simple hit analysis, calculating the mean and standard deviation of all pixels in an homogeneously exposed ROI, is applicable. A typical example of a homogeneously irradiated IP detector and result of the accomplished hit analysis is depicted in fig. 3.17.

For calibration of these detectors, particle fluence as well as average energy in the active layer are quantities of interest. The latter is deduced from a *SIMNRA* simulation, accounting for all layers in the particles path from exit window to the sensitive detector layer. Using this result, the corresponding energy loss $\frac{dE}{dx}$, required for dose calculation (eq. 3.8), is deduced from a *SRIM* table. Φ is the particle fluence and ρ the material density.

$$D = \frac{dE}{dx}\frac{\Phi}{\rho} \tag{3.8}$$

Analysis of EBT2 films

For film analysis, raw pixel values from the red colour channel (pv_{red}) are converted into netOD (eq. 3.3). Here, light transmission T is given, by the ratio of measured pixel value, pv_{red}, to full scanning bit depth of the investigated colour channel (i.e. 16 bit).

$$OD = -\log_{10}\frac{pv_{red}}{2^{16}} \tag{3.9}$$

$$netOD = OD_{irradiated} - OD_{unirradiated} = -log_{10}\frac{pv_{unirradiated}}{pv_{irradiated}} \tag{3.10}$$

For all calibration measurements, uncertainty in netOD is of statistical nature, usually below 5 %, introduced by film inhomogeneity—specified to be less than 1.5 % [139]—as well as

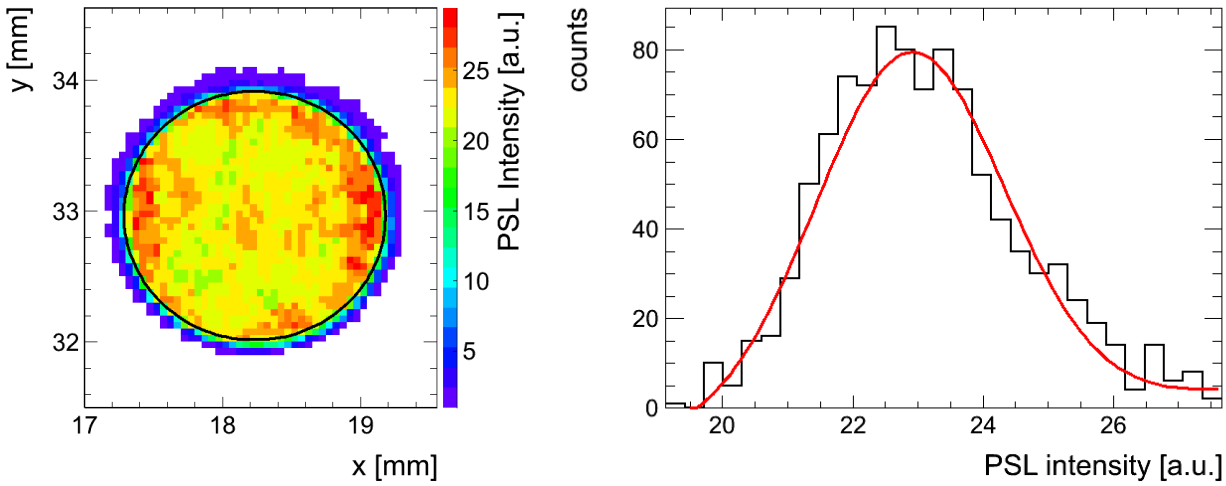

(a) (b)

Figure 3.17: **IP calibration**
a) Typical irradiation pattern on an IP, obtained in calibration measurements at the I–40° beam line. The exposure area was defined by a circular aperture, 2 mm in diameter. The solid black circle represents the ROI that was used for analysis.
b) Distribution of the photo–stimulated luminescence intensity (PSL) that has obtained by the hit analysis algorithm and was fitted by a Gaussian (red curve).

fluctuations of experimental conditions.
Calibration curves, in terms of dose against netOD, are fitted according to reference [204]. In EBT2 film dosimetry, the term dose, always represent the water–equivalent dose ($\rho = 1.0$ g/cm^3 in eq. 3.8).

$$D(netOD) = A \cdot netOD + B \cdot netOD^C \tag{3.11}$$

The second term in eq. 3.11 accounts for non–linearities due to film saturation at high dose levels. To reduce fit uncertainties, the exponent, C, is fixed during the fitting procedure. The optimum value for C, defined by a minimum reduced χ^2 value, was determined by iterative fits for different values of C and free parameters A and B [204]. According to the manufacturer's suggestion of a second or third order polynomial fit, C was always modified in the interval [2.0, 3.0] [136].
For each dose point of film calibration curves obtained at the RPTC and MRI, dose was measured by an ionization chamber, corrected for beam quality and environmental conditions (pressure, temperature). Dose uncertainties, are, thus, related to ionization chamber uncertainties. In case of the Tandem calibrations, dose had to be calculated from the measured particle fluence and mean water–equivalent energy loss value in the active layer of the corresponding experimental setup (eq. 3.8).

3.4.2 Cluster analysis

Division of IP or EBT2 data in pixel is not related to a physical division of these detectors, but is introduced by the scanning procedure, and, therefore related to the chosen resolution setting. In a pixel detector, each pixel is a physical unit, representing an individual detector by itself. Hence, single pixel response is of major interest. However, possible charge sharing effects, resulting in signal spread over neighbouring pixel have to be taken into account when analysing individual, distinguishable particle hits.
A cluster analysis tool has been implemented, accounting for charge spread by merging adjacent responding pixels into a so–called cluster.
Dark current is an important issue in any pixel detector, especially when measuring under potentially damaging conditions. Dark images have been subsequently recorded for the same acquisition settings as for the exposed images, to calculate a noise and noise fluctuation (sigma) map for each measurement. Each exposed pixel map, also called frame, is then background corrected before analysis, thus compensating noise increase in damaged pixels.
For all pixels, a global threshold T_{global} is defined. For analysis an individual threshold level T_i is introduced for each pixel i, as sum of the global threshold and sigma–level dependent factor $n \cdot \sigma_i$ (eq. 3.12).

$$T_i = T_{global} + n \cdot \sigma_i \; (n > 0) \tag{3.12}$$

In presence of charge sharing, values of all cluster pixel have to be summed in order to give a total response signal to an event. However, the centre of mass of the resulting charge distribution is usually at the centre of the cluster. To account for signal level differences between cluster centre and boundary, two individual threshold levels are used for cluster analysis. In a first first step, the lower threshold $T_{i,hit}$, is used to detect all pixels above the noise level, which are subsequently merged into clusters. In a second step, the higher threshold $T_{i,event}$ is the base for decision, if a cluster is to be considered as true event. In doing so, it is sufficient if only one a single cluster pixel exceeds $T_{i,event}$.
The terms cluster and event are used alike in the scope of this work. Associated parameters are cluster size, defined by the number of cluster pixels and cluster sum, which corresponds to the sum of all cluster pixel values, respectively. Pixel values are digital signals, measured in ADU (Analogue–to–Digital Unit). The term pixel value is used, whenever the digital signal of a single pixel is meant.
Cluster analysis is a rather time consuming means of analysis and becomes counterproductive if individual particle tracks are not distinguishable any more. Therefore, a simple hit analysis based on $T_{i,hit}$ was accomplished for all pulsed irradiations. This procedure is justified, as detector response with respect to total pulse flux is the quantity of interest, corresponding to the integrated value of all pixels, referred to as pulse height, in the following. Hence, charge sharing effects are not relevant for this kind of investigation.

4 Experiments with image plate detectors

IPs have been standard detectors for laser–ion diagnostic in all Munich experiments. In the scope of this work, different online detection system have been investigated for real–time detection of laser–accelerated particles to replace the IP–based detection system (chapter 6). However, any online detector, representing a successful alternative for IP–based systems, asks for comparable, or, even improved, sensitivity, dynamic range and spatial resolution as IPs, besides requirements imposed by the peculiarity of laser–accelerated proton pulses, themselves.
Therefore, thorough understanding of IP response is of great importance. Furthermore, calibration and fading corrections are required for quantitative analysis of energy spectra obtained in laser-acceleration experiments with IPs placed in the dispersive spectrometer plane.
Calibration measurements have been accomplished at the MLL Tandem accelerator for different combinations of IPs and reader models (tab. 4.1), in the following referred to as IP systems.

IP–type	**read–out system** *(resolution 50 µm, 16 bit dynamic range 10^5)*		**energy** [MeV]	**nominal fluence** [particles/cm^2]
	reader	**sensitivity**		
TR	*FLA–7000*	10000	8, 10, 12* 15, 20	$10^5 - 10^7$
TR	*FLA–5100*	5000	8, 10*, 15, 20**	$10^5 - 10^7$
MS	*FLA–5100*	5000	8, 10*, 15, 20	$10^5 - 10^6$

* with additional fading measurement
** additional fading measurement with single ions at SNAKE

Table 4.1: **Parameters of IP calibration**

4.1 Calibration measurements

4.1.1 Energy calibration

The intensity of the photo–stimulated luminescence signal depends on the energy loss dE/dx of an incident particle and the particle fluence. IP systems have been calibrated in a continuous proton beam with 8 to 20 MeV energy using three nominal fluence values to allow

additional dose response measurements. A simple hit analysis yields the mean PSL intensity and corresponding standard deviation of an exposed area (sec. 3.4). At least three independent measurements have been accomplished for each energy–fluence combination. The average PSL intensity value, I_{PSL}, was obtained as weighted mean of all these measurements with typical standard deviation of <1 %. Normalization of I_{PSL} per incident proton and pixel, yields the mean single proton response value, I_{PSL}^{norm}.

Fig. 4.1 shows the normalized PSL intensity I_{PSL}^{norm} plotted against proton energy E for all

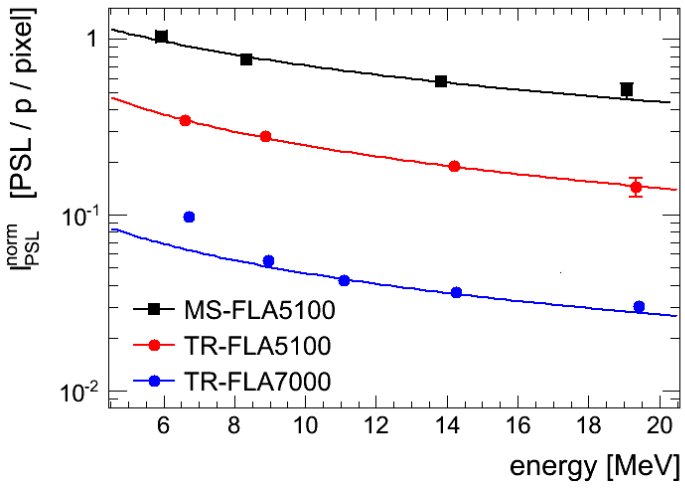

Figure 4.1: **Energy calibration of TR– and MS–type IP**
The signal intensity, normalized per incident proton and pixel, is plotted against proton energy and fitted by a Bethe–Bloch like functional (eq. 4.1). Some error bars are smaller than the corresponding marker symbol. The large deviation for the lowest energy in case of the FLA–7000 calibration is attributed to difficulties in fluence determination.

three different IP systems. Error bars are not visible on this scale. Degrader material in front of the active IP layer reduces the initial proton energy by up to 17 % and 26 % for TR– and MS–type IP, respectively. The mean proton energy in the middle of the active IP layer, obtained from a *SIMNRA* simulation, is used as calibration energy.
Particle energy and energy loss are related by the Bethe–Bloch formula (eq. 2.5), where only the first term is relevant for non–relativistic particles, as used here. Energy dependence of the normalized intensity (fig. 4.1) was fitted with a functional term according to eq. 2.5, using two fit parameters, A and B (tab. 4.2).

$$I_{PSL}^{norm}(E) = const \cdot \frac{dE}{dx}(E) = \frac{A}{E} \ln\left(B \cdot E\right) \tag{4.1}$$

Calibration data, that have been obtained with the *FLA–5100* reader show a good agreement with the fitted function. The same is true for the *FLA–7000* calibration except for the lowest calibration energy, where the normalized PSL intensity I_{PSL}^{norm} has a considerably higher value as expected from the calibration fit. However, for this calibration energy, which corresponds to an initial proton energy of 8 MeV, simultaneous measurement with the PIPS

detector was not possible (sec. 3.2.1). For these measurements the particle fluence has been calculated from the average count rate, measured in between IP exposure. Although the average count rate was stable over a long period of time, it is not impossible that a momentary, strong deviation from the average occurred during IP exposure. A significantly different particle fluence than the one calculated from the average count rate is therefore assumed to be responsible for the deviation of this data point from the fitted curve. The small error of this data point, which is related to the good stability of the average count rate clearly underestimates the uncertainty in fluence determination. For each irradiated spot,

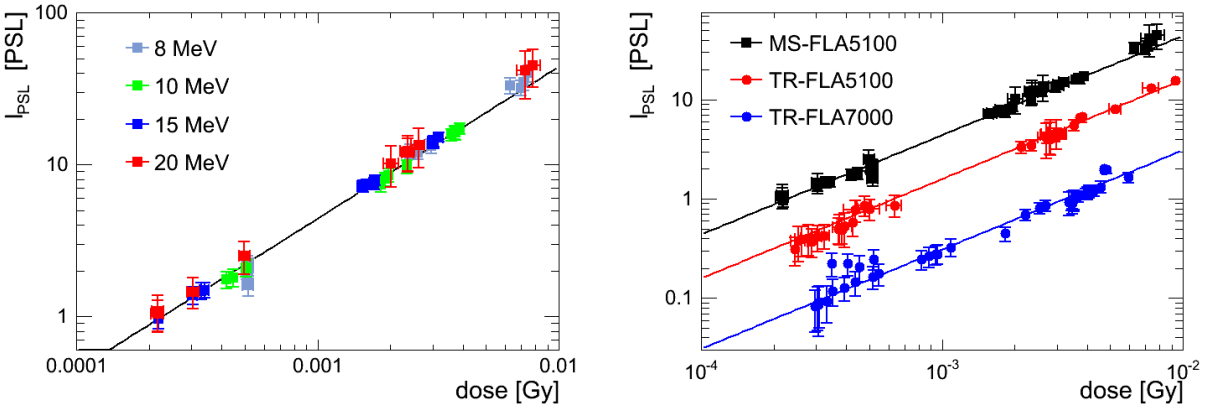

(a) (b)

Figure 4.2: **Dose response curves of IP**
The intensity I_{PSL} increases linearly with the deposited dose (a, b) for all IP systems. Solid lines represent a fit through the origin. No energy dependency of the dose response has been found in the investigated energy range (a).

the deposited dose D in the active layer has been calculated according to eq. 3.8. IPs with similar active layer composition as MS–and TR–type are known to show an under–response in the Bragg Peak region and, hence, LET–dependence [124, 205, 206]. Fig. 4.2a shows the signal intensity plotted against the obtained dose value for the MS–type IP for all calibration energies. Dose uncertainties presented here, are attributed to uncertainties in fluence determination as uncertainty in energy loss is negligible small ($< 0.6\,\%$) for both, MS– and TR–type IP. PSL intensity increases linearly with dose (eq. 4.2). The same fit applies to all data sets, regardless of energy. Hence, there is no LET–dependence for this type of IP in the investigated energy range. Dose response curves of all measurements are summarized in fig. 4.2b, corresponding fit parameters in tab. 4.2. No energy dependence has been found for the TR–type IP, too.

$$I_{PSL}(D) = m \cdot D \tag{4.2}$$

Dose response as well as energy calibration measurements show a strong dependence on the scanner system. For instance, the gradients of the dose response curves of the TR–type differ for both reader models by a factor of 5.2. TR– and MS–type IP have the same sensitive layer composition, though different areal densities of 380.3 g/m^2 (MS) and 142.6 g/m^2 (TR) [207]. A factor of 2.8 is obtained for MS– and TR–type IP, read–out by the same model, which

Energy calibration

scanner type	**FLA–5100**		**FLA–7000**
IP type	**MS**	**TR**	**TR**
$A[PSL/p/pixel/MeV]$	2.446 ± 0.469	0.498 ± 0.200	0.109 ± 0.012
$B[MeV^{-1}]$	1.823 ± 0.973	15.108 ± 29.840	7.171 ± 3.423
$\frac{\sigma_{AB}}{\sigma_A \sigma_B}$ (correlation)	-0.993	-0.998	-0.999

Dose response

scanner type	**FLA–5100**		**FLA–7000**
IP type	**MS**	**TR**	**TR**
$m\ [Gy^{-1}]$	4427.0 ± 79.4	1597.0 ± 31.5	310.7 ± 4.7

Table 4.2: **Fit parameters of energy and dose response curves**

corresponds to the areal density ratio of the sensitive layers. This finding clearly shows the necessity to calibrate each combination of IP–type and scanner model individually.

4.2 Fading investigations

4.2.1 Time–dependent spontaneous fading characteristic

IPs are known to show a characteristic signal fading with time, that depends on IP–type, incident radiation (particle, energy) and temperature, as well as scanner type [129, 131]. Fading characteristic has been investigated for all IP–scanner–systems to obtain fading correction functions.

Both types of IP have been exposed for approximately 2 hours to a standard ^{14}C source (β^-_{max} = 157 keV) to obtain similar dose levels and compare their fading characteristics. Fading has been measured, using the *FLA–5100* reader, over a time period of 14 hours.

Absolute signal levels of TR–and MS–type IP differ by almost one order of magnitude due to different sensitive layer thicknesses. To allow a direct comparison of both types of IP, relative signal levels have been calculated, using the shortest fading period of 30 minutes as reference point (fig. 4.3). Only in case of the TR–plate a clear fading behaviour is visible within the data, fitted according to eq. 3.2 by two exponential decay functions. Fading is most pronounced within the first hour after irradiation, resulting in an intensity loss of 6 %, which increases to only 8 % during the following 13 hours. For the MS–IP no clear fading curve is observed, data points are scattered by ± 5 % around a mean value of 100.8 %.

Further fading investigations were accomplished using protons of different energies, as fading has been reported to depend on particle type and energy [129, 131]. Proton energies of 10 Mev and 20 MeV were employed with the *FLA–5100* reader, and 12 MeV for the *FLA–7000*, respectively. For all fading measurements, the nominal fluence was 10^6 particles/cm^2, and a post–exposure time interval of up to 11.5 hours was covered.

Fig. 4.4 shows fading curves of the TR–type IP for both scanner systems, fitted according to eq. 3.2. Fit parameters are listed in tab. 4.3. All TR–fading curves obtained with the *FLA–5100* reader show a similar fading characteristic. Fading stabilizes within the first two

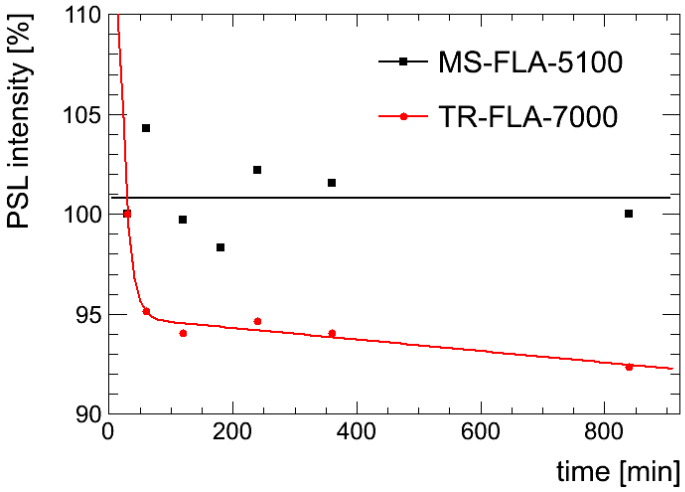

Figure 4.3: **Fading characteristic of MS– and TR–IP**
Data of the TR–type IP are fitted by the sum of two exponential decay functions. In case of the MS–type IP, where fading is not pronounced, the solid line represents the mean value of all fading data. Typical errors (<1 %) are not visible on this scale.

hours to an average value of 93 % considering all three curves regardless of particle type and energy. For a time of 120 minutes, a maximum difference of 3.7 % is obtained for the ^{14}C and 10 MeV proton curves. These differences are of the order of scan to scan fluctuations which have been found to be up to 4.4 % for this scanner model and IP–type (sec. 4.2.3). Fading characteristic measured with the *FLA–7000* scanner differs significantly from all *FLA–5100* fading curves. Fading proceeds over a longer period of time, resulting in a signal reduction of approximately 40.0 % within the first 12 hours after exposure. The strongest signal decrease is observed within the first three hours, yielding 10.5 % signal loss after one hour which increases to 27.2 % during the next two hours.

scanner system	**FLA–5100**			**FLA–7000**
particle type	^{14}C	protons, 10 MeV	protons, 20 MeV	protons, 12 MeV
a_1	66.42	15.27	12.74	43.19
a_2	94.88	89.43	94.27	74.86
T_1	8.17	41.11	30.36	34.12
T_2	2.27 $\cdot 10^4$	1.26$\cdot 10^4$	0.71$\cdot 10^4$	0.28 $\cdot 10^4$

Table 4.3: **Fit parameter of fading curves**

4.2.2 Signal fading with repeated read–out

IPs offer a high dynamic range, whose full exploitation is in practice limited by saturation of the PMT of the reader system. To overcome these limitations of the read–out system, different approaches have been suggested, such as use of neutral density filters for light

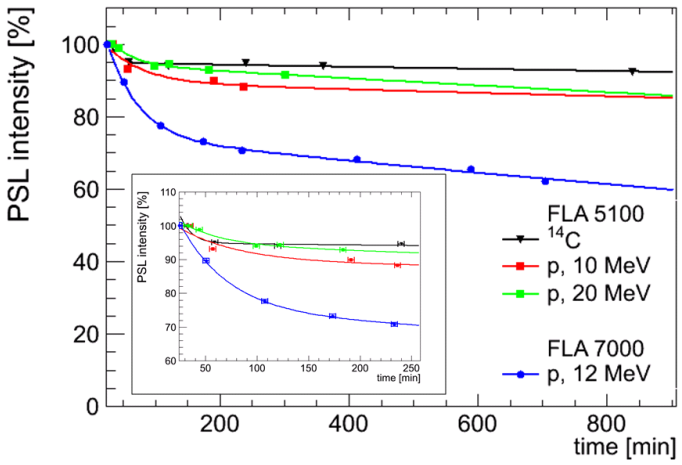

Figure 4.4: **Fading characteristic of TR–IP**
PSL intensity is normalized to the first read-out time of 30 minutes. Fading is most pronounced in the first few hours after irradiation (small inset). Solid lines represent fits by the sum of two exponential decay functions (eq. 3.2). Error bars are not visible on the large scale plot.

attenuation [208] or use of signal erasing with successive scans [207]. The latter method has been investigated within this work for all IP–scanner combinations by means of three successive scans.
In case of the *FLA–5100*, each scan required approximately 5 minutes to complete, thus, defining the time between subsequent scans. No fading correction due to spontaneous fading was applied (sec. 4.2.1) for this scanner system, as fading has shown to vary less than 0.4 % within the investigated time interval. For the *FLA–7000* scanner, read–out of an IP of the same size is accomplished within seconds. However, time periods of approximately 5 minutes were maintained in average between successive scans to match conditions of the *FLA–5100* system. As spontaneous fading is more expressed using this system, fading corrections have been applied to all data acquired with the *FLA–7000* reader.
IPs have been exposed to different nominal fluence values to investigate if the signal loss per scan depends on the initial signal strength and, hence, dose. Ratios of subsequent scans agree within ± 4 %, which is of the order of scan to scan fluctuations (sec. 4.2.3). The typical statistical spread of I_{PSL} is of the order of 1 %. Signal fading per scan is independent of initial signal height and , hence, dose. A dose average value of the normalized PSL intensity, I_{PSL}^{norm}, is, therefore, deduced for all fluence measurements. Fig. 4.5 shows a plot of this value against energy for subsequent scans of MS– and TR–type IP with the *FLA–5100* reader. The qualitative shape of these curves is maintained for all scans.
Signal loss with repeated scans is most pronounced for the MS–type plate, showing more than one order of magnitude intensity loss from the first to the second scan. For the TR–type plate, intensity decreases only by a factor of four for the first two scans. Signal reduction from second to third scan are only about a factor of two, regardless of IP type.
Fig. 4.6 shows the corresponding remaining signal intensity, normalized with respect to

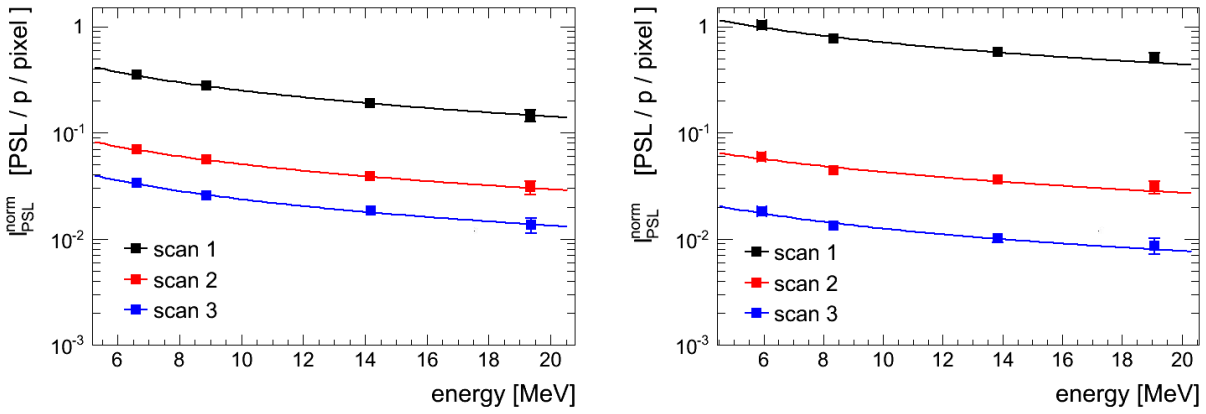

Figure 4.5: **Signal fading with multiple read–out for FLA–5100**
The energy calibration curves of subsequent scans with the FLA–5100 scanner for TR– (a) and MS–type (b) IP show similar behaviour, fitted according to eq. 4.1 by a Bethe–Bloch like functional term.

the first read–out, plotted against the scan number. The residual signal intensity has been averaged for all energies due to dose independence of the signal loss per scan. The signal reduction by successive read–out, depends on both, scanner system as well as IP–type. In case of the MS–type plate, only 6 % of the initial signal remain after the first scan, while for the TR–type still about 20 % are measured when using the *FLA–5100* reader. Residual signal heights are more than a factor of two higher for the *FLA–7000* system. Differences between IP–types, read–out by the same scanner, are only about 14 %.

4.2.3 QA using ^{14}C–standard

Long–term stability of the reader system is an important issue due to the strong dependence of the PSL intensity on the read–out systems. Therefore, a daily routine has been introduced to check scanner as well as IP performance during calibration measurements with the *FLA–5100* scanner.
A ^{14}C source was used to homogeneously irradiate IP pieces to same dose level within 2 hours exposure time. The same read–out waiting period as for calibration measurements was maintained to reduce the influence of spontaneous signal fading.
Fig. 4.7a shows the intensity distribution obtained for the TR–plate within 5 consecutive days. The maximum deviation of the single day average to the average of all days, is only 4.4 %. The development of the mean value over few consecutive measurement days can be seen in fig. 4.7b for both types of IP. The TR–type IP shows a higher signal intensity than the MS–plate, contrary to measurements presented before. This is attributed to the low energy of β^- particles from the ^{14}C decay, in average 49 keV, and, thus, low penetration depth. In case of the MS–IP, decay particles with energies up to about 25 keV are already absorbed within the protection layer, resulting in lower dose levels compared to the unshielded TR–

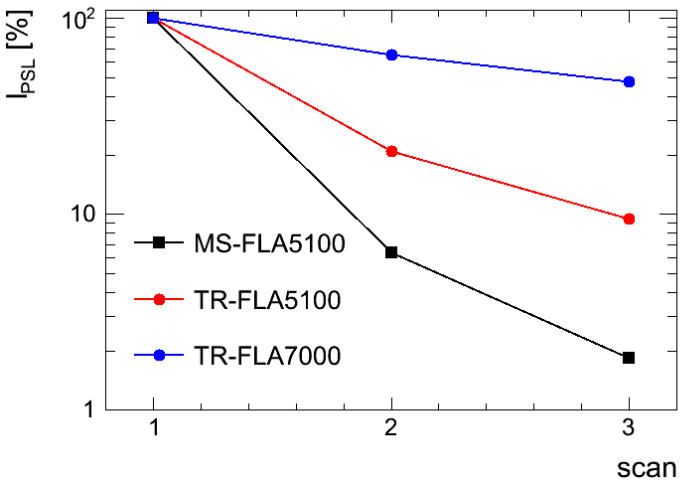

Figure 4.6: **Relative signal intensity after subsequent scans**
The relative signal intensity with respect to the first read–out is plotted against scan number. Solid lines are applied as guide for the eye. The signal loss per scan depends on both, scanner system and IP–type.

type IP.
In case of the MS–type IP, deviations of the daily intensity check from the average of all days are similar to values obtained for the TR–IP, yielding a maximal difference of 4.2 %.

4.3 Cross calibration at the MPQ ATLAS laser

The lowest proton energy available at the Tandem accelerator is 8 MeV, corresponding to an average energy of about 6 MeV within the active layer of the MS–type IP. Maximum energies of laser–accelerated protons at the ATLAS laser are usually well below 8 MeV. A cross–check of the energy calibration was, therefore, carried out at the ATLAS laser for the MS–type IP and *FLA–5100* reader.
Measurements have been accomplished with the small–angle spectrometer and a pinhole of 2.5 mm diameter at it's entrance. The energy resolution was roughly 0.5 MeV at the detector site. As target 40 nm thick DLC foils were used to reach an average maximum energy of about 7 MeV for all shots.
Cross–calibration measurements were accomplished in vacuum, where a blind flange was used for IP and CR39 mounting (fig. 3.15a in sec. 3.2.3). IPs were wrapped in an aluminium foil of 11 μm thickness. C–ions accelerated up to maximum energies of 1.8 MeV/u at these experimental conditions are thus, blocked by the thin foil and protection layer of the IP.
One half of the IP was covered by a piece of CR39, thus allowing simultaneous measurement of the proton fluence on CR39 and IP. Only protons with energies exceeding 4 MeV are deflected onto the detector area. To slow down the protons into the detection energy range of CR39 (sec. 3.1.1), absorbers, made of thin Al foils have been used. Two different aluminium foil thicknesses were sufficient to degrade the initial proton energy spectrum into suitable ranges

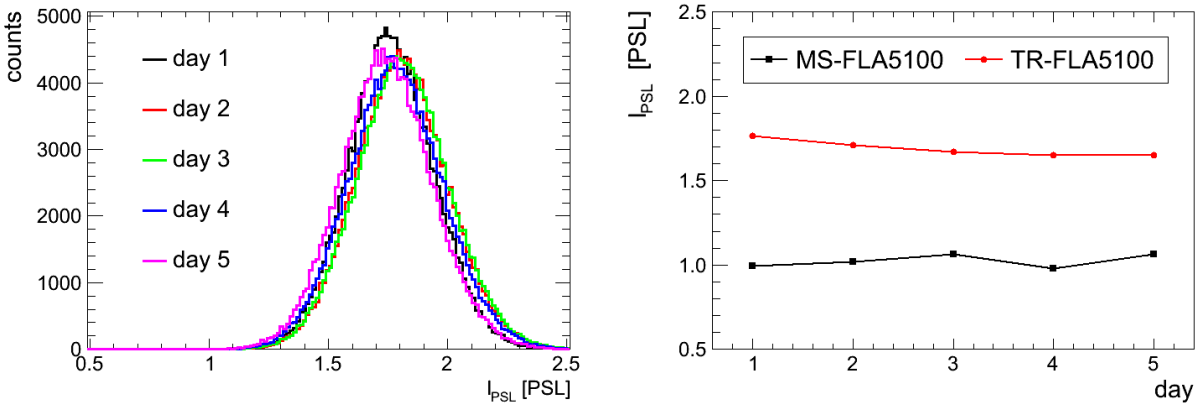

(a) (b)

Figure 4.7: **QA–measurements**
a) Distribution of intensity values measured for TR–IP over 5 consecutive days of beam time, showing an excellent stability of the scanner performance.
b) Daily average intensity measured with the FLA–5100 scanner for MS– and TR–type plates during calibration experiments. Error bars are not visible on this scale.

for CR39 detection. Fig. 4.8a shows a typical PSL intensity distribution, where part of the IP was covered by CR39. The proton signal has a width (FWHM) of approximately 2.5 mm with strongly decreasing signal intensity at the boundaries. The ordinate is correlated to the particle's energy, decreasing with increasing y–values. The small lateral width of the proton focus makes the alignment of CR39 and IP difficult. For the CR39 measurement in the low energy part of the proton energy spectrum (150 μm Al foil), a maximum proton energy of 6.5 MeV is determined from the IP data. IP intensity was analysed in four adjoining regions, corresponding to energy bins of approximately 0.5 MeV, each. An average fluence value can be deduced from the dose response curve (eq. 4.2).

$$\Phi = \frac{I_{PSL}(D)}{m} \cdot \rho \cdot \left(\frac{dE}{dx}\right)^{-1} \tag{4.3}$$

Average energy loss values for each energy bin have been calculated by *TRIM* simulations. An energy loss uncertainty of 10 % accounts for energy loss variations across the sensitive layer as well energy straggling of the incident particles. Uncertainty of the fit parameter m (tab. 4.2) adds 1.8 %. No significant deviation in system performance was observed in the QA–check with the ^{14}C–source. Hence, uncertainties related to the IP–reader system can be neglected.
Table 4.4 lists fluence obtained from IP and CR39 analysis. For the two highest energy ranges, fluence values differ significantly from each other. This is attributed to problems of the CR39 analysis under these experimental conditions, discussed in the following section.
In the laser–driven acceleration process, protons as well as C–ions are accelerated, energies of both, vary from shot to shot. Fig. 4.8b shows the PSL–intensity distribution that was

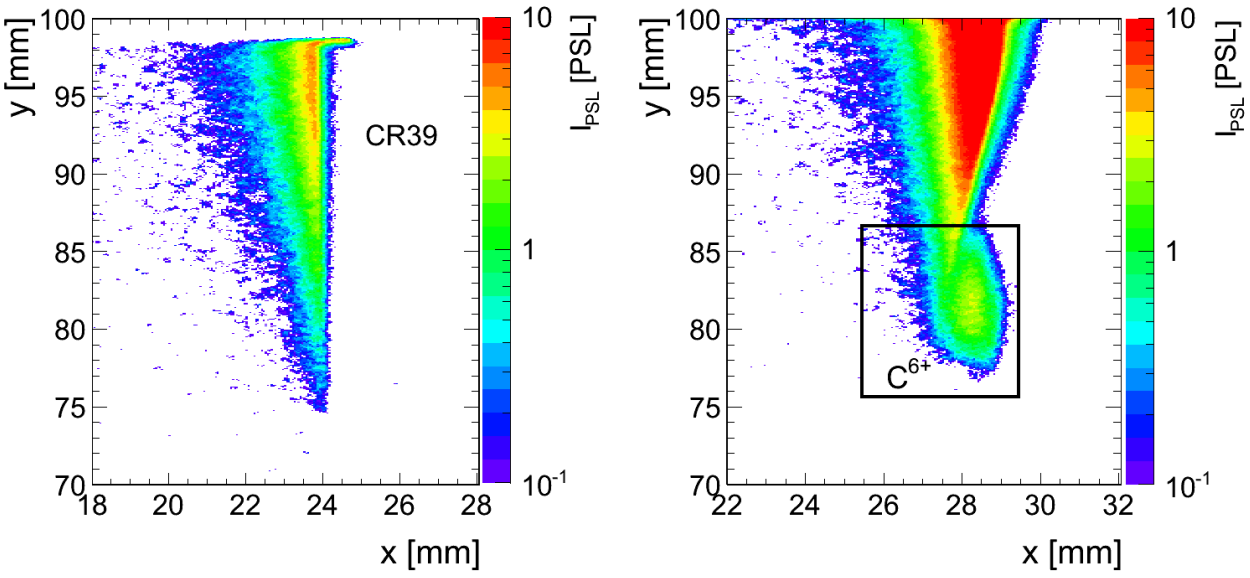

(a) (b)

Figure 4.8: **Examples of laser–accelerated proton foci measured by MS–IP**
Coordinates correspond to the scanner system. Although the y–axis is related to the energy axis, with energy decreasing with y, the absolute energy scale differs for a) and b).
a) The proton distribution, partially covered by a CR39, corresponds to an energy range of 4–6 MeV.
b) A strong signal at the high energy end of the proton spectrum, corresponding to about 7 MeV, is present. It has to be attributed to energetic C^{6+} ions. The junction of IP and CR39 at the left edge of the IP signal is less pronounced as in (a) due to a misalignment error.

measured with CR39 covered by a 240 μm thick Al–degrader. A large signal is visible in a small focus region at the high energy tail, corresponding to a proton energy of 7.2 MeV, which differs strongly from typically measured proton distributions. Furthermore, determined fluence values within this region are an order of magnitude larger as measured by CR39. Carbon ions with energies exceeding 1.8 MeV/u are able to pass the 11 μm thick aluminium foil as well as protection layer of the MS–IP. C^{6+}–ions of this energy range, are furthermore, deflected at the same position as 7.2 MeV protons. The signal is, therefore, attributed to C–ions. No proton fluence can be deduced for this energy range from IP data. The small size of the C–ion focus is attributed to the Al–foil and protective layer, both acting as filters for low–energy C–ions.

energy range $[MeV]$	**IP** Φ [10^4particles/cm^2]	**CR39** Φ [10^4particles/cm^2]
4.3–4.8	8.6 ± 1.9	7.1 ± 10
4.8–5.2	6.6 ± 1.8	6.8 ± 10
5.2–5.7	4.7 ± 1.4	8.7 ± 10
5.7–6.2	2.9 ± 1.1	8.8 ± 10

Table 4.4: **Cross–calibration of MS–type IP**

4.4 Discussion

Signal fading, due to spontaneous charge carrier recombination or successive read–out, as well as calibration curves show a strong dependence on the IP system. First, the influence of the IP reader is discussed, comparing energy calibration and dose response curves of the TR–type IP for both scanner models (figs. 4.1, 4.2). The stored PSL signal is primarily defined by the energy loss and fluence of the incident radiation. However, the measured intensity of the PSL signal is proportional to the photon flux per read–out spot, which strongly depends on the read–out system. Both scanner systems differ strongly in scanning and light collection optics (sec. 3.1.2). The polygon mirror based scanning system of the *FLA–7000* yields a lower photon flux per pixel than the scan head of the *FLA–5100* with light guiding optics. In addition, the time of PSL stimulation per pixel is much shorter in case of the *FLA–7000*. As a result, a higher photon flux per read–out spot is obtained for the *FLA–5100* model. PSL intensities measured with the *FLA–5100* scanner are, therefore, consistently higher than those measured with the *FLA–7000*.
Second, the dependency of the PSL intensity on the IP–type can be determined by comparison of the energy and dose response curves for TR– and MS–type, read–out by the same scanner model (*FLA–5100*). The probability of photo–stimulated luminescence emission depends on the density of filled charge traps [117]. The MS–type IP has the thicker sensitive layer and shows, therefore, consistently higher PSL values compared to the TR–type IP.
The energy calibration is required to determine the proton fluence in a certain energy range of the laser–accelerated proton spectrum. A Bethe–Bloch like functional term (eq. 4.1), yields a fit of the energy calibration curves (fig. 4.1). However a large uncertainty in fluence determination is introduced by the strong correlation of the fit parameters, which is of the same order of magnitude as the fit result itself. The dose response curve can be fitted with only one single fit parameter (fig 4.2). Fit–related uncertainties are below 2 % for all IP systems. Using this fit, simulation of the energy loss within the sensitive IP layer is required, contributing an additional uncertainty in fluence determination that depends on the width of the investigated energy bin. For instance, for the lowest proton energies in the ATLAS experiment and a width of the investigated energy bin of 500 keV, an additional uncertainty in fluence distribution of up to 6 % is introduced by the energy loss simulation. Hence, the accuracy in fluence determination is primarily limited by the energy resolution of the spectrometer. Nevertheless, the combination of energy loss simulation and linear calibration fit offers an order of magnitude higher accuracy in fluence determination than using the Bethe–Bloch like functional term.
The relative signal loss per scan has shown to be independent of the initial dose level. The

filled trap density changes by the read–out process, yielding a non–linear signal fading with repeated scans, which has also been reported for other IP systems [130, 131, 207]. However, the quantitative dependence of the PSL intensity on the energy is maintained for subsequent scans of the IP (fig. 4.5). Saturation limits that are introduced by the PMT of the IP reader can, hence, be overcome by successive IP read–out.
Spontaneous signal fading has been reported to depend on incident particle type and even energy [129–131]. IP systems used in these studies differ from each other and in particular from the systems used, here. Hence, direct comparison of fading characteristics is not possible, but data of [129–131] agree in showing larger fading effects for α–particles compared to γ–rays or β–particles, due to their higher LET. For the *FLA–5100* reader and the TR–type plate fading has been investigated for incident protons of two different energies as well as β–particles (fig. 4.4). Proton stopping power values related to energies used, here, differ by less than a factor of two and are approximately an order of magnitude smaller compared to α–particles. Any particle type dependent fading characteristic, comparing β–particles and protons, is, therefore, expected to be less pronounced than for α– and β–particles.
Although protons tend to show a larger fading effect than β–particles (fig. 4.4), all fading curves agree within scan to scan fluctuations in of the order of 4.2 %. Hence, no significant dependence on incident particle type or energy can be deduced from data presented, here.
Fading measurements of the TR–type IP show a significantly larger fading effect for the *FLA–7000* than for the *FLA–5100*. The measured fading curve is a convolution of the true fading signal for this type of IP and irradiation conditions and the scanner response function. The *FLA–5100*, offering the higher read–out efficiency, thus, mirrors the true fading curve far better than the *FLA–7000* system, showing that only a small amount of trapped charges recombine spontaneously.
However, half–life constants (tab. 4.3) agree for all fading curves related to the TR–type IP. The short half–life constant, in average 35 minutes for proton curves, clearly mirrors the strong signal decrease within the first hour after irradiation. As the long half–life constant exceeds 46 hours for all presented fading curves, a read–out delay of two hours has been maintained for all energy calibration measurements. For a time interval of 10 minutes, centred around the nominal read–out time the change in signal strength is typically less than 0.5 %. For the MS–type IP, no fading effect is present in the data. Fading effects during IP calibration, are, therefore, negligible for all measurements, presented here.
The IP reader has shown to have a major influence on the PSL intensity distribution. Stability of reader performance over long periods of time is a crucial point for the validity of calibration and fading functions. A QA procedure to check the performance of the combined IP–scanner system is, therefore, mandatory to obtain reliable quantitative results using these calibrations. Within a time period of 9 months, no significant performance change has been observed. Reproducibility of intensity measurements are within 4.2 %.
Validity of IP calibrations for energies in the 4–7 MeV range have been tested at the ATLAS laser by means of a CR39 cross–check. Proton fluence obtained by IP analysis decreases with increasing proton energy, as expected for laser–accelerated proton spectra by a factor of three. CR39 data show a proton fluence of about the same order of magnitude as obtained from IP data, but stable within 11.3 %. Results of the cross–check measurement only agree within $\pm$ 33 % with each other. In principle, CR39 allows an absolute calibration in terms of proton number. However, the setup used in this experiment limits the feasible accuracy

of the CR39 detector, responsible for the observed deviations in these cross–check measurements.
The proton fluence has to be determined from both detectors for the same size of the analysis region and, even more important, the same energy range to allow a comparison of obtained fluence data. A general problem in quantitative analysis of simultaneously irradiated CR39 and IP detectors is, therefore the accuracy of CR39 and IP alignment, which is typically about 1 mm. The small lateral width of the proton focus allows only small analysis regions and, hence, limits counting statistics in particular for the CR39 analysis. One major problem in microscopic analysis of the CR39 under these experimental conditions is the need to slow down incident protons by up to a factor of two. Relatively thick Al absorbers of 150 μm and 240 μm, respectively, are required for the initial proton energy range of about 4–7 MeV. The relationship of particle energy and detector coordinate is defined by the spectrometer, the corresponding energy resolution depends also on the aperture size at the spectrometer entrance. Proton track pit diameters can in principle be used in CR39 analysis as energy–specific filters, as they are correlated to the energy of the incident particles. However, lateral straggling within the absorber limits the energy resolution at the CR39 surface and reduces the correlation of pit diameter and energy axis. Hence, it was not possible to use the track pit diameter as filter parameter in CR39 analysis. As a result a significant noise level is present on the CR39 data. Even more important, uncertainties in the absorber thickness further limit the energy resolution on the CR39 surface. The thickness uncertainty per foil is of the order of about 10 %. A mismatch of the overlay of individual foils at the stack boundaries is estimated to contribute an additional thickness uncertainty of 10 %. The energy range of incident protons on the CR39 surface can shift by several hundred keV due to these thickness uncertainties and hence, significantly alter the number of proton tracks within the investigated energy range. Proton numbers determined by CR39 are, thus, in sum only certain up to a factor of two.
Calibration and fading measurements are needed for any specific IP system as both, scanner model as well as IP type have a significant influence on the measured PSL intensity. For quantitative analysis of energy spectra of laser–accelerated protons the accuracy in fluence calculation is primarily defined by the energy resolution of the spectrometer in the detector plane.

5 Experiments with radiochromic film detectors

Application of laser–accelerated proton beams in radiation therapy is widely discussed, although proton energies of up to 60 MeV, achieved with the most powerful lasers, but allowing only single shots every 30 minutes, are far from being sufficient [20]. However, pre–examinations of the biological response to dose deposition within a ultra–short ns–pulse, investigated for tumour cells in vitro as well as in vivo, are already in progress [188, 189].
Only laser systems with few Hz repetition rate are suitable for this task, but, at the price of maximal achievable proton energy. The MPQ ATLAS laser, as one of these systems, offers in its present status a maximum proton energy of about 8 MeV. As fluctuations in proton spectra arise from shot to shot, dosimetric measurements are necessary for each shot. The small range of protons with energies of few MeV (i.e. few mm in water) limits the number of suitable detectors for these experiments, further.
EBT2 films offer a water–equivalent thickness of only 370.5 μm and allow, therefore, for transmission monitoring. An EBT2 based dosimetry has been established for dose verification measurements in bio–medical experiments at the Tandem, as well as ATLAS laser accelerator.
Calibration measurement, carried out in context of these applications, are presented together with energy dependence investigations. Results of both dosimetric applications are summarized at the end of this chapter.

5.1 Calibration measurements

Two batches of EBT2 films (F06110902 and A07160901) have been calibrated with photons and protons of different energies. Film composition was standardized in May 2009 [154]. As both batches are manufactured thereafter, the same nominal active layer composition is valid and allows comparison of both batches.
An overview of all calibration measurements is given in table 5.1. To ensure comparability, the same film handling and scanning procedure was applied for photon and proton calibrations. Markings on the films ensure compliance of the scanning orientations for all films. A minimum read–out waiting period of at least 44 hours was maintained for all calibration films, where films were stored at room temperature, in a light–tight envelope. During all measurements, the thinner surface layer of the films was facing the beam exit window. Details on film analysis are given in sec. 3.4.1.

facility	**MLL**		**MRI**	**RPTC**
particle type	proton	proton	photon	proton
energy	20 MeV 12 MeV	11 MeV 3 MeV	6MV	228 MeV
Film lot	F06110902	A07160902	F06110902 A07160902	F06110902 A07160902

Table 5.1: **Overview of EBT2 calibration measurements**

5.1.1 Photon calibration

EBT2 films have been originally designed for dose verification measurements in photon beams. For comparison with proton calibrations at the Tandem and RPTC, respectively, EBT2 films of both lots have been calibrated in the 0.2–8.0 Gy range in a medical 6 MV photon beam.
Calibration measurements were accomplished at the Clinac 2 [1] of the clinic for radiation oncology (TUM/MRI) in Munich. Film pieces, 50 by 50 mm^2 each, were placed on their substrate layer, at the iso–centre of the linac, corresponding to a depth of 17 mm in a 30 mm thick plexiglas phantom when measured from the top. An ionization chamber measurement with a Farmer type IC[2], connected to a Unidos electrometer[3] yields a calibration factor for the linacs beam monitor reading. Monitor reading of clinical linacs is usually defined in terms of monitor units (MU) where, by convention, 100 MU correspond to a dose of 1 Gy at the iso–centre. The ionization chamber reading was corrected according to the TRS 398 [44] for temperature, pressure and beam quality. Films were calibrated using two different dose rates of 300 MU/minutes and 600 MU/minutes, below and above 3 Gy, respectively. Dose uncertainty is associated to $\pm$ 1 MU for all MRI measurements.

5.1.2 Proton calibration

Both batches have been calibrated in the plateau region of a 228 MeV proton beam at the RPTC. Dose uncertainties of $\pm$ 3 % are related to ionization chamber measurements which have been also corrected for beam quality and environmental conditions (pressure, temperature). Additional proton calibration measurements have been accomplished for both batches in low–energy proton beams between 3 and 20 MeV at the Tandem accelerator.
Calibration procedures at the Tandem accelerator differ from clinical ones, as dose has to be calculated from the determined particle fluence and mean water–equivalent energy loss in the active film layer (eq. 3.8). Fluence was measured in different ways, depending on irradiation mode (sec. 3.2.1) and is, therefore, associated to different sources of uncertainty for each of the measurements.
For all proton calibration energies exceeding 10 MeV, variations in energy loss with projectile energy straggling and active layer thickness can be neglected. Uncertainty in particle fluence

[1] Varian Medical Systems, Palo Alto, United states
[2] PTW Freiburg GmbH, Freiburg, Germany
[3] PTW Freiburg GmbH, Freiburg, Germany

is, therefore, the main uncertainty in dose determination. In case of the 3.1 MeV calibration, energy loss variations within the sensitive layer of 3 % have to be accounted for as additional dose uncertainty.
Different film batches have been applied for dose verification in bio–medical experiments (i.e. tumour and cell irradiation), which use different proton energies. Films of different batches have, therefore, been calibrated with different proton energies in the energy range up to 20 MeV.

Film lot F06110902

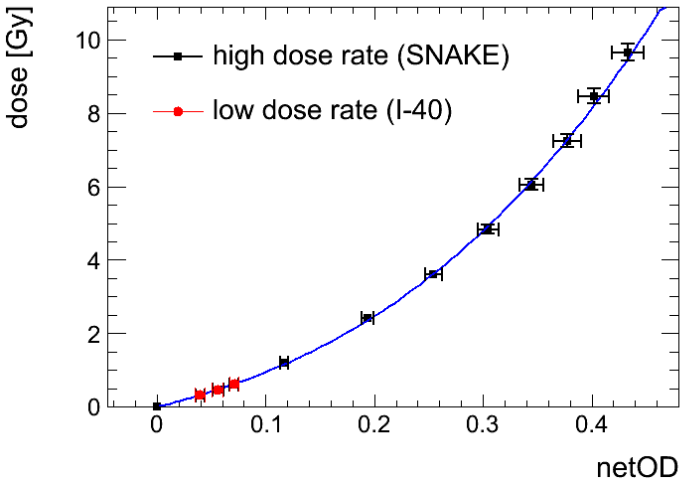

Figure 5.1: **Dose rate dependence of EBT2 films**
The 20 MeV calibration is obtained from two independent measurements with dose rates differing by 5 orders of magnitude. A single fit is applied through all data.

Two independent calibration measurements have been accomplished in a 20 MeV proton beam. In the first measurement, fluence was measured with the PIPS–detector (sec. 3.2.1). The limitation of the maximum counting rate of this detector, yields a film irradiation time of several hours for the highest dose level, which was limited to 1.0 Gy. Higher dose levels up to 10 Gy are obtained in an additional calibration in a continuous 20 MeV proton beam at the SNAKE micro–beam line. The average beam current, measured by a FC, was used to determine the exposure time, required for each of the dose levels.
The dose response curve of both measurements is summarized in fig. 5.1, showing no significant difference of calibration points although dose rates of 57 Gy/s (SNAKE) and $3 \cdot 10^{-4}$ Gy/s (PIPS), respectively, differ by about 5 orders of magnitude. No dose–rate dependence of EBT2 response can be deduced. This is also supported by very recent findings for electrons, measuring dose rate dependence of EBT films for dose rates up to $15{\cdot}10^{9}$ Gy/s [209]. For the tumour irradiation experiment (sec. 5.3.1), dose rate independence of EBT2 films is, therefore, assumed for peak dose rates in the order of Gy/ns.
All calibration curves obtained for lot F06110902 are summarized in fig. 5.2. Dose is plotted

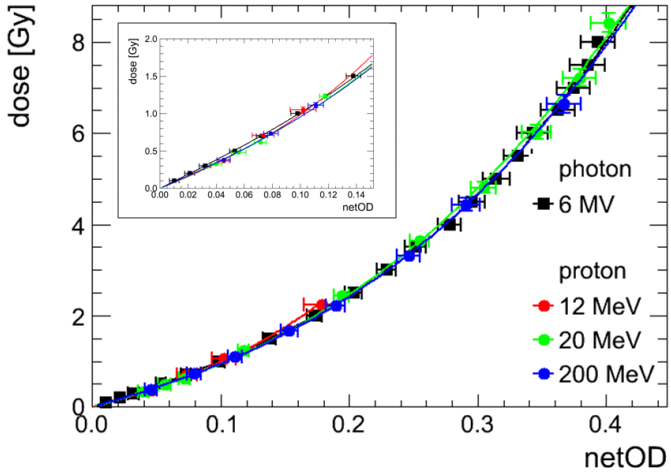

Figure 5.2: **Calibration curves of film lot F06110902**
No significant dependence on particle type or energy is present. The small inset shows an enlargement of the clinical relevant dose range up to 2 Gy.

against netOD and fitted according to eq. 3.11 .
Fit parameters, summarized in table 5.2, show a strong correlation of the free fit parameters, A and B. All dose response curves have comparable fit parameters, except for the 12 MeV curve. However, for this energy calibration, data are only available in the low dose range up to 2.3 Gy. In particular the non–linear term of eq. 3.11 requires data points in the dose range of several Gy to yield a good fit quality. Therefore a large uncertainty in dose determination of 70 % is associated with this calibration curve. The optimum for parameter C is somewhat higher for photon calibrations, suggesting a difference between proton and photon calibrations. However, no significant difference between any of the calibration measurements can be deduced from fig. 5.2.

F06110902:

fit parameter	**MRI**		**MLL**		**RPTC**
	6 MV		*12 MeV*	*20 MeV*	*228 MeV*
a	9.09 ± 0.09	9.35 ± 0.27	7.68 ± 0.93	8.03 ± 0.26	8.32 ± 0.44
b	66.71 ± 1.97	60.93 ± 3.87	69.46 ± 30.44	48.59 ± 1.71	49.919 ± 4.97
c*	3.00	2.90	2.50	2.50	2.60
$\frac{\sigma_{AB}}{\sigma_A \sigma_B}$ (correlation)	-0.543	-0.756	-0.794	-0.835	-0.749
ΔD_{Fit} [%]	1.33	3.78	70	2.7	7.5

*) fixed during fitting procedure

Table 5.2: C
alibration fit parameters for film lot F06110902**Calibration fit parameters for film lot F06110902**

Film lot A07160902

Films have been calibrated in a 11.1 MeV proton beam by single ion irradiation at the SNAKE micro–beam facility in connection with cell irradiations (sec. 3.2.1). A second film attached to the back of the cell holder was used to simultaneously investigate the film response to a proton energy of 3.1± 0.24 MeV, incident on the second film. This energy is the same as present on the film in the ATLAS cell experiment (sec. 5.3.2).
Fig. 5.3 shows all calibration plots in terms of dose against netOD for film lot A07160902, table 5.3 summarizes corresponding fit parameters and correlation coefficients. Nearly the same optima are obtained for C as for batch F, showing the same trend for the photon calibration. However, no significant difference between photons and protons exists down to a proton calibration energy of 11.1 MeV. The 3.1 MeV proton calibration shows a significantly different response compared to all other proton and photon curves. Large fit uncertainties of the Tandem calibrations are attributed to the limited number of calibration points, in particular in the high dose range.

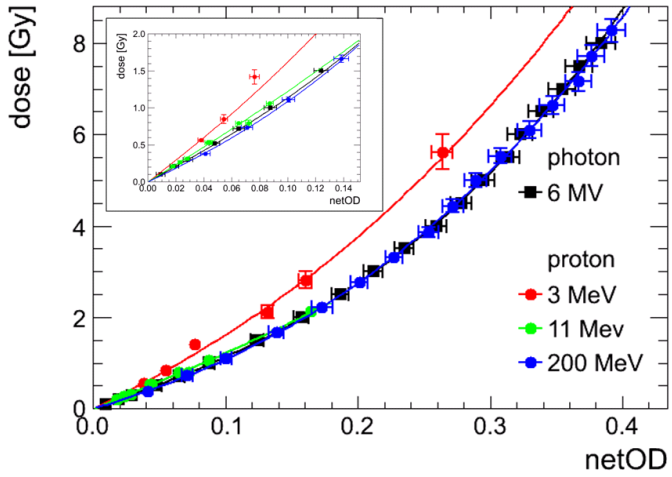

Figure 5.3: **Calibration curves for film lot A07160902**
In particular in the clinical relevant dose range up to 2 Gy no energy and particle type dependence is visible for proton energies down to about 11 MeV. However, the 3 MeV calibration curve shows a significant lower dose response, clearly indicating the energy dependence of EBT2 films for low–energy protons.

5.1.3 Batch comparison

Except for clinical calibration measurements, both film lots have been calibrated with different proton energies. This is attributed to the fact that irradiation condition of the two bio–medical film applications differed from each other. A comparison of dose response curves of both film lots is only possible for clinical calibrations (fig. 5.4). NetOD is plotted against dose up to 8 Gy. Dose levels of the MRI and accordingly RPTC calibration are the same for

A07160902:

fit parameter	**MRI**	**MLL**		**RPTC**	
	6 MV	*3.10 MeV*	*11.10 MeV*	*228 MeV*	
a	10.44 ± 0.30	15.02 ± 0.72	11.60 ± 0.35	9.08 ± 0.40	9.38 ± 0.52
b	59.53 ± 3.60	41.66 ± 12.74	12.78 ± 8.97	44.66 ± 2.67	42.47 ± 4.25
c*	2.80	2.40	2.30	2.40	2.40
$\frac{\sigma_{AB}}{\sigma_A \sigma_B}$ (correlation)	-0.794	-0.707	-0.813	-0.843	-0.794
ΔD_{Fit} [%]	3.73	19	17.1	4.8	7.7

*) fixed during fitting procedure

Table 5.3: **Calibration fit parameters for film lot A07160902**

both lots, allowing direct comparison of corresponding netOD values. Looking at the same particle type, both batches respond considerably different, as batch F shows a significantly higher dose sensitivity than batch A. The ratio of netOD values of both film lots is calculated for photons as well as protons, yielding mean differences of 7.3 % for photons and 11.5 % for protons, respectively. The calibration reproducibility has been checked by means of two independent photon and proton calibrations, yielding average netOD deviations of only 2.0 % and 2.5 %, respectively.

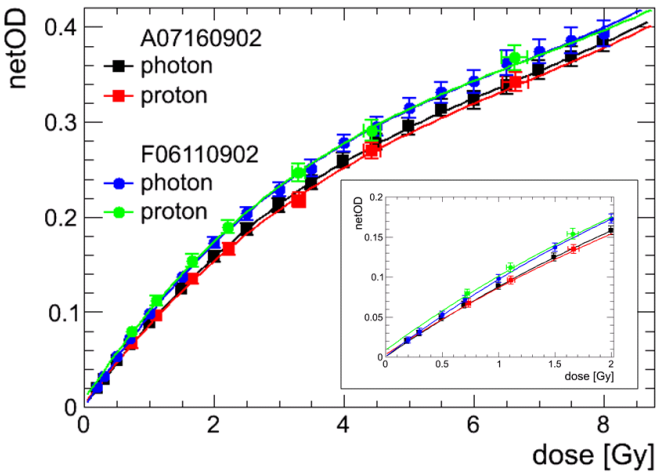

Figure 5.4: **Dose response of different film lots**
The dose response of both film lots has been measured in a clinical photon and proton beam, showing an excellent agreement of photon and proton response curves, in particular in the clinical relevant dose range up to 2 Gy (small inset). However, lot F06110902 shows consistently a significant higher response as lot A07160902.

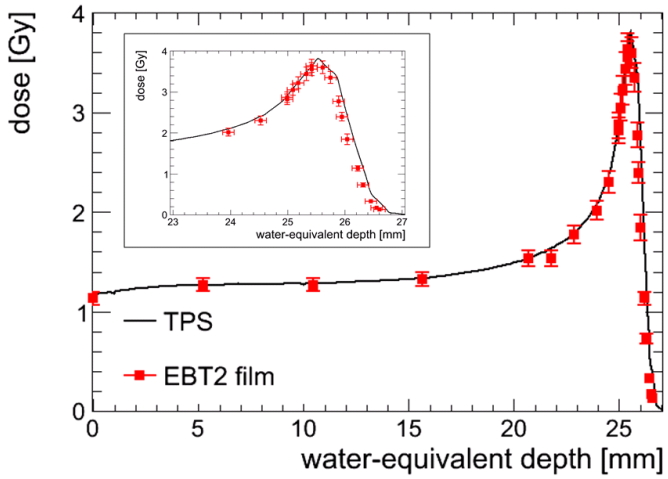

Figure 5.5: **Depth dose of 200 MeV protons in water**
Planned depth dose (TPS) and film dose show a good agreement. An under–response of measured film dose is present in the Bragg peak region, visible in the the small inset.

5.2 Energy dependence of EBT2 films

A two–fold approach is chosen to investigate energy dependence, or rather LET dependence, of EBT2 films. First, by comparison of the measured depth dose curve of an incident 200 MeV proton beam in a water–equivalent RW3 phantom with the treatment planning system (TPS) curve of the RPTC. Second, by calculating the dose of the 3.1 MeV calibration films with the RPTC calibration curve and comparing measured and nominal dose with each other. Consistency of planned and delivered dose distribution is checked on a regular base in any medical irradiation facility, thus, allowing to compare film and TPS dose directly (fig. 5.5). To calculate the correct depth of film pieces, differences of the mass stopping power of film and phantom have to be accounted for, expressing depth in terms of the water–equivalent thickness. The thickness accuracy of a single phantom plate is specified by ± 0.1 mm and used as estimation for uncertainty in film positioning. Error bars of the film dose only account for statistical fluctuations, which are below 5.0 %. An additional dose uncertainty of 4.8 % is introduced by the calibration fit.
Both depth dose curves show an excellent agreement in the plateau region. In the Bragg peak, film dose lies consistently below the planned dose. Fig. 5.6 shows the relative deviation of film and TPS dose plotted against residual proton energy. The residual energy, corresponding to a water phantom depth z, has been determined by eq. 5.1 [210]. R denotes the range of the incident proton beam in cm and α =0.0022 cmMeV^{-p} and p= 1.77 are constants, obtained from [210]. The formula is valid down to a proton energy of 10 MeV, thus covering the whole plateau and Bragg peak region, except for a small region of the tail.

$$E(z) = \frac{1}{\alpha^{\frac{1}{p}}} (R - z)^{\frac{1}{}} \tag{5.1}$$

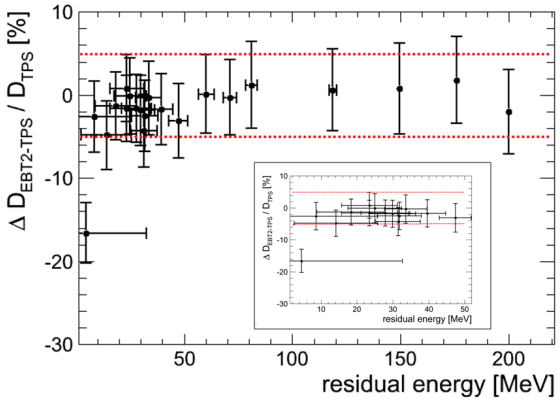

Figure 5.6: **Energy dependence of EBT2 films**
The relative deviation of film and TPS dose is plotted against the residual proton energy, which is related to phantom depth. Error bars are associated to the statistical uncertainty in measured dose, red lines correspond to the ± 5 % uncertainty level.

For all energies down to about 15 MeV, film and TPS dose agree within ± 5 %. Below 10 MeV, under response of up to 20 % is observed.

Films, calibrated with 3.1 MeV protons at the Tandem accelerator have been analysed using one of the RPTC calibration curves. Relative deviation of the measured film to nominal calibration dose is plotted against nominal dose (fig. 5.7). Rather large dose uncertainties account for energy loss variations over the active layer as well as errors in fluence determination. As result, an average under–response value of 32 % is obtained.

5.3 Film dosimetry applications

5.3.1 Irradiation of subcutaneous tumours in mice

The tumour growth delay of human cancer cells in a mouse model was investigated at the Tandem accelerator with conventional (∼ Gy/s) and laser–typical dose rates (up to 20 Gy/ns). As preparation for this kind of experiment, depth dose curves have been measured in an EBT2 film stack for incident proton energies of 20 and 25 MeV, for continuous and pulsed beam mode, respectively. Different energies were used due to problems of the high voltage stability of the Tandem accelerator at that time. This is also the reason, why these energies differ from the finally used tumour irradiation energy of 23 MeV. The same setup as for the later mouse irradiations was used (fig. 3.13 a–b). Film stacks, containing 23 films each, were placed at the designated tumour position and irradiated with the corresponding field and fluence of 10^9 protons/cm^2. A single depth dose curve was obtained for the most distal layer of the SOBP. For comparison, corresponding depth dose curves have been simulated using *Geant4* [200]. Results of simulation and measurement are depicted in fig 5.8. For each energy, an average depth dose curve, deduced from the simulated two–dimensional dose distributions (figs. 5.8a, 5.8c) is plotted together with corresponding depth dose measurements in the film

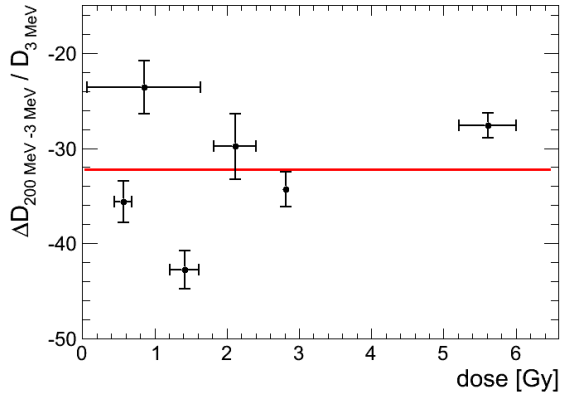

Figure 5.7: **Dose under–response of low–energy protons**
The relative deviation of the dose determined by the RPTC calibration and the nominal calibration dose of the low–energy calibration is plotted against the nominal calibration dose. The solid line represents a polynomial fit (0^{th} order) of the data, yielding an average under–estimation of 32 %.

stack (figs. 5.8b, 5.8d). Error bars on film dose account for statistical dose fluctuations, depth related error bars are not visible on this scale. Fit uncertainty contributes additional 2.7 %.
Both measurements show clear deviations from the simulated dose in the plateau region. The Bragg Peak region can not be resolved due to the large film thickness compared to the Bragg peak width. Film dose of the continuous irradiation exceeds the simulated dose while the opposite is true for the pulsed irradiation. These findings are not related to an energy dependence of EBT2 films, as quenching effects are completely negligible in the plateau region of both, incident mono–energetic 20 and 25 MeV proton beams. The reason for these differences is the built–up of the overall irradiation field used for film stack irradiations, which had the same size as in later tumour irradiations. Beam scanning is only possible for small fields with up to 3 mm side length (sec. 3.2.1). The tumour target field was, therefore, built from small single sub–fields, with small overlapping joint areas. As a result, about 4 % of the total irradiation area get approximately twice the nominal dose, yielding a dose increase of roughly 4 % compared to the nominal level in case of the continuous irradiation. This is most pronounced in the entrance region as lateral straggling smears the edges of overlapping regions with increasing depth. As a result a better agreement of measurement and simulation is obtained with increasing depth. Accounting for dose uncertainties of 9 %, deviations of simulation and measurement in the continuous case of 12 % can be explained by inhomogeneities in built–up of the overall irradiation field.
In case of the pulsed irradiation, the overall field is formed by Gaussian–shaped pencil beams with approximately 100 μm FWHM in each dimension. As a result, dose distribution is far less homogeneous as for the continuous measurement. The overall uncertainty in dose determination adds to 16 %. An average deviation from the simulation of -11 % is, therefore, to be expected.

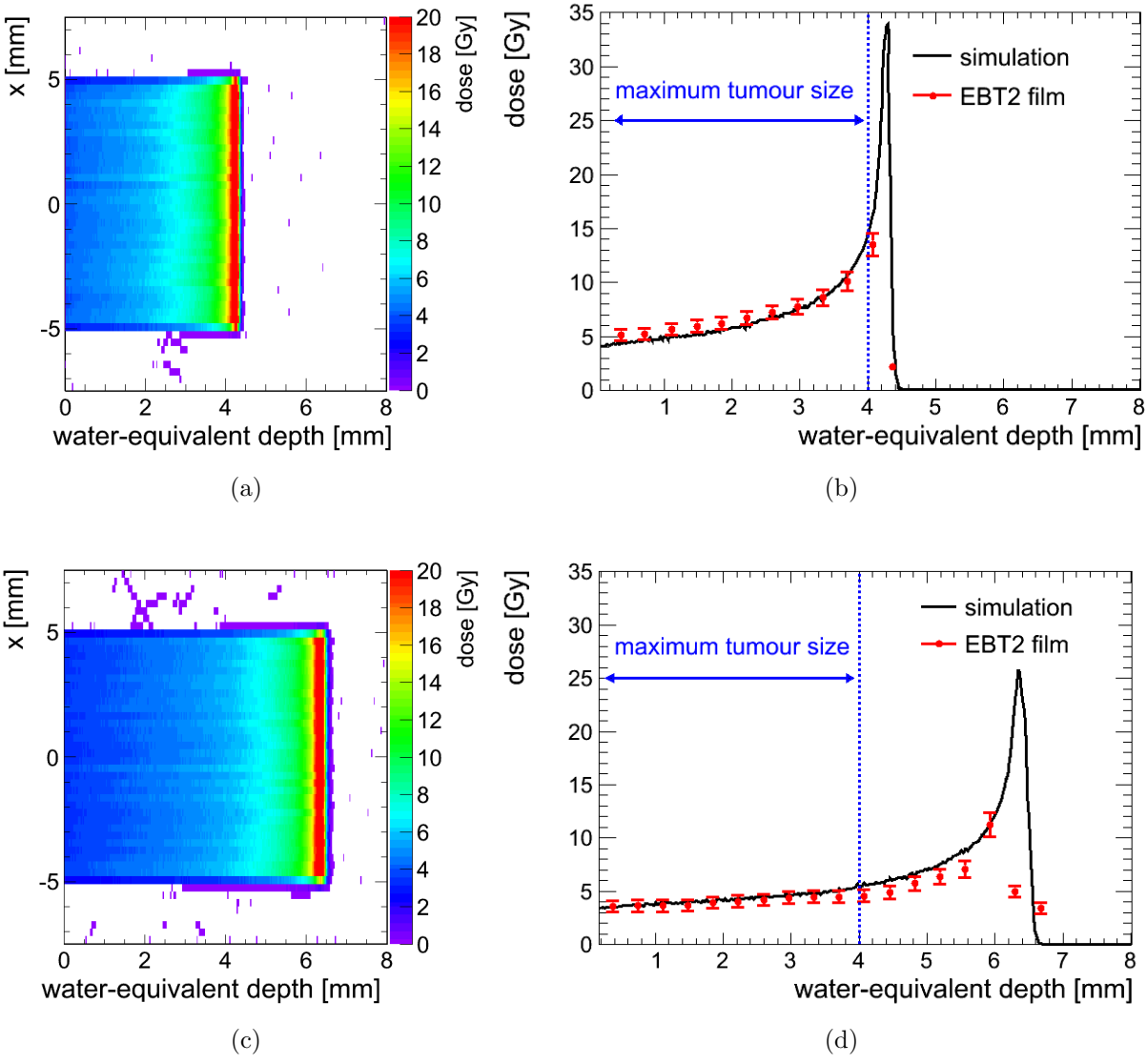

Figure 5.8: **Depth dose distribution of tumour irradiation**
Depth dose distributions of 20 MeV and 25 MeV proton beams in water have been simulated using Geant4 (a, c). A central depth dose profile has been obtained along the simulated dose distribution for comparison with film measurements (b, d). The blue dashed line indicates the maximum tumour size that has been used in the tumour irradiation with 23 MeV protons.

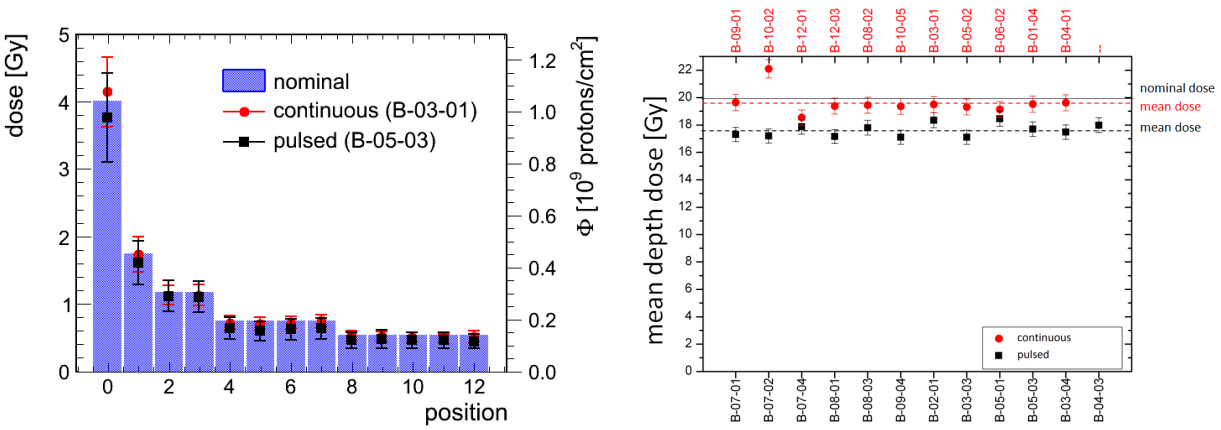

(a) (b)

Figure 5.9: **Fluence and dose distribution of tumour irradiation** ((b) adapted from [211])
a) Typical fluence distribution measured for two representative mouse irradiations in continuous (red) and pulsed (black) beam mode. Blue bars represent nominal fluence values according to treatment planning.
b) The mean tumour dose that has been deduced from film measurements is plotted for each mouse of continuous and pulsed beam mode. The measured dose is systematically underneath the nominal dose level of 20 Gy (solid black line) in particular in pulsed beam mode.

Analysis of film dose and reconstruction of tumour dose was accomplished as part of a diploma thesis [211]. A brief summary of the dosimetric results of the tumour irradiation is given here, for the sake of completeness.
The dose distribution for each energy layer of the SOBP has been measured by EBT2 film, placed in front of the absorber wheel (fig. 3.13). A single conversion factor allows the calculation of proton fluence from the measured dose distribution, as the energy loss in the films active layer is the same for all energy layers. Each of the 13 different energy layers of the SOBP, yields a single film dose in the 0.5 to 4.0 Gy dose range. These dose values correspond to 5 different fluence levels, planned for the tumour irradiations. The actual delivered fluence can be deduced from the dose measurement by means of eq. 3.8 for each energy layer and irradiated mouse. Fig. 5.9a shows a comparison of typical measured fluence distributions for continuous and pulsed beam mode with respect to the nominal fluence. Except for the first energy layer, measured dose or, rather, fluence, is consistently lower than the nominal one for continuous as well as pulsed irradiation mode. A similar trend is observed when comparing continuous and pulsed beam mode, the latter always showing smaller fluence values. Looking at the mean average dose within the tumour volume, which has been calculated from the measured fluence values, the same finding is visible for almost any irradiated mouse tumour (fig. 5.9b).

5.3.2 Cell irradiation experiment at the MPQ ATLAS Laser

The cell response to short laser–accelerated proton pulses was investigated by dose delivery to the cells within a single laser shot [194]. To achieve the minimum required dose of 0.2 Gy within a single shot, a quadrupole doublet had to be used to focus protons of a small energy range (5.2 ± 0.15 MeV) onto the cell irradiation plane, resulting in a strong line focus and, hence, inhomogeneous dose distribution. Fig. 5.10 shows three typical dose distributions measured by EBT2 films. The proton energy in the line focus corresponds to a proton energy of about 3.1 MeV at the films active layer. The inhomogeneous dose distribution, related to the broad energy distribution, as well as known energy dependence in this energy range, pose a special challenge for dosimetric measurements. A calibration, carried out in a 3.1 MeV proton beam for this special application, is, therefore, used to account for associated energy quenching effects. In fig. 5.10, three dose maps, representative for all other shots,

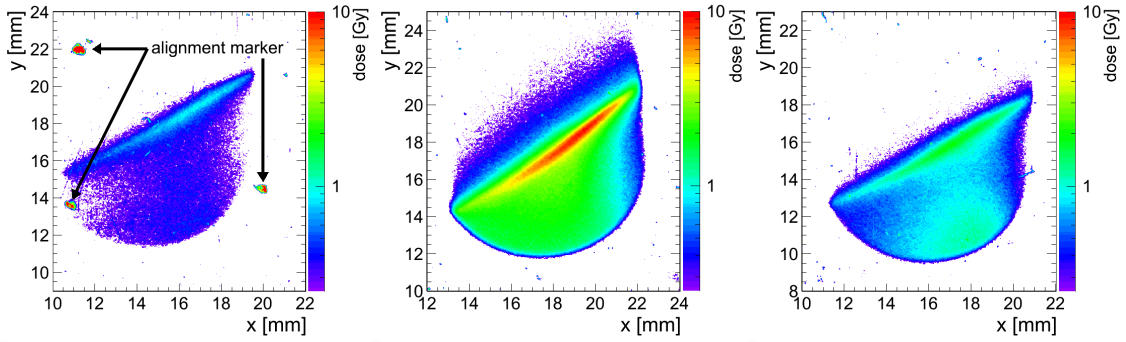

(a) (b) (c)

Figure 5.10: **Dose distributions in cell irradiation experiment**
Coordinates (x,y) correspond to scanner coordinates. The relationship of scanner coordinate and energy, defined by the spectrometer and quadrupoles (fig. 3.15b), differs for each of the presented shots due to differences in film positioning on the flat–bed scanner. The dose in the line focus, corresponding to a proton energy of 5.2 MeV, corresponds to an average dose of 0.5 Gy (a), 3.9 Gy (b) and 1.5 Gy (c).

are depicted. In this picture, proton energy increases roughly with y. All films show an inhomogeneous dose distribution, in particular within the line focus, yielding an average width of the dose distribution of 32 % for 9 out of 10 shots. Only the dose distribution in the line focus region, where the highest dose levels were deposited, was analysed. The focus region also offers the highest energy resolution, yielding well–defined stopping power values. The sharp cut at the bottom of the dose distribution images the edge of the beam exit window, corresponding to an average proton energy of about 4.2 MeV. Typical proton spectra from the ATLAS laser show continuously decreasing particle numbers up to proton energies of about 8 MeV. Only fig. 5.10b shows a significant number of particles at proton energies exceeding 5 MeV. This is also mirrored by an average line focus dose of 3.9 Gy compared to 0.5 Gy (fig. 5.10a) or 1.5 Gy (fig. 5.10c), respectively, as obtained in all other shots.

Fig. 5.11 shows the average film dose, in the line–focus, plotted for each cell sample. Error bars are associated to dose fluctuations in the analysed ROI. Fit uncertainty of the 3.1 MeV calibration adds up with 19 %. The majority of shots have dose levels below 1.0 Gy, yielding an average dose for these shots of 0.4 ± 0.1 Gy. Improvement of the laser accelerator system adjustment during the experiment, resulted in an average line focus dose of 3.9 ± 1.8 Gy, thus, almost a factor of ten higher than in previous measurements. Though, dose of subsequent shots is smaller, nevertheless a factor of three higher line focus dose, in average 1.3 ± 0.2 Gy, compared to the first irradiated sample, is observed. These large

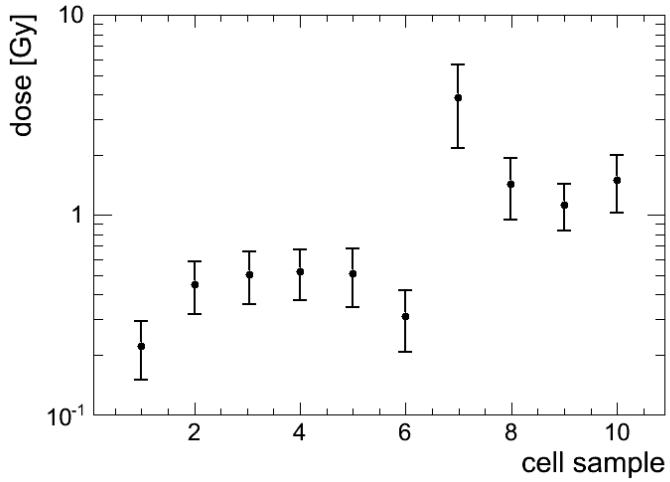

Figure 5.11: **Average dose in line focus**
The single shot dose shows clear fluctuations from shot to shot, which are typical for the laser–acceleration process. The increase of the average dose of more than an order of magnitude with subsequently higher dose levels compared to the first ones is attributed to an improved adjusting of the laser on the target.

differences in dose deposition from shot to shot clearly demonstrate one major problem of laser–based ion acceleration. The scaling of the ion spectra with laser and target parameters is not yet fully understood, although different models exist trying to explain experimental results [12]. Shot to shot stability is a crucial point that has to be solved for a future application of laser–accelerated protons in radiation therapy. The single pulse dose delivery represents a major difference to recently published cell irradiation experiments with laser–accelerated protons, depositing a fixed dose to cells by subsequent laser pulses, thus, in a quasi–continuous way [188].

5.4 Discussion

Absolute sensitivity of both film lots differs significantly despite the same nominal composition (fig. 5.4). However, fluctuations in atomic composition as well as layer thickness are present in any manufacturing process. For the predecessor of EBT, thickness variations in the active layer from batch to batch of up to ± 12.0 % and within a batch of up to ± 3.0 %

are specified [212]. Assuming fluctuations of the same order of magnitude for EBT2 films, observed deviations of up to 11.5 % of both lots can be explained by thickness variations of the active layer. The deviation of roughly 3 % between photon and proton response comparison is insignificant as dose uncertainty as well as thickness fluctuations within a batch are of the same order of magnitude. The same argument holds for fluctuations of up to 2.5 %, observed for the same film lot and the same particle type.
For determination of unknown dose levels, the red colour channel of the scanned film image is converted into a dose map. Less than 1 % uncertainty is given in background determination, required for calculation of a netOD map as intermediate step. Contribution to netOD uncertainty is, therefore, negligibly small. The standard deviation obtained in ROI analysis of the dose map (sec. 3.4) mirrors statistical uncertainties, associated to the film as well as the experiment itself. However, an additional systematic uncertainty in dose determination is introduced by fit uncertainties of parameter A and B. An average fit uncertainty is deduced for each calibration curve from error propagation law.
For all dose response curves up to 8 Gy, fit–related dose uncertainties are below 8.0 %, for the majority of these fits even below 5.0 %. These curves have additionally been fitted, using C as free fit parameter. Overall fit uncertainties are, thus, in average increased by 4.6 %. At the same time, fit quality in terms of χ^2 deteriorates by less than 0.8 %. Hence, showing the validity of the chosen fit procedure with respect to reduction of dose uncertainty.
Fit uncertainties exceeding 10 % in the 3–12 MeV energy range are solely attributed to missing data points in the high dose range. Large uncertainties in the non–linear fit parameter, B, are thus introduced (eq. 3.11).
Although dose response differs absolutely, response behaviour of both films is qualitatively the same (figs. 5.2, 5.3). All proton curves exceeding 10 MeV, match within experimental and fitting uncertainties with each other, as well as with corresponding photon curves. This observation agrees with results recently published for EBT and EBT2 films, comparing photon and proton response curves [147, 153] and also holds for new EBT3 films [162].
For EBT, an under response of about 10 % is given for an average proton energy of 3.1 MeV, obtained from depth dose measurements in a 15 and 29 MeV proton beam [152]. For EBT2 film and the same average proton energy, a three times larger under response of 32 % is observed in measurements presented here. Accounting for lateral straggling, the nominal dose decreases by 7 %, thus, correcting the observed under response to about 26 %. This value agrees with the result obtained in the RPTC depth dose measurements, when interpolating the steep drop in response to lower energies. However, care has to be taken, comparing energy quenching related to different initial energies due to different stopping power distributions for the same depth.
For the 200 MeV depth dose curve, an under estimation of the dose of more than 20 % is observed for proton energies below 10 MeV (fig. 5.6). On the other hand, calibration curves of 11 and 12 MeV do not show such a strong deviation from high–energy proton or photon calibrations (figs. 5.2, 5.3). Furthermore, comparison of the 20 MeV calibration curve of batch F06110902 with a 10 MeV curve, obtained by the OncoOptics group Dresden for the same batch and similar scanner, shows an identical response curve [213].
Energy spread of incident protons and, therefore, also LET, is negligible for all calibration measurements with mono–energetic protons with $E_{proton} \geq 10$ MeV. For similar average energies of the depth dose measurement, energy straggling has to be taken into account, which

increases with phantom depth. To understand the influence of energy, or, rather, LET, spread on the observed dose under estimation, a *TRIM* simulation was accomplished for an initially mono–energetic 200 Mev proton beam incident on a water phantom. The energy spectrum that yields an average residual proton energy of 10 MeV contains a significant number of particles in the energy range of 0–5 MeV. These high LET particles are responsible for the observed quenching effects for average residual proton energies below 10 MeV (fig. 5.6). Hence, energy dependence observed in the depth dose measurements is not inconsistent with energy independence found in calibration measurements with mono–energetic protons down to 10 MeV. As energy straggling, as well as average particle energy, at a certain absorber depth depend on initial particle energy and spread, comparison of energy quenching effects, observed for different beam qualities, is limited. No LET dependence is observed in the depth dose measurement for proton energies exceeding 20 MeV. Here, the number of particles with LET in a range related to quenching effects is negligible. Therefore, comparison with results published for EBT films, comparing LET dependence of proton beams in the 40–200 MeV range is possible and shows consistent results [147].
EBT2 based film dosimetry has been accomplished for bio–medical experiments in low–energy proton beams. Apart from dose fluctuations due to the acceleration process, systematic uncertainties in dose determination, related to fit uncertainties, allow dose determination with an accuracy better 3 % for the tumour irradiation experiment. Assuming comparable energy distributions at the film's active layer during calibration and dose determination for an average proton energy of 3 MeV, a systematic uncertainty in dose determination below 20 % has been achieved for the cell irradiation experiment. A reduction of dose uncertainties during the 3 MeV calibration procedure, certainly will reduce fit–related uncertainties and thus, allow improvement of dose determination accuracy in this energy range. When carefully calibrated and characterized, EBT2 films, allow reliable dosimetry of laser–accelerated proton beams.

6 Experiments with pixel detectors

Different pixel detector systems have been investigated for application as online diagnostic behind a spectrometer. Many camera systems are usually also available in a board camera version, reduced to the pixel detector chip and read–out electronics for application development. These system are the starting point of the ion diagnostic development as they already offer all functionality for basic data acquisition. Without the need to develop a specific read–out systems for a particular pixel detector, it was possible to investigate different types of pixel detector architectures.
As first proof–of–principle tests rather cheap and simple CCD–cameras, available off–the–shelf, were placed in the beam line. These systems were able to image the particle beam but offered no or, if any, rather limited control on the data acquisition. For instance, as no option of external triggering was available, it was not possible to synchronize the data acquisition with the pulse period of the Tandem accelerator. In addition, these simple video cameras record even and odd lines of the image separately and interlace them to yield a full image. In particular in pulsed beam mode image artefacts, appearing as double pulses per frame, are visible in most of the images. However, these measurements clearly demonstrated the possibility to apply off–the–shelf pixel detectors as particle monitors and allowed to determine the basic functionality that is required to operate a camera system in such an application.
Sensitive areas and connection bonds of pixel detectors in these systems are usually protected by cover glasses, which in some cases cannot be removed without destruction of the detector. Therefore, highly flexible systems are required to adapt the camera system to the special needs of charged particle detection.
More sophisticated systems (i.e. *Kappa DX–4*, *RadEye*, *Timepix*) have been tested at the Tandem and in first applications at the laser–accelerator as well as RPTC.

6.1 Kappa DX–4

The first of the three investigated systems, *Kappa DX–4*, is based on an industrial CCD camera system which has been modified for the needs of charged particle detection (sec. 3.1.4). In pulsed beam mode, using 20 MeV protons, two different CCD sensors (Kodak KAI 1020) have been investigated, tagged as *Sensor A* and *Sensor B*, respectively, in the following. Response to single protons has only been measured for *Sensor A*, for 20 MeV and 10 MeV protons, respectively.

6.1.1 Single ion irradiation with 20 MeV protons (SNAKE)

Single protons of 20 MeV were prepared for a first test of the CCD sensor at the SNAKE micro–beam facility. Single ion irradiation is a powerful tool for response measurements.

Using the micro–probe, it is possible to direct a single proton to a single pixel with sub–μm accuracy. Therefore, not only the response of a single pixel to a single protons can be investigated, but in principal also the influence of the impact region, i.e. centre or border region of a pixel. This is of special interest for an interline transfer CCD where a pixel is subdivided into a light sensitive area for charge collection and a light–shielded charge transfer region. However, prevention of charge generation in the transfer channel by light shielding is obsolete in charged particle detection where particles with typically few MeV of energy are able to pass the thin light shield.
The detector was mounted on a motorized microscope stage. (fig. 3.7), where sub–μm and, hence, sub–pixel positioning accuracy can be achieved. The position of the detector with respect to the beam axis was changed in x– and y–direction in steps of 2 μm by movement of the microscope stage, forming a cross–like irradiation pattern.
To minimize scattering material in the beam path, no light–tight shield was placed in front of the sensitive area. Ambient light was reduced, as possible, to ensure measurements with an acceptable low noise level. Furthermore, a background correction was accomplished for all exposed images before analysis.
Preparation of a single ions usually requires a signal from the transmitted ion to close the chopper passage gate, e.g. by a scintillation counter (sec. 3.2.1). Although the CCD–based system is optimized for transmission measurements, the available proton energy of 20 MeV is not sufficient to cross the sensor material. Therefore, a predefined gate length has to be adjusted in such a way, that in average only a single proton arrives at the detector site. For a gate lengths of 1 ms only single protons where measured by the scintillation counter in average. Image recording of the detector was triggered 500 μs before the opening of the chopper gate. Therefore, an integration time of 2 ms was used for this chopper gate length. A major drawback of the pre–defined gate length is a large number of gates where no proton arrived at the detector site, resulting in rather low statistics of the single ion irradiation.
A rectangular ROI of 20 x 20 pixels, thus, covering all exposed pixels, was analysed by the cluster search algorithm described in section 3.4.2.

Pixel response, integrated over all measured images, is plotted in fig. 6.1a. The single proton measurement has the major advantage that the position where the detector was hit by a particle is precisely determined. The detector movement with respect to the beam axis creates a cross–shaped irradiation pattern, visible by the integrated number of proton hits per pixel. However, a large number of single, unexposed pixels, surrounding the hit pattern, also show elevated signal levels and are, thus, recognized as events. Filtering the measured hit map only for single pixel events (cluster size = 1), the true hit pattern disappears. Hence, single pixel events are not associated to protons hits, but to random noise fluctuations.
Fig. 6.1b shows the corresponding distributions of pixel values, for both, filtered and unfiltered events. In the total distribution, accounting for all events, two peaks are visible. The first peak, centred at a pixel value of 50, is strongly correlated to single pixel hits. 73 % of all of these false events are located within the pixel value interval from 49 to 54 ADU, barely exceeding the noise level. None of these events contribute to the second peak, located at a pixel value of 115 ADU. Therefore, single pixel events are attributed to random pixel noise fluctuations.
In the following only events of clusters with more than one pixel are considered. The resulting event distribution, depicted in fig. 6.2a, shows a much cleaner hit pattern alongside with

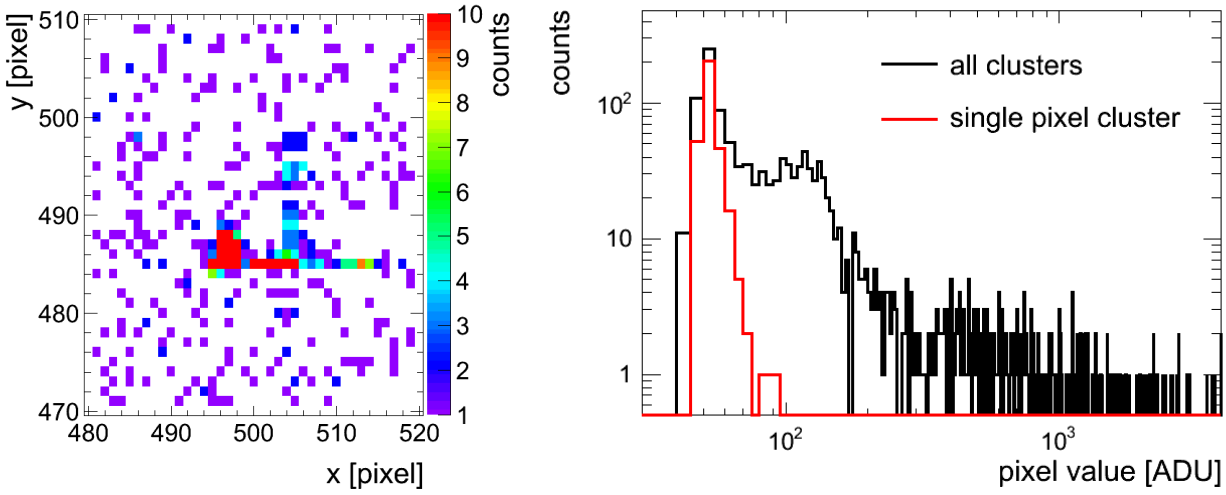

(a) (b)

Figure 6.1: **Event map and pixel value spectrum of the single ion irradiation**
a) Two–dimensional distribution of all events recognized by the cluster search algorithm. The large number of events outside the cross–shaped exposure area, which is related to pixels with higher counts (colour coding), are attributed to noise fluctuations, marked as hits.
b) The total distribution of pixel values is shown for all responding pixels (black) of the event map in a). Noise fluctuations of individual pixels (red) contribute mainly to the first peak in the total spectrum. One of these kind of random pixel fluctuations, is present in approximately every second recorded image.

corresponding x– and y–profiles (figs. 6.2b, 6.2c). Approximately 70 % of all events form clusters of two pixels (fig. 6.2d).
Some pixels have been repeatedly scanned with sub–pixel resolution. Thus, central as well as border regions of the pixels are hit by the impinging particles. However, no difference in response has been observed for these events.

The beam was prepared in such a way, that, in average, only a single proton hit is measured per read–out frame. However, at least two adjacent pixel respond to a single proton, meaning that generated signal charge is distributed over these pixels, forming a cluster. This effect is also known as blooming and typical for CCDs and high charge densities. To obtain the correct response signal, the pixel values of all pixels in a cluster is summed.
In fig. 6.3 the resulting signal distribution for all proton related events is shown. The pixel value is a direct measure of the particle's energy loss in the sensitive detection area. The spectrum is fitted by two Landau distributions. The most probable values (MPV) of both Landau distributions are correlated by a factor of two to account for the fact that clusters are formed by integer numbers of proton hits. A most probable value of (225 +/- 12) ADU for the main peak, which corresponds to a single proton hit, is obtained. Measured and fit distribution show a good agreement and allow to identify contributions of single and double proton hits in the spectrum, despite rather low measurement statistic.

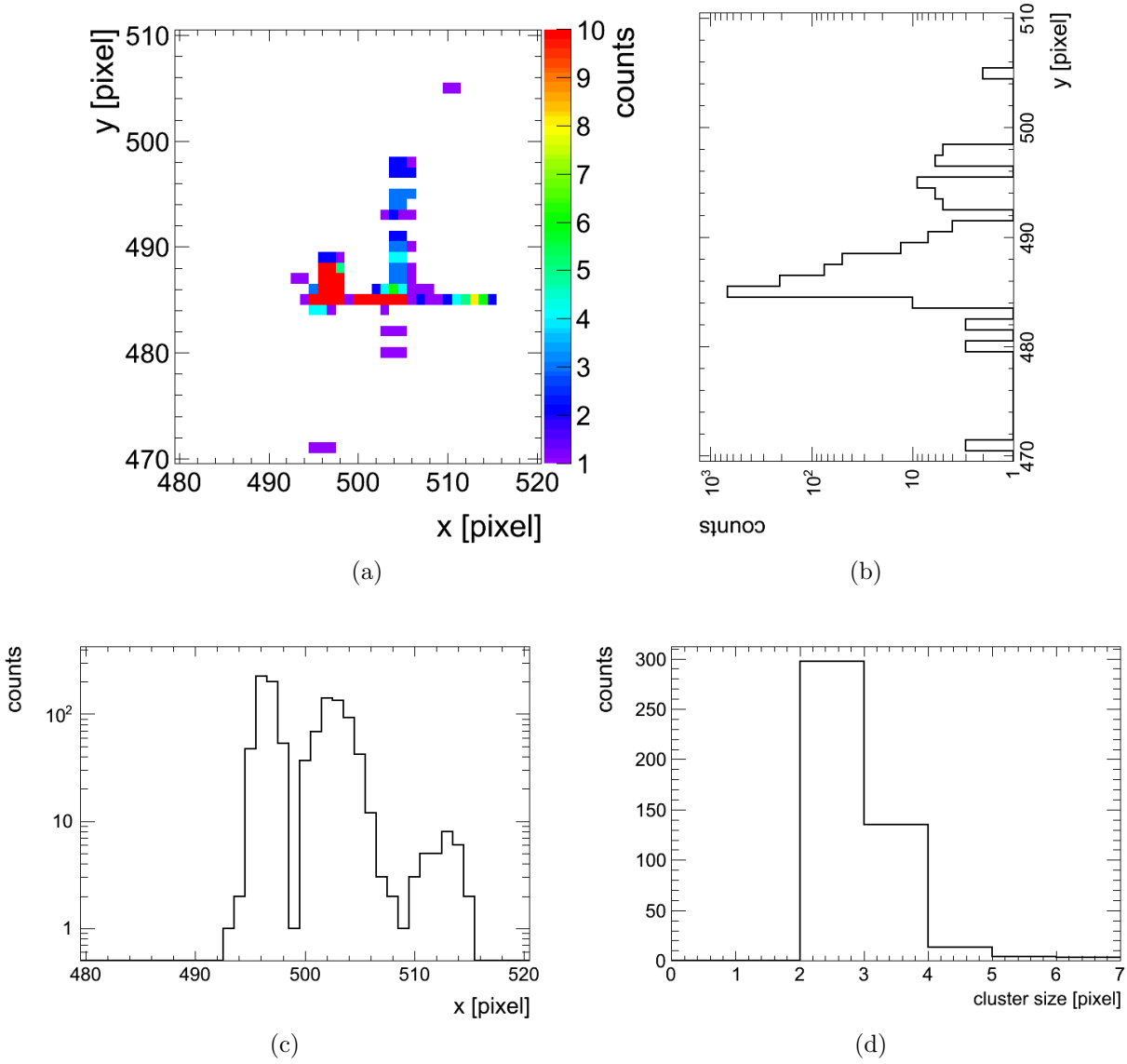

Figure 6.2: **Filtered event map and cluster size spectrum**
The single cross shaped hit pattern(a) and corresponding profiles (b,c) is clearly visible if all single pixels clusters are filtered out. For the majority of the remaining proton hits, signal charge is distributed over two pixels (d). This so–called blooming or charge sharing effect is well known in CCD technology.

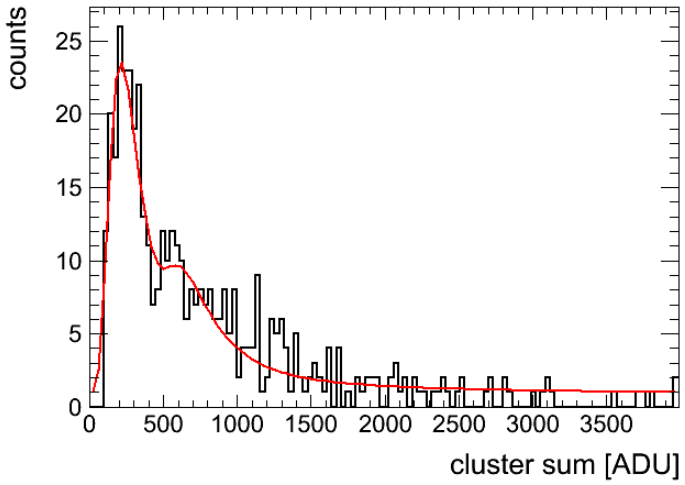

Figure 6.3: **Cluster sum spectrum of 20 MeV protons**
The cluster sum spectrum is fit by a sum of Landau functions, showing two distinct peaks, corresponding to single and double proton hits per pixel.

6.1.2 Continuous irradiation with 10 MeV protons

The pre–defined gate length that had to be used in single ion irradiation of the previous section, yields a large number of gates without passing protons. As a result a small number of pixels was irradiated with limited overall statistic. Therefore, single proton response of the CCD sensor was investigated in a low flux 10 MeV proton beam on a larger detector area, allowing to compare the response to different proton energies, in addition.

For the *Kappa DX–4* only normal incidence was investigated, due to high chip boundaries for bond protection (fig. 3.7). As the sensitive area of the detector matches approximately the size of the beam area, the sensor board, placed on an aluminium holder, was light–tight mounted on the beam exit flange.

A 10 MeV proton beam was wobbled across an area of approximately 25 mm^2, resulting in an average rate of approximately 2000 protons/cm^2/s on the detector surface. A large fraction of the whole sensitive sensor area was covered by the incident beam. A typical measured two–dimensional hit distribution under these irradiation conditions is depicted in fig. 6.4. Individual particle tracks are clearly separated, enabling measurement of the detector's response to single protons in a continuous beam with higher statistics than in case of the previous single ion irradiation at SNAKE. For comparison with the previous measurement, the same amplification setting was used.

Fig. 6.5a a shows an enlarged region of the hit distribution (fig. 6.4). In agreement with the single ion irradiation experiment of the previous section, mainly two pixel clusters are formed. Corresponding profiles along single rows are depicted in fig. 6.5b. The charge of a typical two pixel cluster is usually distributed along the direction of the vertical shift register. Although pixel values of both cluster pixels are well above the noise level, signal charge is unequally distributed over both pixels. All clusters have the same quantitative shape, where the pixel, that is read–out first, consistently shows the higher pixel value. The cluster sum

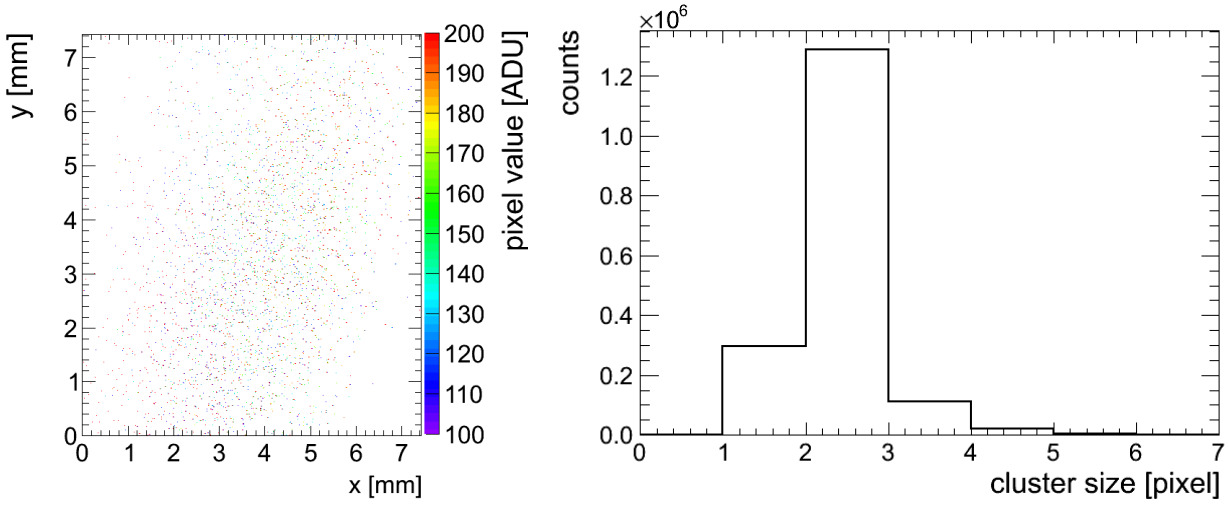

(a) (b)

Figure 6.4: **Event map and cluster size spectrum in continuous beam mode**
a) Snapshot of the two–dimensional proton distribution in a continuous beam of low flux. The spatial distribution of particle tracks within the exposed area (∼ 25 mm², allows the discrimination of individual hits and, shows furthermore good homogeneity achieved by beam wobbling.
b) The cluster size distribution looks similar to the previous measurement (fig. 6.2d), exhibiting a dominant charge sharing between two pixels.

is fitted by a single Landau function as no distinct peak associated with double proton hits is present in the data, yielding a MPV of 346 ADU. The ratio of single ion response values for proton energies of 10 MeV and 20 MeV, determined by the Landau fit (tab. 6.1) agrees with the ratio of related energy loss values from *SRIM* within 13 %.

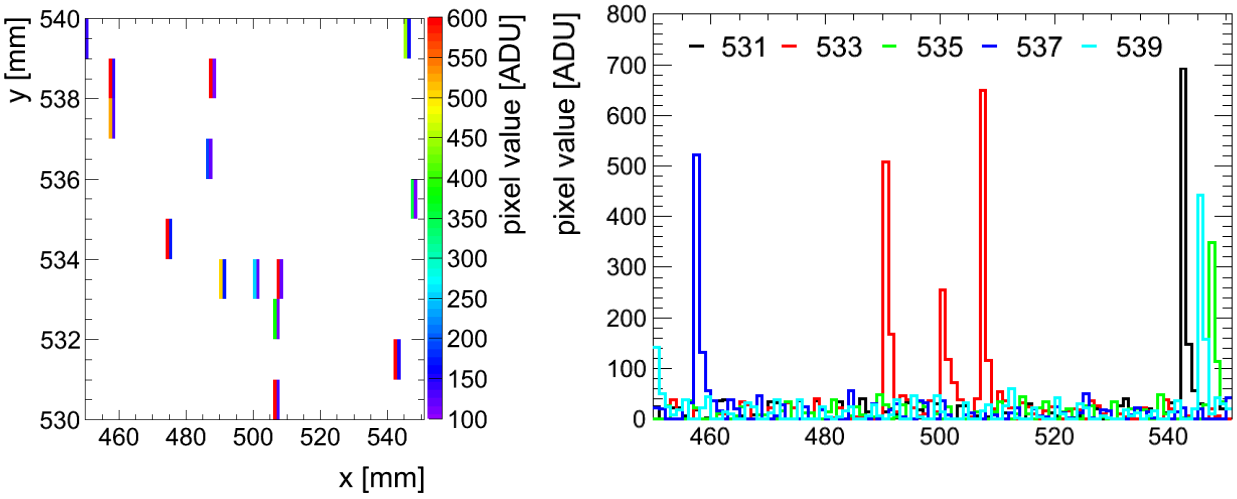

(a) (b)

Figure 6.5: **Charge sharing of the CCD camera system**
All two–pixel clusters are formed parallel to the x–direction, corresponding to the direction of vertical charge transfer register, (a) with consistently higher pixel values for the cluster pixel that is read–out first(b). For clarity only profiles of odd rows are shown in (b).

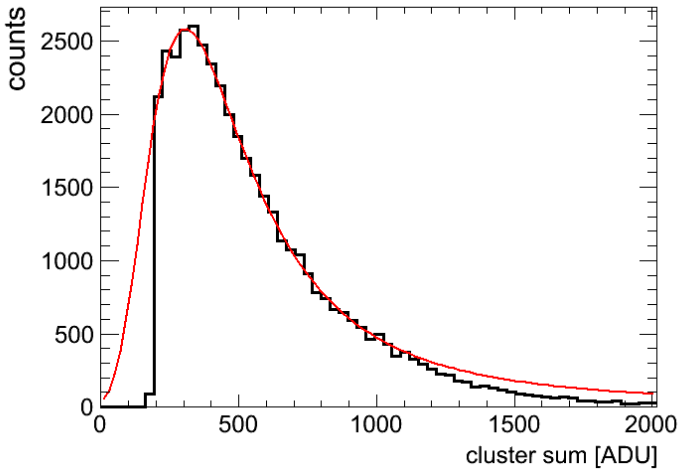

Figure 6.6: **Cluster sum distribution of 10 MeV protons**
The mean single proton response has been determined by a Landau fit.

energy	[MeV]	10	20
energy loss ($SRIM$)	$[\frac{keV}{\mu m}]$	8.075	4.711
most probable value	[channel]	346	225
saturation level	$[\frac{protons}{cm^2}]$	$2.2 \cdot 10^7$	$3.4 \cdot 10^7$

Table 6.1: **Single proton response of *Kappa DX–4* system**

6.1.3 Pulsed beam irradiation with 20 MeV protons

Both sensors, *A* and *B*, have been tested in a pulsed 20 MeV proton beam during two beam times. The same setup as for the continuous measurement has been used. Single ns–pulses with different beam intensities and approximate repetition rates of 10 Hz (*Sensor A*) and 1 Hz (*Sensor B*), respectively, have been prepared as described in section 3.2.1. The S+L pulsing signal was used to trigger the detector's read–out cycle.
For the pulsed beam test of *Sensor A*, the average pulse width (FWHM) was 7 ns, while in case of *Sensor B*, only pulses with a width of 55 ns could be prepared due to technical problems. In any case, pulse durations are much shorter than the detector integration time.
Pulse intensity in terms of p/cm^2 was increased by two orders of magnitude, recording

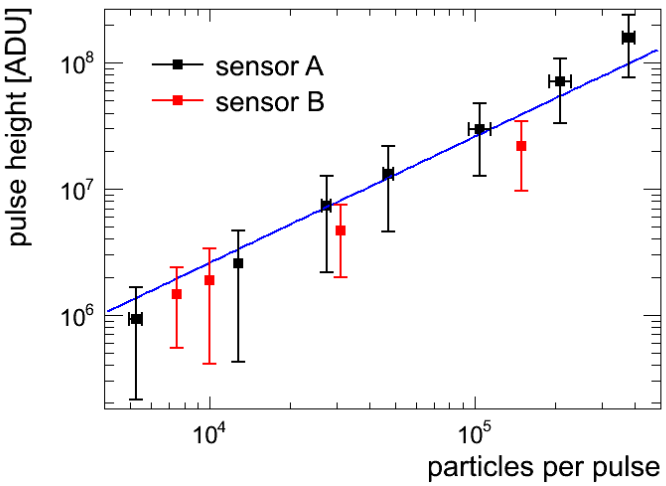

Figure 6.7: **Pulse response of different CCD sensors**
Sensor A and sensor B show the same linear pulse response. The solid line represents a linear fit through the origin of both data sets.

approximately 500 subsequent frames per intensity level. Before and after each of these image acquisition cycles, current was measured to deduce the average number of particles per pulse (eq. 3.5). A simple hit analysis was applied to deduce the mean integrated

response signal per frame. Fig. 6.7 shows a plot of the integrated response signal against pulse intensity for both sensors and an amplification of 9.1 dB. For *Sensor A*, the proton number per pulse was varied between $10^4 - 10^7$, while for *Sensor B* the pulse intensity range was approximately a factor of 10 lower. The signal intensity increases linearly with particle number. There is no significant difference in response of *Sensor A* and *Sensor B*. A linear fit through the origin is applied to the combined data of both sensors. The ratio of signal intensity to proton number yields an average single proton response signal of (262 ± 65) ADU.

For *Sensor A*, pulse response has been measured for different amplification settings, 0 dB, 9.1 dB and 18 dB. Signal intensity plotted against pulse fluence is depicted in fig. 6.8 for amplification settings. The signal intensity increases as expected with fluence. Even for the largest amplification of 18 dB, no saturation effect has been observed. A linear fit through the origin has been applied to all data sets. Determined slope values depend linearly on amplification. At the largest fluence, about 2 % of all exposed pixels are saturated in case of the 18 dB amplification. Looking at the 80 % and 50 % saturation level, still, only about 3 % and 6 % of the pixels exceed these thresholds. For 9.1 and 0 dB amplification less than 1 % pixels are saturated or exceed the 80 % level.

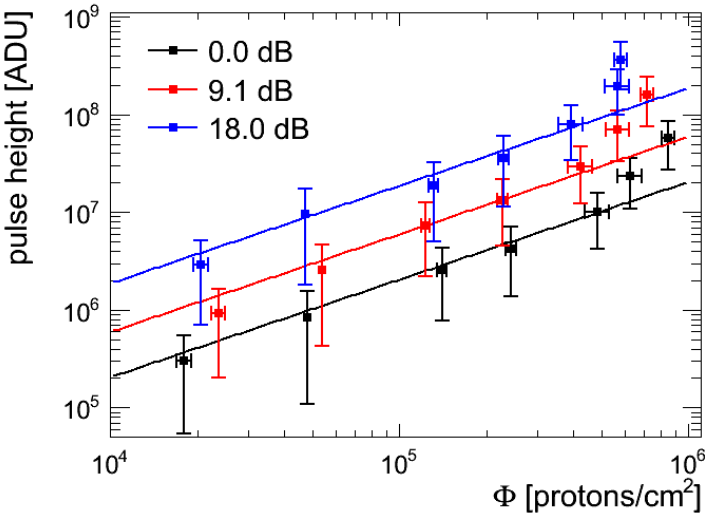

Figure 6.8: **Single pulse response for different sensor settings**
Pulse fluence response of the sensor is linear for all amplification settings, except for the highest fluence point in case of the 18 dB amplification.

Radiation Damage

The total dose on the detector in terms of number of protons has been estimated for the pulsed irradiation of *Sensor A*. The pre–irradiation level due to continuous measurements presented in the previous section is less than $5 \cdot 10^7$ protons/cm^2. To estimate the total dose in pulsed beam mode, the average number of particles per pulse of each intensity levels is multiplied by the number of corresponding recorded images. Thus, the total dose increases to a level of approximately $3 \cdot 10^9$ protons/cm^2. Radiation damage reveals itself mostly for

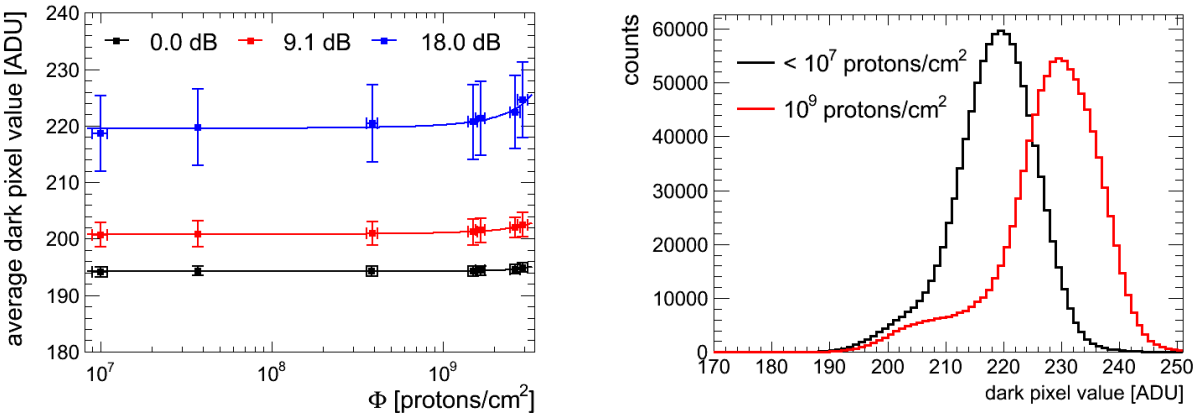

(a) (b)

Figure 6.9: **Radiation damage of the *Kappa DX–4* system**
a) The pixel value increases with accumulated proton dose, solid lines represent an exponential fit of the data.
b) The pixel value peak of unexposed images shifts by 4.7 % towards higher channels, when increasing the dose by more than two orders of magnitude.

the highest amplification. Fig. 6.9b shows the dark pixel value spectra of an unexposed image for 18 dB amplification before and after pulsed irradiation. No dead pixels have been observed even for this acquisition setting. However, for the highest amplification setting the noise level shifts by only 4.7 % towards higher channels. The width of the distribution dose not change significantly. In fig. 6.9a, the average dark pixel value is plotted against total proton number for all acquisition settings. Data have been fit by an exponential fit function.

6.1.4 Discussion 1

In pulsed beam mode the detector was exposed up to a maximum pulse fluence of approximately 10^6 protons/cm^2. A linear detector response over the the whole investigated dynamic range of the detector has been observed. The mean signal response deduced in the pulsed measurement agrees within measurement uncertainties with the single proton irradiation. The saturation level for both energies can, therefore, be estimated from the single ion response, yielding 18 or 11 protons per pixel for 20 MeV or 10 MeV, respectively. These values correspond to a saturation level in the 10^7 protons/cm^2 fluence range, which agrees with the saturation fluence of $2{\cdot}10^7$ protons/cm^2 that has been estimated from sensor specifications (sec. 3.1.4).
Although a small amount of pixels start to saturate at the highest fluence and amplification, no saturation in pulsed beam mode was observed for the 0 dB amplification. Defining the detector lifetime by a minimum residual dynamic range of 90 %, the detector is able to survive more than 100 shots, with 10^7 p/cm^2 (20 MeV), each, when operated with the highest amplification settings. The maximum number of pulses is even larger for reduced

amplification setting as it scales with the amplification.
The CCD–camera shows sufficient linear flux response over the whole investigated range and for all amplification settings for laser–ion diagnostic. Different sensors show similar response curves, allowing to change damaged sensors without the need to determine new calibrations. Radiation damage is no limitation for application in laser–ion diagnostic as sensors can be easily changed. A major drawback is the geometry of the sensor, with a sensitive area smaller 1 cm^2. Even more important, the sensor does not allow to increase the sensitive area by attachment of additional sensor modules due to large chip boundaries. The sensor, is therefore, not suited for the measurement of ion energy spectra behind a spectrometer in laser–acceleration experiments.

6.2 Timepix

The *Timepix* system is the only non–integrating detector system used in the scope of this work. Although the sensitive area is comparable to the *Kappa DX–4* camera, it is possible to tile additional sensor modules to the chip to increase the sensitive area. A complete spectroscopic measurement unit is integrated on a per pixel base. Hence, *Timepix* offers three different read–modes for counting, arrival time (TIM) or energy (TOT) measurement of incident particles. However, for ions only the latter two modes provide reasonable information due to charge sharing effects [179, 181]. Energy as well as time mode are investigated for the purpose of laser–accelerated ion detection.

6.2.1 Energy calibration

For measurements in the energy (TOT) mode a calibration of the individual spectroscopic electronics connected to each pixel is required. This calibration of the *Timepix* chip has been accomplished at the Institute for Experimental and Applied Physics (IEAP) of the Czech Technical University in Prague [180]. An X–ray source was used to produce characteristic X–rays of different fluorescent materials in the energy range of 6 to 60 keV. For each emission line and pixel a spectrum was measured and fitted by a Gaussian distribution. To allow an unambiguous correlation of the TOT signal and energy deposition only single pixel clusters were included into the spectra.
Energy response curves for each pixel are, thus, obtained and fitted by eq. 6.1, with a, b, c and t being free fitting parameters [180]. An energy threshold of about 6 keV, corresponding to the fit parameter t, is defined.

$$TOT(E) = a \cdot E + b - \frac{c}{E - t} \tag{6.1}$$

The validity of the energy calibration was checked by an ^{241}Am source, with its dominant α

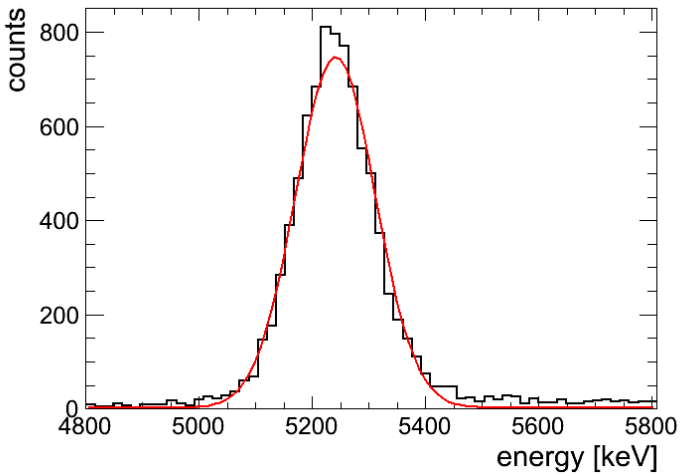

Figure 6.10: **Calibration check with ^{241}Am-source**

line of 5486 keV (84.8 %) [214]. The measured spectrum shows a typical Gaussian distribution, which is centred at 5239 keV with a σ of 65 keV, yielding an excellent energy resolution of 1.7 % (fig. 6.10). However, the energy determination from the γ calibration is wrong by 247 keV.

6.2.2 Continuous irradiation

First test measurements have been accomplished at the Tandem accelerator in a continuous 20 MeV proton beam. For measurements in the energy mode detector and read–out electronic were placed in vacuum (fig. 3.11). The particle flux was reduced to about 10^4 protons/cm^2/s to allow distinction of individual proton hits. The calibration of the previous section (eq. 6.1) has been applied to convert the raw TOT signal into an energy, measured in keV. Fig. 6.11

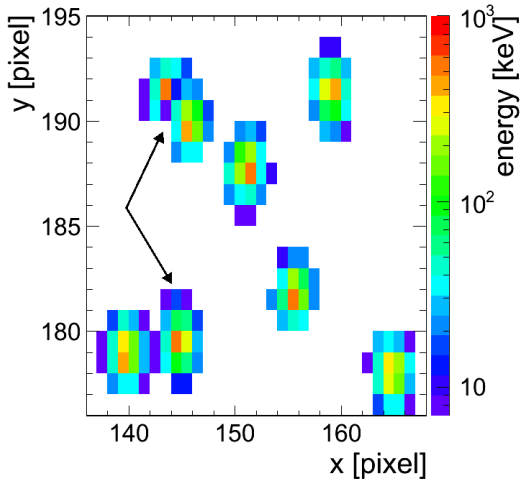

Figure 6.11: **Charge sharing effects of the *Timepix***
Single proton hits show large charge sharing effects in a circularly shaped area surrounding the hit pixel. Clusters start to overlap if hit pixel are separated by less than 8 pixels (marked by arrows).

shows typical hit patterns of incident protons. Charge sharing effects are clearly pronounced yielding large clusters of responding pixel for individual particle hits. All clusters have a similar size—typically more than 10 pixels— and almost circular shape. If proton hits are in close vicinity to each other (i.e. <8 pixel distance) clusters start to overlap. A plot of energy against cluster size (fig. 6.12a) shows an almost linear increase with cluster size. Even more important, five separate agglomerations of energy–size pair of values can be distinguished. These are formed by overlapping clusters, which are detected as single events by the cluster search algorithm. Corresponding peaks for all agglomerations are clearly visible in the energy spectrum (fig. 6.12b), while only the first two can be seen in the cluster size spectrum (fig. 6.12c).

The peaks in the energy and cluster size spectra have been fit by a sum of four and two Gauss distribution, respectively, fit results are listed in tab. 6.12. For the first peak of the energy spectrum, corresponding to a single proton hit, an energy deposition of 1240 $\pm$ 102

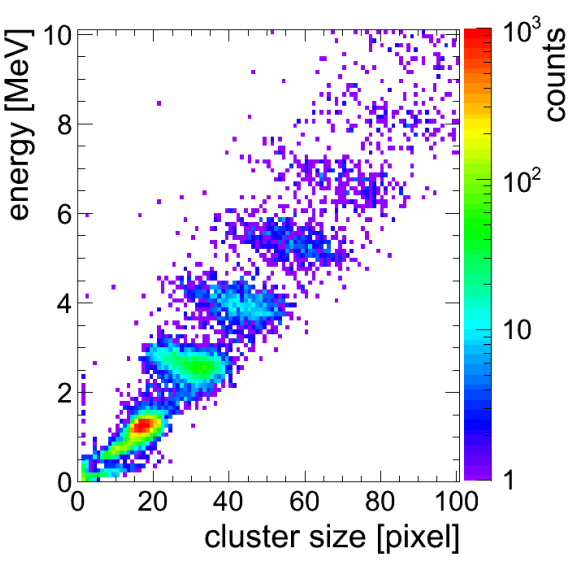

(a)

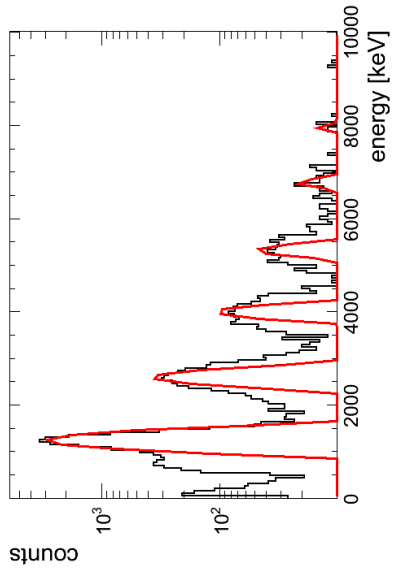

(b)

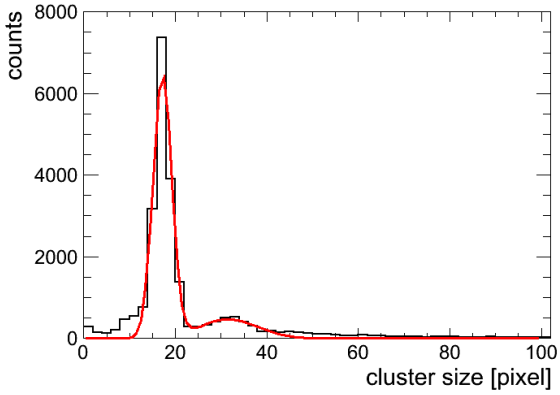

(c)

peak number	energy [keV]	cluster size [pixel]
1	1240 ± 102	17 ± 2
2	2597 ± 192	32 ± 2
3	3988 ± 207	-
4	5357 ± 221	-

Table 6.2: **Energy and size of multiple proton hit clusters**

Figure 6.12: **Cluster analysis of TOT measurements**
Overlapping proton clusters cannot be resolved by the cluster search algorithm. Plotting the cluster sum (i.e. energy) over the cluster size, agglomeration of energy–size pairs are visible (a). They are correlated to the number of overlapping proton clusters, falsely identified as single event. Corresponding peaks are clearly visible in the energy and cluster size spectra (b,c).

keV can be determined. A *TRIM* simulation yields an energy deposition of 1499 keV in the 300 μm silicon sensor for an incident proton of 20 MeV [197]. The underestimation of the measured energy by 259 keV is of the same order of magnitude as for the calibration check with the ^{241}Am source. Peaks associated to higher energy channels correspond to overlapping proton clusters, which can not be separated by the cluster search algorithm. All peaks are, therefore separated from each other by the energy that corresponds to a single proton.
For online visualization of the Bragg curve, the detector was placed under a grazing angle (6.13). Charge sharing effects are most pronounced in the Bragg Peak region due to the high density of generated charge carriers.

To investigate the capability of the TIM mode to resolve the temporal beam structure,

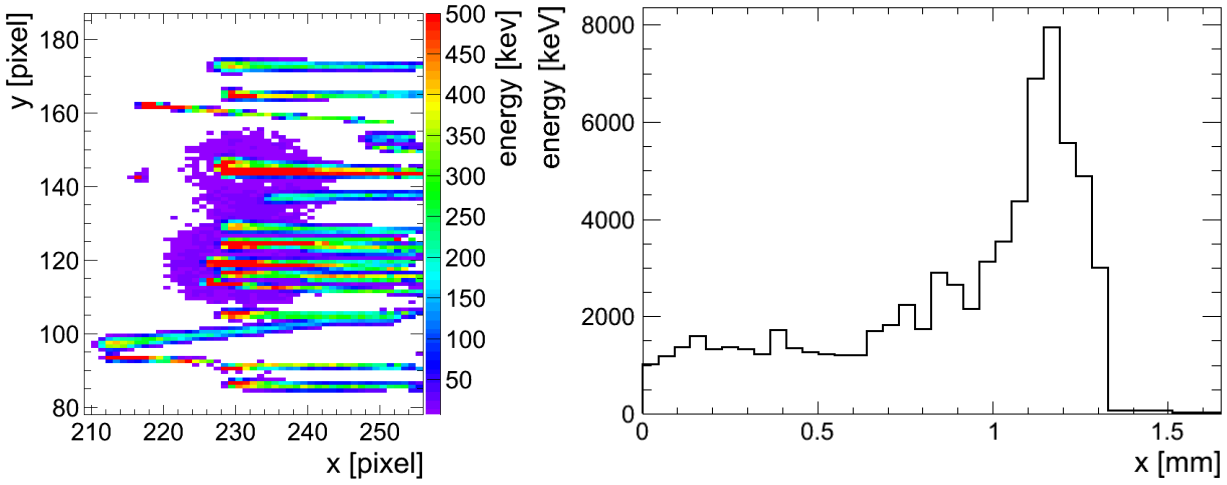

(a) (b)

Figure 6.13: **Bragg curve measurement**
Charge sharing effects are most pronounced for dense track distributions and the Bragg peak region (a). However, all single tracks show the typical Bragg curve (b).

a beam wobbler was used with an approximate ratio of x– and y–direction frequency of 1:1, thus producing typical Lissajous figures. The *Timepix* chip was controlled with a clock frequency of 500 kHz, yielding a time resolution of 2 μs. Fig. 6.14 shows a sequence of snapshots of the beam, each corresponding to an exposure time of 24 ms. Different phases of the produced Lissajous figures can be clearly distinguished.

6.2.3 Pulsed irradiation

All measurements in pulsed beam mode, with protons of 20 MeV energy and an average pulse duration of 31 ns, have been accomplished in air under normal particle incidence. Read–out of the *Timepix* detector was triggered by the Tandem pulsing system to ensure single pulse acquisition per image. The response of the *Timepix* detector in energy mode has been investigated for pulse intensities ranging from few hundred up to $2.5 \cdot 10^5$ protons/cm^2.

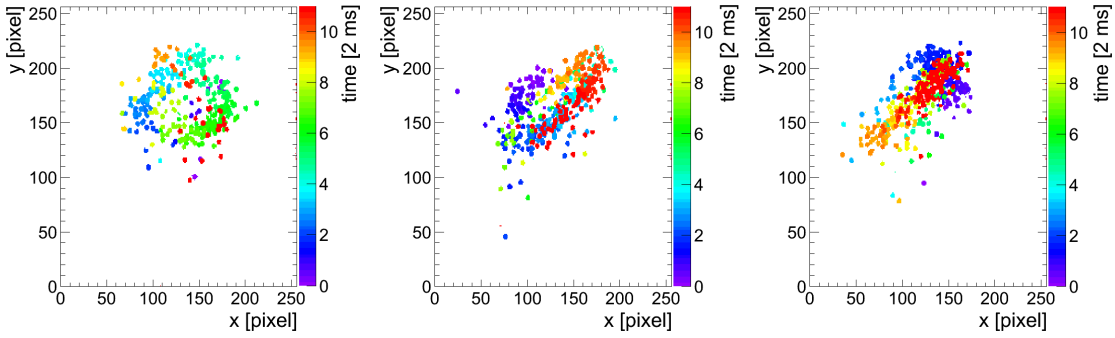

(a) (b) (c)

Figure 6.14: **TIM mode**
Lissajous figures for a frequency ratio of approximately 1:1 and phase difference of $\frac{3}{2}\pi$ (a), $\frac{7}{4}\pi$ (b) and 2π (c).

A main feature of the *Timepix* chip is the possibility to adjust threshold level for each pixel individually by a 4–bit DAC. The standard configuration (STD) is optimized for high sensitivity, thus enabling detection of signals with low SNR. In addition to the standard setting, pulse response has been investigated for threshold levels yielding moderate (HTL1) and low sensitivity (HTL2). As a result the cluster size associated to a single proton decreases with sensitivity as only the centre of mass of the generated charge distribution is registered. For the lowest pulse intensity only a small number of individual hit clusters overlap, which allows to count the number of events per pulse. The measurement with the low sensitivity setting, HTL2, under these conditions yields a significant deficit in the proton number when compared to the STD setting.
For a moderate pulse intensity of about 4000 protons/cm^2, an increase of the noise level of unexposed pixels is observed for the majority of acquired images (68 %) when using the STD setting. For the same setting and highest fluence level, corresponding to $2.5 \cdot 10^5$ protons/cm^2 and pulse, the majority of pixels is saturated (fig. 6.15a). Even more striking is a ring–shaped region of unsaturated pixels corresponding to the boundary region of the incident particle bunch. In this region even lower pixel values are measured than in the surrounding, unexposed region. The same effect is present for HTL1 (fig. 6.15b) and HTL2 settings (fig. 6.15c), though only a small number of pixels appears saturated for these threshold levels. The TIM mode has also been applied for pulsed particle detection. Even for the maximum clock frequency of 10 MHz, the time resolution of 100 ns is not sufficient to distinguish the arrival time of individual protons of the pulse.

6.2.4 Discussion 2

The energy calibration procedure for each pixel requires the collection of the complete signal charge in a single pixel. The probability of charge sharing increases with energy deposition, thus limiting applicable calibration energies to less than 100 keV. As a result, the obtained energy calibration has to be extrapolated over approximately two orders of magnitude to

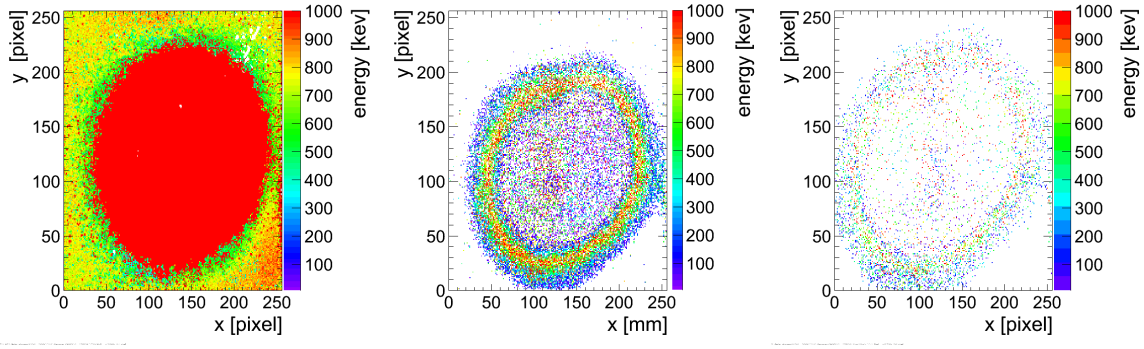

(a) (b) (c)

Figure 6.15: **Saturation at high pulse flux**
The detector shows strong non–linear saturation effects for STD (a), HTL1 (b) and HTL2 (c) sensitivity settings for a pulse fluence of $\sim 2.5 \cdot 10^5$ *protons/cm*^{2}*. The beam spot has a size of 0.8 cm*^{2}*.*

measure the energy loss of a heavy charged particle, which is in the MeV range for α particles and 20 MeV protons used, here. α particles deposit their complete energy within the 300 μm thick sensor, the energy that is measured by *Timepix* is 4 % smaller than what is expected. Protons of 20 MeV are able to pass the sensor, depositing an energy of about 1.2 MeV according to the TOT measurement, which is 17 % smaller than the value calculated in a *TRIM* simulation. The absolute deviation from measured and expected energy deposition is 250 keV for both, protons and α particles. It is likely, that a constant offset was introduced when extrapolating the energy calibration to the MeV range.
A finite number of multiple overlapping proton clusters has been observed in continuous beam mode due to an average cluster size of 17 pixels per single proton. The total energy measured for these multiple proton clusters increases linearly with proton number. The TOT mode can, thus, be applied for an accurate determination of the particle fluence, provided the single particle response is known.
Large regions can be affected by charge sharing effects if a high density of charge carriers is generated as in case of incident intense proton pulses. Even pixels in a distance of several hundred μm from the impact area of an intense proton pulse started to saturate with increasing pulse intensity. Non–linear effects were present for a maximum pulse fluence of $2.5 \cdot 10^5$ protons/cm^2, limiting the possibility to adapt the saturation level by lower sensitivity settings.
For applications with low particle flux, where accurate energy or timing measurements are required, *Timepix* offers many interesting features for beam characterization. However, for direct detection of laser–accelerated ions, the device is not suitable as the dynamic range is not sufficient.

6.3 RadEye

6.3.1 Experiments at the Tandem accelerator

First test measurement of the *RadEye* sensor in continuous and pulsed beam mode have been accomplished in air. Although the read–out electronic of the detector system allows parallel operation of 4 sensor modules, only a single sensor was employed for normal as well as oblique incidence measurements. The sensor was placed as close as possible to the beam exit window to minimize scattering effects and light–shielded(fig. 3.10).

Continuous irradiation with 15 MeV protons (I–40 beam line

Detector response to single protons was investigated in a continuous 15 MeV proton beam of low flux, approximately 10^4 protons/cm^2/s. All images were acquired in free running mode (i.e. without external trigger) with a fixed read–out period of 1000 ms. The average dark signal of each pixel is subtracted to obtain the net response signal. A cluster analysis has been accomplished for all accordingly corrected frames. Fig. 6.16a depicts a typical

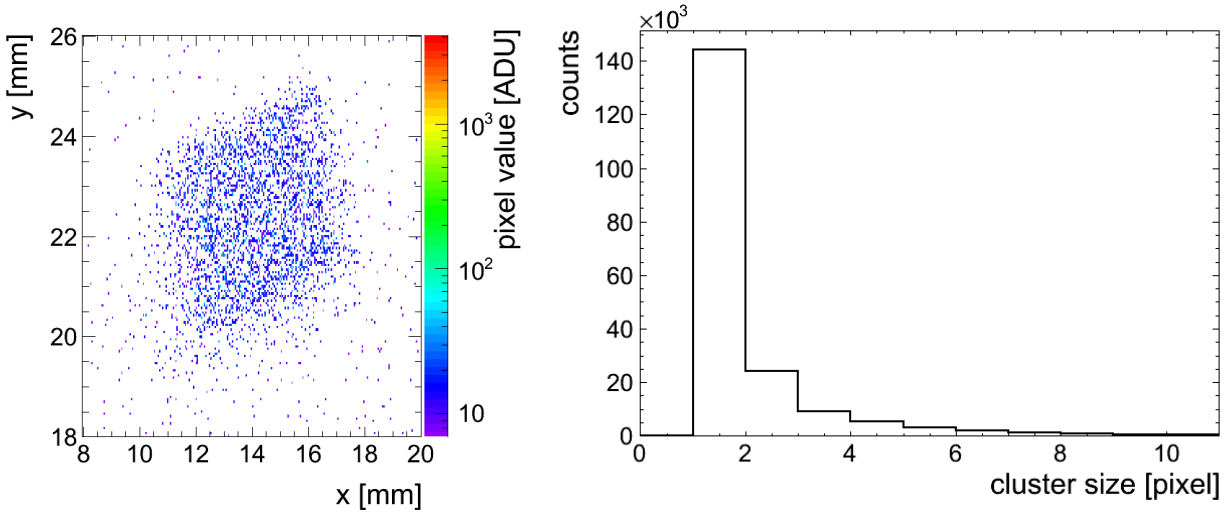

(a) (b)

Figure 6.16: **Event map and cluster size distribution in continuous beam mode** *a) Only a cut–out of the overall sensitive area of approximately 25 mm^2 is shown here. Individual hits are easily distinguishable. Pixel values (colour coded) of hit pixels correspond to less than 2 % of the sensors maximum dynamic range. Differences in pixel values are not visible with this colour coded scale.*
b) The majority of all events that have been detected by the cluster search analysis are single pixel hits (i.e. cluster size = 1 pixel).

two–dimensional event map, showing an exposed area of approximately 25 mm^2. Good homogeneity of the irradiated area is achieved by wobbling of the incident proton beam with two electromagnetic steerer. Under these irradiation conditions, a proton hit probability of

about 25 % per pixel, can be deduced from the applied particle flux. The majority of all detected events (i.e. clusters) are single proton hits. However, 25 % of all events create clusters of two or more pixels (fig. 6.16b) which might be an indication for charge sharing effects, as seen in both previously discussed pixel detectors.
The cluster sum is a measure for the total energy deposition of an event. For clusters of two or more pixels, the pixel value of a cluster pixel is related to the energy deposition per pixel. The cluster sum spectra of all events are depicted in fig. 6.17a. For the sake of consistency, single pixel hits are called 1 pixel clusters. Distributions, filtered for an individual cluster size, are additionally drawn for all events with cluster size < 5, corresponding to 95 % of all events. The total spectrum shows two peaks within the first 40 channels of the cluster sum spectrum, followed by a long tail. The same is true for the single pixel spectrum, which represents the major contribution to the total distribution. With increasing cluster size, characteristic of second peak and tail weaken, while position and width of the main peak increase linearly. Looking a the corresponding pixel value distribution of individual cluster pixels (fig 6.17b), it is possible to distinguish two peaks for all cluster sizes. Peak positions are shifted with respect to each other by a factor of two, and furthermore, related to the same pixel value, regardless of cluster size.
For a 1 pixel cluster, cluster sum and cluster pixel spectra are identical. The main peak is

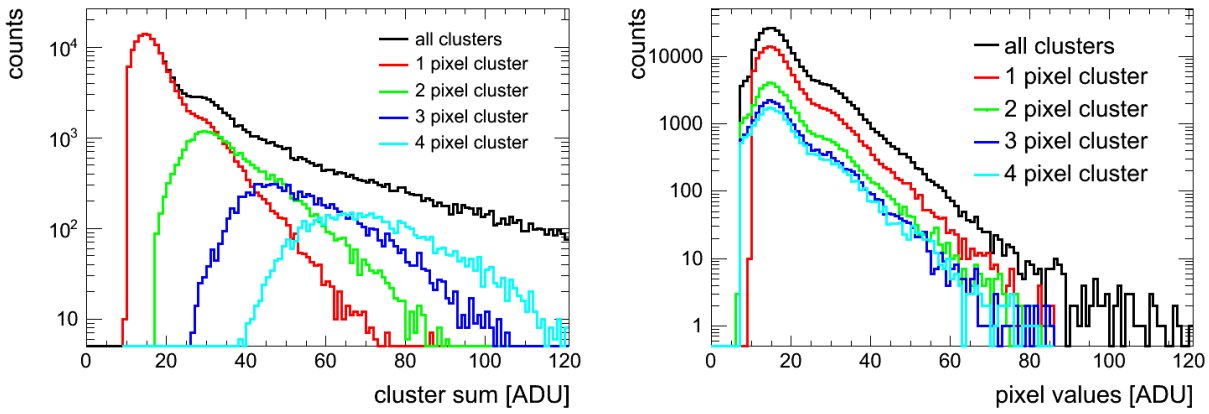

(a) (b)

Figure 6.17: **Cluster sum and cluster pixel spectra in continuous beam mode**
Cluster sum and pixel value are a measure for the energy deposition per event and pixel, respectively. The cluster sum(a) and cluster pixel (b) spectrum of all events (black) is filtered for different cluster sizes (coloured curves).

attributed to single proton hits, which are the majority of all events. The second, smaller peak is shifted towards a higher channel by a factor of two and hence, identified as a double proton hit. All pixel spectra of clusters with two or more pixels show the same pixel value distribution as the 1 pixel cluster spectrum (fig. 6.17b). This is not expected in presence of charge sharing effects, where the signal charge is usually randomly distributed over neighbour pixels, as seen in previous measurements with the *Kappa DX–4* and *Timepix* systems. In particular the fact that peak positions are exactly the same for all cluster sizes, allows

the conclusion that multiple pixel clusters are not attributed to charge sharing effects but simultaneous hits in neighbour pixels. This is also supported by identical peak positions associated to double proton hits in the 1 pixel cluster spectrum and the main peak of the 2 pixel cluster distribution when looking at the cluster sum spectra (fig. 6.17a).

The total cluster pixel spectra has been fitted by the sum of two Landau distributions

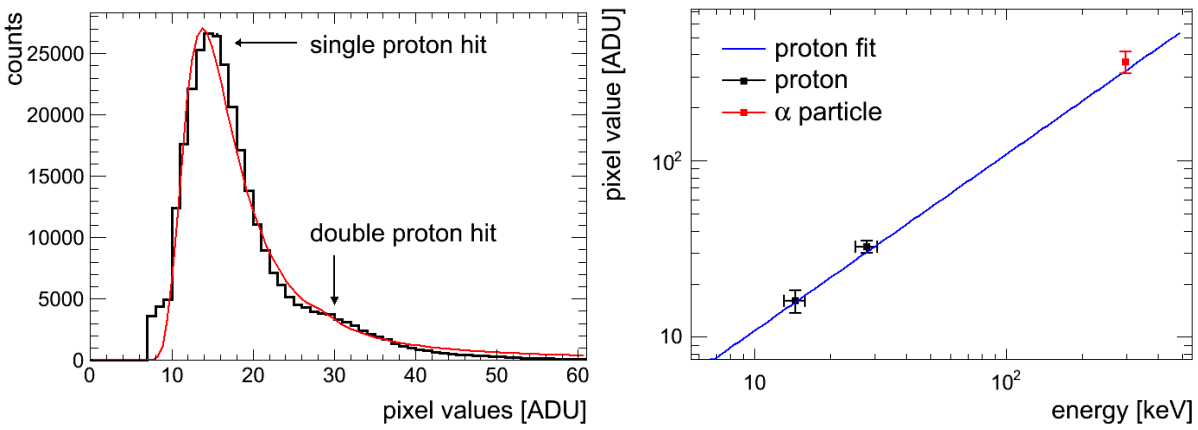

(a) (b)

Figure 6.18: **Energy calibration of the *RadEye* detector**
a) The cluster pixel spectrum has a large peak associated with single proton hits and a smaller peak at higher pixel values, related to double proton hits. The spectrum was fitted by two Landau functions to determine most probable values for these events.
b) Deposited energy of single and double hits, obtained from a TRIM *simulation, is plotted against the most probable response signal obtained from the fit in a). A linear fit through the origin is applied. The detector response to an α–source is additionally drawn for comparison, showing satisfying agreement with the extrapolated calibration curve.*

to obtain the MPV of single and double hits per pixel, which can be used for an energy calibration. For this purpose, the MPV of both Landau distributions were allowed to vary freely during the fitting procedure, yielding most probable values of 14.16 ADU and 29.95 ADU for single and double hits, respectively. Values for the corresponding energy loss within the sensitive detector thickness are obtained from a *TRIM* simulation to account for the energy loss in the beam exit window and passivation layer of the sensor during proton passage. MPV pixel values, related to single and double hits, are plotted against the calculated energy deposition in fig. 6.18a. A linear regression, fitted through the origin, yields an energy loss (ΔE) to pixel value (pv) conversion factor of (1.09 ± 0.12) ADU/keV.

$$pv = 1.09 \cdot \Delta E \tag{6.2}$$

The deduced energy calibration was cross–checked with a mixed nuclide α–source (^{239}Pu, ^{241}Am, ^{244}Cm). The energy resolution of the detector is not sufficient to resolve individual

α lines in the spectrum. An average energy of 300 keV is deposited in the depletion layer by α irradiation, an order of magnitude higher than both calibration energies. Nevertheless, extrapolation of the calibration curve to higher energies shows good agreement with the single α point.
The number of events per recorded image has been deduced for different exposure times (fig. 6.19). A linear increase is observed for both, proton as well as α particles, yielding particle rates of about 12000 and 23000 particles/cm^2/s, respectively. The detector shows a linear response to particle fluence, which is an important prerequisite for use in laser–ion diagnostic that aims for quantitative fluence determination.

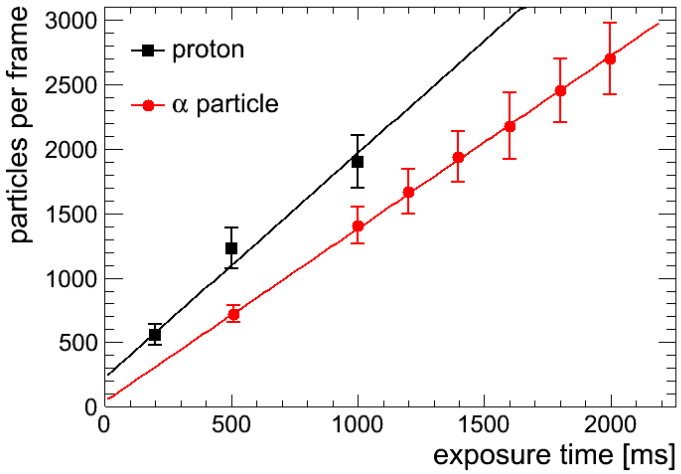

Figure 6.19: **Response of *RadEye* detector as a function of fluence**
The average number of particles per frame has been determined from the number of events detected by the cluster search analysis of all frames. Solid lines represent a linear fit of the data.

Depth dose measurement

Depth dose curves have been measured for grazing incidence for protons of 20 MeV energy. Fig. 6.20b shows a typical track distribution measured within one image. The thin sensitive layer thickness, results in a significant amount of energy deposition outlying the depletion zone for all protons entering the detector with $\alpha \neq 0$. Furthermore, some of the tracks are shortened due to scattering. No energy measurement is, thus, possible, though the majority of tracks show the typical Bragg curve 6.20b.
However, integration of all proton tracks yields an average total track length of 47 ± 2 pixels, corresponding to a track length of 2.26 ± 0.96 mm length. Protons of 20 MeV energy have an expected range in silicon of 2.35 ± 0.10 mm or 48–49 pixel diameters. Accounting for the guard ring surrounding the active matrix, which is of the order of a pixel size, an excellent agreement of measured and expected range is obtained.

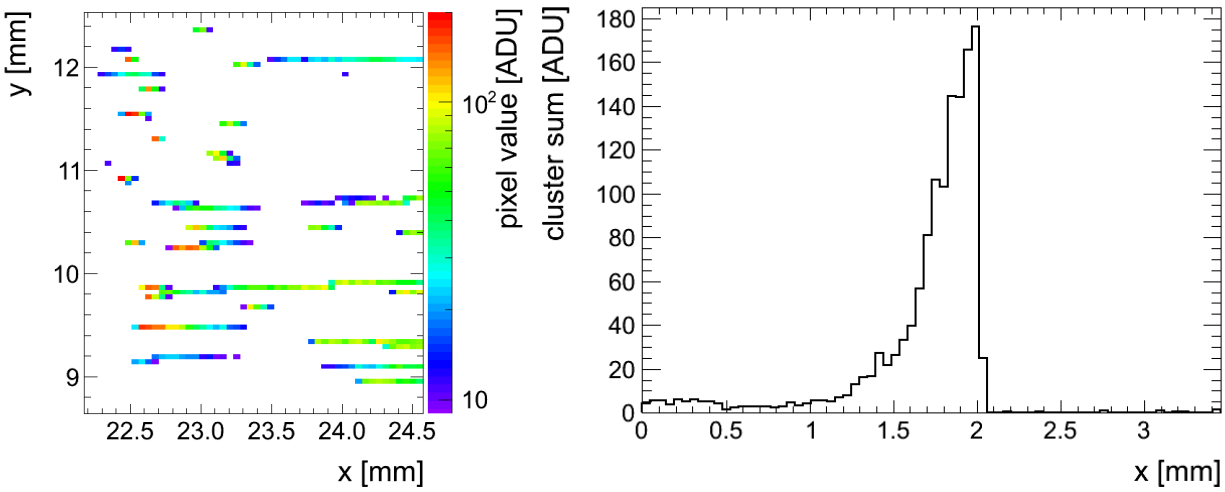

(a) (b)

Figure 6.20: **Depth dose measurement**
a) Two–dimensional track distributions of 20 MeV protons, incident from the right under a grazing angle $\alpha \approx 0°$.
b) Projection of a single proton track shows the typical Bragg curve characteristic.

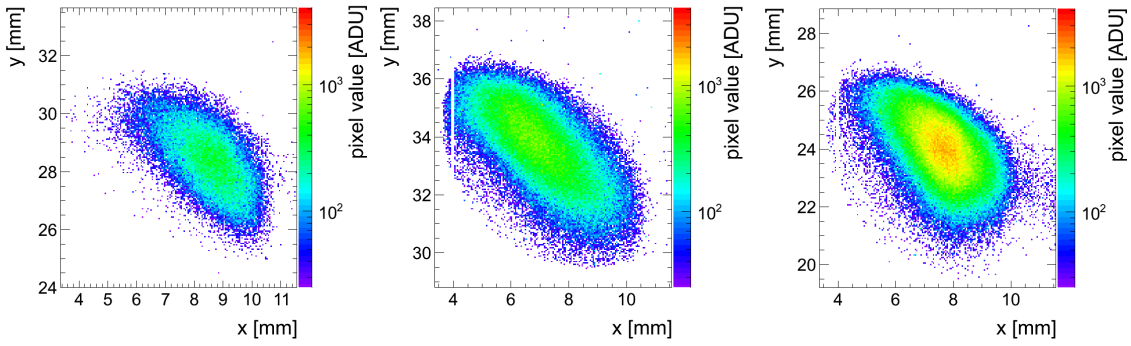

(a) (b) (c)

Figure 6.21: **Snapshots of single proton pulse**
Two–dimensional beam spot images in pulsed beam mode with pulse fluences of approximately $4 \cdot 10^4$ (a), $4 \cdot 10^6$ (b) and $5 \cdot 10^6$ (c) protons/cm^2 and pulse.

Pulsed irradiation mode

The *RadEye* sensor has been tested under pulsed beam conditions with 20 MeV protons. Pulse intensities range from few hundred up to $2 \cdot 10^6$ particles/cm^2 (fig. 6.21). Single particle discrimination, required for cluster analysis, is not possible within the central region of the beam spot. However, only the integrated signal intensity, in the following referred to as pulse height, is relevant in pulsed beam mode. Data have been analysed by a simple hit analysis of background corrected images, summing all values of responding pixels to yield a value for the total signal intensity in each image. The corresponding particle number per pulse has been determined according to eq. 3.5. Average beam current fluctuations contribute about $\pm$ 5 % uncertainty in particle number.
Fig. 6.22a shows the average intensity plotted against the particle number per pulse. The integrated signal of all responding pixels increases linearly with pulse intensity. The gradient of the regression line, fitted through the origin, yields a single proton response of 13.29 ± 2.00 ADU. This value is in good agreement with the result obtained before in continuous mode of 14.29 ADU for a proton energy of 15 MeV. The ratio of these single response values agrees with the ratio of related energy loss values. The excellent agreement of both single response values, furthermore, shows the very similar properties of sensor modules, as different sensors have been used in continuous and pulsed beam mode.
A plot of the total signal intensity against the fluence is depicted in fig. 6.22b. To calculate the fluence from particle numbers per pulse, an average beam spot size has been determined for each intensity level. Fluctuations in beam spot size yield large uncertainties in fluence determination and a large spread of intensity values due to the resulting fluctuations in pulse intensity. In particular for low fluence irradiations large beam spot size fluctuations were observed, which are responsible for deviations of low fluence data from the linear regression fit. Deviations of data set '*pulsed 02*' are more pronounced. They are attributed to large pulse to pulse fluence fluctuations due to technical problem with the pulsing system at that time.

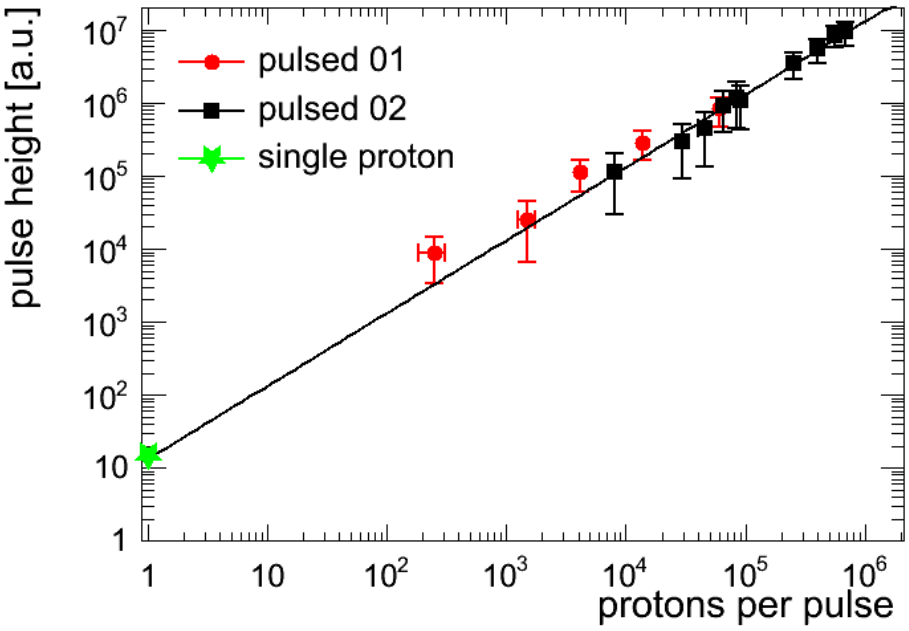

(a)

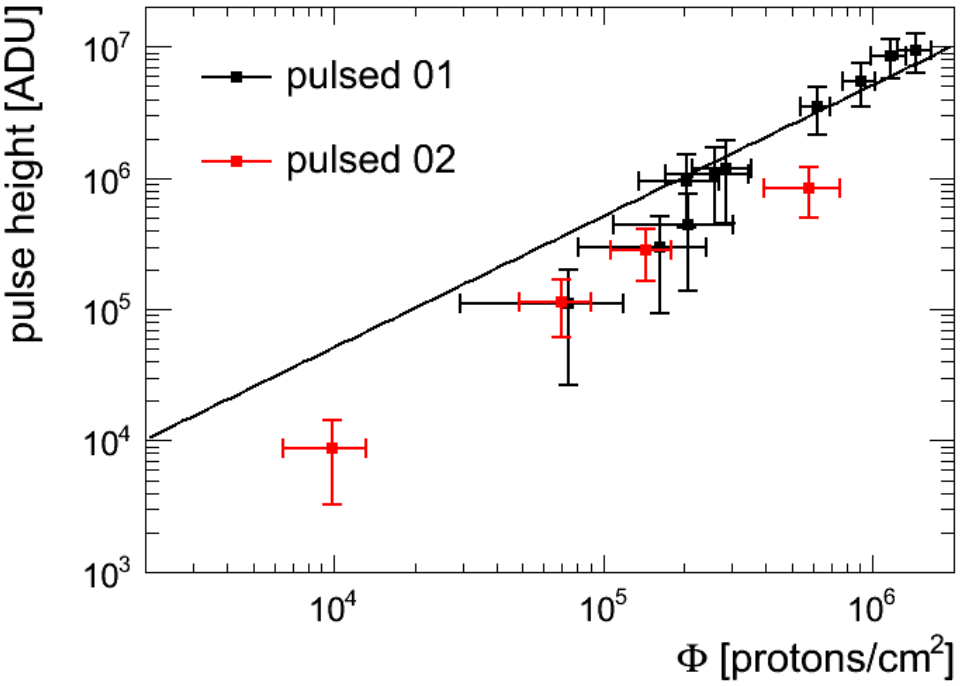

(b)

Figure 6.22: **Response to pulsed beam mode**
The RadEye system shows a linear response with increasing particle number per pulse (a) and corresponding fluence (b). Solid lines represent a linear fit through the origin for both data sets.

Radiation damage

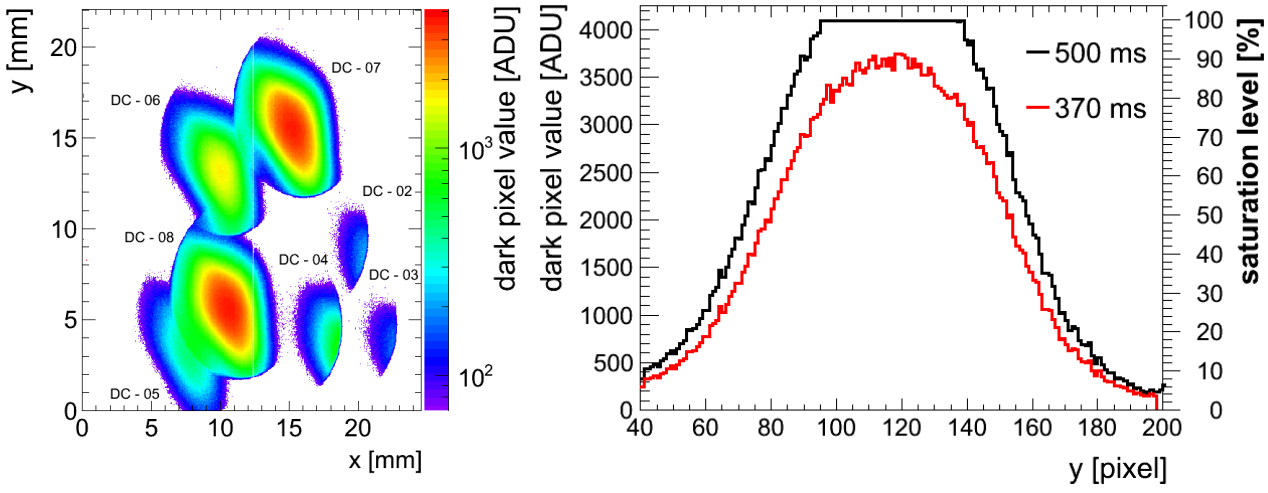

(a) (b)

Figure 6.23: **Radiation damage**
a) Two dimensional distribution of damaged areas, corresponding to a fluence range from $4 \cdot 10^9$ *(DC–02) to* $6 \cdot 10^{10}$ *(DC–07, DC–08).*
b) Profile through the central damage region of damage DC–07 (dashed line in sub–figure a), drawn for two different integration times.

To investigate the sensors radiation hardness, a continuous irradiation with protons of 20 MeV energy has been accomplished. Fig. 6.23a shows a two–dimensional distribution of the dark current after damage measurements with a maximum fluence of $6 \cdot 10^{10}$ protons/cm^2 (DC–07). Although the central region of DC–07 appears saturated when measured with an integration time of 500 ms, decreasing the integration time by only 130 ms, shows no saturation of any pixels any more (fig. 6.23b) and, hence, no dead pixels.

Current measurement by an FC and exposure time define the number of incident particles, the corresponding particle fluence can be calculated from an additional knowledge of the size of the beam spot. For DC–02 to DC–05, the beam spot was not centred in the small vacuum exit window. As a result it is not possible to calculate the particle flux on the detector from the current measurement with the FC. In the course of the measurement, the beam position has been corrected. DC–06 to DC–08 allow an analysis of the damaged area, as fluence calculation is possible for these spots. Additional damage levels, corresponding to integrated fluence levels of up to 10^9 protons/cm^2 have been deduced from pulsed measurements. Fig. 6.24 shows the average dark pixel value, measured in central damaged regions of pulsed and continuously irradiated areas, plotted against proton fluence. The dark pixel values, which is a measure of the leakage current, shows a strong exponential increase with fluence, indicating the dominance of ionization related damage.

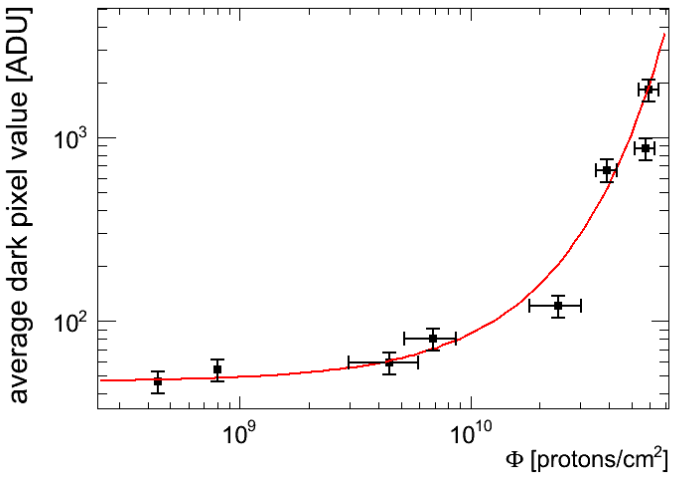

Figure 6.24: **Radiation damage of *RadEye* detector**
The proton dose in terms of fluence Φ has been accumulated in continuous and pulsed beam mode. The dark pixel value increases exponentially with accumulated proton dose.

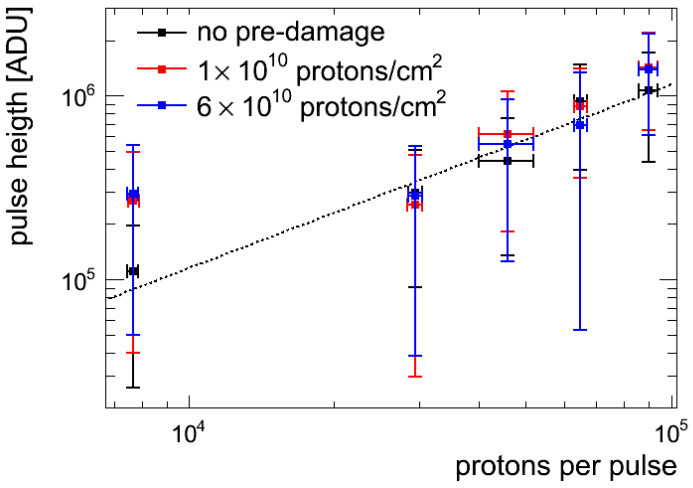

Figure 6.25: **Pulse response in damaged areas**
The pulse height in different pre–damaged areas was measured for different pulse intensities and compared to the response of an undamaged region. A linear fit of the data related to the undamaged region is applied as guide to the eye (dashed line).

Detector response in pre–damaged regions with limited dynamic range, has been investigated under pulsed irradiation with up to 10^5 protons per pulse. Average pulse height, obtained after background subtraction, are compared with pulse response in undamaged areas for different pre–damage levels ($1 \cdot 10^{10}$, $6 \cdot 10^{10}$) (fig. 6.25). No significant response difference depending on damage level is visible within the investigated fluence range.

6.3.2 Experiments at the DRACO Laser Facility

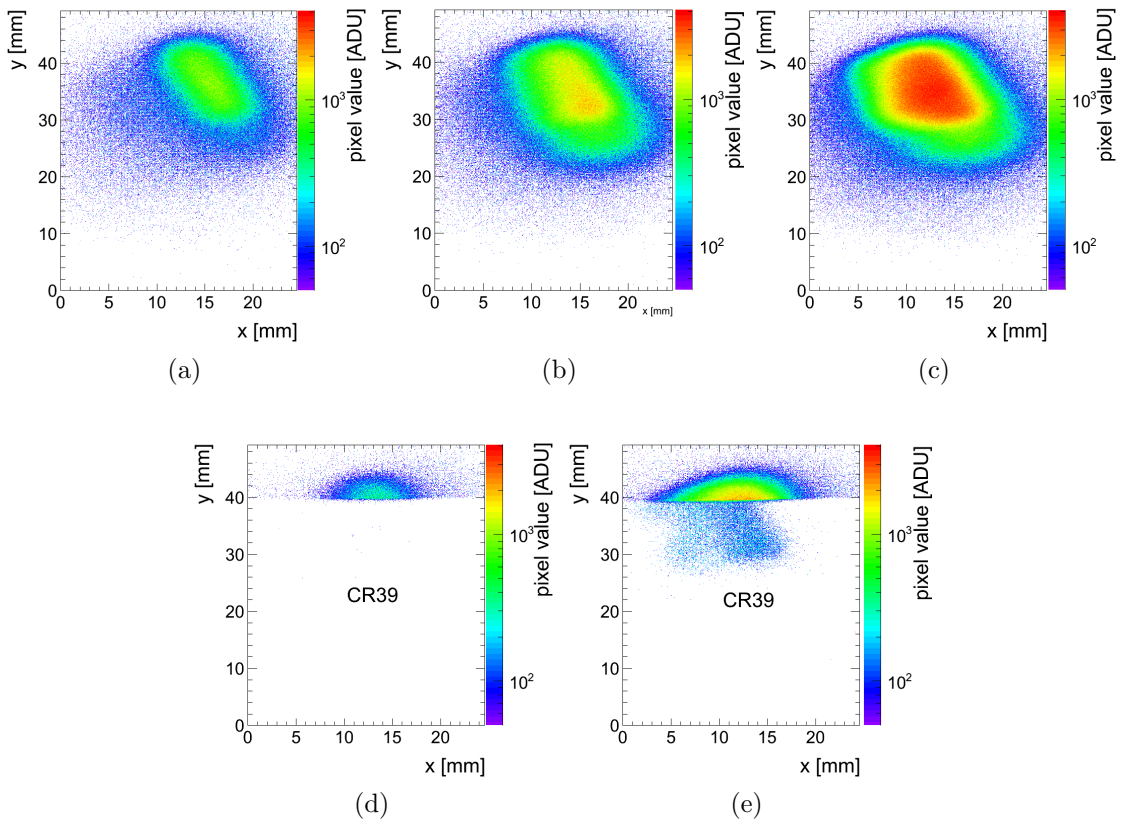

Figure 6.26: **Measurements at the DRACO laser**
Series of laser shots without (a–c) and and with (d–e) CR39 in front of detector, showing strong fluctuations from shot to shot. Some energetic protons are able to pass the CR39 (e).

The first test of the detector in a laser–accelerated proton beam has been accomplished at the DRACO laser. The DRACO system was chosen to investigate the detector operation in the laser environment as it offers a higher intensity as the ATLAS laser. Any possible problems related to EMP are, hence, expected to be more pronounced for this laser system. The detector was mounted in the IDOCIS chamber behind an energy selection system (sec. 3.2.4). Fig. 6.26a–6.26c shows subsequent shots with repetition rates of few seconds on the detector system. A broad energy distribution from 3 to 20 MeV is present at the detector site and related to large intensity fluctuations from shot to shot.

The IDOCIS setup was optimized for the Dresden cell irradiation experiments, where cell holders have been rotated during irradiation to obtain a homogeneous dose distribution on the cells [188]. A high energy resolution at the cell plane, was therefore not required in these experiments, as the cell rotation cancels the energy–coordinate relation on the cell plane, anyway. Although the detector position and, hence, dispersive relation was not changed during the test with the *RadEye* system, the energy resolution is not sufficient for a quantitative analysis of the data.
The energy distribution of protons on the CR39 surface does not generate etchable tracks. However, some proton distributions measured by the *RadEye* sensor when partially covered with CR39, show a clear signal in a sensor region, that was covered by the CR39 (fig. 6.26e). According to *SRIM*, a minimum proton energy of about 11 MeV is required to pass a 1 mm thick plate of CR39. No proton tracks are visible on the backside of the CR39, which is not understood at present. However, the automatic track detection system had severe technical problems during that time. A repetition of the CR39 analysis is, therefore, required, but not yet accomplished.
The average background level of unexposed frames correspond to 1.4 % of the maximum pixel value. Unexposed areas in images with laser–accelerated proton signals do not show any major background increase, e.g. from EMP.

6.3.3 Experiments at the MPQ ATLAS Laser

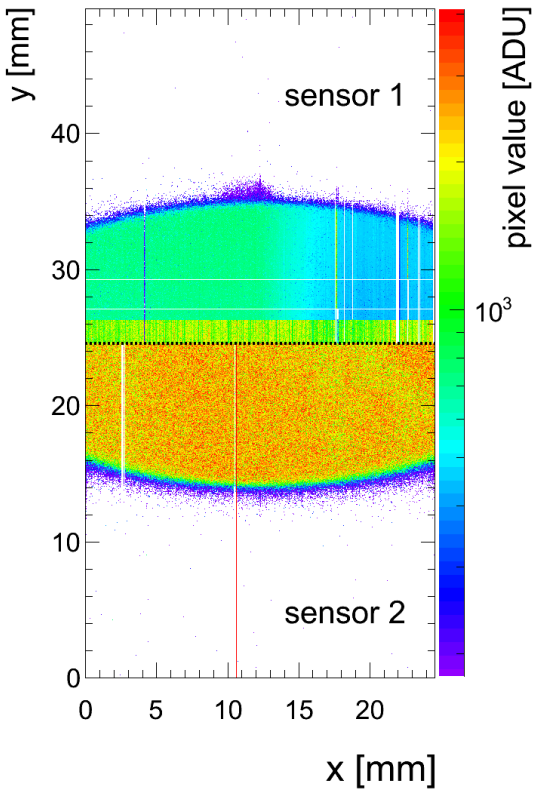

Figure 6.27: **Measurement in a mixed radiation field at the ATLAS laser** *For the first test at the ATLAS two low grade sensor modules have been applied. The dashed line marks the border of both sensors. Edges of the exposed area are defined by the entrance flange of the vacuum chamber (y–direction) and sensor dimensions (x–direction). Large differences of the pixel values within the exposed area and particularly for different sensors are attributed to the low quality of these sensors.*

In Tandem measurements, the *RadEye* sensor has shown to have a linear energy response of the applied particle flux below the saturation limit. Furthermore, no EMP induced problems have been observed at the DRACO laser. Based on these results, the detector system was further tested at the ATLAS laser.
In a first test at the MPQ, the vacuum chamber of the detector system was mounted instead of the spectrometer. Therefore, no particle filter acted in front of the detector and the two tested *RadEye* sensors were exposed to a mixed radiation field (fig. 6.27). The response of the overall system is non–uniform due to a significantly different sensitivity of the sensors. Low grade sensors with high noise levels have been used for this first test in a mixed radiation field, as no quantitative analysis of the data was possible for this proof–of–principle experiment. No saturation was observed for *sensor 1* which has a significantly lower noise level compared to *sensor 2*. However, although no information on particle as well as energy distribution can be obtained from this first measurement, it clearly demonstrates the suitability of the system to be operated in close vicinity to the laser–plasma interaction where the highest EMP levels are expected.

Calibration with the wide angle spectrometer

In Tandem measurements, the detector response was investigated in an energy range which is presently not feasible with the ATLAS laser accelerator. Therefore, a cross–calibration measurement with CR39 for low proton energies in the 1–3 MeV range was directly accomplished in a laser–accelerated proton beam using 5 to 10 nm DLC foils.

Measurement were carried out in vacuum, with the detector system placed behind the

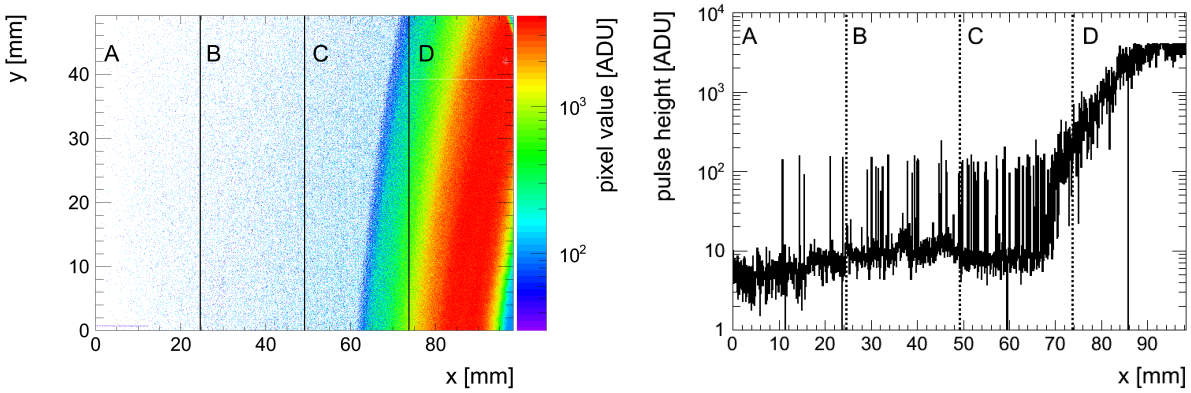

(a) (b)

Figure 6.28: **Measurements with the wide angle spectrometer**
a) To cover a large area of the WAS, four sensors have been operated in parallel. Solid black lines mark the border of individual sensors with corresponding read–out channels labelled as A–D. The proton energy decreases with x and increase with y.
b) Profile along the x–axis, averaged over 10 pixels in y–direction. No sudden jumps of the detector response are visible at the sensor boundaries, marked by dashed lines.

wide–angle spectrometer (WAS) where particles enter through a 0.3 mm wide and 140 mm long slit. To cover an as large as possible energy range, four sensors were employed, tiled at each other at their long sides, resulting in a sensitive area of 50 mm × 100 mm (fig. 6.28a). A 11 μm thick aluminium foil in front of the sensors served as light shield. Carbon ions with typical energies below 2 MeV/u but also protons with energies less than 1 MeV are blocked by the light shield, thus also acting as a particle filter. Not only unwanted ion contributions are stopped by the aluminium foil, but also the majority of uncharged particles such as low–energy X–rays, that are likewise produced during the laser–plasma interaction. As these particles are not deflected within the spectrometer, their signal usually marks the baseline of proton energy and detector coordinate.
A typical hit distribution after background correction is depicted in fig. 6.28a, with proton energies increasing to the left and to the top, respectively. No signal attributed to uncharged particles is visible on the detector. Therefore, the cut–off of the proton spectrum in the low–energy region, corresponding to an energy of 1 MeV, is used to establish the correct energy–position relationship required for data analysis by means of the WAS energy dispersion relation matrix (fig. 6.29).
During data taking for background correction, the sensor at read–out position B showed

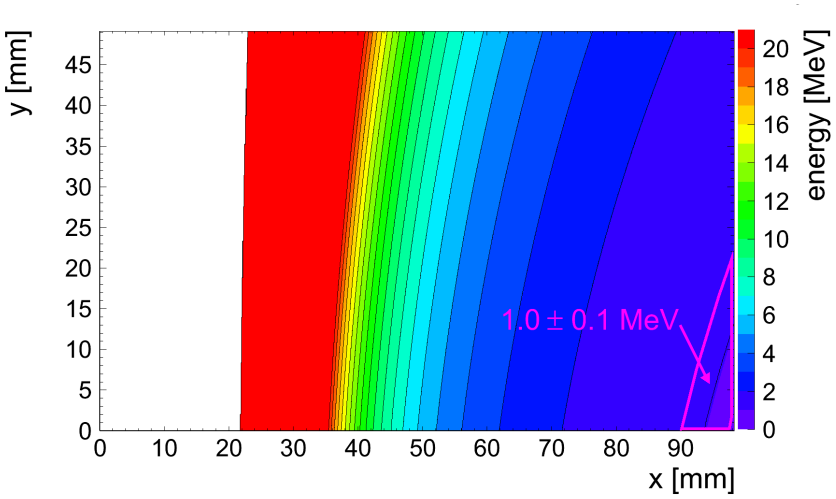

Figure 6.29: **Energy dispersion relation of the wide angle spectrometer**
The coordinates x and y represent spectrometer coordinates in the dispersive plane, the energy is colour coded. The framed area shows the deflection region that corresponds to an energy of 1.0 +/- 0.1 MeV, which is typically used for assignment of detector and spectrometer coordinates.

about a factor of two lower noise level compared to the sensor at read–out channel D, were the main ion signal is detected. Later tests with different read–out electronics (B01, B02) for different sensors have shown a dominant influence of the read–out channel on the noise level. Nevertheless, even the maximum noise levels correspond to less than 3 % of the saturation value of a pixel, showing that the channel dependency is measurable, but, still, only a small effect for unexposed images. The main proton signal covers two sensors, C and D. Channel non–uniformities have to be taken into account for a correct determination of the detector

system's response. However, no sudden changes in signal level are visible at the junction of adjacent irradiated sensors, which becomes more clear when looking at a profile along the x–axis (fig. 6.28b). The applied background correction, is, therefore, in principle able to compensated the effects of the observed channel non–uniformity in dark images to a large extent.

Fig. 6.30 depicts pixel value spectra for different energy ranges of 100 keV width, each. All

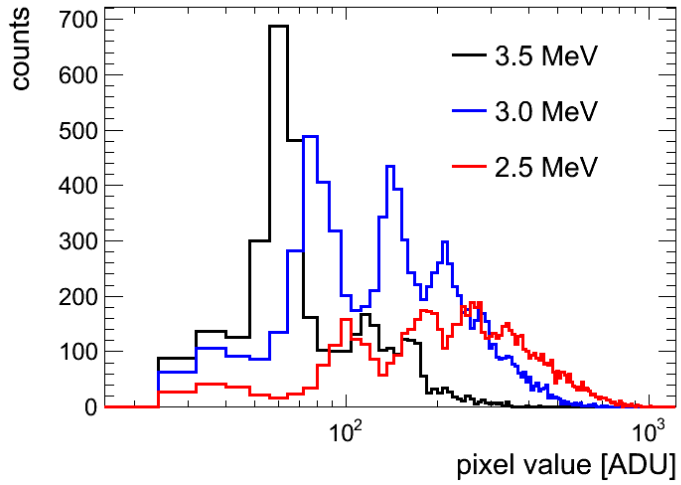

Figure 6.30: **Pixel spectra of different energy bins**
Pixel spectra shift according to the energy loss with increasing proton energy to lower pixel values. The multiplicity or proton hits per pixel increases as expected for an exponentially decaying proton spectrum with decreasing particle energy, indicated by the height of individual peaks.

spectra show a sequence of peaks that can be related to the *average* number of proton hits per pixel. Although each pixel can only be hit by an integer number of protons, the number of proton hits per pixel within an energy bin usually differs from pixel to pixel, yielding an average proton hit number per pixel and energy bin. The corresponding pixel value spectrum is a superposition of all hit distributions associated with integer proton hits per pixel (e.g. n, n+1, ... hits per pixel, $n \in \mathbb{N}$). Peak positions are, therefore, not necessarily associated to multiple integers of the single hit response within the corresponding energy bin. However, all peak positions shift with increasing energy to lower pixel values as expected due to the associated lower energy loss. The probability of multiple proton hits decreases with energy due to the typical decay of the laser–accelerated ion energy spectrum towards high energies. This is mirrored by the peak content, that increases for higher order peaks with decreasing energy.

Each spectrum has been fit by a sum of 4 Landau distributions to obtain the single proton response for the corresponding energy or, rather energy loss. While all other fit parameters of the Landau sum were independent from each other, the most probable values were related by the ratio of 1:2:3:4, to account for the fact that each pixel can only be hit by an integer number of protons. Values for the energy loss within the sensor's sensitive volume have been determined by a *TRIM* simulation. Errors of the signal response are associated with the σ

value of the Landau distribution of the single proton hit. The uncertainty of the energy loss accounts for the finite width of the energy bin as well uncertainty of the depletion width which is assumed to be 5 %.

The response signal (pixel value), which corresponds to the most probable value of the fitted

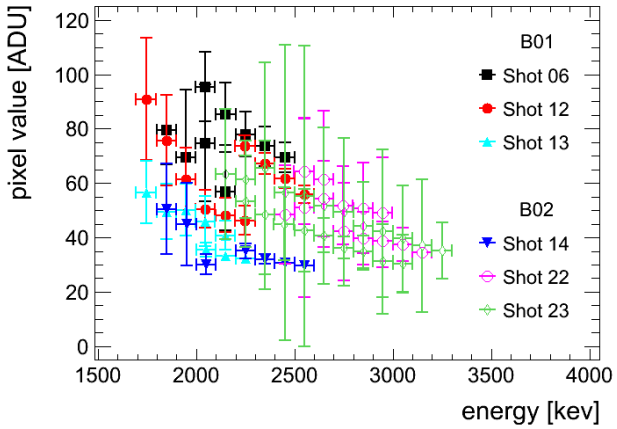

Figure 6.31: **Energy dependency of the single proton response**
The energy corresponds to the lower energy of an analysed energy range of the proton distribution of 100 keV width. Average pixel values are obtained for these energy ranges as MPV of Landau fits of corresponding pixel spectra. Data of a sequence of 6 laser shots have been recorded with different read–out electronics (B01, B02).

Landau distributions, is plotted against particle energy (fig. 6.31). It shows a decrease with increasing particle energy as expected by the related energy loss. The response signals show large fluctuations from shot to shot. For comparison of different shots, a correct relation of sensor coordinate and energy is essential. The relation of energy E and deflection d is non–linear, the change in energy per fixed deflection step Δ_d increases with the deflection distance and, hence, proton energy (fig. 6.29). As a result, there is a long deflection region that corresponds to low–energy proton energies of 1.0+/-0.1 MeV, used for assignment of detector and spectrometer coordinates. This is also visible in fig. 6.28a by the relatively broad junction area from low signal intensity to saturation starting in the lower right corner. The accuracy of the energy–detector-coordinate relation is, therefore, limited to +/- 1 mm, corresponding to an uncertainty in energy determination of up to 200 keV for a maximum proton energy of 3.5 MeV. The large spread of pixel response values from shot to shot is, therefore, attributed to these alignment uncertainties. No systematic dependence on read–out electronic or read–out channel can be deduced from this measurement. The pixel response value is plotted against energy loss for the sensor at position C (fig. 6.32a) and D (fig. 6.32b), respectively. Data of the Tandem calibration (fig. 6.18) are included for comparison. The data of all shots scatter around the extrapolated Tandem calibration fit, showing good overall agreement, although some shots show considerably large deviations from the Tandem fit. However, these deviations are likely attributed to the limited accuracy in energy determination, resulting in a large uncertainty of energy loss values.

For cross–calibration with CR39, one half of the detector was covered by a 1 mm thick plate

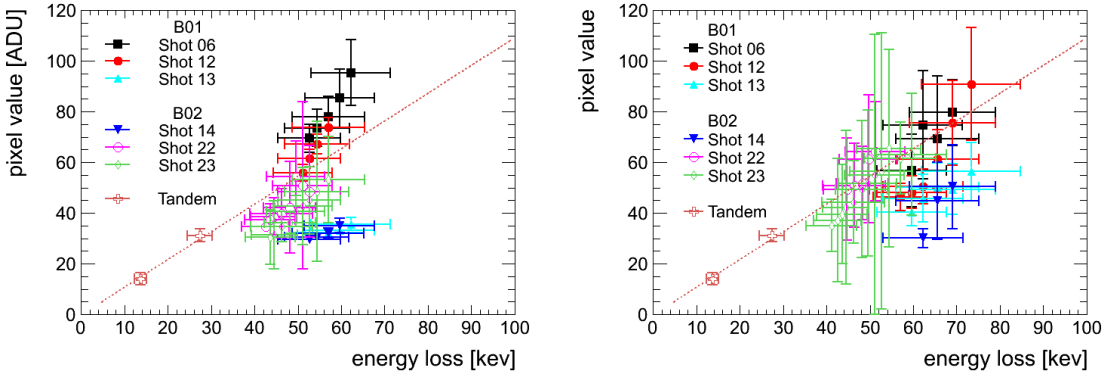

(a) (b)

Figure 6.32: **MPQ energy calibration**
The single proton response with respect to deposited energy is plotted for read–out channel C (a) and D(b) and different read–out systems. The Tandem calibration is included as guide to the eye. Different laser shots show large response deviations. However no clear dependence on the read–out system can be deduced for both channels.

of CR39. An average proton number was deduced for two different energy ranges with a width of about 0.4 MeV and average energies of $\sim$ 1.5 MeV and $\sim$ 2.0 MeV, respectively, from the CR39 measurement. To obtain a value for the average pixel response of each of the analysed energy bins, the integrated detector signal has been divided by the average proton number obtained from CR39. Only energy bins completely lying within sensor D have been considered. The resulting calibration is plotted in fig. 6.33 together with the Tandem calibration and a single data point from an α irradiation (sec. 6.3.1). From the MPQ data an energy to pixel value conversion factor of (1.13 $\pm$ 0.12) ADU/keV is determined, which is in good agreement with the Tandem conversion factor of 1.09. A linear fit through the origin yields a single conversion factor of (1.11 $\pm$ 0.09) ADU/keV for the combined data sets of Tandem and MPQ calibration.

Measurements with the small angle spectrometer

Fig. 6.34b shows a typical hit distribution obtained with the small–angle spectrometer (sec. 3.2.3). For these measurements operation of only two sensor elements, tiled to each other at their smaller sides, offers sufficient sensitive area, due to the small lateral width of the proton distribution. The entrance of the spectrometer is defined by an aperture of 2.5 mm in diameter. As target 20 nm thick DLC foils were used.
Only protons with energies exceeding $\approx$ 4 MeV are able to reach the detector. Maximum proton energies of up to 7 MeV were achieved in this experiment, with an average of 6.0$\pm$0.5 MeV for a sequence of 8 shots. In this measurement the zero point, attributed to uncharged particles is visible, although the same aluminium foil thickness was used for light shielding.
For small energy regions of 0.5 MeV width, each, the proton number has been deduced in the central part of the proton focus over a lateral width of 10 pixels (480 μm). The particle

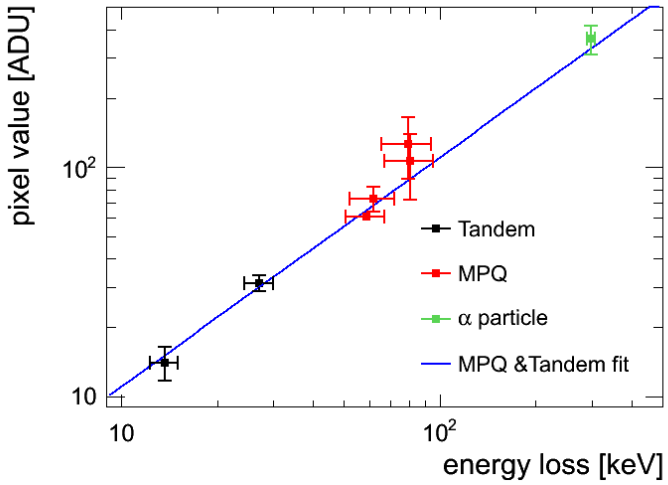

Figure 6.33: **Energy calibration at the ATLAS laser**
MPQ data points are obtained from a CR39 cross–calibration. Results of the previous detector calibration in a continuous proton beam at the Tandem as well as from irradiation with a α source are included for comparison. The solid line represents a fit of the combined MPQ and Tandem data.

number within this analysis region can be calculated from the integrated detector signal, which corresponds to the total energy deposited by all protons. The combined Tandem and MPQ calibration has been used to convert the detector signal into an energy, which is divided by the average energy deposition ΔE of a single particle within this energy range to yield the particle number. The fit uncertainty introduces an uncertainty in particle number determination of roughly 8 %. This is a negligible contribution, as the main limitation in the accuracy of proton number determination is the uncertainty related to the deposited particle energy. The energy resolution within the analysed region defines the accuracy of the ΔE determination. The spectrometer resolution and, even more important, uncertainties in the correlation of spectrometer and detector coordinate, which can yield an uncertainty of energy determination of the order of ± 100 keV, have to be taken into account as well as the energetic width of the analysis region.
Proton spectra obtained from this analysis are depicted in fig. 6.34b. The spectra have been fitted by exponentially decaying functions to apply a guide to the eye. However, proton numbers of individual spectra differ by factors of up to two, thus, clearly demonstrating large shot to shot fluctuations that are one of the main problems of laser–ion–acceleration, today.

6.3.4 Experiments at the RPTC

Application of laser–accelerated protons for radiation therapy is widely discussed, although maximum feasible ion energies of high–repetition rate systems still need to be increased by more than a factor of ten. In this field, quantitative particle detection is mandatory with an accuracy better 5 %. An additional test of the detector system was accomplished in a proton beam of about 200 MeV energy. Two sensors, with their long sides facing each other,

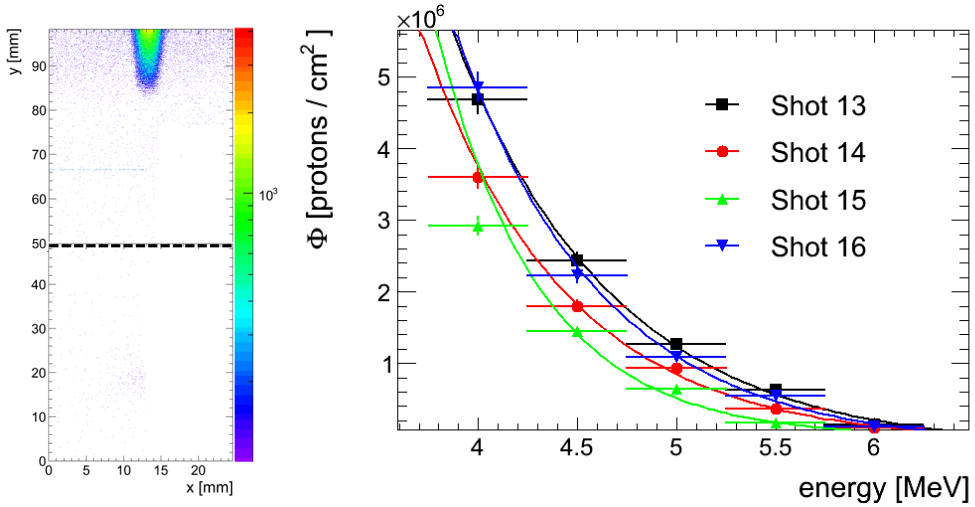

(a) (b)

Figure 6.34: **Measurement with the small angle spectrometer**
a) Typical two–dimensional proton distribution measured by two sensors, tiled at their small sides. The junction of both sensors is marked by the dashed line. b) The energy spectra of different shots show the typical exponential decay. Maximum energies and particle numbers fluctuate from shot to shot. Solid lines represent an exponential fit of the data.

were placed in plexiglas phantom in a depth of 50 mm. For this test, a dose of 0.33 Gy was deposited in a field of 50 x 50 mm^2.
The RPTC uses active dose delivery by magnetically scanning of a small pencil beam over tumour volume. In free running mode, with a read–out period of 370 ms, it is possible to monitor the scanning of the beam. However, central beam spot as well as overlapping beam edges are saturated. Only the rising edge of the pencil beam (Gaussian shape, σ =4 mm), visible at the boundary region, allows a measurement of the deposited energy (fig. 6.35). The width of the boundary regions corresponds approximately with the σ of the pencil beam.

6.3.5 Discussion 3

The dynamic range spans five orders of magnitude allowing single proton detection as well as single pulses of more than 10^6 particles/cm^2/ns. Offering the same dynamic range as IPs, the *RadEye* sensor is suited to replace these offline detectors.
The leakage current shows an exponential increase with proton fluence (fig. 6.24). Bulk damage, associated with displacement damage usually yields a linear increase in dark current. Radiation damage observed, here, is, therefore not dominated by bulk damage in the silicon. The detector is an active pixel sensor, containing a source follower build from three transistors (3T) within each pixel. For MOSFET structures positive charge build–up in the oxide layer is the main damaging mechanism. As a result a change in charge carrier density

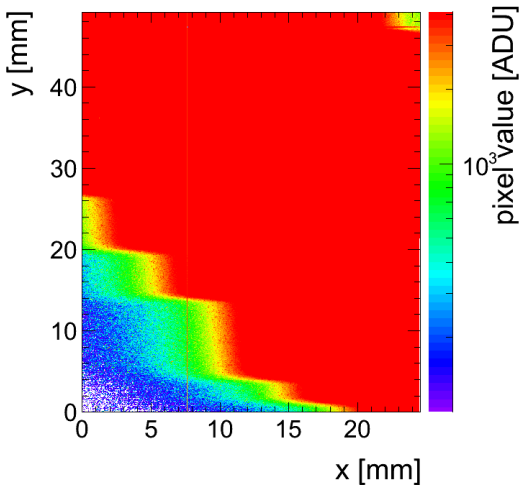

Figure 6.35: **Snapshot of scanned clinical proton beam**
The scanned area is almost completely saturated for a dose of 0.33 Gy, except for the boundary region corresponding to the rising edge of individual pencil beams(Gaussian with σ =4 mm).

in the depletion region leads to an increase in dark current [215]. Average dark signals exceeding pixel values of 2000 have been reported for the *RadEye* sensor when irradiated with doses exceeding 8 kR [215]. For the highest fluence level, corresponding to about 10 kR, average dark signals are of the same order of magnitude.
Measurements at the DRACO laser demonstrate the ability to operate the detector system with repetition rates of about 0.5–1.0 Hz, visualizing difference in energy spectra on a shot to shot base. Operation of the detector did not show any signs of disturbance due to EMP or as background levels of unexposed and exposed images are comparable even in close vicinity to the laser–target interaction point.
The detector shows channel–to–channel variations in unexposed images. However, proton signals do not show the same systematics as noise levels, when an appropriate background correction is applied. A crucial point in all these measurements is the assignment of detector and spectrometer coordinates. In case of the WAS, the low–energy range is characterized by a cut–off of the distribution due to protons stopped in the light shield. This junction is smeared over several tens of pixels due to range straggling. Even more important, typical foil thickness variations of 10–15 % will shift the cut–off energy of $\sim$ 100 keV. Energy and stopping power values shift accordingly. All deviations that have been observed for measurement with the WAS are primarily attributed to these uncertainties in the energy determination. No significant dependence of the response from read–out electronic or sensor can be deduced, which is also supported by the fact, that profiles across sensor junctions of background corrected images do not show any large jumps at the sensor boundaries.
The cross–calibration with CR39 shows an excellent agreement with the Tandem calibration. The accuracy in particle number determination is primarily limited by the energy resolution of the spectrometer and, even more important the accuracy of the mapping of detector coordinate and energy.

The dynamic range of the detector is not sufficient to handle typical therapeutically used doses. A water–equivalent dose of 330 mGy corresponds to a particle fluence of about $5{\cdot}10^8$ p/cm^2 with respect to a proton energy of 200 MeV. For 20 MeV protons, a saturation fluence of 10^7 has been determined. Accounting for the stopping power ratio of 20 and 200 MeV protons, the maximum detectable dose is only 26 mGy.

7 Discussion and Conclusion

7.1 Discussion

The main objective of this work was the development of an online detection system, able to replace the commonly used IP detector in the dispersive plane of the spectrometer. Hence, similar response of the online system with respect to dynamic range, spatial resolution and lifetime as the presently used IP are minimum requirements that have to be fulfilled. In addition, reliable operation of the system in the presence of a certain EMP level during laser–plasma interactions is mandatory.
The measured properties of the *RadEye* system are discussed in view of these requirements and compared in particular to standard IPs as well as online detection techniques which have been tested for laser–accelerated protons by other groups.

7.1.1 Comparison of image plate and pixel detectors

detector system	**IP**	***Kappa DX–4***	***Timepix***	***RadEye***
minimal sensitive area [cm^2]	20 x 25	0.7 x 0.7	1.4 x 1.4	2.5 x 5.0
sensitive area expandable	yes	no	yes	yes
pixel size [μm]	50	7.4	55	48
single particle detection	limited	yes	yes	yes
saturation level (20 MeV p) [p/cm^2]	10^7–10^8	10^7	10^5	10^7

Table 7.1: **Key characteristics of IP and all pixel detector systems**

Spatial resolution and area coverage The energy resolution of the spectrometer–detector system depends on both, the spectrometer resolution, but also on the spatial resolution of the detector. Image plates are typically scanned with pixel sizes of 50–100 μm. As all investigated pixel detectors offer the same, or even smaller pixel sizes the energy resolution of the combined system should remain unchanged.
For use with a spectrometer, a sensitive area of several tens of cm^2 is required. IPs can easily cover such an area and additionally have the advantage that they can be cut into pieces of any size. The sensitive area of a pixel detector is a fixed parameter of typically considerably less than 10 cm^2. However, some detector geometries allow to increase the sensitive area by tiling of additional sensor modules. This is not an option for the the CCD camera, *Kappa DX–4*, with a sensitive area below 1 cm^2, which is, therefore, not suited as sensitive element in a Thomson spectrometer. Attachment of additional sensors is possible in case of the *Timepix* chip with slightly higher sensitive area ($\sim$ 2 cm^2). In one dimension

limited to twice the side length, the second dimension, in principle, can be expanded to any size without geometrical constraints. A minimum number of eight *Timepix* chips would be required to cover the deflection area of the small–angle spectrometer, considering the same setup as for experiments presented in section 6.3.3. In this case, simply the costs of such a system (> 100 k€) set a limit. Only the *RadEye* sensor, offering 25 mm x 50 mm side length and the option to tile further sensor modules a three of it's sides, is, therefore, able to compete at reasonable costs.

Dynamic range and energy resolution A typical ion spectrum from laser–acceleration is characterized by an exponential decay with increasing ion energy: particle numbers easily exceeding 10^7 in the low–energy part of the spectrum going down to single particles in the high–energy tail.
Depending on IP–type 10^7 (MS) –10^8 (TR) protons/cm^2 can be detected by the used scanner system (*FLA–5100*) at a proton energy of 20 MeV. Although IPs offer a high sensitivity and are in principle sensitive to single ions, the SNR is typically not sufficient for single ion discrimination from the background.
All pixel detector systems allow the detection of single ions. Using the *Timepix* device, the energy deposition of the incident particle can be measured with an excellent energy resolution of 1.7 %. Both commercial systems offer a limited energy resolution of about 50 %. Being designed for visible light detection, they have a sensitive thickness of only about 2 μm, where only a small portion ΔE of the incident particle's energy will be deposited, resulting in limited energy resolution. Nevertheless, discrimination of single and double proton hits in a single pixel was demonstrated. For any detector placed behind a spectrometer the energy of a particle is defined by its spatial coordinate on the detector. A good spatial resolution is required to obtain a good energy resolution for the combination of spectrometer and detector but a good energy resolution of the detector itself is not necessary.
The sensitive thickness, however, also sets a limit on the energy of the detectable particles, at least for single ion detection. In case of the *RadEye* sensor an ADU level (pixel value) of 14 has been determined for a 15 MeV proton. Extrapolation of the energy calibration yields a pixel value of about 2 ADU for an incident 200 MeV proton. This value is considerably lower than typical noise fluctuations of about 7 ADU, which set an upper limit of roughly 35 MeV for the maximum energy for single proton detection. Detector cooling is an efficient means to reduce the detector noise and could be used to increase this limit to even higher particle energies.
For *Timepix* a minimum energy deposition of about 6 keV within the sensitive thickness of 300 μm is required for single ion detection, allowing to detect single protons with a few hundred MeV energy. Hence, *Timepix* offers the biggest potential for single particle detection in the high energy tail. However, this system saturates already for incident particle fluence of about $2.5 \cdot 10^5$ protons/cm^2 and is, thus, not suited for a laser–ion diagnostic system.
Both commercial pixel detectors, *RadEye* and *Kappa DX–4*, have a maximum saturation level of about 10^7 p/cm^2 (20 MeV), the same as the MS–type IP. Although limiting the spectroscopic capability of these devices, the thin depletion layer is an advantage with respect to the saturation level. The sensitive thickness of a detector has two sides: thick sensors

offer a good energy resolution but small dynamic range while the opposite is true for thin sensors.

Radiation hardness The performance of any silicon–based detector degrades when exposed to heavily ionizing radiation. In particular for particles with high stopping power, such as heavy ions or low–energy protons, detector lifetime can be severely limited depending on particle flux and dose. For the present state of affairs, proton energies at the ATLAS laser do not exceed 10 MeV, which will change with the upgrade of the laser system. All investigations were, therefore, also performed with regard to expected higher proton energies at the upgraded system, specifically the radiation hardness studies at 20 MeV energy. Radiation damage has only been investigated for the commercial pixel detector systems. The *RadEye* sensor has a residual dynamic range of about 50 % after a dose of $6{\cdot}10^{10}$ protons/cm^2 (20MeV) and still shows a linear response to proton fluences up to 10^5 protons/cm^2. The time period of usability (i.e. lifetime) of a detector is defined by the minimum residual dynamic range that is required for an experiment. For the detection of up to 10^7 p/cm^2 at 20 MeV energy, only 10 % dynamic range degradation are tolerable, yielding to roughly 3000 pulses in case of the *RadEye*. About an order of magnitude lower number of pulses is obtained for the *Kappa DX–4* system and highest amplification setting, which can be increased by the reduction of the amplification factor. If a smaller level of residual dynamic range is tolerable, the total proton dose can be even further increased for both systems.
No damage studies have been made for IP detectors. According to the manufacturer recommendations on re–usability, a number of 1000 shots is given for the MS–type IP, which is comparable to the number of shots that can be detected by the *RadEye* system. The re–usability of the TR–type IP is further limited by mechanical damage due to the lacking of any protective cover on top of the sensitive layer.
None of the irradiated detectors showed completely dead pixels after irradiation, even in laser–acceleration experiments. However, for measurements with the wide–angle spectrometer in the proton energy range of 1–4 MeV, an increase in the dark current level was observed after few shots. The need to replace the detector is triggered by the minimum tolerable dynamic range. Low–energy particles yield higher damage and at the same time also higher signal levels due to their higher LET. Both factors increase the replacement rate drastically. The saturation level decreases correspondingly. However, the most interesting part of a laser–ion spectrum is the high–energy tail, where radiation damage as well as saturation is less problematic. To block contributions from very low–energy protons, which possibly also saturate the detector, is a reasonable approach with respect to detector lifetime. The lifetime issue will relax with increasing particle energies, which are currently not available. Nevertheless, different techniques exist to compensate radiation damage to some extent. A simple method to decrease the noise level during operation is cooling, as the dark current is known to show a strong temperature dependence. Controlled annealing cycles, performed once a specified dark current level is approached, can also help to increase the detector lifetime. The potential of both techniques has to be studied for the presented detector systems, in future.

All in all, it is obvious, that only the *RadEye* sensor is able to compete with the IP in

all respects and hence, has been chosen for the online diagnostic system. The response of this pixel detector based online detection system has been fully evaluated in the proton energy range of 8–200 MeV by means of conventional and up to 10 MeV at a laser–based accelerator. The use in laser accelerators shows no EMP problems, so far.

7.1.2 Comparison with other online detector systems for laser–ion diagnostic

Different types of online detectors have been investigated for laser–ion diagnostic such as MCPs coupled to phosphor screens [34, 104–106], scintillators [33, 38], ICs [36, 188, 209] and diamond detectors [209]. The *RadEye* system is, therefore, in the following compared to these directly competing detector systems.

MCP system

MCP based systems are often referred as single particle detectors, which is in principle true, as a single particle can generate sufficient signal in the MCP. However, for typical present proton energies of few MeV, the emission probability of secondary electrons is only few percent. The ratio of open channel area to total MCP area, typically about 60%, further limits the detection efficiency. For MCP in combination with phosphor screen and CCD camera, collection efficiencies of the camera lens and quantum efficiency of the CCD camera at the phosphor emission wavelength additionally have to be taken into account. For a typical MCP–based system, a detection efficiency of 0.7 % has, thus, been reported for a proton energy of 13 MeV which increases to about 10 % for 2 MeV [104].
All particles of a laser–accelerated ion pulse arrive within few hundred ps to ns. For MCPs that are operated in pulsed mode, an excited channel has a dead time of about 10 ms [100], the MCP saturation limit corresponds, thus, in a first approximation to the number of channels per cm^2. For typical channel diameters of 10 μm a saturation level of about 10^6 particles/cm^2 is calculated. Accounting for the low detection efficiency of MeV ions, the saturation limit shifts accordingly to higher levels, for instance for 2 MeV protons, it is about the same as for the *RadEye* detector.
The intrinsic spatial resolution of a single MCP is determined by the channel spacing of about 12–15 μm for a 10 μm channel diameter. Systems used in laser–ion diagnostic are based on a Chevron MCP coupled to a phosphor screen, with spatial resolution of 40–75 μm [105]. MCP and pixel detector, therefore offer similar spatial and related spectrometer energy resolution.
Considerable gain variations of individual MCP channels up to a factor of 3 have been reported [105, 216], limiting the overall accuracy in particle number determination to about 73 % [105]. The *RadEye* system measures the total deposited energy per pixel with a fit uncertainty of the channel to energy conversion of only 8 %. Assuming a negligible energy spread of incident particles on a per pixel base, the particles number determination is only limited by this fit uncertainty.
Operational requirements of pixel detector and MCP differ significantly. The *RadEye* detector allows operation in vacuum as well as in air, biased by a 6 V source. The MCP, on the contrary, requires a good vacuum of 10^{-6} mbar due to the applied high voltage.

MCPs are subject to ageing effects as gain drops with increasing radiation dose, thus limiting the lifetime of the device. 20% gain degradation have been reported for electrons and an accumulated charge of about 0.1 C/cm^2 [100]. Assuming a gain of 10^7 and single electron generation per incident proton, this value corresponds to a number of $6 \cdot 10^{10}$ protons/cm^2. For the pixel detector, a similar radiation dose yields to a dynamic range degradation by a factor of 2. However, this is only a minor disadvantage in view of the ease of use of the pixel detector compared to a MCP as well as cost of single *RadEye* sensor.

Scintillator

There are two different approaches for a scintillator based laser–ion diagnostic. The first approach, similar to MCP or the *RadEye* system, is a combination of spectrometer and scintillator screen monitored by an EMCCD camera [38]. The second uses stacks of scintillator plates, similar to RCF stacks, to measure the beam profile within different energy ranges in close proximity to the ion source (i.e. foil target). Two such systems are currently investigated, both based on thin organic scintillators with sub–mm thickness [33, 99]. The system described in [33] measures a two–dimensional profile, using three organic scintillator slices with different emission wavelengths, that are imaged by a gated ICCD (Intensified CCD). The second of these stacked systems images the light at the edges of the scintillator with the camera system oriented normal to the beam direction, allowing to determine the angular–resolved beam profile in one dimension for different energy ranges [99].
An important characteristic of organic scintillators, in particular for ion detection, is their LET dependence, resulting in a non–linear light yield with particle energy. Separate calibrations are required when different ion species have to be detected near the laser target.
In case of the scintillator stack approach, energetic electrons or X–rays are not spatially separated as behind a spectrometer. Particle discrimination is made by the use of thin scintillators (few hundred μm), which favour the scintillation light created by ions. In the high–energy tail, with low energy loss and particle number, thin scintillator thickness and typical light yield of 1 photon per 100 eV energy deposition results in weak scintillation light [28]. Therefore, (expensive) amplifying camera systems based on EMCCD or ICCDs have to be applied, which in principle allow single particle detection with their detection efficiency. In test experiments with C–ions, however, single ion sensitivity could not be demonstrated by the scintillator–spectrometer system [38].
All scintillator–based approaches still lack systematic investigations of the scintillation efficiency with respect to high instantaneous pulse flux as typical for laser accelerators. No information on saturation level are, therefore, given for these system.
The *RadEye* comes forward as candidate for a two-dimensional ion beam profiler because of it's large sensitive area. The feasibility to operate the system close to the interaction point was demonstrated at the ATLAS laser. However, the use as an ion beam profiler is only possible if, the dominant signal contribution is attributed to ions, which is presently unknown. The particle flux close to the source is considerably larger as behind a spectrometer and, furthermore, the majority of ions are low–energy. Saturation effects will, therefore, most likely rule out this possibility unless very low–energy ions will be blocked from the detector.

IC

So far, ICs have been only employed for relative dosimetry in cell irradiation experiments at the DRACO laser facility [36, 188]. For these measurements, the IC was calibrated against Faraday Cup or RCF due to dose–rate dependence of the IC for dose rates exceeding 1 Gy/minute [36].
Incomplete charge carrier collection because of recombination in an IC has to be compensated by a saturation correction. Investigations are still required to determine the validity of existing saturation correction protocols due to the high pulse dose of laser–accelerated ions [32, 209].
A direct comparison of IC and pixel detector is difficult in view of different application purposes. The IC is applied to measure the total dose in the laser–accelerated proton pulse, regardless of energy. No information is, therefore, obtained with respect to the ion spectrum. The dose is proportional to the deposited energy. Relative dose measurements are in principle also possible with the *RadEye* system but limited up to a dose level of about 26 mGy, which is considerably lower than what is feasible with an IC.

7.2 Conclusion

Ion acceleration with high intensity laser systems is an active field of research since the beginning of this century, when first results have been published. However, ion diagnostic within this context has achieved little progress over the past decade.
Many experiments still rely on non–electronic, integrating detectors such as CR39, IPs or RCF. All presented online systems were only tested at TW–facilities, where EMP disturbance is much reduced compared to PW–class lasers. Currently built PW–facilities such as PETAL plan their ion diagnostic based on non–electronic detectors as they expect strong EMP effects. Hence, calibrations of offline detectors are not only required for quantitative analysis of ongoing experiments but also for future experiments.
IP efficiency and fading curves show a strong dependence on the scanner system, therefore, requiring its own calibration for any individual combination of IP type and scanner model to obtain reliable, quantitative results. IP measurements within this work allow for the first time a quantitative, time–corrected analysis of proton spectra for the three different IP systems that have been used by the Munich laser–acceleration group. The possibility to extend the dynamic range of the IP system, which is limited by the saturation of scanner electronics, by multiple IP read–out was also demonstrated. For each IP system only IPs from a single batch were calibrated within the scope of this work. It is possible that the response of the IP system also varies with the IP batch as was shown for EBT2 films. The QA-procedure based on the ^{14}C-standard, which was introduced to check the stability of the IP system before an experiment, can also be used as a simple and fast test to determine batch-dependent response differences and decide if a re-calibration is necessary.
Cell and tumour irradiation experiments were accomplished to study high pulse dose rate effects from the biological point of view. Available proton energies of few MeV at the ATLAS laser made the realisation of the necessary dose determination difficult. All detectors

used for laser–ion diagnostic can be ruled out primarily by their water–equivalent thickness, except for ICs and EBT2 films. Air–filled ICs are used as transmission dose monitors in radiation therapy. ICs show a strong dose rate dependence as discussed above, in particular for pulse dose rates of few Gy as given in bio–medical experiments within this work. The IC could, thus, only be used to measure the relative dose per shot if previously cross–calibrated to an dose rate independent detector such as EBT2, provided the dose rate remains stable. This precondition is not given at a laser accelerator, as pulse dose fluctuations can not be excluded at the moment. To deliver minimum doses of 200 mGy within a single pulse, focusing permanent quadrupole magnets were used, yielding steep dose gradients on the cell sample because of the broad initial proton energy distribution. Measurement of the two–dimensional dose distribution with sub–mm spatial resolution was required as a consequence. EBT2 films, offering dose–rate independence and sub–mm spatial resolution, were, therefore, chosen for absolute dose measurements, although these films are known to show considerable quenching effects when exposed to low–energy protons. However, the feasibility of absolute dose determination in the low–energy regime was demonstrated, provided an appropriate calibration exists. For the same reasons, EBT2 films were also used for dose verification of the mouse tumour irradiation.
Stacks of RCF are used in laser–ion diagnostic to determine an energy resolved beam profile, where the energy resolution is defined by the sensitive thickness of individual films. As contributions of energetic electrons or X–ray are usually negligible and low–energy C–ions are typically stopped within the first film, the major signal is attributed to protons. As a consequence of the broad energy distribution of laser–accelerated protons, low–energy contributions are present in any energy slice. Knowledge of the energy dependence of RCF films, as presented for EBT2 films, is, therefore, also mandatory for quantitative film stack analysis. Systematic studies of the LET dependence for mono–energetic low–energy protons are currently not available for most of the RCF types used in these kind of stacks. EBT2 film response measurements over a wide energy range presented within this work, are, therefore also of use for the RCF stack based ion–diagnostic.
In particular the availability of high intensity laser systems with repetition rates up to 10 Hz but also advances in speed of the target preparation make non–electronic detectors inefficient in the near future. A compact, pixel detector based large area detection system was set up for combined diagnostic with a spectrometer. Independent measurements at a conventional Tandem accelerator and the ATLAS laser accelerator showed no dose rate dependence as well as linear pulse dose response of the device. It was demonstrated that real–time diagnosis behind a spectrometer is feasible with this system on similar terms as with IPs. The measurement accuracy is determined by uncertainties of the detector calibration as well as quality of the correlation of detector and energy coordinate, which showed to be the major limitation for IP as well as pixel detector. Improvements of the assignment are, therefore, required to allow particle number determination with an accuracy better 10 %.
The pixel detector system is also able to compete with all online detector types that are currently used behind a spectrometer, not only from a physical point of view but also from an economic one. The ease of use of the *RadEye* system and simple setup are of additional benefit. The saturation level of MCP and *RadEye* system are comparable for few MeV proton energies. The limited MCP detection efficiency for proton energies exceeding 10 MeV makes higher saturation levels feasible in this energy range. However, particle numbers in

the high–energy tail are typically small. The better single particle sensitivity of the pixel detector and the possibility to simultaneously measure the energy deposition, can, therefore, be considered as an advantage compared to the MCP–based system. All scintillator–based technologies still require systematic studies on radiation damage and light yield, when exposed to a typical flux of laser–accelerated ions. The experimental work within this thesis is based on proton irradiations. However, the *RadEye* system is even more capable to detect C–ions due to the higher energy loss and linear energy response of the system. The proton energy calibration can in principle also be used to determine the number of carbon or other ion species if the energy loss of a single ion is known.
Saturation level and radiation hardness of the system set a limit for application as beam monitor for radiation therapy with laser–accelerated protons. However, development of a therapy beam monitor was not the aim of this work, besides, medical application is still a very far future prospect due to stability and maximum achievable energies of laser accelerators. For the present state of affairs of laser–based proton acceleration, saturation limit and radiation hardness are sufficient, particularly in the high–energy tail of the laser–accelerated proton spectrum. A compact system, that combines computer and read–out electronics, has been set up as a first improvement of the system. Very recently, the prototype was successfully used at an irradiation campaign at the ASTRA-GEMINI Laser, detecting protons and C–ions simultaneously. Lately, a first damage study with respect to C–ions has been accomplished. During both experiments, damage levels have been found corresponding to the energy loss. The pixel detector system is, therefore, in its present state a mature system for laser–ion diagnostics with respect to the current performance of laser–ion accelerators.

Figure 7.1: **Prototype of the compact pixel detector system based on the *RadEye* sensor**

7.3 Outlook

The developed system will be applicable as long as ion spectra do not significantly change, which is not expected on a short–time scale. With improved acceleration efficiency in terms of particle number and energies, limits are not only set to the pixel detector system but also other currently investigated online detectors, which makes development in the field of laser–ion diagnostics a demand.
First of all, there are improvements of the pixel detector system possible, some of them even necessary. A gain correction procedure will be established to compensate small channel non–uniformities to improve response characteristics of the system further. The read–out speed of the system is at the present limited by the read–out electronics to about 3 Hz, though up to 5 Hz are possible with respect to the maximum sensor clocking frequency. A modification of read–out electronics is, therefore, required in the medium turn to maximize the read–out speed. As the repetition rate of laser accelerators is currently still afar from the maximum repetition rate of 10 Hz, operation with 5 Hz is still sufficient for the next future. However, if laser repetition rates further increase, faster detectors are required. *MIMOTERA*, a monolithic active pixel detector, allows a frame rate up to 10 kHz [217]. Similar saturation levels as for the *RadEye* can be estimated from sensor specifications, making this system of potential interest for laser–ion-diagnostic. First test measurements are, therefore, planned in the near future.
So far, only qualitative results of the ion spectrum are obtained in real time, quantitative results still rely on an offline data analysis. For analysis of spectra, detector coordinates have to be converted to stopping power values to determine particle numbers per pixel. This can be accomplished online by a software tool, if a valid assignment of dispersive matrix and detector coordinate system exists.
Laser–plasma acceleration is not exclusive for ions, but also yields electrons and X–rays. The large sensitive area offered by the pixel detector system, is also of potential interest for detection of these particles. If this proves to be infeasible, building an energy–resolved ion beam profiler based on a stack of *RadEye*–sensors could be an interesting option. However considerably higher energies are required for such an approach to work. An absorber matrix, with spatially varying absorber thicknesses adapted to the expected energy range, allows to measure a punctually energy–resolved ion beam profile. This approach is already feasible with currently available energies of laser–accelerated protons and will be tested within the next month in collaboration with a group from the HZDR.
Ionization chambers are well–established dose monitors in radiation therapy, their pulsed beam response is, therefore, of particular interest with respect to a future medical application of laser–based ion accelerators. A better understanding of the high pulse flux response of such an established technology is required and has to be investigated further.
In ion beam therapy, there is a growing–interest in position–sensitive beam monitors due to pencil beam scanning techniques. Pixel detectors are currently investigated for this purpose, although limits are still set by their radiation hardness. This is also a crucial point in laser–acceleration experiments, where any detector accumulates dose by subsequent ion pulses. The *RadEye* is not specifically designed for radiation hardness. Therefore, controlled annealing by heating but also the possibility to cool the detector during operation have to be investigated for a reduction of the dark current increase. Detector development is an

active field of research, particularly at large accelerator facilities such as CERN. Many effort is still done to improve the rate capability and radiation hardness of silicon detectors, which has lead to considerable improvements in the past. For instance, defect engineering by oxygenation increased the lifetime of silicon trackers by a factor of two. New radiation–hard detector technologies have to be investigated for their suitability as ion detectors for laser accelerators. Radiation–hard pixel detectors such as 3D silicon sensors which will be used for the high luminosity upgrade of the ATLAS detector [218] or diamond based pixel detectors are only two examples of interesting candidates for future research in laser–accelerated ion instrumentation based on pixel detectors but possibly also as beam monitors for radiation therapy.

Bibliography

[1] Krieger, H., *Strahlungsmessung und Dosimetrie*, Vieweg+Teubner, 1st edition, 2011.

[2] Forukai, E., Li, J. S., Ding, M., Tajima, T., and Ma, C.-M., Medical Physics **30** (2003) 1660.

[3] Luo, W., Fourkal, E., Li, J., and Ma, C.-M., Medical Physics **32** (2005) 794.

[4] Mourou, G. A., Tajima, T., and Bulanov, S. V., Review of Modern Physics **78** (2006) 309.

[5] Strickland, D. and Mourou, G., Optical communication **56** (1985) 219.

[6] Gibbon, P., Lectures based on the book *Short Pulse Laser Interactions with Matter*, available online http://www.2fz-juelich.de/jsc/splim/lectures/, 2012.

[7] Hegelich, B. M. et al, Nature **439** (2006) 441.

[8] Schwörer, H. et al, Nature **439** (2006) 445.

[9] Henig, A. et al, Physical Review Letters **102** (2009) 095002.

[10] Henig, A. et al, Physical Review Letters **103** (2009) 045002.

[11] Henig, A. et al, Physical Review Letters **103** (2009) 245003.

[12] Daido, H., Nishiuchi, M., and Pirozhkov, A. S., Reports on Progress in Physics **75** (2012) 1.

[13] Hegelich, B. M., *Acceleration of heavy Ions to MeV/nucleon Energies by Ultrahigh–Intensity Laser*, PhD thesis, Ludwig–Maximilians–Universität München, 2002.

[14] Andreev, N. E. and Gorbunov, L. M., Physics-Uspekhi **42** (1999) 49.

[15] Tajima, T. and Dawson, J. M., Physical Review Letters **43** (1979) 267.

[16] Tikhonchuk, V. T., Nuclear Instruments and Methods in Physics Research Section A: Accelerators, Spectrometers, Detectors and Associated Equipment **620** (2010) 1.

[17] Ma, W. et al, Nuclear Instruments and Methods in Physics Research Section A: Accelerators, Spectrometers, Detectors and Associated Equipment **655** (2011) 53.

[18] Gibbon, P. and Förster, E., Plasma Physics and Controlled Fusion **38** (1996) 769.

[19] Hatchett, S. P. et al, Physics of Plasmas **7** (2000) 2076.

[20] Snavely, R. A. et al, Physical Review Letters **85** (2000) 2945.

[21] Sokollik, T. et al, Physical Review Letters **103** (2009) 135003.

[22] Rykovanov, S. G. et al, New Journal of Physics **10** (2008) 113005.

[23] Klimo, O., Psikal, J., Limpouch, J., and Tikhonchuk, V. T., Physical Review Special Topics - Accelerators and Beams **11** (2008) 031301.

[24] Robinson, A. P. L., Zepf, M., Kar, S., Evans, R. G., and Bellei, C., New Journal of Physics **10** (2008) 013021.

[25] Mead, M. J., Neely, D., Gauoin, J., Heathcode, R., and Patel, P., Review of Scientific Instruments **75** (2004) 4225.

[26] Stoeckl, C. et al, Review of Scientific Instruments **77** (2006) 10F506.

[27] Linz, U. and Alonso, J., Physical Review Special Topics - Accelerators and Beams **10** (2007) 094801.

[28] Nakamura, K. et al, Journal of Physics G: Nuclear and Particle Physics **37** (2010) 075021.

[29] Kar, S. et al , Physical Review Letters **100** (2008) 105004.

[30] Brüning, O. S. et al, *LHC Design Report—Volume 1*, CERN, Geneva, 2004.

[31] Fischer, C. and Schmidt, R., On the measurement of the beam current, lifetime and decay rate in the LHC rings, Technical Report LHC–BCT–ES–0001, CERN, 2005.

[32] Karsch, L., Richter, C., and Pawelke, J., Zeitschrift für medizinische Physik **21** (2011) 4.

[33] Green, J. S. et al, Scintillator–based ion beam profiler for diagnosing laser–accelerated ion beams, in *Laser acceleration of electrons, protons and ions and medical applications of laser–generated secondary sources of radiation and particles*.

[34] Prasad, R. et al, Nuclear Instruments and Methods in Physics Research Section A: Accelerators, Spectrometers, Detectors and Associated Equipment **623** (2010) 712.

[35] Reinhardt, S., Granja, C., Krejčí, F., and Assmann, W., Journal of Instrumentation **6** (2011) C12030.

[36] Richter, C. et al, Physics in Medicine and Biology **56** (2011) 1529.

[37] Hoch, M., Nuclear Instruments and Methods in Physics Research Section A: Accelerators, Spectrometers, Detectors and Associated Equipment **535** (2004) 1.

[38] XU, M. H. et al, Chinese Physics Letters **28** (2011) 095203.

[39] Knoll, G., *Radiation Detection and Measurement*, John Wiley & Sons, Inc, 3rd edition, 1999.

[40] Krieger, H., *Grundlagen der Strahlungsphysik und des Strahlenschutzes*, Vieweg+Teubner, 3rd edition, 2009.

[41] Jackson, J., *Klassische Elektrodynamik*, Walter de Gruyter GmbH & Co KG, Berlin, 4th edition, 2006.

[42] National Institute of Standards and Technology, pstar - stopping power and range tables for protons, http://physicsnistgov/PhysRefData/Star/Text/PSTARhtml.

[43] ICRU, Clinical proton dosimetry Part 1 : Beam production, beam delivery and measurement of absorbed dose (ICRU Report 59), Technical report, International Commission on Radiation Units and Measurements, 1998.

[44] IAEA, Absorbed dose determination in beam radiotherapy: an international code of practice for dosimetry based on standards of absorbed dose to water, Technical Report Series 398, International Atomic Energy Agency, 2000.

[45] ICRU, Prescribing, recording, and reporting proton-beam therapy (ICRU Report 78), Technical Report 2, International Commission on Radiation Units and Measurements, 2007.

[46] Jones, D. T. L., Radiation Physics and Chemistry **75** (2006) 541.

[47] Ramo, S., Proceeding of the IRE (1939) 584.

[48] Delaney, C. F. G. and Finch, E. C., *Radiation detectors*, Oxford University Press, 1st edition, 1992.

[49] Spieler, H., *Semiconductor Detector Systems*, Oxford University Press, 1st edition, 2005.

[50] Fano, U., Physical Review **72** (1947) 26.

[51] Boag, J. W., The British Journal of Radiology **23** (1950) 601.

[52] Boag, J. W. and Wilson, T., British Journal of Applied Physics **3** (1952) 222.

[53] Palmans, H., Thomas, R., and Kacperek, A., Physics in Medicine and Biology **51** (2006) 903.

[54] Hochhäuser, E. and Balk, O. A., Physics in Medicine and Biology **31** (1986) 223.

[55] Sauli, F., Nuclear Instruments and Methods in Physics Research Section A: Accelerators, Spectrometers, Detectors and Associated Equipment **386** (1997) 531.

[56] Kaminski, J., Micropattern gas detectors, in *Proceedings of Science (VERTEX 2008)*, page 039, 2008.

[57] van de Graaf, H., Physics Procedia **17** (2011) 224.

[58] Bachmann, S. et al, Nuclear Instruments and Methods in Physics Research Section A: Accelerators, Spectrometers, Detectors and Associated Equipment **470** (2001) 548.

[59] van de Graaf, H., Physics Procedia **17** (2011) 224.

[60] Holland, S., Nuclear Instruments and Methods in Physics Research Section A: Accelerators, Spectrometers, Detectors and Associated Equipment **275** (1989) 537.

[61] Perera Solane, B. et al, Nuclear Instruments and Methods in Physics Research Section A: Accelerators, Spectrometers, Detectors and Associated Equipment **550** (2005) 567.

[62] Verbitskaya, E., Eremin, V., and Ruggiero, G., Nuclear Instruments and Methods in Physics Research Section A: Accelerators, Spectrometers, Detectors and Associated Equipment **612** (2010) 501.

[63] Verbitskaya, E., Eremin, V., and Ruggiero, G., Nuclear Instruments and Methods in Physics Research Section A: Accelerators, Spectrometers, Detectors and Associated Equipment **658** (2011) 108.

[64] Lindström, G, Nuclear Instruments and Methods in Physics Research Section A: Accelerators, Spectrometers, Detectors and Associated Equipment **512** (2003) 30.

[65] Moll, M., *Radiation Damage in Silicon Particle Detectors - microscopic defects and macroscopic properties*, PhD thesis, Universität Hamburg, 1999.

[66] Lutz, G., *Semiconductor radiation detectors*, Springer–Verlag, 1st edition, 1999.

[67] Lindström, G. et al, Nuclear Instruments and Methods in Physics Research Section A: Accelerators, Spectrometers, Detectors and Associated Equipment **465** (2001) 60.

[68] Velthuis, J. J. et al., Nuclear Instruments and Methods in Physics Research Section A: Accelerators, Spectrometers, Detectors and Associated Equipment **591** (2008) 221.

[69] Pernegger, H., Physica Status Solidi (a) **203** (2006) 3299.

[70] Dehning, B. et al., Test of a diamond detector using unbunched beam halo particles oai:cdscernch:1258407, Technical Report CERN–ATS–2010–027, CERN, Geneva, 2010.

[71] Gorišek, A., The ATLAS beam condition monitor commissioning, in *Topical Workshop on Electronics for Particle Physics*, edited by Dho, E. and Vasey, F., pages 264–268, Geneva, 2008, CERN, CERN.

[72] Rohe, T., Hügging, F., Lutz, G., Richter, R. H., and Wunstorf, R., Nuclear Instruments and Methods in Physics Research Section A: Accelerators, Spectrometers, Detectors and Associated Equipment **409** (1998) 224.

[73] Asner, D. et al, Nuclear Instruments and Methods in Physics Research Section A: Accelerators, Spectrometers, Detectors and Associated Equipment **636** (2011) 5125.

[74] Bugg, W. et al, Nuclear Instruments and Methods in Physics Research Section A: Accelerators, Spectrometers, Detectors and Associated Equipment **650** (2011) 50.

[75] Tromson, D. et al., Diamond and Related Materials **19** (2010) 1012.

[76] Cuttone, G. et al., Nuclear Physics B **172** (2007) 79.

[77] Betzel, G. T., Lansley, S. P., Baluti, F., Reinisch, L., and Meyer, J., Nuclear Instruments and Methods in Physics Research Section A: Accelerators, Spectrometers, Detectors and Associated Equipment **614** (2010) 130.

[78] Rebisz-Pomorska, M., Ciobanu, M., Kis, M., Pomorski, M., and Voss, B., Nuclear Instruments and Methods in Physics Research Section A: Accelerators, Spectrometers, Detectors and Associated Equipment **620** (2010) 534.

[79] Lan, W. et al., Chinese Physics B **17** (2008) 3644.

[80] Bilei, G. M. et al, Nuclear Instruments and Methods in Physics Research Section A: Accelerators, Spectrometers, Detectors and Associated Equipment **409** (1998) 105.

[81] Caner, A., Banerjee, S., Khanov, A., and Stepanov, N., Nuclear Instruments and Methods in Physics Research Section A: Accelerators, Spectrometers, Detectors and Associated Equipment **435** (1999) 118.

[82] Kreis, B., Nuclear Instruments and Methods in Physics Research Section A: Accelerators, Spectrometers, Detectors and Associated Equipment **650** (2011) 14.

[83] Alam, M. S. et al, Nuclear Instruments and Methods in Physics Research Section A: Accelerators, Spectrometers, Detectors and Associated Equipment **456** (2001) 217.

[84] Dell' Asta, L., Nuclear Instruments and Methods in Physics Research Section A: Accelerators, Spectrometers, Detectors and Associated Equipment **650** (2011) 19.

[85] Brüning, O. S. et al, *LHC Design Report*, CERN, Geneva, 2004.

[86] Dobos, D. and Pernegger, H., Nuclear Instruments and Methods in Physics Research Section A: Accelerators, Spectrometers, Detectors and Associated Equipment **628** (2011) 246.

[87] Goessling, C. et al., Nuclear Instruments and Methods in Physics Research Section A: Accelerators, Spectrometers, Detectors and Associated Equipment **650** (2011) 198.

[88] Parker, S. I., Kenney, C. J., and Segal, J., Nuclear Instruments and Methods in Physics Research Section A: Accelerators, Spectrometers, Detectors and Associated Equipment **395** (1997) 328.

[89] Grenier, P. et al, Nuclear Instruments and Methods in Physics Research Section A: Accelerators, Spectrometers, Detectors and Associated Equipment **638** (2011) 33.

[90] Burke, B., Jorden, P., and Vu, P., Experimental Astronomy **19** (2005) 69.

[91] Meidinger, N. et al, Nuclear Instruments and Methods in Physics Research Section A: Accelerators, Spectrometers, Detectors and Associated Equipment **624** (2010) 321.

[92] Abe, K. et al, Nuclear Instruments and Methods in Physics Research Section A: Accelerators, Spectrometers, Detectors and Associated Equipment **400** (1997) 287.

[93] Brau, J. E., Nuclear Instruments and Methods in Physics Research Section A: Accelerators, Spectrometers, Detectors and Associated Equipment **418** (1998) 52.

[94] Turchetta, R. et al, Nuclear Instruments and Methods in Physics Research Section A: Accelerators, Spectrometers, Detectors and Associated Equipment **582** (2007) 866.

[95] Li, S. and Kleinfelder, S., Nuclear Instruments and Methods in Physics Research Section A: Accelerators, Spectrometers, Detectors and Associated Equipment **579** (2007) 227.

[96] Sipos, A et al, Nuclear Instruments and Methods in Physics Research Section A: Accelerators, Spectrometers, Detectors and Associated Equipment **509** (2003) 328.

[97] Sanchez–Crespo, A. et al, Nuclear Instruments and Methods in Physics Research Section A: Accelerators, Spectrometers, Detectors and Associated Equipment **525** (2004) 289.

[98] Turchetta, R., Nuclear Instruments and Methods in Physics Research Section A: Accelerators, Spectrometers, Detectors and Associated Equipment **583** (2007) 131.

[99] Metzkes, J., Helmholtz-Zentrum Dresden-Rossendorf, Germany , private communication.

[100] Wiza, J. L., Nuclear Instruments and Methods in Physics Research **162** (1979) 587.

[101] Hamamatsu, *MCP & MCP assembly selection guide*, Hamamatsu Photonics KK.

[102] Sternglass, E. J., The Physical Review **108** (1957) 1.

[103] Berdoz, A. R. et al, Nuclear Instruments and Methods in Physics Research Section A: Accelerators, Spectrometers, Detectors and Associated Equipment **307** (1991) 26.

[104] Mróz, W. et al, Review of Scientific Instruments **67** (1996) 1272.

[105] Harres, K. et al, Review of Scientific Instruments **79** (2008) 093306.

[106] Ter-Avetisyan, S., Romagnani, L., Borghesi, M., M, S., and Nickles, P. V., Nuclear Instruments and Methods in Physics Research Section A: Accelerators, Spectrometers, Detectors and Associated Equipment **623** (2010) 709.

[107] Track Analysis Systems Ltd, http://www.tasl.co.uk/plastics.html, 2011.

[108] Xiaojiao, D. et al, Nuclear Instruments and Methods in Physics Research Section A: Accelerators, Spectrometers, Detectors and Associated Equipment **609** (2009) 190.

[109] Gaillard, S., Fuchs, J., Renard-Le Galloudec, N., and Cowan, T. E., Review of Scientific Instruments **78** (2007) 013304.

[110] Fleischer, R. L., Price, P. B., and Walker, R. M., Journal of Applied Physics **36** (1965) 3645.

[111] Sadowski, M. et al, Nuclear Instruments and Methods in Physics Research B **86** (1994) 311.

[112] Matiullmi, M. et al, Nuclear Tracks and Radiation Measurements **15** (1988) 137.

[113] Rusch, G., Winkel, E., Noll, A., and Heinrich, W., Nuclear Tracks and Radiation Measurements **19** (1991) 261.

[114] Trakowski, W. et al, Nuclear Instruments and Methods in Physics Research **225** (1984) 92.

[115] Carl Zeiss AG, Oberkochen, Germany, http://www.zeiss.de.

[116] ELBEK Bildanalyse GmbH, Siegen ,Germany, Samaica Manual.

[117] Suzuki, T. et al, Nuclear Instruments and Methods in Physics Research Section A: Accelerators, Spectrometers, Detectors and Associated Equipment **390** (1997) 155.

[118] Mancic, A., Fuchs, J., Antici, P., Gaillard, S. A., and Audebert, P., Review of Scientific Instruments **79** (2008) 073301.

[119] Tanaka, K. A. et al, Review of Scientific Instruments **76** (2005) 013507.

[120] Zeil, K. et al, Review of Scientific Instruments **81** (2010) 013307.

[121] Mari, C. and Matsumura, A., Nuclear Instruments and Methods in Physics Research Section A: Accelerators, Spectrometers, Detectors and Associated Equipment **312** (1992) 39.

[122] Taniguchi, S., A, Y., T, N., and A, F., Nuclear Instruments and Methods in Physics Research Section A: Accelerators, Spectrometers, Detectors and Associated Equipment **413** (1998) 199.

[123] Bücherl, T., Rausch, C., and von Seggern, H., Nuclear Instruments and Methods in Physics Research Section A: Accelerators, Spectrometers, Detectors and Associated Equipment **333** (1993) 502.

[124] Nohotomi, A. et al., Nuclear Instruments and Methods in Physics Research Section A: Accelerators, Spectrometers, Detectors and Associated Equipment **511** (2003) 382.

[125] Fujifilm Europe GmbH, Düsseldorf, Germany.

[126] Struß, D., Fujifilm Europe GmbH, Düsseldorf, Germany , private communication.

[127] Takahashi, K., Kohda, K., and Miyahara, J., Journal of Luminescence **31–32** (1984) 266.

[128] Takahashi, K., Journal of Luminescence **100** (2002) 307.

[129] Ohuchi, H., A, Y., and Nakamura, T., Nuclear Instruments and Methods in Physics Research Section A: Accelerators, Spectrometers, Detectors and Associated Equipment **450** (2000) 343.

[130] Ohuchi, H. and A, Y., Nuclear Instruments and Methods in Physics Research Section A: Accelerators, Spectrometers, Detectors and Associated Equipment **490** (2002) 573.

[131] Suzuki, T. et al, Journal of Nuclear Science and Technology **34** (1997) 461.

[132] Secu, M., Secu, C. E., Vasile, V., Predoi, D., and Gazdaru, D. M., Journal of Optoelectronics and advanced materials **9** (2007) 1800.

[133] Fujifilm Europe GmbH, Düsseldorf, Germany, FLA 5100 product brochure.

[134] Fujifilm Europe GmbH, Düsseldorf, Germany, FLA 7000 product brochure.

[135] Kato, H., Miyahara, J., and Takano, M., Neurosurgical Review **8** (1985) 53.

[136] ISP, *Gafchromic® EBT2 Self-developing film for radiotherapy dosimetry* , International Specialty Products (ISP), Wayne, NJ, 2009.

[137] Todorovic, M., Fischer, M., Cremers, F., Thom, E., and Schmidt, R., Medical Physics **33** (2006) 1321.

[138] Zeidan, O. A. et al, Medical Physics **33** (2006) 4064.

[139] ISP, *Gafchromic® EBT Self-developing film for radiotherapy dosimetry* , International Specialty Products (ISP), Wayne, NJ, 2007.

[140] Andres, C., del Castillo, A., Tortosa, R., Alonso, D., and Barquero, R., Medical Physics **37** (2010) 6271.

[141] McCaw, T. J., Micka, J. A., and DeWerd, L. A., Medical Physics **38** (2011) 5771.

[142] Rink, A., *Point-based ionizing radiation dosimetry using radio-chromic materials and a fibre-optic readout system*, PhD thesis, University of Toronto, 2008.

[143] Tsibouklis, J. et al, Journal of Materials Chemistry **3** (1993) 97.

[144] Gross, H and Sixl, H and Kröhnke, C and Enkelmann, V , Chemical Physics **45** (1980) 15.

[145] Cheung, T., Butson, M. J., and Yu, P. K. N., Physics in Medicine and Biology **50** (2005) N281.

[146] Niroomad-Rad, A. et al, Medical Physics **25** (1998) 2093.

[147] Martišíková, M and Jäckel, O, Physics in Medicine and Biology **55** (2005) 3741.

[148] Martišíková, M and Ackermann, B and Klemm, S and Jäckel, O , Nuclear Instruments and Methods in Physics Research Section A: Accelerators, Spectrometers, Detectors and Associated Equipment **591** (2008) 171.

[149] ISP, *Gafchromic® MD-55 radiochromic dosimetry films for high energy photons - Configuration, specifications and performance data*, International Specialty Products (ISP), Wayne, NJ.

[150] Piermattei, A. et al, Medical Physics **27** (2000) 1655.

[151] Vatnisky, S. M., Applied Radiation Isotopes **48** (1997) 643.

[152] Kirby, D. et al., Physics in Medicine and Biology **55** (2010) 417.

[153] Arjomandy, B, Medical Physics **37** (2010) 1942.

[154] Lindsay, P., Rink, A., Ruschin, M., and Jaffray, D., Medical Physics **37** (2010) 571.

[155] Devic, S. et al, Medical Physics **32** (2005) 2245.

[156] Hupe, O. and Brunzendorf, J., Medical Physics **33** (2006) 4085.

[157] Menegotti, L., Delana, A., and Martignano, A., Medical Physics **35** (2008) 3078.

[158] Devic, S. et al., Medical Physics **37** (2010) 2207.

[159] Butson, M. J., Cheung, T., and Yu, P. K. N., Australasian Physical and Engineering Sciences in Medicine **29** (2006) 281.

[160] Saur, S. and Frengen, J., Medical Physics **35** (2008) 3094.

[161] Desroches, J., Bouchard, H., and Lacroix, F., Medical Physics **37** (2010) 1565.

[162] Reinhardt, S., Hillbrand, M., Wilkens, J. J., and Assmann, W., Medical Physics (2012).

[163] Epson Deutschland GmbH, *EPSON Perfection V 700 Photo*, Epson Deutschland GmbH, Meerbusch, Germany.

[164] Kappa optronics GmbH, *Kappa DX-4 Manual*, Kappa optronics GmbH, Gleichen, Germany.

[165] Eastman Kodak Company, *Kodak KAI 1020 Image Sensor*, Eastman Kodak Company, Rochester, New York 14650–2010, 2010.

[166] Eastman Kodak Company, *Application Note Solid State Image Sensors Terminology*, Eastman Kodak Company, Rochester, New York 14650–2010, 1994.

[167] Cavadore, C., Eastman Kodak Company, private communication.

[168] Rad-icon Imaging Corp, RadEye1 Large Area Image Sensor, http://www.rad-icon.com/knowledge-doclibphp.

[169] Graeve, T. and Weckler, G. P., Large Area Digital X-ray Specific Imager, http://www.rad-icon.com/knowledge-doclibphp.

[170] Graeve, T. and Weckler, G. P., High-resolution CMOS imaging detector, http://www.rad-icon.com/knowledge-doclibphp.

[171] Schmid-Fabian, R., RSF-systems, private communication.

[172] Pleora Technologies Inc, *PT1000-LV*, Pleora Technologies Inc, Ontario, Canada.

[173] Rad-icon Imaging Corp, Remote RadEye Product Family Data Sheet, http://www.rad-icon.com/pdf/Remote%20RadEye%20Product%20Familypdf.

[174] Rad-icon Imaging Corp, Guide to Image Quality and Pixel Correction Methods, http://www.rad-icon.com/knowledge-doclibphp.

[175] Llopart, X. and Campbell, M., Nuclear Instruments and Methods in Physics Research Section A: Accelerators, Spectrometers, Detectors and Associated Equipment **509** (2003) 157.

[176] Llopart, X., Ballariga, R., Campbell, M., Tlustos, L., and Wong, W., Nuclear Instruments and Methods in Physics Research Section A: Accelerators, Spectrometers, Detectors and Associated Equipment **581** (2007) 485.

[177] Jakůbek, J, Journal of Instrumentation **4** (2009) P03013.

[178] Granja, C., Jakubek, J., Köster, U., Platkevic, M., and Pospisil, S., Nuclear Instruments and Methods in Physics Research Section A: Accelerators, Spectrometers, Detectors and Associated Equipment **633** (2010) S198.

[179] Campbell, M. et al, Nuclear Instruments and Methods in Physics Research Section A: Accelerators, Spectrometers, Detectors and Associated Equipment **591** (2008) 38.

[180] Jakůbek, J. et al., Nuclear Instruments and Methods in Physics Research Section A: Accelerators, Spectrometers, Detectors and Associated Equipment **591** (2008) 155.

[181] Bouchami, J. et al, Nuclear Instruments and Methods in Physics Research Section A: Accelerators, Spectrometers, Detectors and Associated Equipment **607** (2009) 196.

[182] Vykydal, Z., Jakůbek, J., and Pospíšil, S., Nuclear Instruments and Methods in Physics Research Section A: Accelerators, Spectrometers, Detectors and Associated Equipment **563** (2006) 112.

[183] Datzmann, G. et al, Nuclear Instruments and Methods in Physics Research B **181** (2001) 20.

[184] Dollinger, G. et al, Nuclear Instruments and Methods in Physics Research B **267** (2009) 2008.

[185] Moser, M. et al, Nuclear Instruments and Methods in Physics Research B (2011) .

[186] Rohrer, L., Jakob, H., Rudolph, K., and Skorka, S. J., Nuclear Instruments and Methods in Physics Research **220** (1984) 161.

[187] Hauptner, A. et al, Radiation and Environmental Biophysics **42** (2004) 237.

[188] Kraft, S. et al, New Journal of Physics **12** (2010) 085003.

[189] Greubel, C. et al., Radiation and Environmental Biophysics **50** (2011) 339.

[190] Ziegler, J., Biersack, J., and Ziegler, M., *SRIM - The Stopping and Range of Ions in Matter*, Ion Implantation Press, 2008.

[191] Krischel, D. et al, IEEE-Transactions on applied superconductivity **17** (2007) 2307.

[192] Weber, A. et al, Biomedizinische Technik **50** (2005) 122.

[193] PTW Freiburg GmbH, Freiburg, Germany, *0125 cm^3 Semiflex Chamber, type 31010*, PTW Freiburg GmbH, Freiburg, Germany.

[194] Bin, J. et al., A laser–driven nano-second proton source for radiobiological studies, Applied Physics Letters, accepted for publication, 2012.

[195] Agostinelli, S. et al, Nuclear Instruments and Methods in Physics Research Section A: Accelerators, Spectrometers, Detectors and Associated Equipment **506** (2003) 250.

[196] Ziegler, J. F., Ziegler, M. D., and Biersack, J. P., Nuclear Instruments and Methods in Physics Research B **268** (2010) 1818.

[197] SRIM 2008, homepage, http://www.srim.org.

[198] SIMNRA, homepage, http://www.simnra.com.

[199] Mayer, M., SIMNRA User's guide, Technical report, Max-Planck-Institut für Plasmaphysik, 1997.

[200] Geant 4 Collaboration, Geant 4 homepage, http://geant4cernch/.

[201] Geant 4 Collaboration, Geant 4 User's Guide for Application Developers, Technical report, Geant 4 Collaboration, 2011.

[202] Geant4 collaboration, *Physics reference manual*, Geant4 collaboration.

[203] Brun, R. and Rademakers, F., Nuclear Instruments and Methods in Physics Research Section A: Accelerators, Spectrometers, Detectors and Associated Equipment **389** (1997) 81.

[204] Devic, S. et al, Medical Physics **31** (2004) 2392.

[205] Nohtomi, A. et al, Nuclear Instruments and Methods in Physics Research Section A: Accelerators, Spectrometers, Detectors and Associated Equipment **424** (1999) 569.

[206] Kohno, R. et al, Nuclear Instruments and Methods in Physics Research Section A: Accelerators, Spectrometers, Detectors and Associated Equipment **481** (2002) 669.

[207] Hidding, B. et al, Review of Scientific Instruments **78** (2007) 083301.

[208] Tanimoto, T. et al, Review of Scientific Instruments **79** (2008) 10E910.

[209] Karsch, L. et al, Medical Physics **39** (2012) 2447.

[210] Bortfeld, T., Medical Physics **24** (1997) 2024.

[211] Siebenwirth, C., Tumorbestrahlung mit gepulsten und kontinuierlichen Protonen am Mausmodell, Master's thesis, Technische Universität München, 2010.

[212] Falk, C., Elimpex-Medizintechnik GmbH, private communication.

[213] Richter, C., OncoOptics group, private communication.

[214] National Nuclear Data Center, information extracted from the *Chart of Nuclides database*, http://www.nndcbnl.gov/chart/.

[215] Rad-icon Imaging Corp, Detector Lifetime and Radiation Damage, http://www.rad-icon.com/knowledge-doclibphp.

[216] Lehmann, A., Britting, A., Eyrich, W., and Uhlig, F., Journal of Instrumentation **4** (2009) P11024.

[217] Boll, R., A monolithic active pixel sensor as direct monitor for therapeutic antiproton an ion beams, Master's thesis, Universität Heidelberg, 2010.

[218] Da Via, C., Cern Courier, International Journal of High-Energy Physics **52** (2012) 19.

List of abbreviations

AAPM American Association of Physicists in Medicine

ADC analogue–to–digital converter

ASE amplified spontaneous emission

ATLAS (laser) Advanced Titanium:Sapphire LASer

ATLAS (detector) A Toroidal LHC ApparatuS

CCD charge coupled device

CMOS complementary metal–oxide semiconductor

CMS Compact Muon Solenoid

CPA chirped–pulse amplification

CVD chemical vapour deposition

DAQ data acquisition

DLC diamond like carbon

DRACO Dresden Laser Acceleration Source

EMCCD electron multiplying charge coupled device

EMP electro–magnetic pulse

FC Faraday cup

FWHM full width half maximum

GEM gas electron multiplier

GUI graphical user interface

HEP high energy physics

HZDR Helmholtz–Zentrum Dresden–Rossendorf

IAEA International Atomic Energy Agency

IEAP Institute for Experimental and Applied Physics of the Czech Technical University

IC ionization chamber

ICCD intensified CCD

IDOCIS integrated dosimetry and cell irradiation system

IMPT intensity modulated proton therapy

IMRT intensity modulated radiotherapy

IP image plate

LET linear energy transfer

LHC Large Hadron Collider

MAPS monolithic active pixel sensor

MCP micro–channel plate or multi–channel plate

Micromegas micro–mesh gaseous structures

MIP minimum ionizing particle

MLL Maier–Leibnitz–Laboratory

MPGD micro–pattern gaseous detectors

MPQ Max–Planck Institut für Quantenoptik

MPV most probable value

MRI Klinikum rechts der Isar, München

MU monitor unit (100 MU = 1 Gy)

MWPC multi–wire proportional chamber

NE Niederenergie

netOD net optical density

NIEL non–ionizing energy loss

OD optical density

PADC poly allyl diglycol carbonate

PCB printed circuit board

PCDA pentacosa–10,12–diynoic acid

pCVD poly–crystal CVD

PIPS passivated implanted planar silicon

PMMA poly methyl methacrylate

PMT photomultiplier tube

PSL photo–stimulable luminescence

PW petawatt

QA quality assurance

RCF radio–chromic film

ROI region of interest

RPA radiation pressure acceleration

RPTC Rinecker Proton Therapy Center

SAS small–angle spectrometer

sCVD single–crystal CVD

SNAKE Superconducting Nanoscope for Applied nuclear (Kern–) physics experiments

SNR signal–to–noise ratio

SOBP spread–out Bragg peak

SSNTD solid–state nuclear track detector

TIFF tagged image file format

TIM time mode (*Timepix*)

TNSA target normal sheath acceleration

TOT time over threshold mode (*Timepix*)

TPS treatment planning system

TUM Technische Universität München

TW terawatt

WAS wide–angle spectrometer

List of publications and conference contributions

Publications

2011

- Christoph Greubel, Walter Assmann, Christian Burgdorf, Günther Dollinger, Guanghua Du, Volker Hable, Alexaner Hapfelmeier, Ralf Hertenberger, Peter Kneschaurek, Dörte Michalski, Michael Molls, Sabine Reinhardt, Barbara Röper, Stefan Schell, Thomas Schmid, Christian Siebenwirth, Tatiana Wenzl, Olga Zlobinskaya, and Jan Wilkens, *Scanning irradiation device for mice in vivo with pulsed and continuous proton beams*, **2011**, Radiation and Environmental Biophysics, **50**,3, 339-344

- Sabine Reinhardt, Carlos Granja, Frantisek Krejčí and Walter Assmann, *Test of pixel detectors for laser-driven accelerated particle beams* in Journal of Instrumentation, 2011, **6**, C12030

- S. Reinhardt, W. Assmann, C. Granja, J. Jakůbek, F. Krejčí, *Investigation of different pixel detectors for laser-driven accelerated particle beams*, Radiotherapy and Oncology, **2011**, 99 Suppl. 1, S154

- O. Zlobinskaya, T.E. Schmid, D. Michalski, C. Greubel, V. Hable, C. Siebenwirth, S. Reinhardt, P. Kneschaurek, W. Assmann, C. Burgdorf, G. Du, T. Wenzl, S. Schell, J.J. Wilkens, B. Röper, M. Molls, G. Dollinger, *Scanning device for mice in vivo irradiation with pulsed and continuous proton beams*, Strahlentherapie und Onkologie, **186**, Supplement 1, 52-53

- D. Michalski, T.E. Schmid, O. Zlobinskaya, C. Siebenwirth, C. Greubel, V. Hable, C. Burgdorf, G. Du, L. Tonelli, T. Wenzl, S. Schell, S. Reinhardt, W. Assmann, B. Röper, G. Multhoff, M. Molls, R. Krücken, G. Dollinger, J.J. Wilkins, *Tumor growth delay experiment with a pulsed nanosecond proton microbeam*, Strahlentherapie und Onkologie, **187**, Supplement 1, 62

2012

- S. Reinhardt, C. Granja, W. Assmann, F. Krejci, *Test of different pixel detector for laser-accelerated protons*, Radiotherapy and Oncology, **2012**, 102 Suppl. 1, S21

- N. Humble, K. Allinger, W. Assmann, J. Bin, G. Dollinger, G. Drexler, A. Friedl, P. Hilz, D. Kiefer, W. Ma, D. Michalski, M. Molls, S. Reinhardt, T. Schmid, O. Zlobinskaya, J. Schreiber, J. Wilkens, *Single shot high dose cell irradiations with laser-driven protons*, Radiotherapy and Oncology, **2012**, 102 Suppl. 1, S30

- Sabine Reinhardt, Martin Hillbrand, Jan Wilkens and Walter Assmann, *Comparison of Gafchromic EBT2 and EBT3 films for clinical photon and proton beams*, Medical Physics, **2012**, 39, 8, 5257–5262

- J. Bin, K. Allinger, W. Assmann, G. Dollinger, G. A. Drexler, A. Friedl, D. Habs, P. Hilz, R. Hoerlein, N. Humble, S. Karsch, K. Khrennikov, D. Kiefer, F. Krausz, W. Ma, D. Michalski, M. Molls, S. Raith, S. Reinhardt, B. Röper, T. E. Schmid, T. Tajima, J. Wenz, O. Zlobinskaya, J. Schreiber and J. J. Wilkens, *A laser–driven nano-second proton source for radiobiological studies*, Applied Physics Letters, 2012, accepted for publication

Conference Contributions

2009

- 440th WE Heraeus Seminar on 'Laser-driven particle and X-ray sources for medical applications', September 13–17, 2009, Frauenwörth Monastery, Germany, *Radiation therapy with laser-driven accelerated particle beams: physical dosimetry and spatial dose distribution*

2010

- Instrumentation for Diagnostics and Control of Laser-Accelerated Proton (Ion) Beams: First Workshop, August 09-10, 2010, Abingdon, United Kingdom, *Radiation therapy with laser-driven accelerated particle beams: physical dosimetry and spatial dose distribution*

- Deutsche Physikerinnentagung, November 04-07, 2010, München, Germany, *Radiation therapy with laser-driven accelerated particle beams: physical dosimetry and spatial dose distribution*

2011

- DPG Spring Metting, March 13-18, 2011, Dresden, Germany, *Radiation therapy with laser-driven accelerated particle beams: physical dosimetry and spatial dose distribution*

- 11^{th} Biennial ESTRO, Conference on Physics and Radiation Technology for Clinical Radiotherapy, May 09-12, 2011, London, United Kingdom, *Investigation of different pixel detectors for laser-driven accelerated particle beams*
- The 13th International Workshop on Radiation Imaging Detectors (IWORID), July 03-11, 2011, Zurich, Switzerland, *Test of different pixel detector for laser-driven accelerated particle beams*
- Medizinische Physik 2011, 3 Ländertagung der ÖGMP, DGMP und SGSMP, September 28- October 1, 2011,Wien, Austria, *Test of different pixel detector for laser-accelerated particle beams*
- Medizinische Physik 2011, 3 Ländertagung der ÖGMP, DGMP und SGSMP, September 28- October 1, 2011, Wien, Austria, *Optimizing the experimental components required in a laser accelerated particle cell irradiation*
- HEPTech Matching Event: Industry meets Academia on Beam Monitoring, November 10-11, 2011, GSI, Darmstadt, Germany, *Detection of laser accelerated proton beams using Image Plates (IP)*
- HEPTech Matching Event: Industry meets Academia on Beam Monitoring, November 10-11, 2011, GSI, Darmstadt, Germany, *Detection of laser accelerated proton beams using radiochromic films (RCF)*
- HEPTech Matching Event: Industry meets Academia on Beam Monitoring, November 10-11, 2011, GSI, Darmstadt, Germany, *Pixel detectors for laser-accelerated proton beams*

2012

- International Conference on Translational Research in Radio-Oncology and Physics for Health in Europe (ICTR-PHE), February 27- March 02, 2012, Geneva, Switzerland, *Test of different pixel detector for laser-accelerated protons*
- International Conference on Translational Research in Radio-Oncology and Physics for Health in Europe (ICTR-PHE), February 27- March 02, 2012, Geneva, Switzerland, *Single shot high dose cell irradiations with laser-driven protons*
- Instrumentation for Diagnostics and Control of Laser-Accelerated Proton (Ion) Beams: Second Workshop, June 07-08, 2012, Paris, France, *tba*

Summer School

2010

- International Max Planck Research School of Advanced Photon Science, August 1-6, 2010, Wildbad Kreuth, Germany, *Radiation therapy with laser-driven accelerated particle beams: physical dosimetry and spatial dose distribution*

Danksagung

Bei der interdisziplinären Zusammenarbeit, wie sie im Rahmen dieser Arbeit und des Munich Centers of Advanced Photonics (MAP) stattfand, sind natürlich eine Vielzahl an Leuten beteiligt, deren Aufzählung im Einzelnen den Rahmen dieser Ausführungen sprengen würde. Ich möchte mich daher zunächst einmal generell bei allen, die in irgendeiner Form zum Gelingen dieser Arbeit beigetragen haben, recht herzlich bedanken.

Mein besonderer Dank gilt dabei Herrn PD Dr. Walter Assmann, der mir diese interessante Arbeit an der Schnittstelle zwischen Medizin, Detektor- und Laserphysik angeboten hat. Dank seiner Erfahrung und engagierten Betreuung konnte ich in den letzten Jahren viel Neues hinzulernen. Er ermöglichte mir auch die Teilnahme an internationalen Workshops und Konferenzen, wodurch ich wertvolle Kontakte knüpfen konnte, ohne die meine Arbeit in dieser Form nicht möglich gewesen wäre.

Mein Dank geht auch an Herrn Prof. Dr. Jörg Schreiber für die vielen interessanten Diskussionen und seine großartige Unterstützung.

Herrn Prof. Dr. Jan Wilkens danke ich für viele wertvolle Informationen zu Fragen der Dosimetrie und Medizinphysik und für die gemeinsamen Filmkalibrierungen, für die er immer Zeit erübrigt hat.

Ganz herzlich möchte ich auch dem gesamten Team vom Tandem Beschleuniger in Garching für die Unterstützung und Hilfe bei der Vorbereitung und Durchführung der Strahlzeiten danken. Ohne deren Hilfe wären all die notwendigen und interessanten Experimente nicht möglich gewesen. Hier möchte ich besonders auch Herrn Walter Carli Dank sagen, der nicht nur jederzeit ein offenes Ohr für meine Fragen hatte, sondern sich auch immer sehr engagiert für die Erfüllung meiner speziellen Wünsche zu einzelnen Bestrahlungen eingesetzt hat.

Ich danke auch der gesamten Rechner-Betriebsgruppe in Garching, die nach wie vor sehr engagiert die Datenaufnahme am Leben erhalten. Mein besonderer Dank gilt Herrn Rudolf Lutter und Herrn Otto Schaile, die bei meinen diversen (Anfangs-) Schwierigkeiten mit "Root" immer hilfreich mit Lösungen zur Seite standen.

Ein Dank geht auch an den "Pulsungsspezialisten", Herrn Raimund Strauß, der längst vergessene Möglichkeiten des Pulsungssystems wieder entdeckt und zu neuem Leben erweckt hat.

Herzlichen Dank auch an die gesamte SNAKE-Gruppe unter der Leitung von Herrn Prof. Dr. Günther Dollinger. Christoph Greubel, Dr. Volker Hable und Christian Siebenwirth

haben für alle gemeinsamen Experimente, ob es nun Detektoren oder Mäuse waren, die bestrahlt wurden, hervorragende Arbeit bei der Präparation des Mikrostrahls geleistet und viele interessante Anregungen für die Experimente gegeben.

Ein besonderer Dank gilt auch Herrn Dr. Andreas Bergmaier, bei dem ich sehr viel über unser spezielles Datenaufnahmesystem sowie Messelektronik im Allgemeinen gelernt habe und der mir viele hilfreichen Korrekturvorschläge gab. Auch hatte er immer den passenden, gerade fehlenden "Einschub" zur Hand, der manche Messungen erst ermöglichte.

Ich danke auch Herrn Wolfgang Draxinger für sein großes Engagement beim Aufbau des Systems und der Durchführung gemeinsamer Experimente.

Maßgeblich für das Gelingen eines jeden Experimentes ist der jeweils verwendete Aufbau. Mein Dank geht deshalb auch an die Mechanischen und Elektronischen Werkstätten der LMU und TU, sowie an Herrn Peter Hartung für die technischen Zeichnungen.

Ich möchte mich auch bei meinen Kollaborationspartnern der Technischen Universität in Prag, allen voran Herrn Dr. Carlos Granja und Herrn Frantisek Krejci, für die gemeinsam durchgeführten Experimente bedanken. Herrn Dr. Stanislav Pospisil und Herrn Dr. Jan Jakubek danke ich dafür, dass sie sich für unser Projekt begeistern konnten und dadurch die Messungen mit dem Timepix-Detektor erst ermöglicht haben.

Dem Team der Laser-Ionen-Beschleunigung, Klaus Allinger, Jianhui Bin und Wenjun Ma danke ich für die gute Zusammenarbeit bei den nächtlichen Experimenten am ATLAS Laser.

Einen herzlichen Dank richte ich auch an Herrn Dr. Martin Hillbrand vom RPTC in München für die Unterstützung bei den Kalibriermessungen.

Dem Team vom HZDR in Dresden, insbesondere Herrn Dr. Stephan Kraft und Herrn Prof. Dr. Ulrich Schramm, danke ich für die Möglichkeit, Experimente an deren DRACO-Laser durchzuführen.

Christian Richter, Dr. Leonhard Karsch und Dr. Jörg Pawelke vom OncoRay in Dresden möchte ich für den regen Erfahrungsaustausch über Filmdosimetrie danken.

Mein Dank gilt auch Herrn Dr. Robert Andritschke für die Hilfe mit dem Clustersearch Algorithmus sowie Herrn Dr. Stefan Schell für die Hilfe bei den Geant4 Simulationen.

Last, but not least, gilt mein besonderer Dank meinen Eltern, die mich in allem meinem Streben immer ermuntert und bedingungslos unterstützt haben. Ohne sie wäre all dies nicht möglich gewesen.

Diese Arbeit wurde durch den DFG Exzellenzcluster "Munich Center for Advanced Photonics (MAP)" finanziert.